



UNIVERSITÉ CATHOLIQUE DE LOUVAIN

LPHYS2299 - MASTER'S THESIS

---

Cascade collapse dynamics of the  
thermohaline circulation and the  
Greenland ice sheet in the  
SURFER climate model

---

*Professeur :*  
Michel CRUCIFIX

*Travail réalisé par :*  
Amaury LARIDON

École de Physique  
Faculté des Sciences

19 mai 2024

## Table des matières

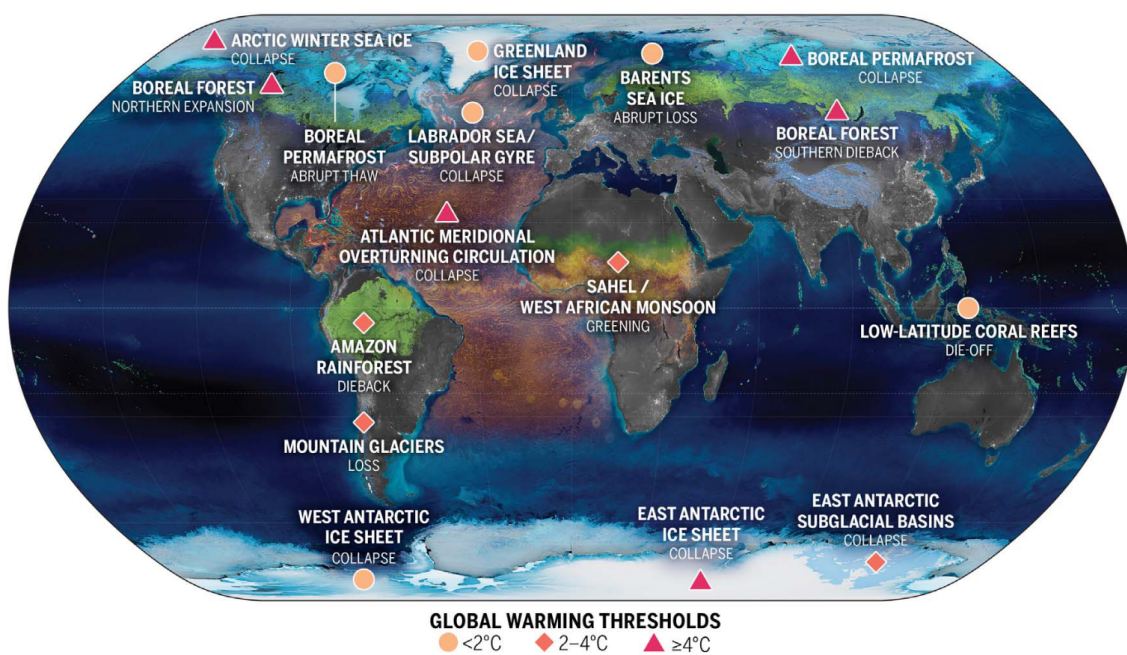
<b>1</b>	<b>Introduction</b>	<b>1</b>
<b>2</b>	<b>Chapter I - The Dynamics of Cascade Collapse in AMOC and GIS : Understanding the Knowledge</b>	<b>1</b>
2.1	Tipping in the Earth Climate System . . . . .	1
2.1.1	Tipping point, Tipping Element and Tipping Cascade . . . . .	1
2.1.2	Why should we care about Tipping Elements, what are their impacts ? . . . . .	6
2.2	The mathematical and physical dynamics behind tipping . . . . .	10
2.2.1	The limitations of the Earth System Models (ESM) approach . . . . .	10
2.2.2	The Dynamical System Theory . . . . .	10
2.3	AMOC, role in climate, dynamics and impact of its collapse . . . . .	24
2.3.1	The AMOC and its role in climate . . . . .	25
2.3.2	The AMOC as a Tipping Element . . . . .	26
2.3.3	What could be the impacts of an AMOC collapse ? . . . . .	33
2.3.4	An AMOC-GIS Cascade Collapse . . . . .	35
2.4	An AMOC-GIS Cascade Model . . . . .	39
2.4.1	The Couplet model for the AMOC-GIS Cascade . . . . .	39
2.4.2	The limitations of the model . . . . .	41
<b>3</b>	<b>Chapter II - Integrating an AMOC-GIS Cascade Model into a Climate Model</b>	<b>1</b>
3.1	Motivation for Linking a Tipping Cascade Model with a Carbon Cycle-Climate Model . . . . .	1
3.2	A Reduced Model Named SURFER . . . . .	4
3.2.1	The evolutions of SURFER . . . . .	4
3.2.2	The Tipping Element Module in SURFER v3.1 . . . . .	6
3.2.3	The Shortcomings of SURFER v3.1 in Modeling the Cascade Collapses of AMOC and GIS . . . . .	7
3.3	AMOC-GIS Tipping Cascade Calibration Model (AGTCCM) . . . . .	8
3.3.1	The AMOC-GIS Model in AGTCCM . . . . .	10
3.3.2	The Calibration Algorithm in AGTCCM . . . . .	18
3.3.3	Validation Test : Calibration with the model itself . . . . .	33
3.4	Calibration with cGenie . . . . .	40
3.5	Limitations of the AGTCCM and Paths for Improvement . . . . .	53
3.5.1	Limitations of the Conceptual Approach . . . . .	55
3.5.2	The Hypothesis of Forcing Independence . . . . .	56
3.5.3	Limitations of the AMOC-GIS Model and Paths for Improvement . . . . .	58
3.5.4	Limitations of the Calibration Module and the best trade-off . . . . .	60
3.6	SURFER v3.2, coupling AGTCCM with SURFER v3.1 . . . . .	68
3.6.1	Modification of the carbon cycle model of SURFER . . . . .	70

<b>4 Chapter III - Results and Discussion</b>	<b>1</b>
4.1 Methodology . . . . .	1
4.2 Discontinuities in the carbon cycle . . . . .	3
4.2.1 Results . . . . .	3
4.2.2 Discussion . . . . .	6
4.3 Cascade collapse of the AMOC-GIS in SURFER v3.2 . . . . .	8
4.3.1 Results . . . . .	9
4.3.2 Discussion . . . . .	16
4.4 Overshooting phenomena in the bifurcation diagram . . . . .	25
4.4.1 Results . . . . .	25
4.4.2 Discussion . . . . .	28
<b>5 Conclusion and outlook</b>	<b>1</b>
5.1 <i>Tipping Points, Tipping Elements and Tipping Cascade</i> . . . . .	1
5.2 The Importance of the AMOC and the GIS as Tipping Elements . . . . .	1
5.2.1 AMOC . . . . .	1
5.2.2 GIS . . . . .	2
5.3 The Physical Coupling Mechanisms for the AMOC-GIS Tipping Cascade . . . . .	2
5.4 A Simplified AMOC-GIS Model Capable of Emulating Complex Models . . . . .	3
5.5 SURFER v3.2, the integration of the AGTCCM into SURFER, and its impact on the carbon cycle . . . . .	5
5.6 Cascade Collapses of the AMOC-GIS . . . . .	6
5.6.1 AMOC collapses . . . . .	6
5.6.2 GIS collapses . . . . .	7
5.6.3 Overshoot Without Tipping . . . . .	7
5.6.4 The innovative methodology of the AGTCCM and its perspectives . . . . .	7
<b>Références</b>	<b>9</b>

**Foreword**

**Acknowledgements**

# Introduction



# 1 Introduction

1. What is the effect of a realistic coupling between the AMOC and the GIS on their collapse dynamics ?
  - (a) What are tipping points, tipping elements, and tipping cascades ?
  - (b) What is the importance of the AMOC and the GIS on future climate ?
  - (c) What are the important physical coupling phenomena to consider for their potential cascading collapses ?
  - (d) How to construct a simplified emulation of the AMOC-GIS dynamics that can be calibrated on hysteresis from complex models ?
  - (e) How can we coherently integrate this calibration module for AMOC-GIS couplings into the SURFER model ?
  - (f) What cascade collapse dynamics can we create with these couplings ?
2. What is the effect on the carbon cycle of an AMOC collapse ?

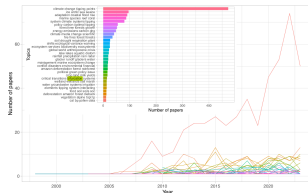


FIGURE 1 – Number of papers through the years for different topics in climatology. Unique topic clusters generated using BERTopic ranked by the associated volume of publications within each. Figure from Global Tipping Report 2023.[75]

# Chapter I - The Dynamics of Cascade Collapse in AMOC and GIS : Understanding the Knowledge



## 2 Chapter I - The Dynamics of Cascade Collapse in AMOC and GIS : Understanding the Knowledge

### 2.1 Tipping in the Earth Climate System

#### 2.1.1 Tipping point, Tipping Element and Tipping Cascade

This thesis focuses on the Atlantic Meridional Overturning Circulation (AMOC) and the Greenland Ice Sheet (GIS), which are referred to as *tipping elements* capable of exhibiting *cascading collapse* behavior. The terms *tipping point*, *tipping element*, and *tipping cascade* have become increasingly prevalent and widely used in climatology, to the extent that they have become some of the most popular themes in publications [75], but what do they mean ? Before delving into the study of potential cascade collapses between the thermohaline circulation and the GIS, and their modeling through an original methodology, we must **address this initial scientific question (1a)** to grasp the big picture within which our scientific research question fits.

#### Tipping Point

Here is the definition provided by the IPCC Glossary [1] of a tipping point.

**Tipping point :** *A critical threshold beyond which a system reorganizes, often abruptly and/or irreversibly. See also Tipping element, Irreversibility and Abrupt change.*

While these definitions may appear theoretical, everyday examples illustrate the notion of tipping points. Consider a chair. Common experience tells us that a chair is in a state of *equilibrium* when resting on its four legs. Even without a rigorous mathematical definition, we are inclined to intuitively say that this equilibrium is *stable*. By stable, we mean that unless someone deliberately lifts and tips the chair by making a very large movement, the chair will never fall. However, in addition to this initial equilibrium, we are all aware of another of a distinctly different nature with which we sometimes engage. This is the one where we create an angle between the chair's backrest and the vertical by pushing with our legs once seated on the chair. Once on these two back legs, it is possible to achieve a new equilibrium. Yet, any slight movement forward or backward moves us away from this equilibrium. Although this has not yet been formally defined, we are inclined to characterize this latter equilibrium as *unstable* because we have the intuition that, once in this position, even a tiny change in the force we exert with our legs could cause us to tip backwards or forwards. Finally, if we lean a bit too much on our legs once we are in this unstable equilibrium with the tilted chair, we will fall backward until we painfully reach the ground. We will have reached the third equilibrium of the system, which is the chair lying on the ground with the backrest touching the

floor. If we revisit our notion of stability defined intuitively earlier, we would similarly say that this latter equilibrium is stable because only a significant and substantial effort to lift the chair will be able to move it out of this equilibrium. The critical force exerted in our legs, causing us to fall backward when we depart from this unstable equilibrium to reach another equilibrium (stable in our case), aligns with the concept of a tipping point as defined earlier and also in the dynamical systems literature. Drawing an analogy from Tim Lenton[43], we understand that the tipping point is the critical threshold at which a small perturbation can fundamentally alter the state or trajectory of a system. In essence, it represents the juncture where "small things can make a big difference".

Moreover, the IPCC defines a tipping point as a critical threshold from which the system can reorganize in an *abrupt* manner. Formally, a change is considered abrupt when it significantly outpaces historical rates of change in the system. Drawing from our chair analogy, we can interpret this as the rapid descent of the chair's backrest compared to its gradual movement into an unstable equilibrium on its back legs.

Another crucial aspect emphasized by the IPCC is *irreversibility*. In the IPCC glossary, irreversibility refers to a perturbed state of a dynamical system that persists longer than the timescale of interest, indicating that natural processes take substantially longer to restore equilibrium. Returning to our analogy, irreversibility means that once the chair has fallen (our perturbed state), without intervention, it will remain in that state indefinitely, unable to return to its previous equilibrium. In this specific scenario, the recovery time from the collapsed state is infinite.

Beyond our office chair, tipping points are present in many places in nature [39, 84]. One area where tipping points are also prevalent, and which is of significant importance and consequences for us, is in the climate, as captured by the concept of tipping elements.

## Tipping Element

But what relevance does this analogy with chairs have for our climate system ? As highlighted in a highly influential paper by Tim Lenton et al. in 2008 [43], there are large components of the Earth System that may reach a tipping point. These components are referred to as tipping elements.

In 2023, a comprehensive synthesis directed by T. Lenton of all our knowledge on tipping points was published. Tipping elements are present in all major components of the climate (see Figure (2)), including the atmosphere, hydrosphere, biosphere, and cryosphere. In total, more than 25 Earth system tipping elements were identified in this synthesis report, the *Global Tipping Point Report 2023* [75], based on evidence of past changes, observational records, and computer models. In the cryosphere, six Earth system tipping points were identified, including large-scale tipping points for the Greenland Ice Sheet and Antarctic ice sheets. In the biosphere, 16 Earth system tipping points were identified, while

in ocean and atmosphere circulations, four Earth system tipping points were identified : the AMOC, the North Atlantic Subpolar Gyre (SPG), the Southern Ocean Overturning Circulation, and the West African monsoon.

However, despite their abundance, each tipping element is unique and possesses its own dynamics leading to critical thresholds beyond which collapse may begin to occur. To understand this, another key concept for studying tipping elements is that of *feedback mechanisms*. A feedback mechanism (or feedback loop) is a closed loop of causality whereby a change in a system feeds back to amplify or dampen that change. Feedback mechanisms can be mathematically positive or negative, depending on whether they amplify or dampen the effects of a change. Tipping can occur when amplifying/reinforcing (positive) feedback mechanisms overwhelm damping/balancing (negative) ones and become strong enough to support self-perpetuating change.[75] Feedback mechanisms are specific to the physics of the tipping element under consideration, and it is through the identification and study of these mechanisms that we are able to attribute, as shown in Figure (2), critical warming thresholds beyond which collapse is highly probable.

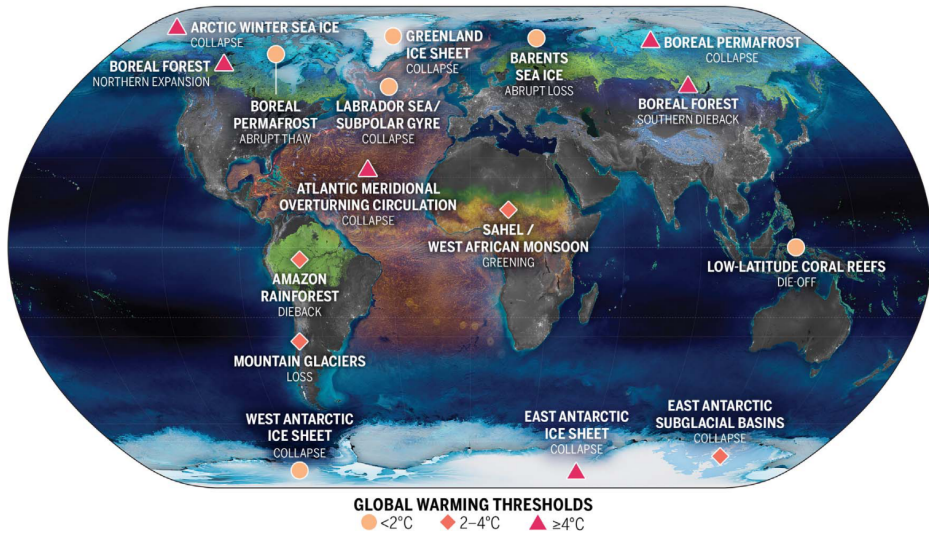


FIGURE 2 – *The location of climate tipping elements in the cryosphere (blue), biosphere (green), and ocean/atmosphere (orange), and global warming levels at which their tipping points will likely be triggered. Figure from Armstrong McKay et al./2]*

Indeed, as illustrated in Figure (2), certain tipping elements such as the West Antarctic Ice Sheet (WAIS) and the Greenland Ice Sheet (GIS) could collapse with a global average temperature warming of less than  $2^{\circ}\text{C}$ , while for others such as the East Antarctic Ice Sheet (EAIS), a global average temperature anomaly exceeding  $4^{\circ}\text{C}$  would be required. Figure (3) from the paper by Wang et al. [80] in 2023, based on the most recent scientific knowledge, illustrates approximate time frames over which some tipping elements might be expected to respond to climate forcings. However, as this latter figure already demonstrates,

significant uncertainties remain regarding many tipping elements, and their collapse strongly depends on emission scenarios and thus on the societal choices we will make in the future. Furthermore, beyond the issue of the inability to currently obtain a very precise value of the critical threshold in terms of temperature anomaly, and thus of  $CO_2$  emissions, it is not only the forcing of  $CO_2$  that matters. For example, tipping elements such as the Indian summer monsoon, as well as the Amazon rainforest and the Sahel, are sensitive to localized aerosol pollution. Therefore, a thorough investigation using observations, past climate data, models, and numerical simulations is fundamental to understanding the collapse dynamics specific to each tipping element.

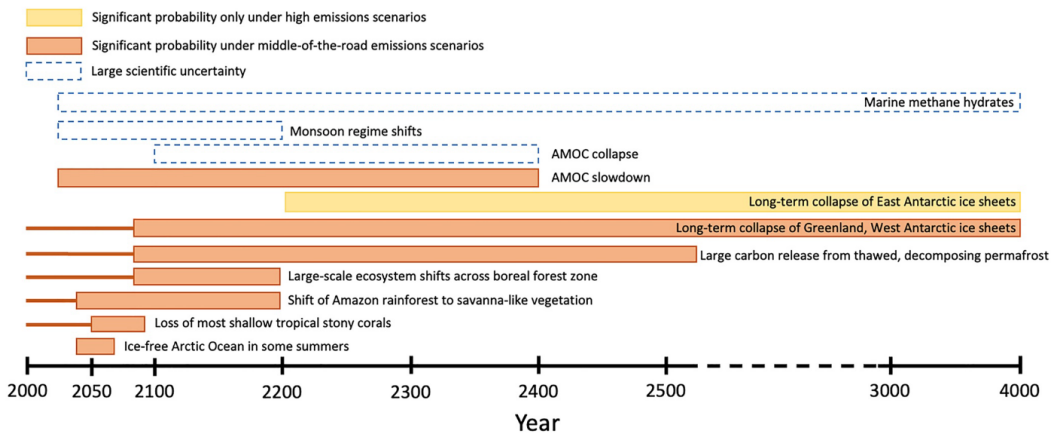
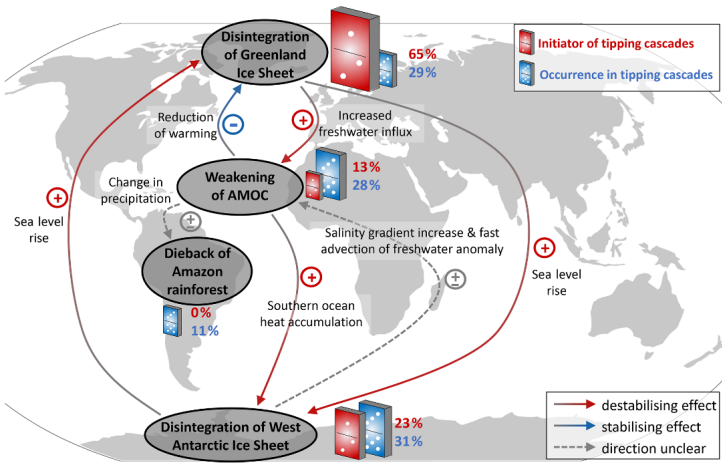


FIGURE 3 – Approximate time frames over which some tipping elements might be expected to respond to climate forcings. Horizontal lines to the left of some bars indicate that while the majority of large-scale system response may be projected to occur at some point in the future for certain Earth system elements, some shifts are already underway and are expected to continue. Figure from Wang et al.[80]

Lastly, it is important to note that the term *tipping point* is also a victim of its increasing popularity and dissemination outside academic circles. As demonstrated earlier, the assessment of whether a component of the climate system is indeed a tipping point can sometimes be subject to debate. As emphasized by Milkoreit et al. [54], there is a risk of abusive labeling of the term *tipping point*, particularly in the social sciences. A common pitfall is to consider situations where big changes make significant differences to a system as tipping points. As reiterated in the *Global Tipping Point Report 2023*, it is crucial to evaluate the strength of amplifying feedback loops and consider the presence of damping feedback loops before asserting the potential existence of a tipping point [75]. To avoid falling into these notational abuses and improve the quality of our analysis, we will establish the foundations of the mathematical framework in subsection (2.1.3), enabling a rigorous analysis and understanding of the physics of tipping elements. In the specific case of interest in this dissertation, which focuses on AMOC and the GIS, we will then meticulously examine the inherent physics of these systems that confer upon them the status of tipping elements.

## Tipping Cascade

Beyond the collapse behaviors specific to each tipping element, they can also interact with each other, leading to what is called a tipping cascade phenomenon. The phenomenon of tipping cascades, akin to the domino effect[38, 45], arises from interactions across space and time among tipping elements, whereby the collapse or even the onset of collapse of one element can facilitate the collapse of others. Due to these interactions, tipping cascades cannot be ruled out on centennial to millennial timescales at global warming levels between 1.5 and 2.0°C, or on shorter timescales if global warming exceeds 2.0°C [88].



**FIGURE 4 – Interactions between climate tipping elements and their roles in tipping cascade.** Where tipping cascade arise, the relative size of the dominoes illustrates how many ensemble members the respective climate component initiates tipping cascade (red domino) or how many tipping cascades the respective climate component occurs in (blue domino). Figure from Wunderling et al.[85]

The known interactions to date between major tipping elements of the climate are represented in Figure (4). As observed, there exist both physical interactions between tipping elements that can be stabilizing, such as, for example, a weakening of the AMOC, which would diminish heat transport towards the North and thereby favor Arctic sea ice growth, as well as destabilizing interactions. An example of this is a weakening of the AMOC, which, by retaining more heat in the South Atlantic, would promote the melting of the West Antarctic Ice Sheet (WAIS). Behind each of these interaction arrows, however, lie sometimes highly complex dynamics, the effects of some of which are not yet fully captured and understood. Thus, caution must be exercised regarding the conception of a clear critical threshold capable of mechanically producing multiple collapses. Contrary to the notion of a distinct threshold, the coupling between subsystems, competing feedbacks, and spatial heterogeneity may promote subtle yet abrupt reorganizations of geophysical flows before a catastrophic tipping point [48]. What is important to understand is that these interactions occur between tipping elements with highly diverse spatiotemporal dynamics and extensions,

which can lead to complex collective collapse dynamics. Therefore, as concluded by Wunderling et al. [88], tipping elements should not only be studied in isolation, but also more emphasis has to be put on potential interactions.

### 2.1.2 Why should we care about Tipping Elements, what are their impacts ?

#### Human activities push Tipping Elements out of equilibrium

The primary justification for the significance of paying attention to tipping elements lies in the fact that contemporary human activities and the consequent emissions of greenhouse gases introduce an additional forcing factor on tipping elements by raising average temperatures, potentially displacing these systems from their present equilibrium state [43]. Thus, while the collapse of certain tipping elements may be characterized as improbable events, this characterization no longer holds if future global warming exceeds  $2^{\circ}\text{C}$ , and certainly not if warming exceeds  $4^{\circ}\text{C}$  [45, 42]. Therefore, the *Global Tipping Point Report 2023* concludes that : "*Global warming is rapidly approaching levels that could trigger individual tipping points in systems that can interact with and destabilize other tipping systems*" [75]. Indeed, it is particularly the assessments of tipping point thresholds that have partly led to the societal aspiration to limit global warming to low levels, such as  $2^{\circ}\text{C}$  or even  $1.5^{\circ}\text{C}$  above pre-industrial levels.[66, 44]

#### Past evidences of Tipping Points

Furthermore, even though we have seen the critical importance of greenhouse gas emissions in potential future tipping point collapses, it is important to note that the disturbance leading to the collapse of a tipping element may not necessarily originate from anthropogenic forcing. Indeed, critical conditions may be reached autonomously, without human interference, and natural variability could trigger a qualitative change [43]. Climate history is already filled with several cases of tipping element collapses, as demonstrated by paleoclimate data and global climate models [3].

#### The *Hothouse* narrative

Based on this consideration, the concept of *planetary scale tipping* has been developed. Planetary scale tipping is a phenomenon of global cascading collapse in the climate involving the collapse of multiple key systems due to global warming. Explored in the seminal paper by Steffen et al. [69], they investigate in this study the risk that self-reinforcing feedbacks could push the Earth System toward a planetary threshold at approximately  $2^{\circ}\text{C}$ , which, if crossed, could prevent stabilization of the climate at intermediate temperature rises and cause continued warming on a "*Hothouse Earth*" pathway even as human emissions are reduced. Crossing this threshold would result in a much higher global average temperature than any interglacial period in the past 1.2 million years and

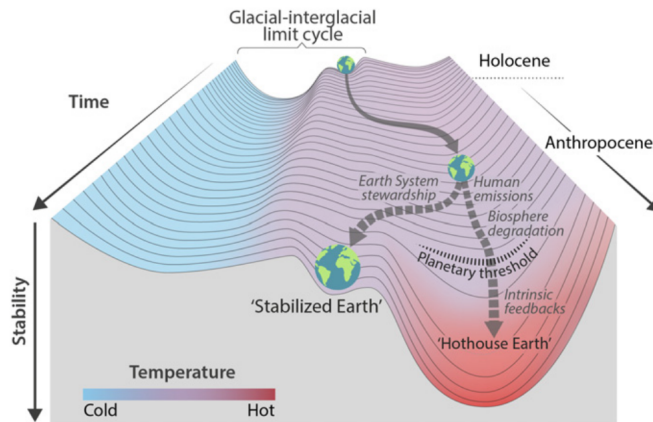


**FIGURE 5 – Stability landscape showing the pathway of the Earth System out of the Holocene and thus, out of the glacial–interglacial limit cycle to its present position in the hotter Anthropocene. Figure from Steffen et al./69]**

significantly higher sea levels than at any time in the Holocene. This trajectory is depicted in Figure (5), with the stability landscape showing the pathway of the Earth System out of the Holocene and thus, out of the glacial–interglacial limit cycle. The fork in the road shows the two divergent pathways of the Earth System in the future : one leading to the Hothouse Earth pathway and the other to the Stabilized Earth pathway. What, then, is the current trajectory, and where do we stand? As stated by the IPCC in AR6 [26] : "There is no evidence of such non-linear responses at the global scale in climate projections for the next century." However, the potential of tipping points to drive a transition to a hothouse climate state within centuries remains unclear, according to Wang et al.[80]. The hothouse narrative is relevant to this thesis because the new version of SURFER that we will create, integrating a more improved and realistic dynamics of the coupling between the AMOC and the GIS, help to better constrain the regimes of emission scenarios that could lead to a hothouse narrative in the future.

### Impacts on Global Mean Temperature

In the case of planetary scale tipping, Steffen et al. [69] conclude that if the threshold is crossed, the resulting trajectory would likely cause serious disruptions to ecosystems, society, and economies [69]. More specifically, what are some examples of impacts resulting from the collapse of tipping elements?

On the global average temperature, tipping elements such as the Amazon rainforest, permafrost, or Arctic sea ice melt will have significant effects on this key climatic variable. Indeed, a collapse of the permafrost, which represents a vast carbon reservoir releasing methane as it thaws, could release an amount equivalent to ten years of current carbon emissions by 2300, making a substantial contribution to global warming [80]. As for the Amazon rainforest, it has been

simulated that the Amazon rainforest dieback scenario under moderate emissions produced an additional  $0.3^{\circ}\text{C}$  of global warming due to enhanced carbon emissions [4]. This is attributed to differences in the role of the Amazon rainforest, which, although currently acting as a carbon sink in the carbon cycle, could become a source if it collapses into a savanna-like ecosystem. This collapse, partly already observed, will result from an irreversible threshold where the forest is no longer able to sustain the regional water cycle, leading to drying and a shift toward a savanna-like ecosystem [51, 23]. As for the impact of Arctic sea ice melt on the global average temperature, this is due to a significant decrease in the albedo of the surface of regions currently covered by sea ice. By altering the radiative balance towards more absorption of solar radiation, additional warming of the atmosphere compared to the current state will occur. Thus, Wang et al. [80] show that by 2100, the additional warming from these tipping elements is approximately  $0.13^{\circ}\text{C}$  (low :  $0.06^{\circ}\text{C}$ , high :  $0.23^{\circ}\text{C}$ ) under SSP2-4.5 and approximately  $0.21^{\circ}\text{C}$  (low :  $0.10^{\circ}\text{C}$ , high :  $0.36^{\circ}\text{C}$ ) under SSP5-8.5 relative to the original scenarios. By 2300, they find that the selected tipping elements may produce additional warming of approximately  $0.24^{\circ}\text{C}$  (low :  $0.11^{\circ}\text{C}$ , high :  $0.49^{\circ}\text{C}$ ) under SSP2-4.5 and approximately  $0.52^{\circ}\text{C}$  (low :  $0.24^{\circ}\text{C}$ , high :  $1.09^{\circ}\text{C}$ ) under SSP5-8.5 relative to the original scenarios. Hence, it is more readily understood that if these tipping elements collapse and thereby increase the global average temperature, they will also contribute to the forcing of other tipping elements that may further promote their cascading collapses.

## Impacts on Human Societies

During the 22nd century, under middle-of-the-road emissions scenarios, there is a significant probability that the Amazon rainforest, AMOC, and permafrost will reach their critical thresholds and irreversibly collapse [2, 80]. Such collapses of these systems have the potential for severe impacts on water, food and energy security, health, ecosystem services, communities, and economies [75]. In a more general sense, regardless of the tipping point considered, as concluded by the *Global Tipping Point Report 2023*, the full damage caused by negative tipping points will be far greater than their initial impact. Indeed, the effects will cascade through globalized social and economic systems, and could exceed the ability of some countries to adapt. Negative tipping points indicate that the threat posed by the climate and ecological crisis is far more severe than commonly understood and is of a magnitude never before faced by humanity [75].

In terms of impacts, however, it should be noted that significant changes in the state of the considered tipping element may occur either directly after the trigger or much later [43]. As detailed further in section (2.2.4), this is typically the case for cryospheric components such as the Greenland Ice Sheet or Antarctic Ice Sheet, with their potential sea level rise of approximately 70 meters.[55] Indeed, for the Greenland Ice Sheet (GIS), its critical threshold is likely to be

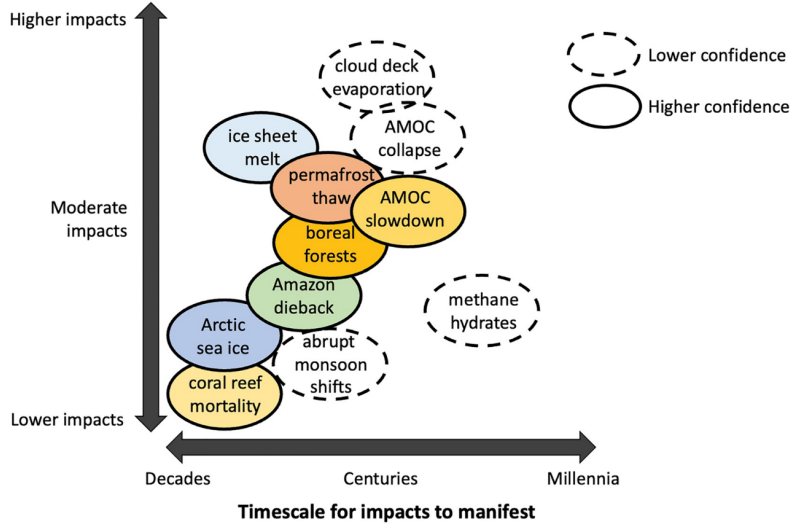


FIGURE 6 – Qualitative two-dimensional organization of individual candidate tipping elements. Candidate tipping elements are organized vertically according to expected negative global-scale climate impacts upon human societies considering added warming potential, sea-level rise, ecosystem shifts, and atmospheric and oceanic circulation changes (y-axis) and horizontally based on the timeframe over which those impacts are expected to manifest under a middle-of-the-road to high-end emissions scenario. Figure from Wang et al./80]

reached within decades as the literature associates its critical threshold with a global mean warming of  $1.5^{\circ}\text{C}$ , but its total melt will not occur for over 1000 years due to the significant inertia involved in melting such a large amount of ice. However, once this threshold is reached, collapse may be irreversible, or in other words, unstoppable.[75] Thus, as shown in Figure (6), it is essential to consider the impacts implied by each tipping element based on the characteristic time scales inherent in its dynamics.

Therefore, given the increasingly critical proximity of certain tipping elements due to climate change, the past existence of cascading collapses, and the considerable impacts such collapses would have on human societies, studying tipping elements is fundamental. While there is still much uncertainty about the exact state of certain tipping elements and the location of their critical collapse thresholds, as T. Lenton et al. [44] assert, tipping elements are "*Too risky to bet against.*" In addition to advancing our broader understanding of tipping phenomena in nature, beyond just climate, it is essential, for the purpose of guiding and constraining mitigation and adaptation policies, to have an excellent research paradigm on tipping points. This is certainly true for the AMOC and the GIS, which, as we will later present, are the prime candidates for tipping elements capable of triggering cascading collapses, making their study highly relevant and necessary.

## 2.2 The mathematical and physical dynamics behind tipping

It is now clear that tipping elements are a fundamental and urgent subject of study. In this subsection, we aim to explain the research paradigm used thus far. We will discuss the limitations of the approach of high-resolution models, such as Earth System Models (ESMs), to introduce the most commonly used research methodology, which provides the best results : the theory of nonlinear dynamical systems. **This, along with the numerous concepts that will be introduced, will be essential to address our main scientific methodological question (1.4) : how to model, in a simplified and realistic manner, the dynamics of cascade collapse phenomena between the AMOC and the GIS.**

### 2.2.1 The limitations of the Earth System Models (ESM) approach

Earth System Models integrate a representation of all components of the climate system. While they are the ideal candidates for quantifying the complex interactions between tipping elements ([69, 75]), so far, cascade collapse simulations have only been conducted in models of reduced complexity or conceptual models[68]. There are two reasons for this. The first is due to a lack of integration in the latest generation of Earth System Models of essential process modeling capabilities related to tipping elements, such as the Amazon rainforest, primarily due to the absence of dynamic vegetation models. Thus, by not achieving sufficient parameterization of the interactions between the tipping elements, current Earth System Models are suspected to exhibit a bias towards excessive stability concerning tipping elements.[46] The second reason for the lack of their use in studying tipping elements is due to operational constraints. Running fully coupled simulations of Earth System Models with all the climatic components they contain is excessively computationally intensive. However, in the case of tipping elements, and this is particularly true for those arising from the cryosphere, the time scales involved span several centuries to thousands of years. However, within the couplings, for instance, between components of the cryosphere and the atmosphere, certain dynamics may occur on considerably smaller time and space scales. Therefore, it is practically almost impossible with Earth System Models to study these various time scales at the same time. This is why, in contrast to the methodology of achieving the finest possible description of the physics of the climatic components supported by Earth System Models, research on tipping points has turned more towards conceptual models.

### 2.2.2 The Dynamical System Theory

The approach used by conceptual models aims primarily to describe the interactions among tipping elements and the first-order dynamics that create their potential collapse behavior. The mathematical framework employed for this

purpose is that of dynamical system theory, and more specifically, nonlinear dynamics. In this type of model, each tipping element  $x_i$  with its own typical time scale  $\tau_i$  is described by an ordinary differential equation (ODE), within which is also the variable associated with other tipping elements  $x_j$  [86, 87]. Thus, with a system of coupled ODEs, the aim is to describe the state and interactions among the tipping elements using coupling coefficients  $s_{ij}$  for interaction calibrations. To describe forcing, such as temperature  $\Delta GMT$  on the tipping elements, prescribed functions can be added, or an Energy Balanced Model can be used. With calibration coefficients, where in this case  $T_{limit,i}$ , can encode the critical bifurcation threshold specified for each tipping element. Typically, the ODE associated with a tipping element takes the following form in this type of approach :

$$\frac{dx_i}{dt} = \left\{ -x_i^3 + x_i + \frac{\Delta GMT}{T_{limit,i}} + d \sum_{j,j \neq i} s_{ij}(x_j + 1) \right\} \frac{1}{\tau_i} \quad (2.1)$$

The first obvious advantage of this approach is that we have a generic representation of each tipping element, making the model for each tipping element much simpler to construct than if we had to model the actual physical interactions occurring in the dynamics of the system under consideration.[15] A second, no less important advantage relates to the operational use of this type of model. Being a simple network of ODEs, these models are extremely lightweight to run on computers, allowing for a large number of simulations in a short amount of time. Finally, and this is what we will develop further in the remainder of this subsection, this type of model allows us to use tools and concepts from nonlinear dynamics analysis, which enable us to better understand what is happening in our tipping element and tipping cascade model.

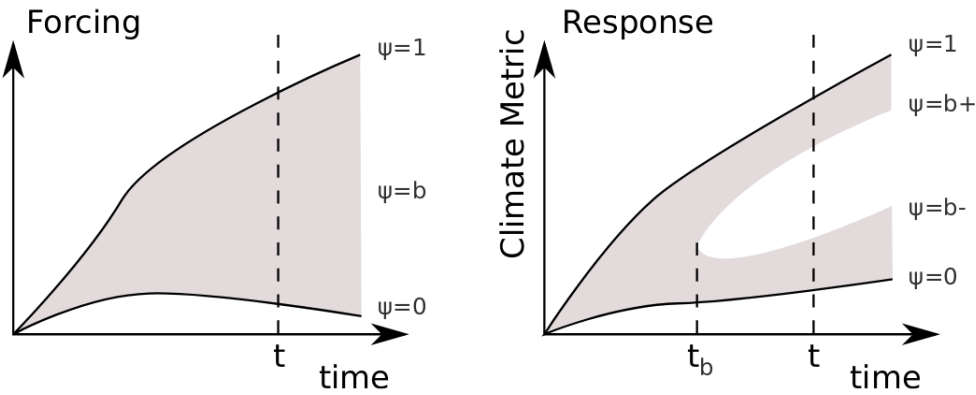


FIGURE 7 – Response of a conceptual model to a family of forcing which shows a discontinuity in a specific climate metric  $\Psi$ . Figure V.Couplet.[15]

With this type of model, we aim to investigate the occurrence of tipping element collapse if, for a family of forcing scenarios of our system (we can consider a

family of functions  $\Delta GMT$  encoding different scenarios in our equation (2.1), a certain climatic metric denoted as  $\Psi$  exhibits a discontinuity in response to the model output. This is illustrated in Figure (7). The climatic metric used can vary, such as, for example, sea level rise (SLR), the globally averaged temperature, or the state of a tipping element.

### Concepts of Non-Linear Dynamics

To understand why the canonical form of the model described in equation (2.1) takes the specific form of a third-order polynomial, one must delve into the theory of nonlinear dynamics. This theory also provides numerous concepts useful for the analysis of these systems; we will introduce those essential for us within the scope of this thesis, which will be utilized in constructing our simplified model of AMOC-GIS dynamics and in analyzing the results. This entire introductory section to the key concepts of nonlinear dynamics is primarily based on the excellent reference book in this field by S. Strogatz.[73]

### Dynamical System, Trajectory, and Phase Space

A dynamical system is a system whose temporal evolution is governed by a specific law. In this discussion, we will focus solely on deterministic systems, where knowledge of an initial condition corresponds to a unique future state at every subsequent moment. There are two primary categories of dynamical systems : **differential equations** and **iterated maps**. We will concentrate on differential equations since they describe the evolution of systems in continuous time, as opposed to iterated maps which operate in discrete time. Therefore, a general dynamical system with  $n$  variables  $x_i$  takes the following form :

$$\frac{dx_i}{dt} = f(x_1, \dots, x_i, \dots, x_n) \quad (2.2)$$

where the function  $f$  encodes the law or dynamics of the system under consideration. A major challenge in the laws governing climate physics is that they are predominantly nonlinear. Even the first-order descriptions of tipping elements can be nonlinear functions of the states of the considered tipping elements. The fact that the function  $f$  is generally a nonlinear function of the variables  $x_i$  complicates the analytic solution of these equations, often rendering them insoluble without resorting to approximation techniques and linearization.

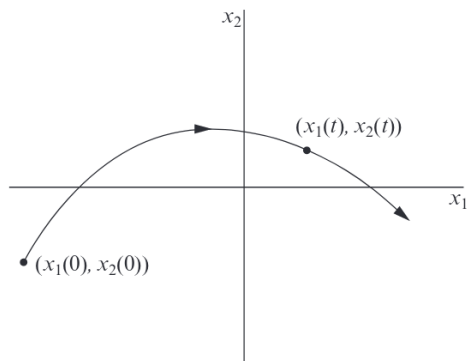


FIGURE 8 – Representation of a trajectory and phase space for a two-dimensional system. Figure from S.Strogatz.[73]

Consider, for example, the description of the motion of a simple pendulum, where  $x_1(t)$  encodes its position and  $x_2(t)$  its velocity. Constructing an abstract space with coordinates  $(x_1, x_2)$ , the solution to the pendulum's equations of motion,  $(x_1(t), x_2(t))$ , corresponds to a point moving along a trajectory in this space (Figure (8))[73].

The curve is called a **trajectory** and the space is called the **phase space** for the system. The phase space is completely filled with trajectories, since each point can serve as an initial condition. The goal of the nonlinear dynamics approach is to perform this construction in reverse; given the system, we aim to sketch the trajectories, thereby extracting information about the solutions. In many cases, geometric reasoning will allow us to sketch the trajectories without actually solving the system![73] This is the strength of dynamical systems theory.

### Fixed Points and Stability

One of the most fruitful analytical techniques for this purpose is to interpret differential equations as vector fields. Thus, a general differential equation  $\dot{x} = f(x)$  can be depicted as in Figure (9).

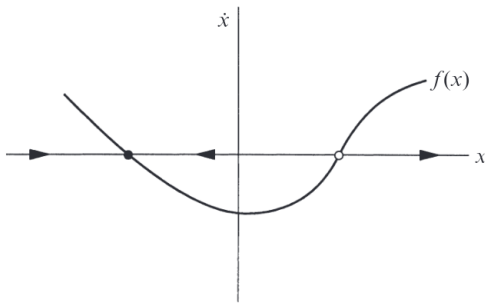


FIGURE 9 – Interpretation of the Differential Equation  $\dot{x} = f(x)$  as a Vector Field. Figure from S.Strogatz.[73]

The equation  $\dot{x} = f(x)$  represents a **vector field** on the line, which dictates the velocity vector  $\dot{x}$  at each point  $x$ . A useful convention is to represent the sign of the velocity vector at each point  $x$  with an arrow on the  $x$ -axis. The arrows point to the right when  $\dot{x} > 0$  and to the left when  $\dot{x} < 0$ . A more physical way to interpret this vector field is to imagine a fluid flowing steadily along the  $x$ -axis, with a velocity that varies from place to place, according to the rule  $\dot{x} = f(x)$ . As shown in Figure (9), the

**flow** is to the right when  $\dot{x} > 0$  and to the left when  $\dot{x} < 0$ . At points where  $\dot{x} = 0$ , there is no flow. Such points are therefore called **fixed points**. There are two main types of fixed points, both represented in Figure (9). The solid black dots represent what are called **stable fixed points**, also sometimes referred to as **attractors** or **sinks**, because the flow moves toward them. Conversely, open circles represent **unstable fixed points**, also called **repellers** or **sources**, as the flow moves away from them.

In terms of semantics, the Figure (9), when showing all the different qualitative trajectories of the system, is also referred to as a phase portrait. It is understood that the appearance of this **phase portrait** is controlled by the position and nature of the fixed points it contains. Mathematically, for the original differential equation, fixed points represent **equilibrium** solutions. Thus, we understand why the paradigm of dynamical systems theory becomes a theory of dynamic

equilibria, as it is the study of the nature and position of these equilibria that allows for a qualitative reasoning-based intuition of the actual evolution of the system, without the need to explicitly solve the overly complex equations.

We will call an equilibrium stable if all sufficiently small disturbances away from it damp out in time. Thus, stable equilibria are represented geometrically by stable fixed points. Conversely, unstable equilibria, in which disturbances grow in time, are represented by unstable fixed points.[73] It is important to note that when we speak of disturbances, we consider "reasonably small" disturbances. Hence, to emphasize this, we sometimes refer to points as *locally stable* compared to *globally stable* points, for which even a very large disturbance does not cause them to change equilibrium points after some time. To have an analytical criterion for analyzing equilibrium stability, a common technique is to linearize the system near its equilibrium point. Indeed, if we linearize the nonlinear system near a fixed point  $x^*$  based on a small disturbance  $\eta(t) = x(t) - x^*$ , we obtain, using the fact that  $x^*$  is a fixed point,  $\dot{\eta} \approx \eta f'(x^*)$  at first order. Thus, we understand that a disturbance  $\eta(t)$  grows exponentially if  $f'(x^*) > 0$  and decays if  $f'(x^*) < 0$ . This allows for a quantitative measure of the stability of a fixed point based on the magnitude of  $f'(x^*)$ . This magnitude plays the role of an exponential growth or decay rate. Moreover, its reciprocal  $1/|f'(x^*)|$  serves as a characteristic time scale ; it determines the time required for  $x(t)$  to significantly vary in the neighborhood of  $x^*$ .

Another way to visualize the dynamics of systems of the form  $\dot{x} = f(x)$  is based on the physical idea of potential energy. As described in S. Strogatz [73], we can picture a particle sliding down the walls of a potential well, where the *potential*  $V(x)$  is defined by,

$$f(x) = -\frac{dV}{dx}. \quad (2.3)$$

The negative sign in the definition of  $V$  follows the standard convention in physics ; it implies that the particle always moves “downhill” as the motion proceeds. Using the chain rule, we can compute that,

$$\frac{dV}{dt} = - \left( \frac{dV}{dx} \right)^2 \leq 0. \quad (2.4)$$

Thus,  $V(t)$  decreases along trajectories, and so a particle describing this dynamics always moves toward lower potential. Of course, if the particle happens to be at an equilibrium point where  $dV/dx = 0$ , then  $V$  remains constant. This is to be expected since  $dV/dx = 0$  implies  $\dot{x} = 0$  ; equilibria occur at the fixed points of the vector field. Note that local minima of  $V(x)$  correspond to stable fixed points, as we expect intuitively, and local maxima correspond to unstable fixed points. Figure (10) depicts the graph of the potential of the system  $\dot{x} = x - x^3$ , on which we can intuitively identify two local equilibrium points. This equation is not incidental as it represents the generic form of the model described earlier in equation (2.1).

Furthermore, revisiting Figure (5), we can better understand it based on this newly introduced concept. Stability on the vertical axis is defined here as the inverse of the potential energy of the system. Systems in a highly stable state (deep valley) have low potential energy, and considerable energy is required to move them out of this stable state. Systems in an unstable state (top of a hill) have high potential energy, and they require only a little additional energy to push them off the hill and down toward a valley of lower potential energy.

### Bifurcations and the Saddle-node

What we have described so far in the general form of a system  $\dot{x} = f(x)$  can be used to represent the internal dynamics of a tipping element. However, how can we account for additional terms of external forcings such as temperature? This involves adding into the dynamics of our system the dependence on certain parameters. As one might expect, and as we will see with simplified dynamics, the qualitative structure of the flow can change as parameters are varied. In particular, fixed points can be created or destroyed, or their stability can change. These qualitative changes in the dynamics are called **bifurcations**, and the parameter values at which they occur are called **bifurcation points**. Bifurcations will be fundamental in our analysis as they provide models of transitions and instabilities as some control parameter is varied.

The **saddle-node bifurcation** is the basic mechanism by which fixed points are created and destroyed. As a parameter is varied, two fixed points move toward each other, collide, and mutually annihilate. In addition to illustrating the concept, this type of bifurcation will be useful for understanding the bifurcation model by which we will approximate the first-order dynamics of the tipping elements, which will heavily rely on the saddle-node bifurcation. The prototypical example of a saddle-node bifurcation is given by the first-order system

$$\dot{x} = r + x^2 \quad (2.5)$$

where  $r$  is a parameter that may be positive, negative, or zero. As shown in Figure (11), when  $r$  is negative, there are two fixed points, one stable and one unstable. As  $r$  approaches 0 from below, the parabola moves up and the two fixed points move toward each other. When  $r = 0$ , the fixed points coalesce into a half-stable fixed point at  $x^* = 0$ . This type of fixed point is extremely delicate—it vanishes as soon as  $r > 0$ , and now there are no fixed points at all.

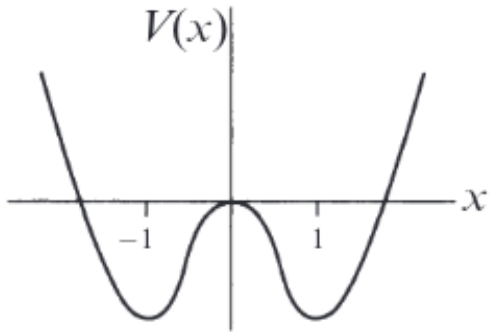


FIGURE 10 – Potential of the  $\dot{x} = x - x^3$  system. Figure from S.Strogatz.[73]

In this example, we say that a **bifurcation** occurred at  $r = 0$ , since the vector fields for  $r > 0$  and  $r < 0$  are qualitatively different. Another important concept that will be reused in this case is that of **normal forms**. In the case of the saddle-node bifurcation, the equation  $\dot{x} = r \pm x^2$  actually generically describes all saddle-node bifurcations on the line. The idea is that near the bifurcation point, the dynamics locally around the equilibrium points typically resemble a form  $r \pm x^2$ .

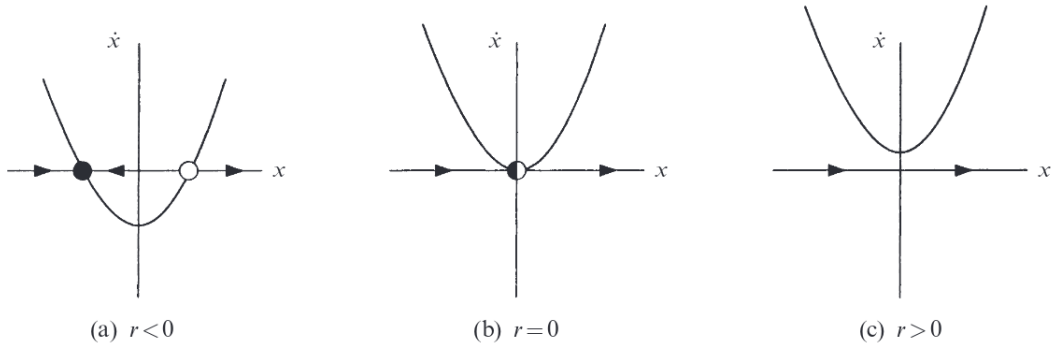


FIGURE 11 – Illustration of a saddle-node bifurcation. Figure from S.Strogatz.[73]

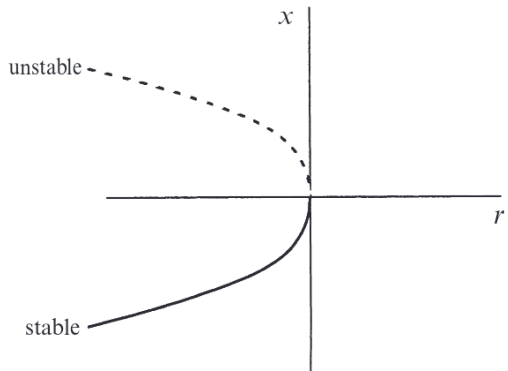


FIGURE 12 – Bifurcation Diagram of a saddle-node bifurcation on the line. Figure from S.Strogatz.[73]

In addition to the graphical conventions of arrows already introduced, as well as filled or unfilled points to express the stability of the considered fixed point, the most common way to depict the bifurcation is to invert the axes and plot the bifurcation parameter  $r$  as a variable. This type of figure is depicted in Figure (12) and represents what is called a **bifurcation diagram**. We will extensively use this concept later to analyze and understand the cascade collapse dynamics of the AMOC and the GIS.

Based on all these concepts, we can visually understand a tipping point by

representing the **potential landscape** or the **attractor** associated with the underlying dynamical system as shown in Figure (13). By attractor, we mean the topological variety around an equilibrium point such that if the trajectory lies on it, after some time the system's state will return to the equilibrium point. A general sufficient definition in our case is therefore to say that an attractor is the set of points in the phase space to which all neighboring trajectories converge.[73] On Figure (13), we understand that the system starts in blue on the left in one of the two stable equilibrium states represented by the ball in the

left valley. Under external forcing over time (left to right), which is a bifurcation parameter, this state loses stability (purple), represented by the valley getting shallower, lowering the hilltop. Past a tipping point, the initial stable state disappears, and the system undergoes an abrupt, self-propelling change into the alternative, remaining stable state (red).[75]

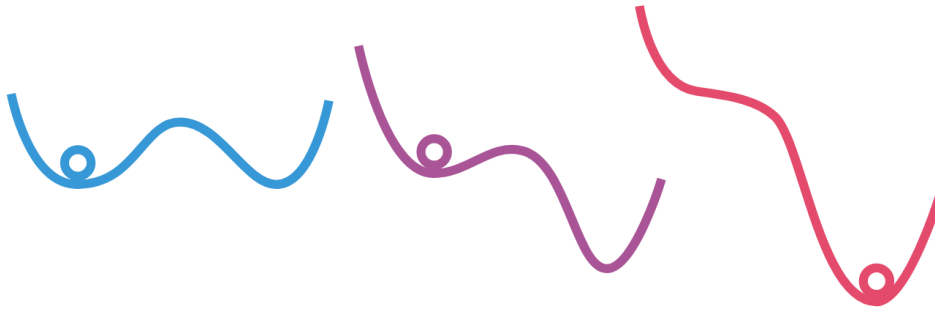


FIGURE 13 – *Schematic representation of the forcing of a dynamic system until a tipping point is reached. Figure from Global Tipping Report 2023.[75]*

### Double-fold Bifurcation and Tipping Elements

Although there are mathematically numerous possible bifurcations, the most common one that appears to best model what is observed in the dynamics of tipping elements is known as the **Double-Fold Bifurcation**.[43] Indeed, the canonical model for a tipping element is the double fold, where a slow-varying control/bifurcation parameter causes the system to evolve in a quasi-adiabatic manner and leads to an abrupt transition when a critical threshold is crossed.[15]. We introduced the fold bifurcation because the principle of the double-fold bifurcation is simply, as its name suggests, having two possible fold bifurcations based on the existence of two equilibria instead of one. To achieve this, the potential function of a generic double fold is described in Figure (10) and the normal form of this type of dynamics is the following equation :

$$\frac{dx}{dt} = -x^3 + x. \quad (2.6)$$

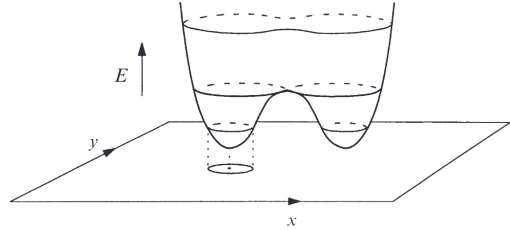


FIGURE 14 – *Energy Surface of the double well potential associated to a double-fold bifurcation. Figure from S.Strogatz.[73]*

Of course, the dynamics of natural systems and, in our case, tipping elements that we will need to model are often more complex than one-dimensional dynamics as presented so far. However, the framework of nonlinear dynamics with concepts of fixed points, stability, or even normal forms easily extends to the

case of multiple dimensions. Moreover, adding dimensions allows for much more complex dynamics such as oscillations or limit cycles. From a three-dimensional system, chaotic behavior can even emerge. The complexification of possible dynamics can be understood by the fact that trajectories then have "more room" than on a simple line. The advantage of two-dimensional systems is that they still allow for some graphical interpretation. For example, in the case of the normal form of a double-fold bifurcation described by equation (2.6), one can analytically compute its double well potential  $V(x) = -\frac{1}{2}x^2 + \frac{1}{4}x^4$ . In the case of a generic two-dimensional system of the form,

$$\dot{x} = y, \quad (2.7)$$

$$\dot{y} = x - x^3 \quad (2.8)$$

We can thus compute an energy function of the system as  $E(x, y) = \frac{1}{2}y^2 - \frac{1}{2}x^2 + \frac{1}{4}x^4$ , whose trajectories will follow curves of equal energy due to the conservation of energy principle. We can thus visually understand the dynamics of this two-dimensional system through Figure (14).

### The success of modeling tipping elements with double-fold bifurcations

In the pursuit of describing tipping elements using the theory of dynamical systems, they are often represented by double-fold bifurcations because tipping elements are systems to which two physically distinct stable equilibrium states can typically be attributed. The first state, known as the *nominal state*, represents, for example, the pre-industrial condition of the Amazon rainforest, where nearly the entire geographical area considered is associated with rainforest. The second stable equilibrium is termed the *collapse state*, which, in the case of the Amazon rainforest, signifies the collapse of the forest, giving way to a savanna-like ecosystem. In reality, the initial example illustrating a tipping point with an office chair taken at the very beginning of this chapter is an example of *bistability*. There existed two alternative states of stable equilibrium : one with the chair on all four legs and one where it had fallen over. Between the two lay an unstable equilibrium where a minute alteration in the force we exert with our legs, which serves as our bifurcation parameter, can lead to the critical point of tipping our system of attractors and, thus, stable equilibrium, resulting in a fall.

What physically justifies describing the simplified dynamics of tipping points using double-fold bifurcations ? Numerous simulations based on process-based models as well as observations show that the complex dynamics of tipping elements can, at first order, resemble that of a dynamical system with two stable equilibria and one unstable equilibrium, whose bifurcations can be explained by a double-fold. For example, if we examine bifurcation diagrams generated for Antarctica using process-based models by Garbe et al. (2020), we observe a dynamics that, at first order, resembles that of a double-fold. This can be

seen in Figure (15), where the percentage of ice volume of the Antarctic ice sheet relative to its pre-industrial level is displayed in this bifurcation diagram as a function of the bifurcation parameter, which is the forcing by global mean temperature. This reinforces the epistemological validity of approximating the first-order dynamics of tipping elements by double-fold bifurcations.

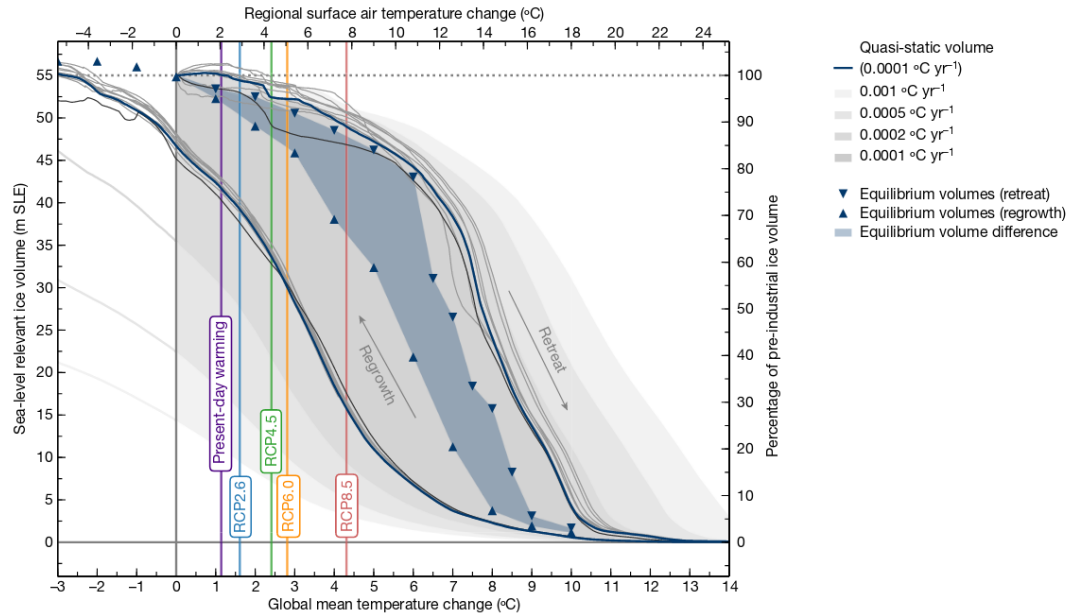


FIGURE 15 – *Hysteresis of the Antarctic Ice Sheet. The Sea-level relevant ice volume (in meters sea-level equivalent, mSLE) for the quasi-static reference simulations performs (blue curve) as well as the corresponding equilibrium states at discrete temperature levels (blue triangles). Figure from Garbe et al.[24]*

Therefore, it is common in the literature to represent the dynamics of a tipping element with a double fold. The generic ordinary differential equation describing the dynamics of the tipping element in question then takes the following form :

$$\frac{dx}{dt} = -x^3 + x + \mu = \frac{-\partial V}{\partial x} \quad (2.9)$$

with,

$$V(x) = \frac{1}{4}x^4 - \frac{1}{2}x^2 - \mu x \quad (2.10)$$

In this form, the bifurcation dynamics take the form shown in Figures (16). The temporal evolution of the generic forcing parameter  $\mu$  is depicted in the bottom right plot. In the top right figures, potential landscapes are shown along with their qualitative changes as a function of the bifurcation parameter value. When it reaches a critical threshold, a bifurcation occurs. The bifurcation diagram on the left illustrates this, depicting the evolutions of the positions of stable and unstable equilibria as a function of the forcing at a given time.

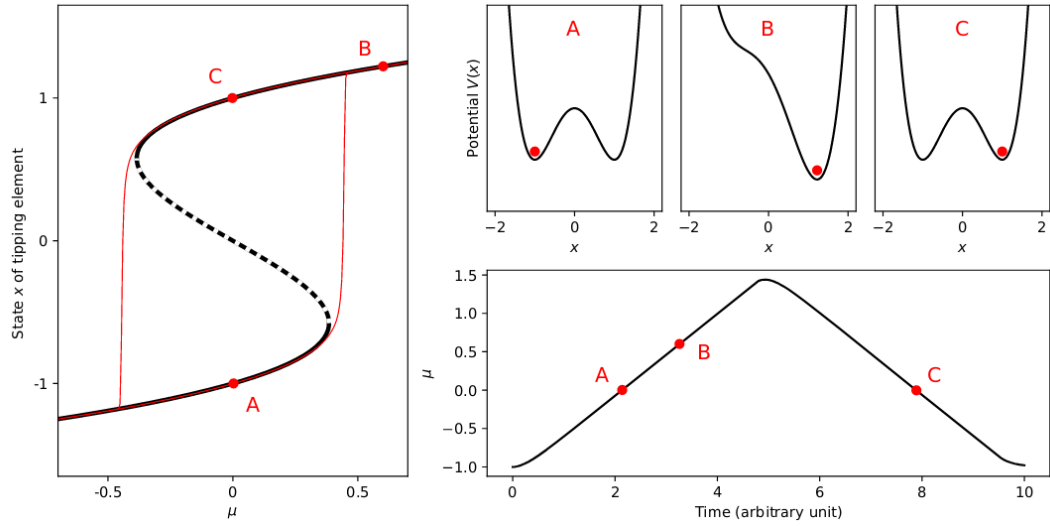


FIGURE 16 – *Bifurcation diagram and potential landscape for modeling a tipping element with a double fold.* Figure from V.Couplet[16]

### Hysteresis behavior

Another concept with significant implications in the behavior of nonlinear systems and observed in many tipping elements is what is called **hysteresis**. Figure (17) shows a schematic representation of this phenomenon. Hysteresis occurs when a system has alternative stable states (attractors). Describing a system as exhibiting hysteresis means that the system's state depends on its past history. More explicitly, when the system is forced in one direction, it may traverse a tipping point, transitioning from one stable state (attractor) to another. However, if the direction of the forcing is subsequently reversed to the original magnitude, the system might persist in its new state (attractor), necessitating a further decrease in forcing to reach an alternative tipping point. This hysteresis phenomenon exemplifies a critical source of irreversibility associated with crossing tipping points.[75] In other words, hysteresis can be seen as the lack of reversibility of a system as a parameter is varied.[73] For instance, the Greenland Ice Sheet may be driven towards irreversible loss by a certain degree of global warming. Should the ice sheet be lost, it would not regenerate at the same level of warming, nor would it reform at preindustrial temperature levels; rather, a significant global cooling would be required. Hysteresis thus demonstrates path dependence, wherein historical events shape and constrain future possibilities. The current presence of the Greenland Ice Sheet is a consequence of conditions established during the last ice age. Consequently, accurately predicting future transformations in such systems necessitates a comprehensive understanding of their historical evolution.[75] Now that this concept is introduced, we can revisit Figures (15, 16), which show, whether for data from a process-based model of Antarctica or in the very nature of double-fold dynamics, a hysteresis behavior. To conclude this important subsection presenting key concepts of nonlinear

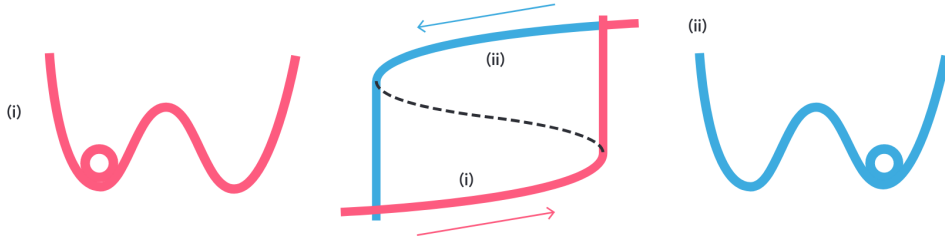


FIGURE 17 – A simple representation of hysteresis. A system starts in one of two alternative stable states (red) at position (i). Forcing the system in one direction (red arrow from left to right) causes it to pass a tipping point into the other stable state (blue). Then when the forcing is reversed (blue arrow from right to left), there is a path dependence : The system remains in the alternative stable state, passing through position (ii). An alternative tipping point has to be passed to tip the system back into the original stable state. Figure from Global Tipping Report 2023.[75]

dynamics that will be useful to us, we will finish with two examples of applications of what has been discussed. The first is the analysis framework of cascade tipping by Dekker et al. [19], and the second is the phenomenon of *overshoot without tipping* by Ritchie et al. [61]. These two articles utilize the framework of dynamical systems theory to introduce phenomena that will be essential for our examination of the results from our model.

### The framework of Dekker et al. for Cascade Tipping

To investigate cascade tipping, Dekker et al.[19] established a mathematical framework for elementary deterministic cascading tipping points in dynamical systems containing the double-fold process. In this study, they highlight the significance of one of the considered tipping elements for the global cascade phenomenon, providing a background state for the evolution of another tipping element. When one subsystem undergoes a transition, altering the background state of another subsystem, it may induce a transition in that second subsystem as well. This offers an original perspective on the cascade collapse phenomenon or the domino effect.[38] They particularly focus on B-Tipping and consider, among others, the double-fold dynamics of bifurcation. They demonstrate that mathematically, coupling two systems introduces a direction to the cascade, which can be accounted for by defining the ***leading system***. During its transition, the leading system changes a parameter (shared coupling terms) in the ***following system***. It is this parameter change in the following system that can bring it closer to a bifurcation point, potentially resulting in a second transition. Therefore, transitions in the leading system lead to changes in the coupling term that may induce transitions in the following system. To achieve these results, they employ the following mathematical model.

$$\begin{cases} \frac{dx}{dt} = a_1 x^3 + a_2 x + \phi \\ \frac{dy}{dt} = b_1 y^3 + b_2 y + \gamma(x) \end{cases}$$

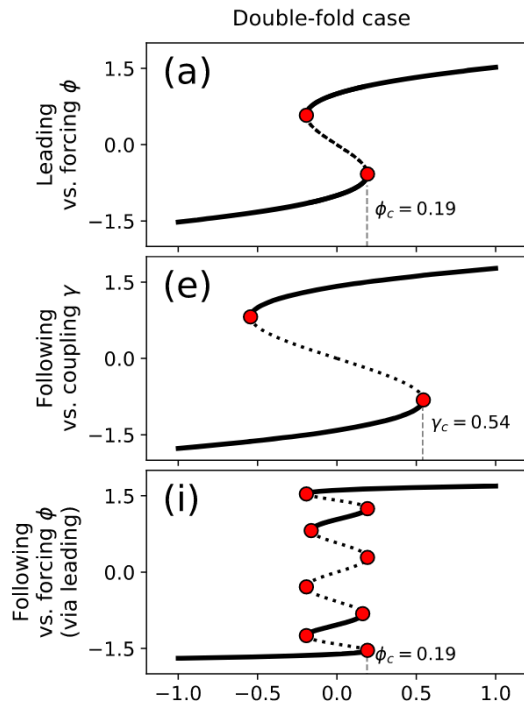


FIGURE 18 – Stable (solid), unstable (black dotted) regimes of double-fold cascading bifurcation. Red dots indicate fold bifurcation. Figure from Dekker et al.[19]

by Dekker et al.[19] is that in bifurcation diagrams versus forcing, the bifurcation points (for deterministic systems) can overlap. However, the transitions are distinguishable in transients because the following system always tips after the completion of the first transition, as shown in Figure (19).



FIGURE 19 – Example simulations for double-fold cascading tipping are illustrated. Dashed lines represent the evolution of the systems before they reach their critical bifurcation values. The transient response of the leading system is depicted in black, while that of the following system is shown in red. Figure from Dekker et al.[19]

Based on these couplings between the two systems, there exist four stable states in the following system corresponding to the bistable regime of the leading system, two per state of the leading system. Thus, the state of the leading system serves as a background condition modulating the position of the equilibria in the following system; consequently, in the event of a transition, the state of the leading system may significantly reposition the equilibria of the following

In this equation,  $x$  represents the state vector of the leading system,  $y$  represents the state vector of the following system, and  $a_i, b_i, i = 1, 2$  are calibration constants.  $\phi$  is the forcing parameter in the leading system, but the key element is the  $\gamma(x)$  function, which serves as a forcing parameter in the following system, depending on the state of the leading system. It is important to note that the forcing  $\phi$  does not directly affect  $y$ , and  $y$  is only influenced through a change in  $x$ .

In Figure (18), bifurcation diagrams are shown for the two systems, along with the state of the following system as a function of  $\phi$ . Figure (19) depicts the transient response of the leading system (in black) and the following system (in red). Dashed lines indicate time before the critical threshold in the forcing  $\phi$  and  $\gamma$  is reached, while solid lines indicate time after this. An interesting observation from the study

system.[19] This is evident in Figure (19), where a time series illustrates a cascading tipping event. When the leading system (black) is forced (by changing  $\phi$ ) to transition from a bistable to a monostable regime, it moves towards a new equilibrium. During this transition, the following system (red) is influenced and departs from the regime in which it had four possible equilibria, also transitioning to a different state.

In conclusion, this mathematical model by Dekker et al. [19] highlights the importance of timescale separation and the existence of multistability in the dynamics of tipping elements, which can lead to cascade collapses among them. Far from being merely theoretical, an example of a double-fold cascade in the climate could be the impact of a bistable AMOC on the bistable land ice formation on the Antarctic continent. This assertion finds support in paleoclimate data.[19] In addition to providing a relevant analysis of cascade collapse mechanisms, it is on this methodological basis that we will construct our cascade collapse model using two coupled double-folds for the AMOC and the GIS.

### The *overshoot without tipping* phenomena

The last intriguing phenomenon for our future analysis that we wish to present is that of *overshoot without tipping*. In a impactful paper, Ritchie et al.[61] further investigated the dynamics of a tipping element once the bifurcation parameter has crossed its critical value. A classical scenario for tipping is when a dynamical system undergoes a bifurcation once the critical value of the bifurcation parameter exceeds the critical threshold, the tipping point. However, they demonstrated, by finding an analytical relationship, that it is entirely possible for a system representing a tipping element not to tip even as its bifurcation parameter exceeds its critical value. They derived a criterion that relates how far the parameter exceeds the tipping threshold maximally

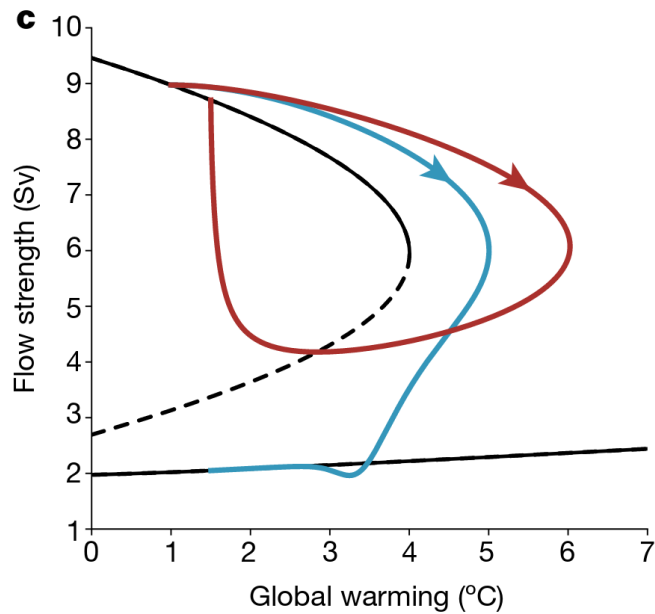


FIGURE 20 – Flow strength versus global warming in an AMOC-fold model. The blue trajectory represent a slow and small overshoot while the red is a fast but much larger overshoot. The AMOC ‘on’ state is the upper solid black curve while the ‘off’ state is the lower solid black curve. The unstable branch is the dashed line. Figure from Ritchie et al.[62]

and how long the parameter stays above the threshold to avoid tipping in an inverse-square law to observable properties of the dynamical system near the fold. The technical details are not inherently interesting in our case since Ritchie's criterion is based on assumptions that are too restrictive compared to the model we are developing. Furthermore, the criterion does not work when considering forcings that are rapid compared to the characteristic time scale of the internal dynamics of the system under consideration.[15] Thus, the analytical results of Ritchie et al.[61] are not relevant to our research, but the studied phenomenon of *overshoot without tipping* is.

What the phenomenon of overshoot without tipping demonstrates is the importance of separating the characteristic timescales of forcing, denoted as  $d$ , and those of the internal dynamics of the system, denoted as  $\tau$ . Indeed, if the forcing occurs over a time span sufficiently short compared to the response time of the perturbed system, even if the forcing surpasses the tipping point of the system for a significant duration, it is possible that the system does not bifurcate due to its dynamic inertia.

This result has practical implications because in terms of mitigation policy, it implies that it might be possible for certain tipping elements to emit too much greenhouse gas for a period of time, but if significant reductions are achieved later on, these systems may not tip. This type of forcing would then be what is called *meteoric shock* types of forcing.[15] In subsection (2.3), we will present a model of the AMOC based on the double-fold, which illustrates this overshooting behavior. Finally, in the simplified cascade collapse model that we will develop for the AMOC and the GIS in Chapter II, we will also incorporate this phenomenon in the analysis of the results in Chapter III. With this result, we conclude this subsection aimed at **presenting the key concepts and phenomena of dynamical systems theory upon which we will base our model and analyze its output to address our scientific questions (1d) and (1).**

## 2.3 AMOC, role in climate, dynamics and impact of its collapse

In this section, we will motivate our main topic of analysis, the Atlantic Meridional Overturning Circulation (AMOC), also known as the thermohaline circulation. First, we will explain the significance of this oceanic circulation in climate dynamics, and then describe why and how the AMOC constitutes a tipping element. Subsequently, we will discuss the impacts that a collapse of the AMOC would entail to further justify its study. Finally, we will detail the specific coupling between the AMOC and the Greenland Ice Sheet (GIS), which may result in cascading collapse dynamics. Thus, **we will address scientific questions (1b) and (1c).** Based on these considerations, we will motivate in the last section of this chapter the foundation for constructing a model of simplified nonlinear dynamics for the cascading collapse of the AMOC and GIS.

### 2.3.1 The AMOC and its role in climate

The Atlantic Meridional Overturning Circulation (AMOC) is a key component of the climate system that effectively transports heat and salt through the global ocean, exerting a strong influence on regional and global climate dynamics.[77] A commonly used metaphor to illustrate the global oceanic circulation is that of a *conveyor belt*, which is driven by both wind stress and buoyancy fluxes at the ocean-atmosphere interface.[28, 20] In reality, the AMOC manifests as a complex three-dimensional flow pattern in the Atlantic Ocean (see Figure (21)), wherein warm, salty surface waters are transported northward from the vicinity of Southern Africa to the North Atlantic. Upon reaching the northern latitudes, these waters cool, sink, and then return southward as cold, deep currents, constituting the lower branch of the AMOC.

The driver of the AMOC is what is known as the *ocean advective feedback* or *salinity advection feedback*. It is a positive feedback mechanism with a relatively simple mechanism. As mentioned earlier, the thermohaline circulation has the effect of transporting relatively warm and salty waters from the South Atlantic to the North Atlantic. Furthermore, it is the differences in water density which underlie this advective driver and fuel the formation of deep-water convection at high northern latitudes and their resurgences at the surface in the South Atlantic. Therefore, the AMOC is also referred to as the thermohaline circulation<sup>1</sup> At first order, water density differences are described by the temperature and salinity of the water volume under consideration. If the circulation decreases due to a disturbance (whether in temperature or salinity), the transport of salinity towards high latitudes is reduced. This results in a decrease in density there, and thus in the intensity of the flow, which will amplify the initial disturbance.[27] Based on this fundamental feedback, we will see in the following section that the AMOC exhibits tipping element behavior.

Therefore, based on this dynamic, this circulation system plays a pivotal role in transferring heat from the Southern to the Northern Atlantic. To understand this circulation, Figures (22(a,b)) show the absolute value of the streamfunction  $\Psi$ , which measures the intensity of the AMOC. In Figure (22(a)), the AMOC operates as it does currently, while in Figure (22(b)), it has ceased. Hence, the AMOC's crucial function in maintaining meridional heat transport is vital for the Earth's climate system. Due to the AMOC, the Atlantic basin is the only ocean basin that transports northward heat across both the Southern and Northern Hemispheres. The amounts of energy associated with AMOC transport are indeed impressive, as nearly 0.8 PW is transported northward at 30°N latitude.[27] This is more than twice the estimated amount of oceanic heat transport in the wider Pacific at the same latitude! Consequently, the AMOC

---

1. A subtle distinction between the two terms is that the thermohaline circulation is the more generic term that describes the global oceanic circulation driven by differences in temperature and salinity. When referring to the AMOC, the focus is on specific branches of this thermohaline circulation in the Atlantic. In this thesis, however, we will use both semantics without any real difference in meaning.

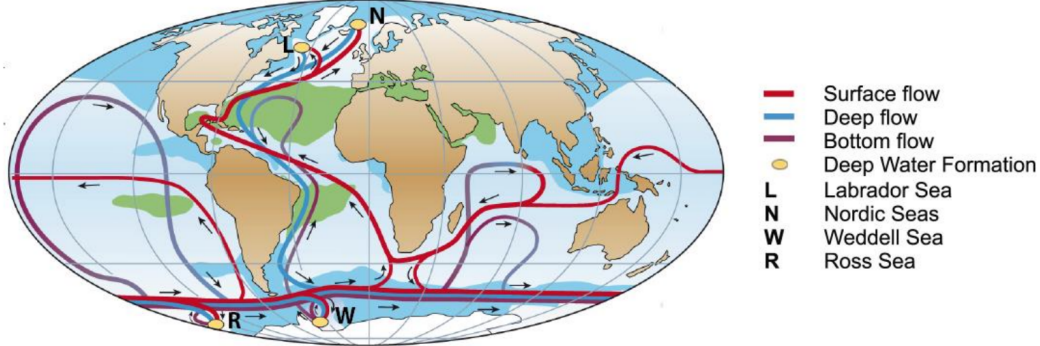


FIGURE 21 – Schematic representation of the oceanic thermohaline circulation illustrating the surface (red), deep (blue) and bottom (magenta) flow. The main regions of deep water formation are indicated by a small yellow circle while the areas characterized by a sea surface salinity higher than 36 are in green and lower than 34 in light blue. Figure from Goosse et al.[27]

has a profound influence on global climate patterns, including a  $1 - 2^{\circ}\text{C}$  temperature differential between the Northern and Southern Hemispheres and the distribution and intensity of tropical rainfall.[7] Additionally, the AMOC is largely responsible for the temperate climate of Western and Northern Europe.[75] As we will see later in this section, a complete collapse of the AMOC would have colossal consequences on the global and regional climate in the North Atlantic, further motivating the study of its potential tipping point.

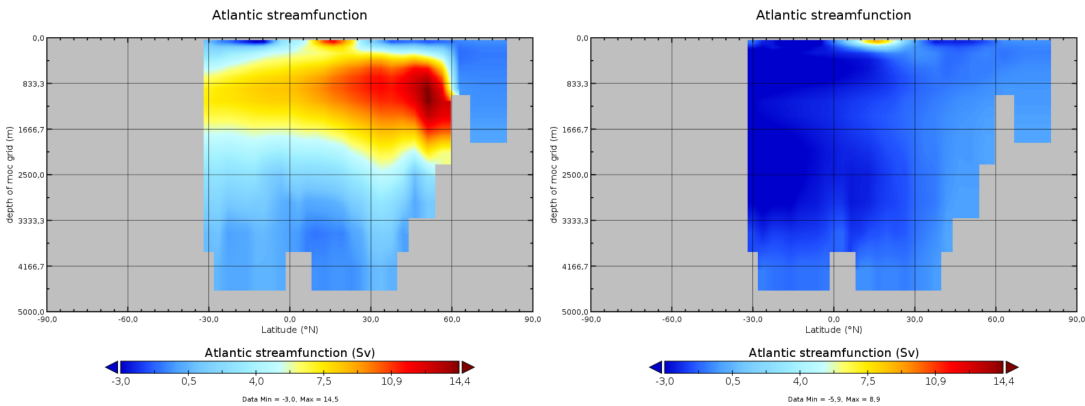


FIGURE 22 – Atlantic Streamfunction Intensity  $\Psi$  from cGenie experiments conducted for this thesis. (a) AMOC in its present state. (b) Collapsed AMOC. Further details on these simulations can be found in Section (3.4).

### 2.3.2 The AMOC as a Tipping Element

Due to its importance, the future development of the AMOC under climate change is a hot topic of research.[21] To measure the intensity of the AMOC, a metric commonly used in both observations and models is a stream function[8],

which represents the zonally integrated meridional volume transport. In depth coordinates, it takes the following form,

$$\Psi(y, z) = \int_z^\eta \int_{x_w}^{x_e} v dx dz, \quad (2.11)$$

where  $v$  is the meridional velocity,  $z$  is a vertical coordinate increasing upward,  $\eta$  is the height of the free surface, and  $x_w(z)$  and  $x_e(z)$  are the westward and eastward positions of the bathymetry at a particular depth.<sup>2</sup> Based on Equation (2.11), the strength of the AMOC at each latitude is defined as the maximum of the stream function over the water column. It is this maximum value that we will use to diagnose and analyze the state of the AMOC thereafter. There is evidence that the AMOC has slowed down since the early 20th century with inferred reconstructions showing a decrease of 15% over the past  $\approx 50$  years.[10] Although this longterm declining trend of AMOC strength is subject to great uncertainty.[8]. In addition, simulations using state-of-the-art Earth System Models (ESMs) from the Climate Model Intercomparison Project Phase 6 (CMIP6) project suggest that the strength of the AMOC will gradually decrease by the end of this century, with relatively little difference between the various Shared Socioeconomic Pathway scenarios.[82] Furthermore, paleodata and simulations indicate that significant slowdowns of the AMOC have occurred in the past.[50] But why are those weakening occurring ?

### Thermal forcings Slowing Down the AMOC

As explained, the maintenance of the AMOC relies on differences in water density between the South Atlantic and the North Atlantic, which are in turn due to differences in temperature and salinity. Thus, any forcing that contributes to modifying the surface water temperature in the North Atlantic, near the regions of deep convection formation (NADW), and any forcing that reduces the salinity of surface waters arriving at NADW sites will have the effect of reducing the intensity of the AMOC. This is why climate warming tends to slow down the intensity of the AMOC due to the increase in the average atmospheric temperature, which subsequently affects the temperature of surface waters. As a result, the surface water transported by circulation in the North Atlantic, being less dense, will reduce deep convection at NADW sites and consequently slow down the circulation as a whole.

Furthermore, it is important to note that R-Tipping phenomena driven by this thermal forcing have already been simulated in several studies using simplified models such as those by Stocker et al. [70], Lohmann et al.[47] and Klose et al.[37] They have shown that if the ocean surface warms too rapidly, the deep ocean does not have time to adapt, reaching a critical stratification threshold leading to a collapse of circulation. This is an important mechanism that we aim to reproduce in our simplified model to be constructed in Chapter II.

---

2. There is a standard sign convention : a positive stream function is a clockwise circulation, with northward flow at the surface and southward flow at depth.[8]

### Cryospheric Haline Forcings Slowing Down the AMOC

In the case of haline forcings, they can have various sources, and their characterization is more complex than that of the thermal branch of the thermohaline circulation. The physical nature of haline forcings involves freshwater fluxes that decrease the salinity of the water, thereby reducing its density. This effect promotes stratification of water in the North Atlantic, consequently slowing down convection and the sinking of surface waters to deeper levels. To simulate these effects in models, it is necessary to introduce what are termed *hosing experiments*, which we will need to utilize in Chapter II to calibrate our simplified model of the AMOC. A hosing experiment is a numerical simulation in which a freshwater flux is artificially added. This flux is used to emulate a physical freshwater flux that may originate from various sources that we will now explain.

The primary physical source of these freshwater fluxes, which is the most studied, originates from the melting of cryospheric components such as the GIS. The additional input of freshwater into the North Atlantic, near the sites of NADW formation, has an even more significant impact on the AMOC and is destabilizing.

However, there is a strong dependence on where freshwater is added. Indeed, while the GIS may have a destabilizing effect on the AMOC due to its melting (further discussed in subsection 2.3.4), the West Antarctic Ice Sheet (WAIS) has a stabilizing effect on the AMOC. This outcome arises from the fact that, in the case of the WAIS, freshwater is introduced into the Southern Atlantic, thereby promoting upwelling in these regions due to the creation of less dense water. In a conceptual model, Sinet et al.[68] investigate the response of the AMOC to WAIS melting. Although the tipping element dynamics of the WAIS are less well understood than those of the GIS, it is demonstrated that freshwater input into the Southern Atlantic has a stabilizing effect on the AMOC, especially in the case of relatively fast and early WAIS tipping.[68] Additionally, this stabilizing effect on the AMOC is a behavior shared by many box model representations of the AMOC.[12, 57]

### *P – E* Haline Forcings Slowing Down the AMOC

A second source of freshwater flux that can influence the AMOC, though less studied than those from cryospheric components, is a change in the precipitation-evaporation balance. Indeed, as surface water is transported across ocean basins, it alternates between regions characterized by higher evaporation and others where precipitation predominates. When water evaporates, it is the pure water,  $H_2O$ , that transitions to a gaseous state, while the salt contained in seawater remains in the ocean, meaning that the evaporation process increases the salinity of the water volume under consideration. Conversely, precipitation consists of pure water, which decreases the salinity of oceanic waters by increasing the volume of unsalted water in the ocean.

### Multi-model zonal mean long-term changes in P, E and P-E

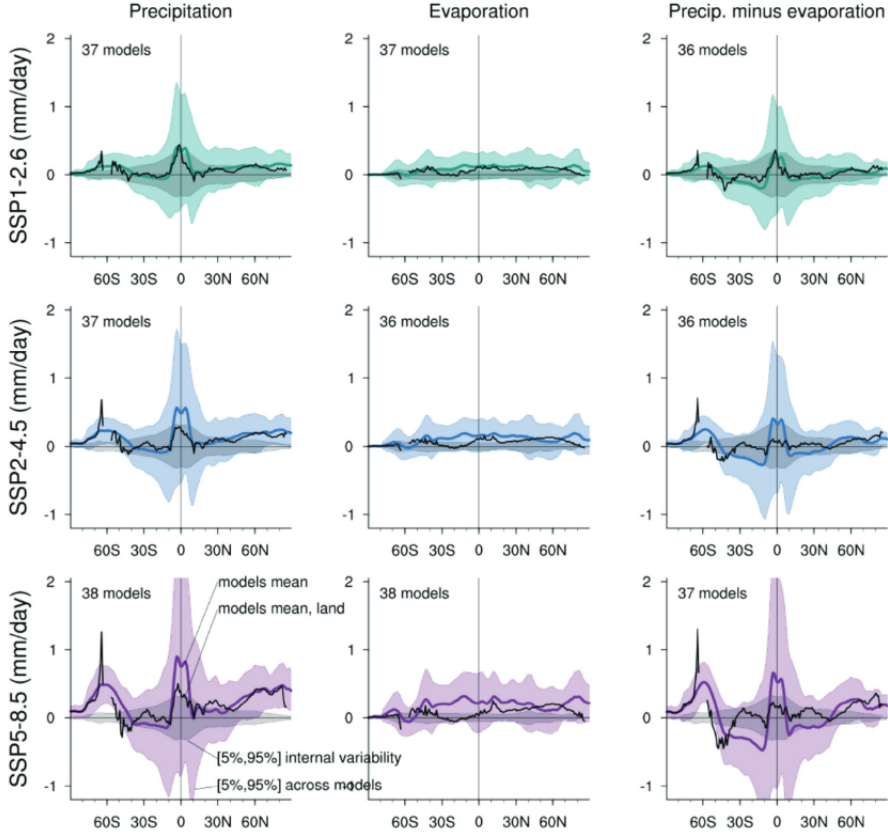


**FIGURE 23 – Zonal and annual-mean projected long-term changes in the atmospheric water budget from CMIP6 models.** Coloured lines represents the water budget over both land and ocean while black lines for land only. Shading denotes confidence intervals estimated from the CMIP6 ensemble under a normal distribution hypothesis. Colour shading denotes changes over both land and ocean. Grey shading represents internal variability derived from the pre-industrial control simulations. All changes are estimated for 2081–2100 relative to the 1995–2014 base period. Figure from IPCC WG1[31]

This net precipitation-evaporation  $P - E$  balance has been, and will continue to be, affected by regional variations due to global warming and basic thermodynamic processes. Although evaporation is measured at very few locations across the global ocean, making direct assessments of  $P - E$  over the ocean is highly challenging and dependent on indirect reanalysis estimates[63], the AR5 from the IPCC has presented robust evidence of an intensified oceanic  $P - E$  pattern since the 1960s, evidenced by both regional and global surface and subsurface salinity measurements and reanalyses.[31] The AR5 also concluded that globally averaged precipitation is virtually certain to increase with rising temperatures, particularly within the Arctic, which will result in bringing water directly close to the critical sites of the NADW.[2] Even though evaluating evaporation is thus more difficult, CMIP6 projections for long-term changes in  $P - E$  (cf. Fig.(23))

indicate that, across all scenarios,  $P - E$  is expected to increase over the tropics and high latitudes and decrease over the subtropics, a result of the thermodynamically driven amplification of  $P - E$  patterns.[31] However, it should be noted that studies on the  $P - E$  balance over the Atlantic remain very limited and the data involve significant uncertainties.

Nevertheless, studies highlight the impact that variations in the P-E balance over the Atlantic Basin could have on the AMOC.[56, 46] In a 2023 study, Nobre et al.[56] report that in AMOC sensitivity experiments using a process-based model with quadrupled  $CO_2$  concentrations, the global mean surface salinity steadily decreases. They hypothesize that this freshening in various regions results from enhanced upper ocean convection driven by increased evaporation due to higher sea surface temperatures. Although its implications are not yet fully understood, the potential contribution of a future P-E anomaly over the Atlantic Basin appears to be a significant factor in the dynamics of AMOC collapse, albeit playing a secondary role that may enhance or reduce the primary mechanism, which is ice melt.[65]

### The dominant thermal forcing

Ultimately, concerning the two branches of forcings, the thermal and the haline, it should be noted that the AMOC shutdown under global warming is primarily caused by thermally induced buoyancy reduction.[46] Moreover, the collapse signatures from models for the AMOC vary depending on the type of forcing applied. Salinity differences can be attributed to advective dynamics, whereas temperature-related changes are due to convective processes. Due to these dynamic differences, data show that forcing through the thermal branch results in a less abrupt decrease in AMOC compared to the haline branch. Furthermore, the literature[58] that simulates AMOC collapses using models that realistically incorporate a substantial amount of physical processes indicates a less abrupt collapse of the AMOC, thus substantiating that the dominant forcing is primarily on the thermal branch. This justifies, when necessary, the choice to prioritize thermal forcing in the optimization decisions in Chapter II on our AGTCCM model due to its increased significance in the dynamics of AMOC collapse.

### A Tipping Element

Therefore, while the weakening of the AMOC due to rising average surface water temperatures and freshwater input is one aspect, can we classify the AMOC as a tipping element?

Unfortunately, yes. Referring to the definition provided by the *Global Tipping Point Report 2023*, once a critical threshold of Atlantic water stratification is surpassed, this forcing becomes self-perpetuating, leading to substantial and widespread impacts on the Earth system.[75] Indeed, at least two stable states have been clearly identified : one in which the AMOC is active in a nominal state,

as it is currently, and another stable equilibrium where the AMOC is in a collapsed state. In more sophisticated and process-based climate models, evidence suggests the existence of multiple equilibrium states of the Atlantic Meridional Overturning Circulation (AMOC) attributable to hysteresis effects. Studies, including one of the first and most famous by Rahmstorf et al.[58] in 2005, have demonstrated that when freshwater forcing in the North Atlantic is increased incrementally, allowing the AMOC to maintain near-equilibrium conditions, it tends to collapse in numerous Earth System Models of Intermediate Complexity (EMICs). Conversely, when this freshwater forcing is reversed, recovery of the AMOC is observed at significantly lower levels of freshwater forcing compared to the levels that initially triggered its collapse, indicative of pronounced hysteresis behavior (cfr. Figure (24)). These results are consistent across different model complexity ranges, demonstrating the possibility of producing hysteresis typical of tipping elements in both EMICs and more conceptual models.

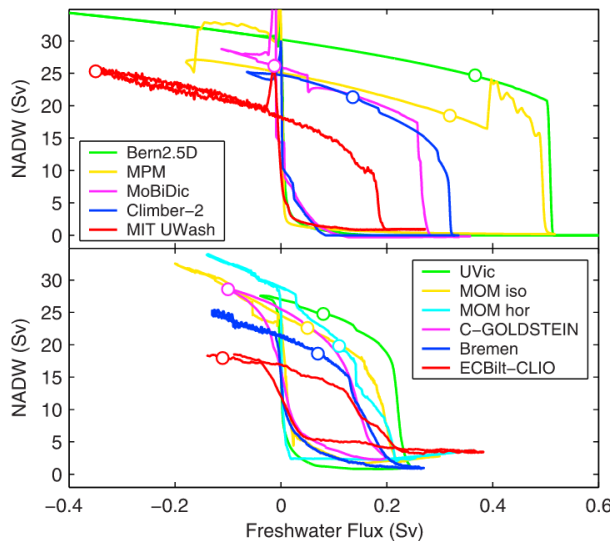


FIGURE 24 – *Hysteresis curves. The bottom panel shows coupled models with 3-D global ocean models, the top panel those with simplified ocean models. Circles show the present-day climate state of each model. Figure from Rahmstorf et al.[58]*

AMOC ([33, 81]). These experiments have demonstrated markedly weaker or even collapsed states of the AMOC.[36, 53, 72] A possible rate-induced tipping of the AMOC for a quickly changing, time-dependent freshwater forcing in a three-dimensional ocean model has also been recently demonstrated.[49] In addition, establishing a specific freshwater forcing regime or temperature forcing that triggers hysteresis has proved challenging.[35] Consequently, it might be argued that AMOC tipping phenomena are absent in advanced GCMs, as these models incorporate a broader range of feedback mechanisms, particularly negative ones,

Moreover, this hysteresis phenomenon for the AMOC has also been documented in relatively coarse climate models, including the FAMOUS model as reported by Hawkins et al.[29] and in an early iteration of the Community Climate System Model as per Hu et al.[30]. Hence, the AMOC has been recognized as a climate tipping element.[2, 75] However, in contemporary global climate models (GCMs), simulating hysteresis behavior associated with the AMOC is a resource-intensive process. Until recently, only transient experiments involving significant freshwater disturbances have been conducted to induce collapses in the

unlike more simplified climate models such as EMICs and FAMOUS.[25] Furthermore, some CMIP models neglect meltwater forcing from rapid Greenland Ice Sheet (GIS) melt [49]. In a recent paper published in the journal *Science*, van Westen et al. [78] demonstrated for the first time in a state-of-the-art Earth System Model (CESM2) a tipping event of the AMOC under realistic forcing projections rather than idealized hosing experiments. This once again confirms that the AMOC is indeed a tipping element and that this can be demonstrated across the full spectrum of possible model categories.

Despite these numerous simulations, precise estimations of the current state of the AMOC on its hysteresis loop and when it could tip are still elusive. Simulations based on CMIP suggest that a full collapse is unlikely within the 21st century, while other studies estimate a collapse of the AMOC to occur around mid-century under the current scenario of future emissions [21]. Therefore, it is not straightforward to identify the precise critical thresholds at which an increase in global mean temperature or freshwater input would trigger an irreversible collapse of the AMOC, due to significant differences between models. Hence, for temperature forcing, Armstrong and McKay et al. [2] provide an estimation of the critical threshold at a  $4^{\circ}\text{C}$  anomaly in global mean atmospheric temperature relative to the pre-industrial period, with a low estimation at  $1.4^{\circ}\text{C}$  and a high estimation at  $8^{\circ}\text{C}$ . Furthermore, estimating the timescale of an AMOC tipping is also complex. The study by Armstrong McKay et al.[2] takes the most probable value range to be 15 to 300 years. However, this range is very dependent on the strength of the freshwater forcing applied in experiments, which in many cases is unrealistically large compared to projected melting of the Greenland Ice Sheet and increases in precipitation and river runoff.[75]

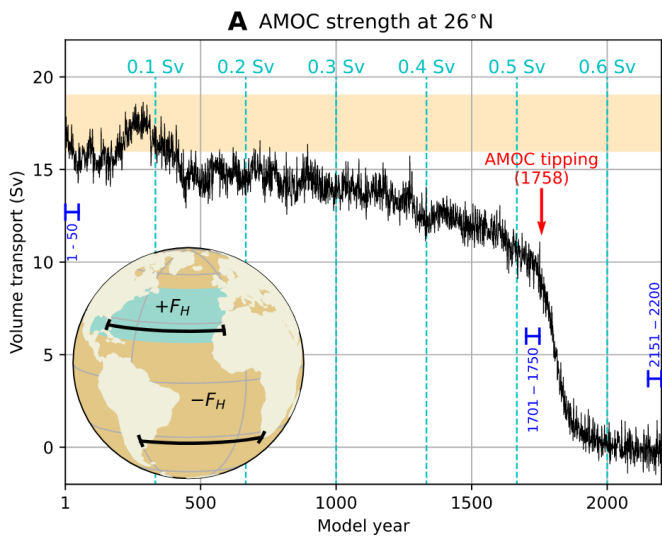


FIGURE 25 – AMOC strength at 1000m and  $26^{\circ}\text{N}$  where the yellow shading indicates observed ranges. The cyan-colored lines indicate the magnitude of  $F_H$  in the hosing forcing applied. Figure from van Westen et al./78]

Capturing tipping with low order dynamics

Finaly, it is highly interesting for our methodological objective to note that conceptual models, aimed at capturing the primary dynamics of the AMOC, already illustrate this nonlinear behavior of the AMOC. Indeed, initial ideas re-

garding the tipping of the Atlantic Meridional Overturning Circulation (AMOC) were first proposed in the early 1960s, notably by Stommel in 1961[71], utilizing a highly conceptual model in which the ocean circulation was represented merely by the flow between two compartments. In this simplified framework, the contemporary state of the AMOC is recognized as being particularly sensitive to alterations in the North Atlantic surface freshwater flux, driven by the so-called and previously introduced salt-advection feedback mechanism. Anomalies in freshwater within the North Atlantic can diminish the AMOC's strength, consequently reducing the northward transport of salinity and thereby exacerbating the initial freshwater anomaly. In these conceptual models, tipping of the AMOC is triggered by an increase in freshwater flux forcing, leading to transitions between multiple equilibrium states of the AMOC that coexist under identical freshwater forcing conditions.[11] Therefore, the importance of conceptual models, which allow us to separate constraints in terms of computational time and analysis of physical processes inherent in highly complex models such as ESMs, is once again evident. This motivates our desire to also develop a conceptual model to simulate the AMOC.

### 2.3.3 What could be the impacts of an AMOC collapse ?

#### Impacts on Temperature

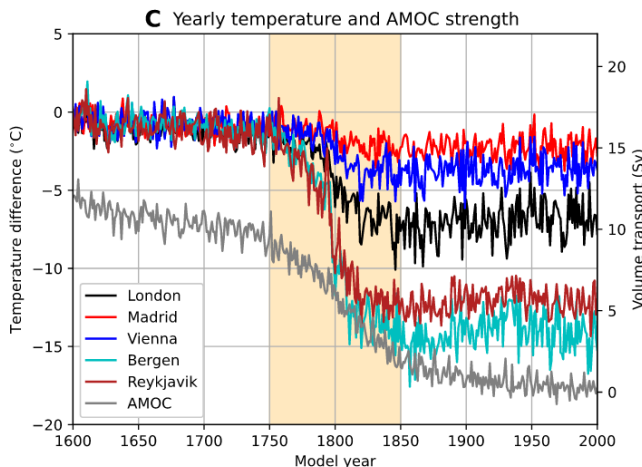


FIGURE 26 – *Temperature difference (with respect to model year 1600) for five different cities, including the AMOC strength. The trends are determined over model years 1750 to 1850 (yellow shading) during which the AMOC strength strongly decreases. Figure from van Westen et al.[78]*

North Atlantic. As shown by van Westen et al.[78], a complete halt of the AMOC would result in a mean temperature decrease of nearly  $15^{\circ}\text{C}$  in cities like Bergen and around  $7^{\circ}\text{C}$  for London. These projections are also supported

Thus, due to its fundamental role in the global and regional climate by transporting such large quantities of heat into the North Atlantic and its nature as a tipping element, model experiments and paleoclimatic data suggest that changes in the thermohaline circulation can have a major impact on climate, particularly around the northern Atlantic.[58] A complete collapse of the AMOC would result in a decrease in the global mean temperature of  $-0.5^{\circ}\text{C}$ .[2] However, the most significant impact would occur in the

by paleodata. Indeed, strong fluctuations in AMOC strength have occurred in the geological past, such as during the Dansgaard-Oeschger events, leading to local temperature variations of more than 10°C in Greenland.[50]

### **Impacts on Carbon Cycle**

The AMOC's significant impact on the carbon cycle cannot be overlooked. Through this circulation, substantial amounts of atmospheric carbon are absorbed by the ocean's surface waters and subsequently sequestered deep into the NADW's convective sites. If the AMOC were to cease, this ocean ventilation, along with the resurgences of water in the Southern Atlantic, would be greatly affected. Thus, assuming a steady-state natural carbon cycle, it has been demonstrated that a reduction in ventilation, coupled with cooling of surface waters in the North Atlantic, can diminish the ocean's  $CO_2$  uptake by as much as about 30%. [70] In a study, Zickfeld et al.[89] quantified the equilibrium impact on atmospheric  $CO_2$  concentration following an AMOC shutdown and found an increase of approximately 20 ppm. Indeed, the rise in atmospheric  $CO_2$  ranges from 13 ppm to 34 ppm by 2500, depending on the degree of AMOC weakening, the magnitude of anthropogenic CO<sub>2</sub> perturbation, and the future CO<sub>2</sub> fertilization effect. Relative to the total increase in atmospheric CO<sub>2</sub> since pre-industrial times, these numbers represent an increase of 1.6% to 6%. [89] Although modest, this increase is significant. Indeed, in the contrary scenario, a decrease in  $CO_2$  concentration resulting from AMOC activation could have triggered AIS glaciation in the past. This is a potential explanation considered for the rapid glaciation of the Antarctic continent around the Eocene-Oligocene boundary 34 million years ago.[22] **We thus address the first part of the second scientific question (2) regarding the impact on the carbon cycle of an AMOC shutdown. At the end of Chapter II, we will address the second part of this question concerning how to realistically account for this effect in SURFER.**

### **Impacts on ITCZ, Monsoon, SLR, Sea Ice and Marine Ecosystems**

Furthermore, an AMOC collapse would result in significant redistribution of heat within the ocean and atmosphere, with less warmth reaching the North and a southward shift of the Intertropical Convergence Zone (ITCZ). This would impact monsoon systems globally and cause substantial changes in storminess and rainfall patterns.[34] Additionally, a collapse of the AMOC would affect sea level rise (SLR) along the boundaries of the North Atlantic, alter Arctic sea ice and permafrost distribution[67, 9], and potentially lead to ocean deoxygenation[40] and severe disruption of marine ecosystems, impacting North Atlantic fish stocks.

## Impacts on other Tipping Elements

Lastly, and perhaps most significantly, due to multiple interactions that exist between the AMOC and other tipping elements, an AMOC collapse could either promote or inhibit the collapse of other tipping elements. For instance, when the AMOC collapses, precipitation patterns may change, altering the equilibrium structure of vegetation cover in the Amazon rainforest, potentially leading to another transition related to forest growth or dieback.[88, 19] An AMOC collapse, by preventing a portion of the Southern Hemisphere's heat from being transported northward, could also accelerate the melting of the WAIS. Finally, although not strictly considered a tipping element but rather a nonlinear earth system component with global feedback on global mean temperature, ENSO could be amplified due to a connection via the trade winds with the AMOC.[19] Ultimately, as we will explore in the following subsection, if there is one tipping element whose interactions with the AMOC are critical for our future, it is that of the GIS.

### 2.3.4 An AMOC-GIS Cascade Collapse

#### GIS as a tipping element

The Greenland Ice Sheet (GIS) is the second-largest ice cap after Antarctica and is currently melting at an increasing rate due to global warming.[2] Moreover, it is a tipping element because there is a melting threshold beyond which the melt-elevation feedback becomes strong enough to support self-propelling melt (as an ice sheet surface loses height, it enters warmer air and thus melts faster).[43] Again, determining the critical threshold is not straightforward, but the accepted value of the tipping point is approximately 1.5°C, with a probable range between 0.8°C and 3.0°C.[64, 2] Thus, it is one of the first tipping elements that could see its critical threshold exceeded in the years to come. However, due to the enormous amount of ice that must melt, the timescale of ice sheet meltdown becomes shorter the greater the temperature threshold is exceeded,[76] with a minimum of approximately 1000 years.[2]

#### Impacts of a Melting

In terms of impacts, a complete melting of the Greenland Ice Sheet (GIS) would result in a sea level rise (SLR) of 7.42 meters[55], which would simply erase cities like Jakarta, New York, or Bangkok from the map, as well as large parts of countries like Bangladesh. Furthermore, recent observations and modeling have suggested that the contribution of ice caps to future SLR has been underestimated in recent IPCC reports. Defrance et al.[18] examined the worst-case scenario where these additional freshwater fluxes could induce megadrought episodes in the Sahel region, akin to those experienced during the last glacial/interglacial period. They combined these climatic projections with demographic projections

and an analysis of impacts on regional agriculture, concluding that without adaptation policies, tens to hundreds of millions of people could be compelled to migrate from the Sahel by the end of this century.

### Destabilizing Effect of the GIS on the AMOC

A melting of the GIS thus produces an associated freshwater flux that will be released into the North Atlantic, with a significant portion directly impacting NADW sites. Therefore, the GIS has a negative effect on the stability of the AMOC as it increases water stratification by reducing the density of surface waters, thereby bringing the AMOC closer to its tipping point. However, the extent of this slowdown and the quantity of associated freshwater remain unclear due to limitations in model parameterizations and where the freshwater is effectively added.

In a 2023 hosing experiment, Jackson et al. [32] established the North Atlantic Hosing Model Intercomparison Project (NAHMIP), where they introduced varying amounts of freshwater into the North Atlantic in two different geographical manners. One approach involved uniform freshwater addition across the zonal band between  $50^{\circ}\text{N}$  and  $66^{\circ}\text{N}$  latitude (see Fig.(27a)), referred to as the UH experiment for *Upper Hosing*, while the other employed a more realistic detour around the sides of Greenland (see Fig.(27b)), termed the GH experiment for *Greenland Hosing*, aimed at simulating the freshwater flux associated with Greenland's melting. In these experiments, they apply a uniform freshwater flux of  $0.1\text{Sv}$ , which is already considered to be on the high end of what could realistically occur from rapid Greenland melting.

Compared to the UH experiment, the GU hosing experiments show a much smaller decrease in AMOC intensity. One of the early conclusions of their study is that there is a considerable variation in model responses to this more realistic hosing around Greenland. Indeed, some models show no slowdown of the AMOC, while others experience a slowdown of several Sverdrups over 50 years. Furthermore, the AMOC exhibits no hysteresis behavior in the hosing experiments GH, although a significant slowdown, even without complete collapse,

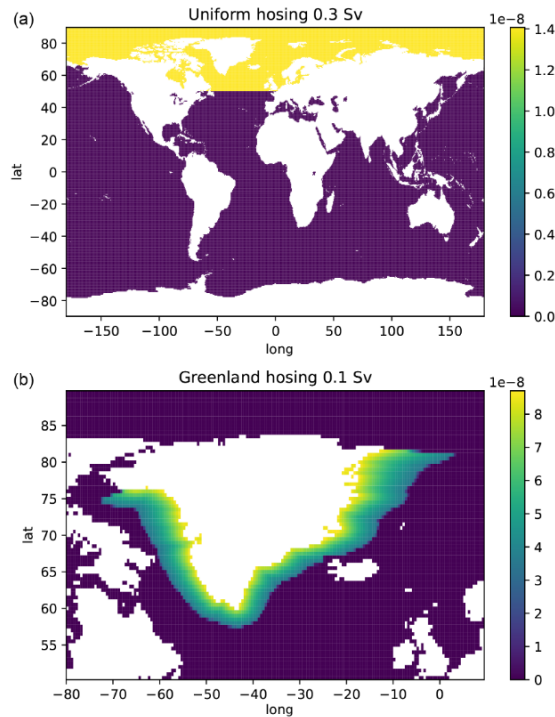


FIGURE 27 – *Hosing fields selected in the NAHMIP. Figure from Jackson et al.(2023)[32]*

would already have very significant impacts on the climate [77]. In addition, Jackson et al. find that for nearly half of the CMIP6 models participating in these NAHMIP experiments, states of the AMOC where it does not recover after a hosing of  $0.3Sv$  are simulated. It is important to recall that a freshwater flux of  $0.3Sv$  for Greenland is a physically unrealistic flux, even considering very rapid melting. This seems to indicate that an AMOC tipping solely based on a Greenland freshwater flux is highly improbable. Additionally, regardless of the physical source of the freshwater fluxes, the results of Jackson et al.[32] imply unrealistic freshwater fluxes, with values larger than what could actually occur even under the most extreme warming scenarios. These fluxes also do not take into account the non-linear melting characteristics of a tipping of the ice sheet on Greenland.[64] Finally, their simulations are pure hosing experiments, meaning they only force through freshwater flux, while greenhouse gas concentration is held constant. These experiments should not be viewed as plausible future scenarios but serve the purpose of studying the sensitivity and behavior of the AMOC in CMIP6 models under a freshwater flux forcing.

In another study, Swingedouw et al.[74] conducted a sensitivity analysis of the AMOC to a freshwater flux originating from Greenland Ice Sheet (GIS) melting using a high-resolution ocean model ( $1/24^\circ$ ). This ocean model has much higher resolution than the Earth System Models (ESMs) used in the study by Jackson et al. [32] derived from CMIP6. Due to its improved representation of diffusion and advection phenomena at the mesoscale, freshwater fluxes and their transport to critical deep convection zones are better captured in the study by Swingedouw et al.[74] This results in a larger freshening of the Labrador Sea in the high-resolution model, which then strongly influences deep convection activity. In the simulation incorporating Greenland melting, the AMOC weakens by about  $2 Sv$  after only 13 years, much more pronounced than what is observed in the CMIP6 model. Consequently, according to them, this difference raises serious concerns about the ability of CMIP6 models to accurately assess the potential impact of Greenland Ice Sheet melting on AMOC changes over recent decades and its future trajectory. They suggest that urgent progress should be made in the parameterization of mesoscale processes in ocean models to enhance confidence in Greenland Ice Sheet freshwater impacts on climate simulations and, consequently, AMOC projections.

Thus, the literature indicates that melting of the GIS has a destabilizing effect on the AMOC, but modeling and projecting the impact of AMOC on Greenland hosing is far from precisely understood. Improvements in the parameterizations of very high-resolution ocean models, as well as more realistic parameterizations of freshwater fluxes that could be produced by the GIS under realistic emission scenarios, are necessary and crucial to determine the response of the AMOC. However, the literature demonstrates that tipping the AMOC solely through a realistic freshwater flux associated with Greenland melting is not feasible.

### Stabilizing Effect of the AMOC on the GIS

On the other hand, it is acknowledged that a weakening or complete collapse of the AMOC will have a stabilizing effect on the GIS.[34] Indeed, by ceasing a significant portion of heat transport to the North Atlantic, an AMOC shutdown will significantly reduce atmospheric temperatures around Greenland, as explained in the preceding subsection. Thus, an AMOC shutdown represents a potentially strong negative feedback, which may result in a safe overshoot of the GIS tipping point.[62] This will be a key interaction phenomenon that we aim to incorporate into our model and analyze its consequences.

### The couplings to be considered

In conclusion, we can therefore provide an **answer to our sub-scientific question (1.c) regarding which important coupling phenomena to consider between the AMOC and the GIS.** To account for the destabilizing interaction of GIS melting on the AMOC, our dynamic model of the AMOC must include a term that considers the freshwater flux originating from the GIS. Physically, this term should be proportional to the derivative of the GIS volume. To incorporate the stabilizing effect of an AMOC collapse on the GIS, the dynamic model of the GIS must encode a dependence on the intensity of the AMOC, such that as the AMOC collapses, a stabilizing forcing term emerges. Furthermore, in addition to this ***positive-negative feedback loop***, we have discerned that concerning the AMOC, the primary forcing terms that should be incorporated into our model are those related to the global mean temperature and an additional contribution from the  $P - E$  balance. Conversely, for the GIS, we encapsulate the core dynamics by integrating solely a forcing term based on the global mean temperature into our model.

### The first relevant tipping cascade to study

It is due to the approach of the AMOC and the GIS towards their tipping points, as well as the mechanisms of interactions between them, and the colossal impacts that their collapses could produce on the climate, that they represent one of the first coupled tipping element systems fundamental to further study in the phenomenon of tipping cascade. It is also recognized that cascade effects in the climate are predominantly initiated by the polar ice caps[68], and the AMOC serves as a mediator between them, with interactions also affecting other tipping elements. Furthermore, the effect of the positive-negative feedback loop between the AMOC and GIS on the overall stability of the coupled system of climatic tipping elements is largely unknown.[37] Moreover, gaining a better understanding of the mechanisms of cascading collapse between the AMOC and the GIS would also benefit paleoclimatology by providing insights into events such as Dansgaard-Oeschger and other abrupt changes due to ice-ocean interactions that may have occurred in the past as suggested by paleo evidence.[6]

All of this motivates prioritizing the study of interactions between the AMOC and the GIS in tipping cascade phenomena.

In conclusion, **the preceding sections have addressed the sub-scientific question (1.b) of the importance of the AMOC and the GIS on future climate and have outlined possible cascading collapses between them.** However, we now seek to go further **by posing our main scientific question (1) of this thesis, which is to understand the implications of the effects of a realistic coupling between the AMOC and the GIS on their collapse dynamics.**

## 2.4 An AMOC-GIS Cascade Model

In this final section of this substantial literature review chapter, we will present the AMOC-GIS cascade model by V. Couplet, which will heavily inform the construction of the model used in this thesis. Our model will primarily aim to address the calibration limitations of the coupling coefficients present in V. Couplet's model and, importantly, integrate it within SURFER, a climate and carbon cycle model, to further analyze the impact of interactions between the AMOC and the GIS on their cascading collapse dynamics.

### 2.4.1 The Couplet model for the AMOC-GIS Cascade

To identify the interaction regimes of cascading collapses of two tipping elements, V. Couplet[15] developed the following model,

$$\dot{y}_1 = \left( y_1 - y_1^3 + \sqrt{\frac{4}{27}} \frac{q(t)}{q_{crit,1}} \right) \frac{1}{\tau_1}, \quad (2.12)$$

$$\dot{y}_2 = \left( y_2 - y_2^3 + \sqrt{\frac{4}{27}} \frac{q(t)}{q_{crit,2}} + c_{21}(1 + y_1) \right) \frac{1}{\tau_2}. \quad (2.13)$$

This model is based on the modeling approach of Wunderling et al.[87], as introduced in Equation (2.1). It incorporates the normal form of two dynamic systems, each undergoing a double-fold bifurcation as suggested by the literature. The terms  $\tau_1$  and  $\tau_2$  represent the characteristic timescales of collapse for the systems under study. The term  $q(t)$  denotes a generic forcing, such as the global mean temperature, parameterized by a Gaussian with a characteristic time  $\tau_f$ . Assuming that index 1 represents the GIS and index 2 the AMOC, the coefficient  $c_{21}$  encodes the coupling from the AMOC to the GIS.

By adopting reasonable values from the literature, with critical temperatures  $q_{crit,1} = 1.5^\circ C$  for the GIS and  $q_{crit,2} = 5^\circ C$  for the AMOC, a Gaussian maximum representing the temperature forcing  $a = 4^\circ C$ , and timescales  $\tau_f = 500$  years,  $\tau_1 = 1000$  years, and  $\tau_2 = 100$  years, V. Couplet obtains the results shown in Figure (28). It is observed that under this temperature forcing, neither tipping element undergoes a transition, even though the bifurcation point

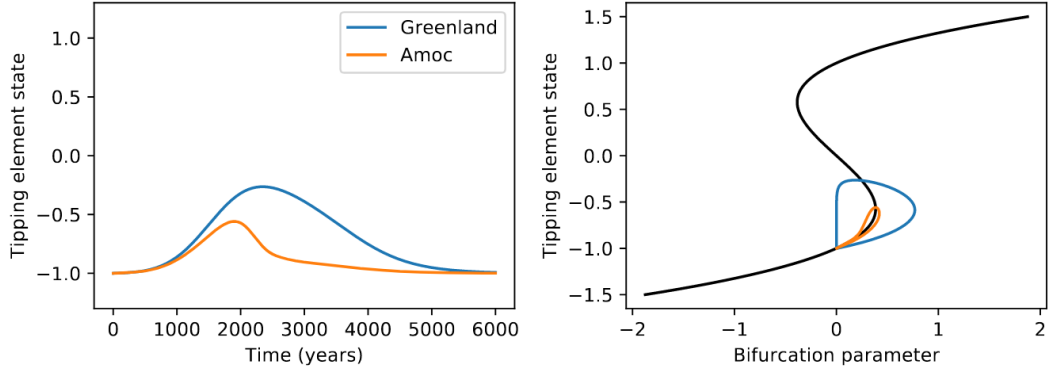


FIGURE 28 – Time evolution of Eq.(2.12,2.13) with  $a = 4^{\circ}\text{C}$ . Figure from V.Couplet[15]

is exceeded at times for each of them. Indeed, the forcing reaches values significantly above the critical temperature for Greenland, but because  $\tau_1 > \tau_f$ , the GIS does not have time to tip before the forcing begins to decline. This results in an *overshoot without tipping*. Interestingly, the AMOC crosses its bifurcation point not due to the direct forcing but because of its coupling with the GIS, even though the time spent beyond its bifurcation point and the maximum distance reached are not sufficient to ultimately tip the AMOC. In Figure (29), the same simulation is run but with a higher maximum intensity of the temperature forcing at  $a = 4.3^{\circ}\text{C}$ . In this scenario, the GIS still does not tip, however, it melts sufficiently to tip the AMOC.[15]

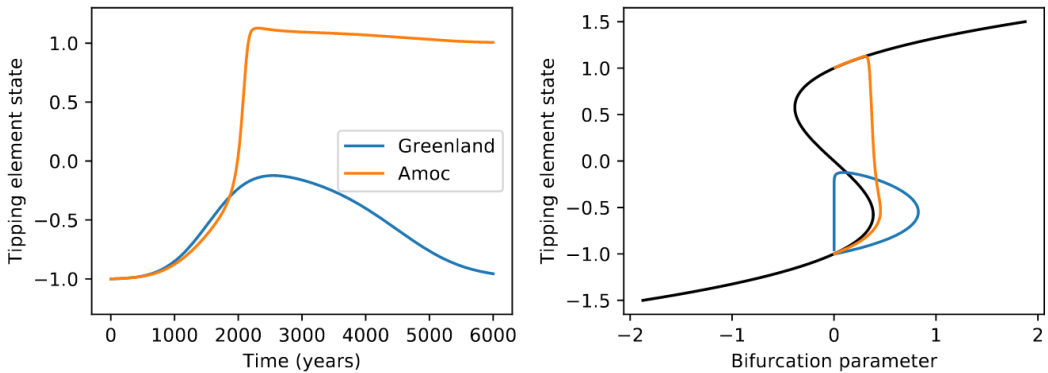


FIGURE 29 – Time evolution of Eq.(2.12,2.13) with  $a = 4.3^{\circ}\text{C}$ . Figure from V.Couplet[15]

Thus, these two experiments utilizing a simplified nonlinear dynamics model already serve to illustrate intriguing interaction phenomena. The interactions allow for the lowering of their critical tipping temperatures, even without observing cascades in the latter case where the AMOC tips even though the GIS has not, and the critical temperature of the AMOC was not reached. Consequently, a significant distinction between the AMOC and GIS is observed, as the GIS may remain stable even with lower critical temperatures due to their long tip-

ping time scales, whereas the AMOC, through its interactions with the GIS, can collapse before reaching its critical threshold due to destabilizing interactions with the GIS.[15]

#### 2.4.2 The limitations of the model

Based on this model and the findings, we aim to construct our *AMOC-GIS Tipping Cascade Calibration Model* (AGTCCM) in the following chapter to address the question of the effects of realistic couplings between the AMOC and the GIS on their cascade collapse dynamics. The advantage of V.Couplet's model (2.12,2.13) is that by utilizing the framework of nonlinear systems dynamics, it effectively captures the essential dynamics necessary for modeling cascade collapses. With the array of concepts and phenomena developed in subsection (2.2.2), this allows us to analyze the possible cascade collapses between the AMOC and the GIS efficiently.

#### Lack of stabilizing feedback from the AMOC on the GIS

However, three significant limitations to this model exist that we aim to address in this thesis. The first is of a physical nature, namely, that the stabilizing feedback of the AMOC on the GIS is not accounted for in the equations (2.12,2.12). This was also the case in the conceptual model of Sinet et al. [68], which did not incorporate the stabilizing effect on GIS melting from cooling in the northern hemisphere due to a halt or weakening of the AMOC. As concluded in that study, this strong negative feedback may result in significant qualitative differences in collapse dynamics, allowing for a safe overshoot of the GIS.

#### Calibration of coupling coefficients

In subsequent work by V. Couplet, which was communicated to me via personal communication, a new coupling term incorporating this stabilizing feedback of the AMOC on the GIS has been added to his model. However, the greatest methodological challenge of these models remains, and this is the lack of calibration of these couplings. Indeed, the coupling coefficients  $c_{12}$  (impact of the GIS on the AMOC) and  $c_{21}$  (impact of the AMOC on the GIS) were found in part arbitrarily by resorting to qualitative judgments based on the literature and posterior calibration to reproduce results deemed probable given the state of the art. However, the possible cascade collapse dynamics are highly sensitive to the values assigned to these coefficients. Therefore, constraining them based on data from process-based models is important, especially considering the nonlinear impacts that different collapse combinations may create in the future.

#### Integrating the tipping model into a climate model

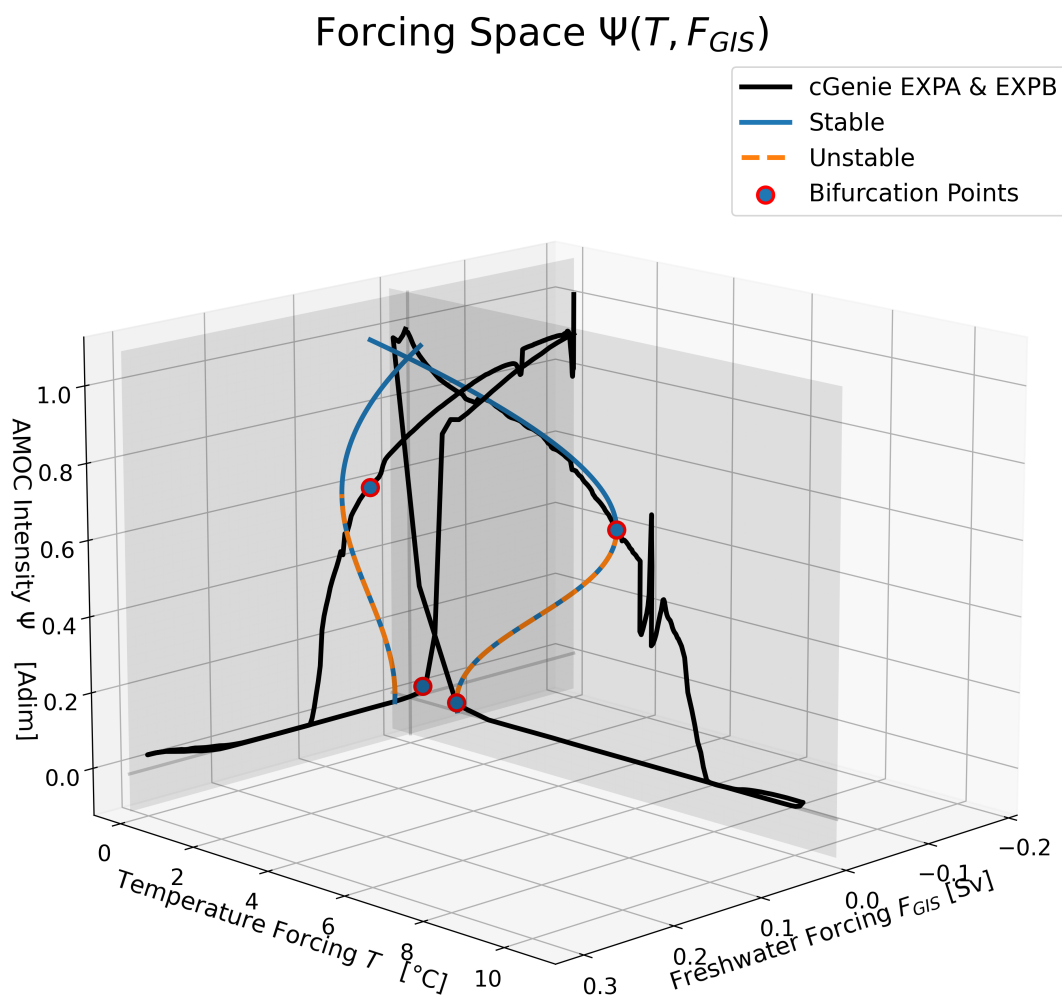
Finally, conceptual models such as that of V. Couplet (2.12,2.12) or those of Sinet et al.[68] and Klose et al.[37] use ad-hoc parameterizations for temperature

forcing. Due to the critical dependencies of possible cascade collapse dynamics on the forcing scenarios imposed, it would be highly relevant to integrate a simplified model of AMOC and GIS cascade collapse into a fast-running climate model. Indeed, testing numerous realistic emission scenarios would be very useful given the time constraints of computation and analysis of Earth System Models (ESMs), the uncertainties that remain regarding the exact positions of critical thresholds, and those concerning the current positions of tipping elements in their hysteresis loops. Version 3.1 of SURFER, incorporates a tipping element module, notably for the AMOC and GIS. However, this module suffers from the aforementioned limitation regarding how the coupling coefficients are calibrated. Furthermore, the AMOC is built independently of the carbon cycle of the model, whereas, as we have seen, an AMOC collapse would have a significant impact on the distribution of carbon within the various oceanic and atmospheric reservoirs.

## Conclusions

In conclusion, based on all that has been presented in this Chapter I, **We have motivated the reasons why, and now we aim to address our sub-scientific question (1d) of how to construct a simplified emulation of the AMOC-GIS dynamics that can be calibrated against more complex models. Subsequently, the second challenge will be to address sub-scientific question (1e) of how to integrate this model into SURFER to enable, notably, coherent integration with the carbon cycle. The following Chapter aims to answer these questions by developing the AGTCCM and the new version v3.2 of SURFER that incorporates it.** With SURFER v3.2, we will be able to address the main scientific question (1) regarding the effect of a realistic coupling between the AMOC and the GIS on their collapse dynamics in Chapter III.

# Chapter II - Integrating an AMOC-GIS Cascade Model into a Climate Model



### 3 Chapter II - Integrating an AMOC-GIS Cascade Model into a Climate Model

This chapter constitutes the technical core of this thesis, focusing on the development of an innovative and original approach to address our fundamental scientific question regarding the effects of a realistic coupling between the AMOC and the GIS on their collapse dynamics. After identifying the utility of modeling with a simplified nonlinear dynamics model that retains only the leading terms of interactions, we aim to create such a model that encodes these interactions but remains realistic by being calibrated as closely as possible to sensitivity data derived from more complex models. Subsequently, in order to examine the implications of these couplings between the AMOC and the GIS on future climate, we seek to integrate this simplified yet effective cascade-collapse model into a climate model. The methodological challenge is therefore to construct a model that maintains the flexibility and mathematical understanding of a simplified model while offering the quality of results derived from more complex models.

This chapter is structured as follows. Firstly, we will provide a rationale for linking a tipping cascade model of the AMOC and the GIS to a climate model. Subsequently, we will introduce SURFER v3.1, a conceptual and partially process-based climate model that offers numerous advantages and is highly relevant as a tool for our scientific inquiry. Thirdly, and central to this chapter, the *AMOC-GIS Tipping Cascade Calibration Model* (AGTCCM) will be presented. This original model encapsulates, in a simplified manner, the coupling dynamics between the AMOC and the GIS. Importantly, the AGTCCM incorporates a calibration method for the simplified AMOC-GIS model using hysteresis curves derived from more complex models. Following the presentation of the AGTCCM, an example of its calibration application with hysteresis curves derived from cGenie will be provided. This will serve as the initial evaluation of our model's quality. Subsequently, we will discuss the limitations of this model. Finally, the last section will detail the technical process of merging between the AGTCCM and SURFER v3.1. To achieve this, a parameterization and calibration of the impacts on the biogeochemical cycle of SURFER v3.1 by the AMOC will be introduced. The resulting SURFER v3.2 model, arising from the fusion of SURFER v3.1 and the AGTCCM, will enable us in Chapter III to address the primary scientific question of identifying the effects of a realistic coupling between the AMOC and the GIS on their collapse dynamics.

#### 3.1 Motivation for Linking a Tipping Cascade Model with a Carbon Cycle-Climate Model

Choosing and developing a model to address a scientific question necessarily entails considering which phenomena one aims to simulate and what dynamics are essential to incorporate for simulation. This deliberation is particularly crucial

in climatology, given the significant hierarchy among existing models. Indeed, there are considerable differences between Energy Balance Models (EBMs), which describe temperature evolution within a layer through a simple ordinary differential equation, and high-resolution models that solve, with very fine grids on the order of a few hundred meters, the fluid dynamics equations within the atmosphere or oceans. As depicted in Figure (30) by Von Der Heydt et al. [79], depending on the number of processes one intends to model and their scales, a spectrum of models is available, ranging from Conceptual Models to Earth System Models (ESMs).

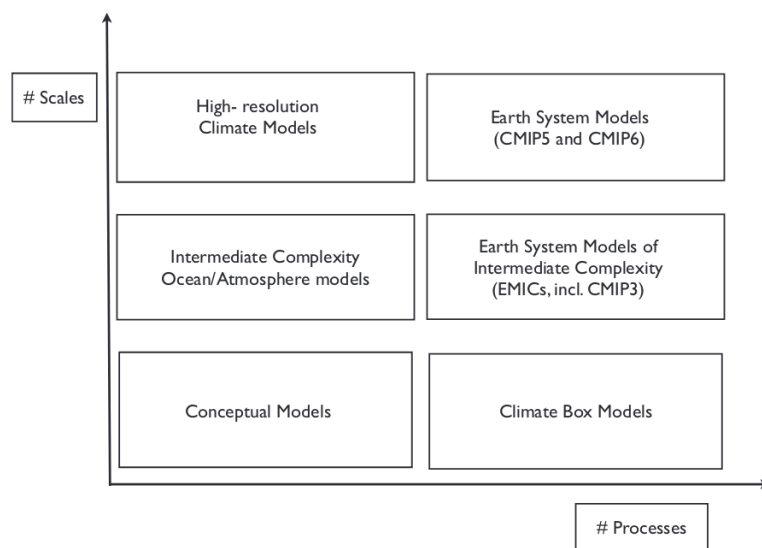


FIGURE 30 – *Classification of climate models according to the two model traits : number of processes and number of scales. Figure from Von Der Heydt et al.[79]*

In our case, we aim to simulate the potential cascade collapse dynamics between the AMOC and the GIS. As discussed in Chapter I, the AMOC and the GIS are two distinct dynamic systems with very long timescales. The characteristic timescale for the AMOC is on the order of centuries, while for the GIS, it is on the order of millennia. Furthermore, the literature review in Chapter I demonstrated that for our goal of investigating the coupling effects between the AMOC and the GIS, it is not necessary to have a detailed description and simulation at very small spatial scales of their dynamics. Indeed, both for their individual dynamics and for their coupling dynamics, the reductionist research paradigm aiming to capture dominant effects at first order proves to be very satisfactory. This is particularly evident in the work of Sinet et al. [68] and V. Couplet with his model of nonlinear dynamics (Eq.(2.12-2.13)). Additionally, as stated in subsection (2.2.1), it has been demonstrated that Earth System Models (ESMs) and High-resolution Climate Models exhibit a lack of integration of essential processes regarding tipping dynamics, which generally induces a stabilizing bias in these models. These initial considerations already allow us to

eliminate the need to use, in our specific case, High-resolution Climate Models or ESMs.

Moreover, sensitivity experiments and collapse of tipping elements such as the GIS and the AMOC are quite complex to conduct. Indeed, due to the time scales involved, there is a computational cost associated with calculating quasi-equilibrium hysteresis curves in models that are at least Earth Models of Intermediate Complexity (EMICs).[58]. Therefore, there is a genuine interest in being able to produce hysteresis loops for these tipping elements at a lower computational cost, which is the major advantage of simplified models.

In addition to the success of first-order simplified dynamics and the difficulty of producing realistic hysteresis loops, we face operational constraints regarding the computational time required to effectively probe the potential cascade collapse dynamics over long time scales. Indeed, even if irreversible collapse may be imminent, the GIS would likely take nearly a thousand years to fully melt. Therefore, we need climate models with computational times sufficiently low to allow simulations over large time scales, while also capturing the necessary physical processes to provide a coherent description of the climate over such periods. Moreover, phenomena such as *overshoot without tipping* or *rate-induced tipping* may also occur. These phenomena depend on the emission scenarios considered, and for the purpose of providing useful projections for society, having a climate model available that can simulate the climate while accounting for these tipping points under many probable emission scenarios is highly beneficial. For computational efficiency reasons, we are therefore leaning towards EMICs, Conceptual Models, or Climate Box Models.

In addition to their collapses, these phenomena would have significant impacts on the remaining climate, which are important to capture. A collapse of the GIS would notably have a significant impact on Sea Level Rise, while that of the AMOC would have important consequences on the biogeochemical cycle as well as temperature distributions around the Atlantic. It is thus understood that having a reliable climate model capable of simulating plausible emission scenarios to then make coherent projections of possible tipping element collapse scenarios and their consequences is a necessity. This is both necessary for the scientific exploration of potential dynamics in themselves and as an exploration aimed at suggesting mitigation and adaptation policies to climate warming.

For all these justifications regarding the objectives of our scientific research, we have decided to construct a simplified model capable of simulating cascade collapses of the AMOC and the GIS (AGTCCM). This model can serve as an emulator by calibrating itself to hysteresis loops of more complex models and then integrating this model into a carbon cycle-climate model. The carbon cycle model that we need must, based on the requirements of the scientific endeavor presented here, be a conceptual model but still requires effective parameterizations and calibrations that allow it to be used as a tool for projecting various relevant future climates over long timescales.

### 3.2 A Reduced Model Named SURFER

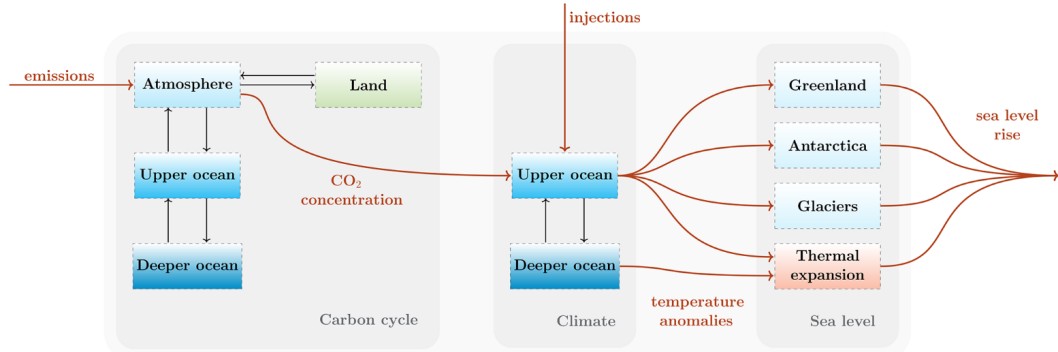


FIGURE 31 – *Conceptual diagram of SURFER v2.0. The state variables are indicated by the boxes, interactions and sources are depicted by black and dark orange arrows respectively. Figure from Martinez Monteiro et al.[79]*

SURFER is a reduced model designed to estimate global mean temperature increase, sea level rise, and ocean acidification in response to CO<sub>2</sub> emissions and aerosol injections based on only nine differential equations. Due to its simplicity, SURFER is capable of simulating these data over time scales of several thousand years. It is fast, easy to understand, and modify, making it appropriate for use in policy assessments as well as for our personal modifications. The model is based on a combination of conservation laws for the masses of atmospheric and oceanic carbon and for oceanic temperature anomalies, and ad hoc parameterizations for different contributors to sea level rise : ice sheets, glaciers, and ocean thermal expansion. Despite its simplicity, SURFER is efficiently calibrated and can replicate the results of more sophisticated, high-dimensional ESMs over time scales up to millennia[52].

#### 3.2.1 The evolutions of SURFER

Although SURFER is a recent model (2022), it has already undergone significant development. To facilitate understanding, we define the following semantics among different versions. Specifically, we will refer to SURFER v2.0, v3.0, v3.1 and v3.2. The differences between these three versions are summarized in Table (1).

The most significant and notable differences between SURFER v3.0 and SURFER v2.0 aim to address the limitations of SURFER v2.0, which stem from its absence of key processes in the carbon cycle over time scales of several millennia. Indeed, SURFER v2.0 can only reliably simulate carbon-related quantities for up to two or three millennia and only considers carbon dioxide emissions in the carbon cycle. In SURFER v3.0, Couplet et al. [17] introduced several enhancements, including a representation of atmospheric methane, a distinction between land-use and fossil emissions, an additional oceanic layer, a dependency of solubility and dissociation constants on temperature and pressure, a dynamic

SURFER Version	Key Features
SURFER v2.0	<ul style="list-style-type: none"> <li>- Basic Carbon Cycle Model</li> <li>- Two-layer Model</li> <li>- 2 Tipping Elements (GIS,AIS).</li> <li>- Basic SLR Model</li> <li>- Basic Climate Model</li> </ul>
SURFER v3.0	<p>SURFER v2.0 +</p> <ul style="list-style-type: none"> <li>- Upgraded Oceanic Model, Climate Model and Carbon Cycle Model with the addition of an intermediate layer.</li> <li>- Upgraded Carbon Cycle Model with the addition of a sediment layer</li> <li>- Addition of a <math>CH_4</math> Model.</li> </ul>
SURFER v3.1	<p>SURFER v3.0 +</p> <ul style="list-style-type: none"> <li>- Tipping Cascade Module (AMOC, GIS, WAIS, EASB, EAIS, AWSI, AMAZ, PERM)</li> </ul>
SURFER v3.2	<p>SURFER v3.1 +</p> <ul style="list-style-type: none"> <li>- AMOC/GIS Tipping Cascade Calibration Model (AGTCCM)</li> <li>- Impacts of an AMOC collapse on the Carbon Cycle</li> </ul>

TABLE 1 – *Definition of the semantics used to describe the different versions of the SURFER model utilized in this thesis.*

representation of alkalinity, a 65 sediments box, and weathering processes. The conceptual diagram of SURFER v3.0 is depicted in Figure (32).

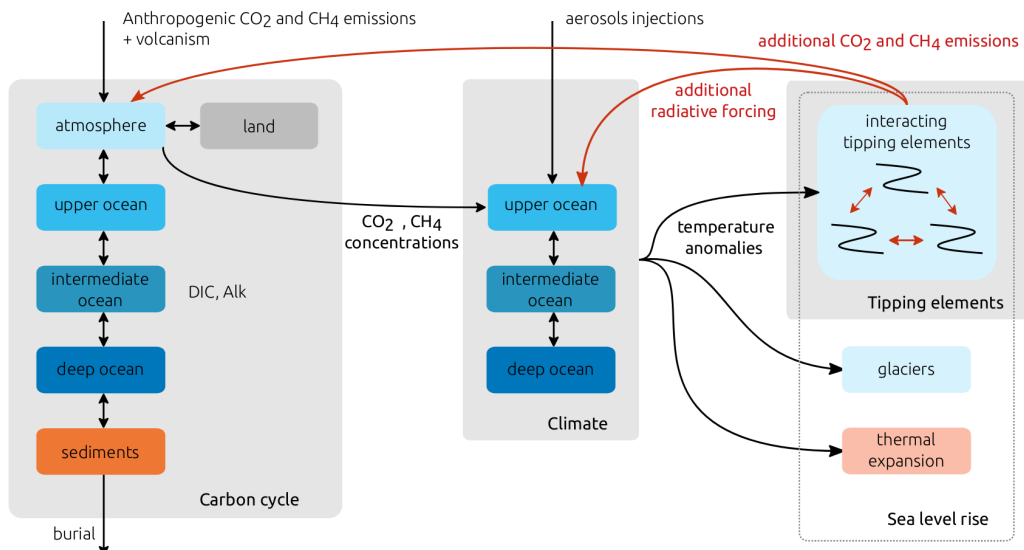


FIGURE 32 – *Conceptual diagram of SURFER v3.0. The state variables are indicated by the boxes, interactions and sources are depicted by black arrows. Figure from Couplet et al./13/*

### 3.2.2 The Tipping Element Module in SURFER v3.1

However, these improvements in SURFER v3.1 regarding the modeling of the carbon cycle are not what interests us the most in relation to our scientific inquiries. The most significant aspect for us is the version v3.1 of SURFER with the addition of a tipping element module within the philosophy of nonlinear dynamical models presented in subsection (2.3.4), with all the advantages described.<sup>3</sup> Indeed, this version of SURFER includes a modeling of 8 tipping elements listed with their acronyms in Table (2)<sup>4</sup>. Each of these tipping elements is described by the following ODE,

$$\frac{dx_i}{dt} = \left\{ \underbrace{-x_i^3 + a_i x_i^2 + b_i x_i + c_i}_{\text{Internal Dynamics}} + \underbrace{d_i T}_{\text{Temperature Forcing}} - \underbrace{\sum_{j=1}^8 e_{ij} L_j}_{\text{Couplings with other TE}} \right\} \frac{1}{\tau_i} \quad (3.1)$$

where  $i = 1, 2, 3, 4, 5, 6, 7, 8$ , depending on the tipping element considered.

<b>1</b>	<b>GIS</b>	Greenland Ice Sheet
<b>2</b>	<b>AMOC</b>	Atlantic Meridional Overturning Circulation
<b>3</b>	<b>WAIS</b>	West Antarctic Ice Sheet
<b>4</b>	<b>EASB</b>	East Antarctic Subglacial Basins
<b>5</b>	<b>EAIS</b>	East Antarctic Ice Sheet
<b>6</b>	<b>AWSI</b>	Artcic Winter Sea Ice
<b>7</b>	<b>AMAZ</b>	Amazon rainforest
<b>8</b>	<b>PERM</b>	Permafrost

TABLE 2 – of the 8 Tipping Elements modeled in SURFER v3.1

We thus find a third-order polynomial with the normal form of a double fold to describe the internal dynamics of each tipping element. In addition to this, a forcing term is systematically imposed by the anomaly of global mean temperature, which will be calculated in SURFER. The coefficients  $a_i, b_i, c_i, d_i$  are constants specific to each tipping element, which are calibrated based on the critical coordinates of the bifurcation points of the tipping elements under a temperature forcing. The method used to determine the values of these coefficients is described in Martinez Monteiro et al. [52] and will be further developed

3. The v3.1 version of SURFER does not yet have an official paper published to describe it. I personally gained access to the code for this version through personal communication with Victor Couplet. However, the original version of this model is available on the GitHub repository associated with this thesis.

4. In SURFER v3.1, the indices of the tipping elements are actually different, but we have redefined them to have the GIS as number 1 and the AMOC as number 2. In the numerical code of the new version of the SURFER v3.2 model presented at the end of the chapter, this facilitates modeling and understanding of the model.

later in this chapter. The entire dynamics of the tipping elements is multiplied by the inverse of a characteristic time scale specific to each, in order to account for the diverse time scales between the tipping elements. Furthermore, the tipping element module already present in SURFER v3.1 incorporates parameterizations of feedbacks in terms of emissions of CO<sub>2</sub> and CH<sub>4</sub>, as well as additional radiative forcing that may occur following tipping events of certain tipping elements.

The most interesting term for us, on which we will indeed focus in the case of AMOC-GIS, is that of couplings with the other tipping elements. This modeling of coupling effects that may exist between the tipping elements themselves allows the model to illustrate the effects of cascade collapse that can occur in the climate system. The matrix  $S_{moy}$  encodes all coupling coefficients  $e_{ij}$  between the tipping elements and is provided in Table (3).

	<b>GIS</b>	<b>AMOC</b>	<b>WAIS</b>	<b>EASB</b>	<b>EAIS</b>	<b>AWSI</b>	<b>AMAZ</b>	<b>PERM</b>
<b>GIS</b>	0	-1,1	0,3	0,3	0	0	0	0
<b>AMOC</b>	0	0	0	0	0	0,3	0	0
<b>WAIS</b>	1,1	0,25	0	0	0	0	0	0
<b>EASB</b>	1,1	0,25	0	0	0	0	0	0
<b>EAIS</b>	0	0	0	0	0	0	0	0
<b>AWSI</b>	0	-0,3	0	0	0	0	0	0
<b>AMAZ</b>	0	0,1	0	0	0	0	0	0
<b>PERM</b>	0	0	0	0	0	0	0	0

TABLE 3 – Matrix  $S_{moy}$  that lists all coupling coefficients between the tipping elements.

The latest modeling of tipping elements in SURFER v3.1 includes the incorporation of parameterizations for climate feedbacks resulting from the collapse of certain tipping elements. As noted in Chapter I, a complete melting of the Greenland Ice Sheet (GIS), for instance, exposes a previously ice-covered continent with high albedo, significantly impacting the Earth's radiative balance by altering the surface albedo. This albedo feedback is similarly applicable to other components of the cryosphere. Additionally, tipping elements such as the Amazon rainforest and permafrost, upon collapse, are modeled to emit significant quantities of CO<sub>2</sub> and CH<sub>4</sub>. Therefore, in SURFER v3.1, these consequences, which also impact other tipping elements, thereby promoting cascade dynamics, are parameterized. Although these parameterizations are simplified using a unique coefficient for each tipping element, they nonetheless contribute to enriching the dynamics of potential collapses.

### 3.2.3 The Shortcomings of SURFER v3.1 in Modeling the Cascade Collapses of AMOC and GIS

The primary limitation in the tipping element module of SURFER v3.1, as presented in equation (3.1), resides in the method used for calibrating the co-

efficients  $e_{ij}$ . Indeed, these coefficients are partially determined in an arbitrary manner, based on comparing orders of magnitude between the expected coupling effects of the tipping elements, as suggested by the literature, and subsequent adjustments made according to the outcomes from the fixed values. Referring to Table (3), we can see that there is already (with the aforementioned flaws) a parameterization of the stabilizing effect of the AMOC on the GIS with a value  $e_{21} = -1.1$ . However, for the destabilizing effect of the GIS on the AMOC, no parameterization exists in SURFER v3.1.

Therefore, building on the insights described in Chapter I, we aim to explicitly model the respective dependencies of the AMOC and the GIS to illustrate the cascade collapse dynamics that can occur between these two tipping elements. We seek to enhance the physical modeling of their dynamics beyond equation (3.1). Specifically, we intend to incorporate, for each of these two tipping elements, a forcing term that directly depends on the state of the other. Consequently, we are developing a new model of simplified nonlinear dynamics for the AMOC and GIS that accounts for their mutual coupling. Subsequently, we need to devise an effective calibration method for their coupling coefficients from the GIS to the AMOC, denoted as  $e_{12}$ , and from the AMOC to the GIS, denoted as  $e_{21}$ . This model, referred to as the AGTCCM, is presented in the following section.

### 3.3 AMOC-GIS Tipping Cascade Calibration Model (AGTCCM)

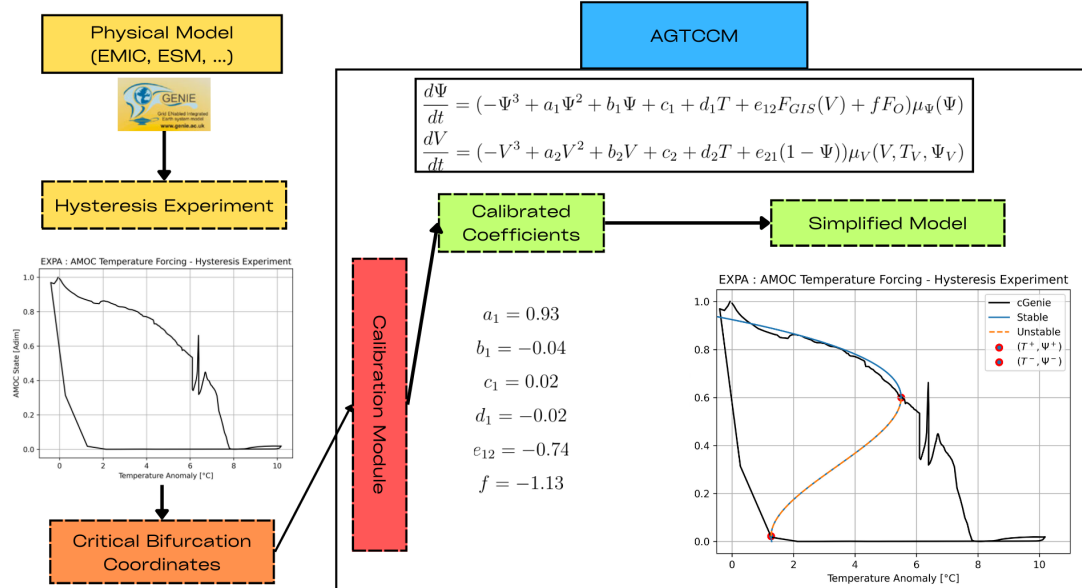


FIGURE 33 – Methodology for Utilizing the AMOC-GIS Tipping Cascade Calibration Model (AGTCCM)

We aim to develop a new dynamic model capable of simulating the states of

the AMOC and GIS, incorporating their coupling to underscore potential cascade collapse behaviors. The goal is to develop a simplified model of nonlinear dynamics in line with that described in section (2.3) to take advantage of mathematical benefits and interpretations of results while maintaining a model as realistic as possible in the values it produces. To do so, the AGTCCM incorporates an algorithm for calibrating the dynamics of the AMOC and the GIS using hysteresis loops produced by any more complex model. Each part of the AGTCCM will be described and explained, and the big picture of this methodological approach is illustrated in Figure (33). In this section, we will explore the fourth scientific sub-question, which focuses on creating an emulator that captures the simplified dynamics of the AMOC and the GIS, thereby illustrating their cascading collapse dynamics. As introduced at the beginning of the chapter, the AGTCCM will serve as an essential tool to address our primary scientific inquiry of studying the effects of a realistic coupling between the AMOC and the GIS on their collapse dynamics.

Contrary to the oceanic component of the carbon cycle model and the climate model employed by SURFER, the tipping element model we aim to construct is not directly derived from physical processes. This decision is deliberate for two reasons : firstly, as motivated in Section (2.3.1), there is a significant efficiency provided by the nonlinear dynamics paradigm in understanding and analyzing dynamic systems by capturing only the first orders of their complex dynamics. Secondly, as motivated in Section (3.1), the ultimate goal is to integrate AGTCCM into the SURFER model to produce a climate, carbon cycle, and tipping element model that is both robust and computationally efficient. This methodological necessity is crucial to effectively address our scientific questions. Thus, the AGTCCM model should be capable of either being directly simulated in SURFER or introducing parameterizations that enable the connection of these new variables to what is calculated within SURFER.

Thus, the AGTCCM adopts the form of a general dynamic system, namely a coupled system of ODEs, based on the concept of a double-fold bifurcation introduced earlier. In addition to finding a modeling approach that effectively captures the first-order effects of the intrinsic dynamics as well as the coupling between the AMOC and the GIS, the second and primary technical challenge of this model lies in devising the most effective method to calibrate the simplified dynamics based on hysteresis from more process-based models, such as cutting-edge ESMs or EMICs. These models are particularly valuable for simulating the complex hysteresis dynamics of the AMOC based on advanced physical principles. In this regard, our model functions as an emulator.

### 3.3.1 The AMOC-GIS Model in AGTCCM

The coupled ODE system representing the dynamics of the AMOC and the GIS in the AGTCCM is formulated as follows<sup>5</sup> :

$$\frac{d\Psi}{dt} = (-\Psi^3 + a_1\Psi^2 + b_1\Psi + c_1 + d_1T + e_{12}F_{GIS}(V) + fF_O)\mu_\Psi(\Psi) = h(\Psi, T, F_{GIS}, F_O) \quad (3.2)$$

$$\frac{dV}{dt} = (-V^3 + a_2V^2 + b_2V + c_2 + d_2T + e_{21}(1 - \Psi))\mu_V(V) = g(V, T, \Psi). \quad (3.3)$$

As anticipated, we maintain the form of a third-order polynomial to generalize the normal form of a double fold given by  $-x^3 + \alpha x$ . To the normal form of a double fold, we add a term of the form  $\beta x^2$  in order to better fit the simplified model to the bifurcation diagram of experiments derived from more complex models. It's important to emphasize that we are engaged in conceptual modeling aimed at emulating, based on the insights from more complex models, the dynamics of the tipping elements under study. Thus, the various coefficients  $a_i, b_i, c_i, d_i$  are not included because they represent specific physical processes, but rather because collectively they generate a state space structure that aligns with that of reality, or at least, that of the future emulated model. The functions  $h$  and  $g$  serve to explicitly present the dependencies and what the dynamics of the AMOC and GIS in our model depend on.

#### The State Variables $\Psi$ and $V$

The state variable  $\Psi$  represents the state of the AMOC, while the state variable  $V$  pertains to the GIS. We might opt to express  $\Psi$  in units of  $Sv$  (Sverdrups) as a measure of circulation intensity and  $V$  in cubic meters as a unit of volume for the Greenland ice sheet, but we will adhere to the philosophy already present in SURFER v3.1. This involves normalizing the state variables of the tipping elements on an interval from  $[0, 1]$  to more easily compare their relative states to their pre-industrial equilibrium states. Thus, the state variables  $\Psi$  and  $V$  are dimensionless.

#### The characteristic timescale function $\mu$

The functions  $\mu_\Psi(\Psi)$  and  $\mu_V(V)$  represent the characteristic time scales of the AMOC and GIS, respectively. These time scales are crucial to consider, as described earlier in the context of cascade collapse dynamics, to acknowledge the fact that coupled systems can have very different characteristic collapse time scales. This is indeed the case for the AMOC and GIS, where the characteristic time scale for the AMOC is  $\tau_\Psi^+ = \tau_\Psi^- = 10$  years, while for the GIS, it is  $\tau_V^+ = \tau_V^- = 700$  years. These are the values obtained from SURFER v3.1 that we

---

5. The term  $F_{GIS}(V)$  in equation (3.2) is explicitly written with the dependence on  $V$  to emphasize the coupling between the dynamic equation of the AMOC and that of the GIS. In subsequent notations, this dependence will be omitted to streamline the notation.

will not alter in order to compare subsequent results with the AGTCCM. The distinction between  $\tau^+$  and  $\tau^-$  serves to encode the fact that physically, there can be characteristic times associated with the dynamics of tipping elements that differ depending on whether the tipping element has tipped (denoted by a " $-$ ") or has not tipped (denoted by a " $+$ "). Although the mathematical framework as well as the numerical framework will allow for this generalization, we will initially consider these time scales to be identical for each tipping element. Mathematically, these  $\mu$  functions are defined as follows :

$$\mu_\Psi(\Psi) = 1/\tau_\Psi^+ \quad \text{if } \Psi < 1, \frac{d\Psi}{dt} > 0 \quad (3.4)$$

$$\mu_\Psi(\Psi) = 1/\tau_\Psi^- \quad \text{if } \Psi > 0.01, \frac{d\Psi}{dt} < 0 \quad (3.5)$$

$$\mu_V(V) = 1/\tau_V^+ \quad \text{if } V < 1, \frac{dV}{dt} > 0 \quad (3.6)$$

$$\mu_V(V) = 1/\tau_V^- \quad \text{if } V > 0.01, \frac{dV}{dt} < 0 \quad (3.7)$$

### The temperature forcing $T$

In both equations (3.2) and (3.3), we find the first forcing term to be due to temperature  $T$ .<sup>6</sup> As described in more detail in Chapter I, it is important to recall that temperature forcing is the primary driver in terms of magnitude to consider in the dynamics of AMOC and GIS collapse. Physically, the dynamic of the AMOC is influenced by ocean stratification, where an increase in atmospheric temperature increases the buoyancy of surface waters, leading to reduced convection into the depths at NADW sites. Similarly, for the GIS, it is evident that a rise in surface temperature will lead to more significant ice melting and consequently, a decrease in its volume.

### The freshwater flux forcings

Upon closer examination of equation (3.2) for the AMOC, we note additional terms beyond the temperature forcing term  $d_1 T$  introduced in Couplelet's model (refer to section (2.3.4)) :  $F_{GIS}$  and  $F_O$ . These terms represent freshwater flux forcings, indicating that the primary-order dynamics of the AMOC are influenced by the stratification of the Atlantic Ocean, which depends not only on temperature but also on salinity. Similarly, a change in salinity corresponds to a change in freshwater flux that can enter the considered water basin.  $F_{GIS}$  encodes the freshwater flux associated with the melting of the GIS, while  $F_O$  includes both the freshwater fluxes<sup>7</sup> associated with the melting of other

---

6. To avoid overburdening the equations, I have decided not to denote, despite the convention for anomalies,  $\delta T$  instead of  $T$  for example.

7. The  $O$  in  $F_O$  stands for "Others"

cryospheric components simulated in SURFER v3.1 and the freshwater flux associated with the variation of the  $P - E$  balance over the Atlantic basin. As described in Chapter I, these are the essential forcings to be considered at the first order to describe the dynamics of AMOC collapse. We will now detail the parameterizations of  $F_{GIS}$  and  $F_O$ .

### The $F_{GIS}$ forcing

$F_{GIS}$  represents the freshwater flux associated with the melting of the Greenland ice sheet. As described in Chapter I, melting of the Greenland ice sheet releases freshwater, which can, to a non-negligible extent, reach the deep water formation sites of the AMOC. Thus, by increasing the buoyancy of surface waters, it enhances the stratification of the water column and reduces deep convection. Therefore, we force Equation (3.2) with the term  $F_{GIS}$ . The natural parameterization chosen for  $F_{GIS}$  is as follows :

$$F_{GIS} = \alpha_{GIS} \dot{V}. \quad (3.8)$$

The rate of melting of the GIS, and thus its freshwater contribution, is evidently proportional to the temporal variation of its volume, in other words, its derivative  $\dot{V}$ . What should be the units of the constant  $\alpha_{GIS}$ ? It is used to relate the temporal variation of the (dimensionless) fraction of the GIS volume relative to its pre-industrial reference state to a freshwater flux. In the SURFER model that we will be using, the default temporal resolution is one year. Therefore, we have that  $[\dot{V}] = [yr^{-1}]$ . For simplicity of comparison with the literature, we want to be able to express  $F_{GIS}$  in Sverdrups. Therefore, the units of  $\alpha_{GIS}$  must be in  $[Sv.yr]$  so that,

$$[F_{GIS}] = [Sv] = 10^6 \left[ \frac{m^3}{s} \right] = [Sv.yr][yr^{-1}] = [\alpha_{GIS}][\dot{V}] \quad (3.9)$$

Beyond its units based on dimensional analysis, through physical reasoning we realize that  $\alpha_{GIS}$  must be expressed in  $[Sv.yr]$ , which is a volume representing the maximum freshwater flux volume associated with the complete melting of the Greenland ice sheet. By converting the units appropriately, we obtain the following equality,

$$\alpha_{GIS} = \kappa S_{pot}^{GIS} \quad (3.10)$$

with,

$$\kappa = 11, 47. \quad (3.11)$$

$S_{pot}^{GIS}$  represents the Sea Level Rise (SLR) potential from a complete melting of the GIS. In a recent paper by Morlighem et al.[55], they estimate that  $S_{pot}^{GIS} = 7.42m$ , which is a significantly different and more precise value than the one initially present in SURFER v3.1. The factor  $\kappa$  is utilized for unit conversions and does not have any real physical meaning; however, it encodes the global

ocean surface area in square meters and facilitates numerical conversions to ensure the results are expressed in the correct units. Based on the values of  $\kappa$  and  $S_{pot}^{GIS}$ , it is found that,

$$\alpha_{GIS} = 85,1074 \text{ Sv.yr} \quad (3.12)$$

One might rightly wonder whether our parameterization should also take into account a so-called "geographical" correction factor, namely that not all the meltwater from Greenland will necessarily reach the critical deep water formation zones of the NADW. In other words, not all the water melting from the GIS will impact the AMOC in the same critical manner. However, in our experimental protocol, which will be further developed in Section (3.4), we will calibrate the model Eq.(3.2) using a sensitivity experiment that directly adds freshwater to the critical convection zones of the AMOC. Therefore, due to the chosen calibration methodology, we should not introduce such a geographical correction factor.

### The $F_O$ forcing

As explained in Chapter I, studies have shown that solely perturbing the AMOC through the freshwater flux from the GIS appears rather idealistic ; such an occurrence is only plausible under extreme thresholds [32], at the limits of physically achievable values. Conversely, other studies[68, 56, 65, 46] have demonstrated that significant contributions to freshwater flux in a warming climate, such as contributions from other ice caps like Antarctica, and the effect of the difference between precipitation and evaporation over ocean basins  $P - E$ , play a substantial role in the freshwater balance reaching the Atlantic Ocean. Therefore, to enhance the physicality of the AMOC model, I introduce the freshwater flux forcing term  $F_O$ , which is modeled as follows :

$$F_O = F_W + F_{P-E}. \quad (3.13)$$

### The freshwater forcing from other components of the cryosphere $F_W$

$F_W$  represents all contributions of freshwater flux from the cryosphere, excluding those from the GIS, which has its dedicated parameterization through the term  $F_{GIS}$ . The model does not account for the contribution of glaciers to the freshwater flux impacting the AMOC. This exclusion is justified by the minimal quantity of freshwater flux attributed to glaciers compared to that from the Greenland and Antarctic ice sheets. Additionally, the spatial distribution of glaciers suggests that even if they were to completely melt, the resulting freshwater flux into critical AMOC zones would be negligible. However, the Antarctic ice sheet represents a significant potential source of freshwater that we will include in the parameterization of  $F_W$ . The advantage lies in SURFER v3.1's existing simulation of the WAIS, EASB, and AWSI. Consequently, we adopt a similar methodology for parameterizing  $F_W$  as we did for  $F_{GIS}$ , namely,

$$F_W = F_{WAIS} + F_{EASB} + F_{EAIS}, \quad (3.14)$$

with,

$$F_{WAIS} = \alpha_{WAIS} \dot{V}_{WAIS}, \quad (3.15)$$

$$F_{EASB} = \alpha_{EASB} \dot{V}_{EASB}, \quad (3.16)$$

$$F_{EAIS} = \alpha_{EAIS} \dot{V}_{EAIS}, \quad (3.17)$$

Again, the significance of the coefficients  $\alpha_{WAIS}$ ,  $\alpha_{EASB}$ , and  $\alpha_{EAIS}$  is the same as that for  $\alpha_{GIS}$ . These coefficients do not inherently have a physical meaning but are used for unit conversions in order to obtain associated freshwater fluxes in Sverdrups. These coefficients are defined as follows,

$$\alpha_{WAIS} = \beta \kappa S_{pot}^{WAIS}, \quad (3.18)$$

$$\alpha_{EASB} = \beta \kappa S_{pot}^{EASB}, \quad (3.19)$$

$$\alpha_{EAIS} = \beta \kappa S_{pot}^{EAIS}. \quad (3.20)$$

The unit conversion factor  $\kappa$  always takes the same value as defined in equation (3.11), while the values of the potential sea level rise associated with the melting of the different components of Antarctica are as follows,

$$S_{pot}^{WAIS} = 5 \text{ m}, \quad (3.21)$$

$$S_{pot}^{EASB} = 9 \text{ m}, \quad (3.22)$$

$$S_{pot}^{EAIS} = 45 \text{ m}. \quad (3.23)$$

However, there are two significant differences and complications in the parameterization and calibration of  $F_W$  compared to that of  $F_{GIS}$ . The first originates from an epistemological standpoint, while the second is methodological in nature. The first challenge is that, as explained more extensively in Chapter I, the effect of a freshwater forcing from the Southern Atlantic on the AMOC is less clear than that of the GIS. The second challenge is that we have not been able to access a cGenie sensitivity experiment for hosing added in the Southern Atlantic near Antarctica, so as to provide emulation of the impact of Antarctic melting on the AMOC.

Indeed, as will be detailed in Section (3.3.6), our second hosing experiment involves introducing a freshwater flux forcing between 20°N and 50°N within the Atlantic. Consequently, it becomes imperative to introduce a "geographical" reduction factor to account for the fact that not all the freshwater associated with the melting of Antarctic components will reach this region. Qualitative assessments and literature estimates suggest a reduction factor of  $\beta = 10\%$ . In essence, we assume that only 10% of the freshwater flux linked to the melting of Antarctic components will exert a significant hosing effect in the zone

between 20°N and 50°N of the Atlantic. Admittedly, reducing the dynamics of Atlantic circulation transport in this manner is complex, and furthermore, obtaining plausible values from the literature presents significant challenges. We are aware of the complex distribution of ocean currents originating from the Atlantic, starting with the Antarctic Circumpolar Current, and recognize that the northward circulation reality does not consist solely of surface advective flow but involves a much more complex dynamic. This includes, notably, the upwelling zones in the Southern Atlantic. Additionally, as discussed in Chapter I, a freshwater input in the Southern Atlantic could potentially enhance the stability of the AMOC [68]. The choice of the value for this coefficient is primarily dictated pragmatically to ensure it generates freshwater fluxes in physically plausible quantities comparable to those of  $F_{GIS}$ .

Therefore, considering all these epistemological challenges, in the SURFER model v4.0, it is straightforward to set  $F_W = 0Sv$  to focus the investigation on  $F_{P-E}$ , which is recognized as the second major source of freshwater flux essential for the dynamics of the AMOC that we aim to examine in depth. Nonetheless, despite its potentially limited validity, we have opted to parameterize  $F_W$  in order to assess whether its inclusion produces qualitatively interesting findings in the subsequent chapter. At the end of this section, the limitations of the AGTCCM will be discussed, and concrete avenues for improvement will be proposed. Even though the epistemic validity of this parameterization is seriously questionable, we will not base all our analyses on it; at the very least, this modeling lays the groundwork and establishes the mathematical and numerical framework for future improvements, some of which are readily achievable.

### The freshwater forcing from the $P - E$ anomaly $F_{P-E}$

Subsequently, parameterizing the third AMOC forcing term through a freshwater flux,  $F_{P-E}$ , poses an even more significant challenge. Once again, we aim to relate this quantity to variables simulated within SURFER v3.1. As discussed in Chapter I, it is physically reasonable to parameterize the anomaly of the evaporation minus precipitation balance over the global ocean basin as a function of the temperature anomaly. This is why we opt for the following equation :

$$(P - E) = (P - E)^* + \theta\delta T \quad (3.24)$$

with  $(P - E)^*$  representing the value of this balance at pre-industrial equilibrium, which can be expressed in terms of anomalies as follows,

$$\delta(P - E) = \theta\delta T. \quad (3.25)$$

We must introduce a new coefficient,  $\theta$ , which encapsulates the relationship between the temperature anomaly and the anomaly in the evaporation-precipitation balance across the global ocean basin. The standard units for an  $P - E$  balance in the literature are  $\frac{mm}{day}$ , where  $mm$  denotes millimeters of precipitation over a square meter. The coefficient of proportionality between an anomaly of  $P - E$

in  $[\frac{mm}{day}]$  and an anomaly of temperature in  $^{\circ}C$  is denoted by the letter  $\gamma$ . As mentioned earlier, the nominal temporal resolution used in SURFER is annual. Thus, we intend to use the coefficient  $\theta$  to perform the unit conversion so that  $\delta(P - E)$  represents the anomaly in cumulative precipitation in millimeters resulting from a change in the evaporation-precipitation balance over a year, per square meter, relative to the pre-industrial period. In other words, we aim for the units of  $\delta(P - E)$  to be  $[\frac{mm}{year}]$ . Given that  $\delta T$  is the global average temperature anomaly relative to the pre-industrial level, its units are  $^{\circ}C$ . A dimensional analysis thus indicates that the units of  $\theta$  are,

$$\theta = \left[ \frac{mm}{^{\circ}C \cdot year} \right]. \quad (3.26)$$

Thus, Equation (3.25) accurately calculates, for a temperature increase, the amount of freshwater in millimeters over a surface of 1 square meter that will be added over a year, stemming from a change in the evaporation-precipitation balance. The coefficient  $\theta$  represents the constant of proportionality between these two quantities in this linear model. However, as discussed in Chapter I, obtaining a reliable estimate for this value is highly challenging, as a linear parameterization masks a reality far more complex, with a significantly important spatial dependency. Indeed, the sensitivity of the evaporation-precipitation balance to a global average temperature increase varies greatly in both magnitude and qualitative effect, depending on whether it is over continents, oceans, and especially according to latitude. In the region of interest for our calibration, which is between  $20^{\circ}N$  and  $50^{\circ}N$  in the Atlantic, Section (2.3.2) has shown that the best linear regression we can perform on the value of  $\gamma$  yields the following value,

$$\gamma = 0.089 \frac{mm}{^{\circ}C \cdot day} \quad (3.27)$$

We then elaborate on the definition of  $\theta$  as follows,

$$\theta = \zeta \gamma \quad (3.28)$$

Where  $\zeta$  is a dimensionless coefficient that will translate the unit conversions between  $\gamma$  and  $\theta$ . After calculation and based on the unit differences described previously, we find,

$$\zeta = \frac{1}{150} \quad (3.29)$$

Similarly to the explanations provided at the end of the presentation of the parameterization of  $F_W$ , we encounter here a likely oversimplified modeling approach with a very limited domain of validity. As described in Chapter I and reiterated above, the dynamics of the evaporation-precipitation balance anomaly as a function of the temperature anomaly is a highly complex science with which our knowledge is still very limited. Since the literature[46, 56, 65] emphasizes the

importance of freshwater flux balances on the state of the AMOC, we deemed it useful to provide a more comprehensive parameterization of these fluxes than just  $F_{GIS}$ . However, we acknowledge, and this will be clearly delineated in the next analysis chapter, that the results we can obtain by considering the forcings of  $F_W$  and  $F_{P-E}$  must be interpreted with great caution. Therefore, we will not focus our analysis on these, and as with  $F_W$ , the code of SURFER v3.2 has been developed so that it is easily configurable before launching simulations to deactivate the forcing term  $F_{P-E}$  in order to avoid contaminating the results with potentially problematic dynamics. However, for pragmatic purposes, we find a value of  $\zeta$  to obtain freshwater fluxes associated with  $F_{P-E}$  that are of comparable magnitude to those of  $F_{GIS}$ . By developing an initial parameterization framework for  $F_{P-E}$ , whether mathematically or numerically in SURFER v3.2, we provide the opportunity to improve this dynamics subsequently, with concrete avenues for improvement to be presented at the end of this chapter.

One might also wonder why it was deemed necessary to still allow for an explicit representation of the forcing  $F_{P-E}$ , linked to the temperature anomaly, rather than implicitly including this forcing in the term  $c_1 T$ . However, two reasons underlie the decision to explicitly specify the forcing  $F_{P-E}$ . The first reason pertains to the significance of distinguishing this freshwater flux, which originates fundamentally differently from that originating from the cryosphere. As mentioned earlier, it also represents a significant source of freshwater flux variations that will destabilize the AMOC in the future. The second reason is methodological. As we will illustrate in the subsequent section, through specific sensitivity experiments conducted, in our case, with cGenie, we can isolate the effect of a freshwater input directly into the NADW zone from that at the equatorial level of the Atlantic basin. In other words, we can conduct experiments that allow us to isolate and then calibrate the distinct effects of  $F_{GIS}$  from those of  $F_{P-E}$ , thereby enabling a more comprehensive physical analysis of the mechanisms of AMOC collapse in the AGTCCM.

### The dual coupling of AMOC-GIS

After introducing the chosen models for the forcings  $F_{GIS}$  and  $F_O$ , we can clearly understand the dual coupling that occurs between the ODEs (3.2) and (3.3), simulating the AMOC and the GIS. In the case of the AMOC, the dependence is implicit in the forcing term by the freshwater flux from the GIS,  $F_{GIS}$ , while in the model (3.3) of the GIS, its state is explicitly impacted by the state of the AMOC. Thus, the term  $e_{21}(1 - \Psi)$  qualitatively ensures that a decrease in the intensity of the AMOC will result in a greater formation of ice on the GIS due to the diminished heat transport resulting from a weaker Atlantic oceanic circulation.

Due to the challenges outlined in parameterizing  $F_W$  and  $F_{P-E}$ , we will denote two different variants of the AMOC model to clarify the distinct methodological choices we will make in the analysis of results. The first, which we will refer to as **Param B**, is the most comprehensive one with the explicit forcings of  $F_O$

written in equation (3.2). The second parametrization, called **Param A**, does not consider the term  $F_O$  to focus solely on the freshwater flux forcing from the GIS. In **Param A**, the AMOC model takes the following form :

$$\frac{d\Psi}{dt} = (-\Psi^3 + a_1\Psi^2 + b_1\Psi + c_1 + d_1T + e_{12}F_{GIS}(V))\mu_\Psi(\Psi) = h_A(\Psi, T, F_{GIS}, F_O). \quad (3.30)$$

The most significant difference to note, as it will have a significant impact on calibration techniques and the results that can be produced, is that in **Param A**, we have only two forcing variables on the AMOC ( $T, F_{GIS}$ ), whereas in **Param B**, we have three ( $T, F_{GIS}, F_O$ ). However, whether it is **Param A** or **B**, we retain two forcing variables on the GIS ( $T, \Psi$ ).

After detailing the AMOC and GIS models and their coupling in the AGTCCM, we will now elaborate on the calibration algorithm that will be used to find the optimal values of the coefficients  $a_i, b_i, c_i, d_i, e_{12}, f, e_{21}$ . Depending on the choice of **Param A** or **B** for the AMOC, the details of the calibration method will be substantially different, although the methodology will remain the same.

### 3.3.2 The Calibration Algorithm in AGTCCM

Now that we have introduced the simplified dynamic models of the AMOC and the GIS that we will be using, in other words, their evolution over time based on the different forcings that govern them at first order, we need to calibrate the effect of the chosen forcings and the model against empirical data. As explained in the introduction, we lack empirical data on the hysteresis of the AMOC and the GIS. Therefore, we must rely on simulations of more complex systems, which are process-based and built upon the best understanding of the physical equations that govern the dynamics of these natural systems. Mathematically, the objective of the calibration algorithm is to find the values of the coefficients  $a_i, b_i, c_i, d_i, e_{12}, f, e_{21}, (i = 1, 2)$  that best adjust the two double-folds corresponding to the dynamics of the AMOC and the GIS described by (3.2,3.3) to hysteresis curves derived from process-based models.

#### The Martinez Monteiro method

In the paper describing the SURFER v2.0 model, Martinez Montero et al.[52] develop a mathematical framework that allows, in the case of the Antarctic and Greenland ice sheets modeled by ODEs with a canonical double-fold form, to calibrate these models against bifurcation diagrams derived from more physically realistic experiments. The idea is to extract the coordinates of the bifurcation points from hysteresis loops originating from a complex model and to fit the simplified double fold dynamics so that it passes through these critical points. However, the mathematical framework of Martinez Montero et al.[52] for describing each individual ice sheet consists of a single ODE with only one forcing

parameter, which is temperature (cf. section 3.2.3). It is reminded that the model chosen to describe the dynamics of the ice sheets is as follows,<sup>8</sup>

$$\frac{dV}{dt} = f^{Mont}(V) = \mu(V)(-V^3 + aV^2 + bV + cT + d) \quad (3.31)$$

Nevertheless, in our case, we need to calibrate our model (3.2,3.3), which is a system of two coupled ODEs with respectively three (in the case of **Param B**) and two forcing parameters for each. To find a mathematical and then algorithmic framework allowing us to calibrate the coupling coefficients  $e_{12}, e_{21}$  as well as the coefficients  $a_i, b_i, c_i, d_i, f, (i = 1, 2)$ , we will start by developing the mathematical framework of Martinez Montero et al.[52] to be able afterwards to generalize it. In this section, we will first detail the calibration by Martinez Montero et al.[52] and then show how it can be generalized to apply to our model.

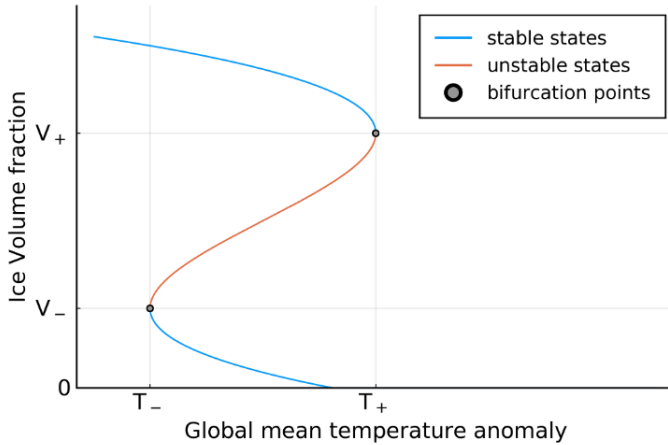


FIGURE 34 – *Ice sheet steady states for model defined in Eq.(3.31). Figure from Martinez Montero et al.[52]*

The double fold described by equation (3.31) is depicted in Figure (34), where  $((T_-, V_+)(T_-, V_-))$  denotes the critical coordinates of bifurcation points of a GIS hysteresis derived from a process-based model. The calibration model of coefficients by Martinez Montero et al.[52] where the constant coefficients  $a, b, c, d$  are defined based on the coordinates of critical bifurcation points is the following,

$$a = \frac{3(V_- + V_+)}{2}, \quad (3.32)$$

$$b = -3V_-V_+ \quad (3.33)$$

---

8. The function  $\mu$  in the case of the SURFER v2.0 model by Martinez Montero et al.[52] is not detailed here, but it refers to the term that encodes the characteristic time scale for the ice sheet considered, in a manner analogous to that described earlier for  $\mu_V$  and  $\mu_\Psi$  (cf. (3.4,3.6)).

$$c = -\frac{(V_+ - V_-)^3}{2(T_+ - T_-)} \quad (3.34)$$

$$d = \frac{T_+ V_-^2 (V_- - 3V_+) - T_- V_+^2 (V_+ - 3V_-)}{2(T_- - T_+)} \quad (3.35)$$

As requested, one can observe in Figure (35) that this calibration methodology allows the simplified double-fold dynamics of Equation (3.31) to pass through the critical bifurcation points obtained from a hysteresis of a more complex model. In the case of Figure (35), it is an hysteresis for the sensitivity of the GIS to the temperature anomaly derived from a more advanced physics model by Robinson et al.[64]

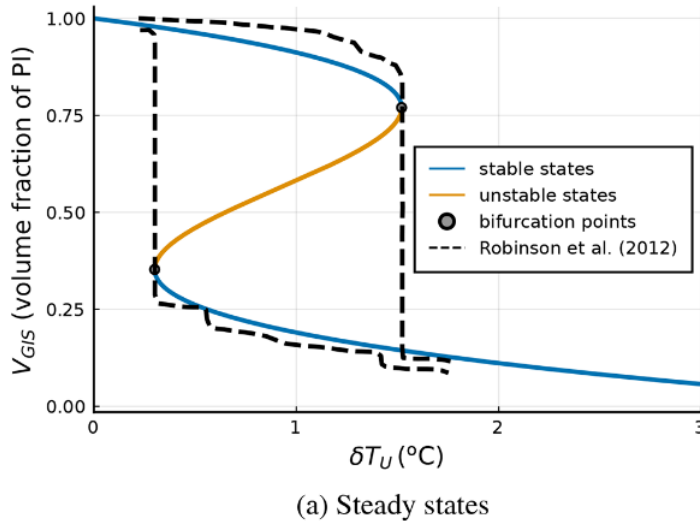


FIGURE 35 – SURFER v2.0 Greenland ice sheet against the work of Robinson et al.[64]. Figure from Montero et al.[52]

One issue is that the calculations and the method to arrive at these latter equations are not developed in Montero et al.’s work [52]. It is yet necessary in our case to derive these equations, understand their origins, and then be able to generalize and apply them to our model (3.2,3.3). To illustrate the mathematical intuition behind this calibration, it is useful to plot (cfr. Fig.(36)) the phase portrait of  $g(V, T, \Psi)$  described by equation (3.3). The Figure (36) remains qualitatively valid for our AMOC model (3.2) as well as for the Martinez Monteiro model (3.31), it is solely aimed at capturing the phase space associated with a double fold.

We observe that the dynamics follow those of a cubic function, which tends toward  $g(V) \rightarrow -\infty$  as  $V \rightarrow \infty$  and  $g(V) \rightarrow \infty$  as  $V \rightarrow -\infty$ . Since  $g(V)$  is a third-order polynomial, we know it has three roots. Through mathematical insights and graphical analysis, we can derive the calibration coefficients  $a, b, c, d$  based on the coordinates of the critical bifurcation points  $V_+, T_+, V_-, T_-$ . Re-

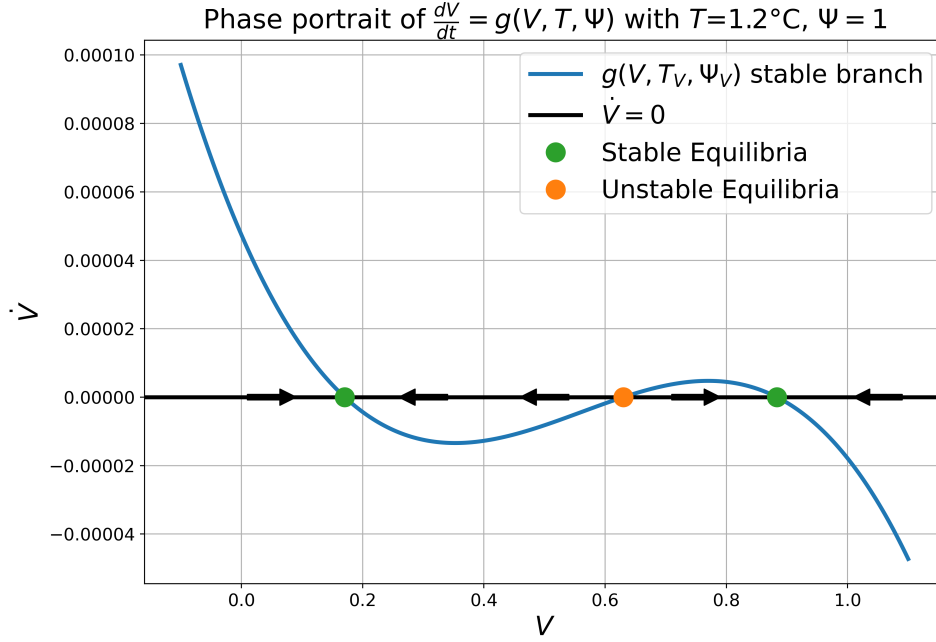


FIGURE 36 – Phase portrait of the equation for the GIS (3.3).

calling the basic concepts and definitions of nonlinear dynamics outlined in Chapter I, we know that by definition,  $V^*$  is an equilibrium point if,

$$g(V^*) = \frac{dV}{dt}|_{V=V^*} = 0. \quad (3.36)$$

Furthermore, we know that by definition, at  $(T_+, V_+)$  and  $(T_-, V_-)$  these equilibrium points change stability.

Mathematically, we understand that the effect of an increase in a forcing (whether it be that of temperature or the intensity of the AMOC for equation (3.3) is inconsequential) is to vertically shift the blue curve in Figure (36). For simplicity, in the following thought experiments, we will only consider a forcing on temperature, in other words, we will only consider the bifurcation parameter as the variable  $T$  and assume  $V$  to remain constant. Formally, the fold bifurcation will occur when the bifurcation parameter  $T$  reaches a critical value denoted  $T_1^c \equiv T_+$  such that the stable equilibrium point on the right and the unstable equilibrium point merge. This result is visible in Figure (37). Indeed, as the bifurcation parameter increases, the curve of  $g(V)$  will shift downward, which will bring these two equilibrium points closer together on the  $V$  axis. By definition, the exact location on the  $V$  axis where these equilibrium points merge is the coordinate  $V^+$ . A similar reasoning holds in the case of a decrease in the forcing parameter  $T$ , which could reach its second critical value denoted  $T_2^c \equiv T_-$ . In this case, the curve  $g(V)$  will shift upward, leading to the bifurcation point which is the fusion of the stable equilibrium point on the left with the unstable equilibrium point. The value of  $V$  at which this bifurcation occurs

is by definition that of  $V_-$ . In both bifurcations, we are indeed dealing with cases explained in Chapter I as a saddle-node bifurcation or fold bifurcation. Indeed, we have two equilibrium points that, for a critical value of a bifurcation parameter, collide and annihilate each other.

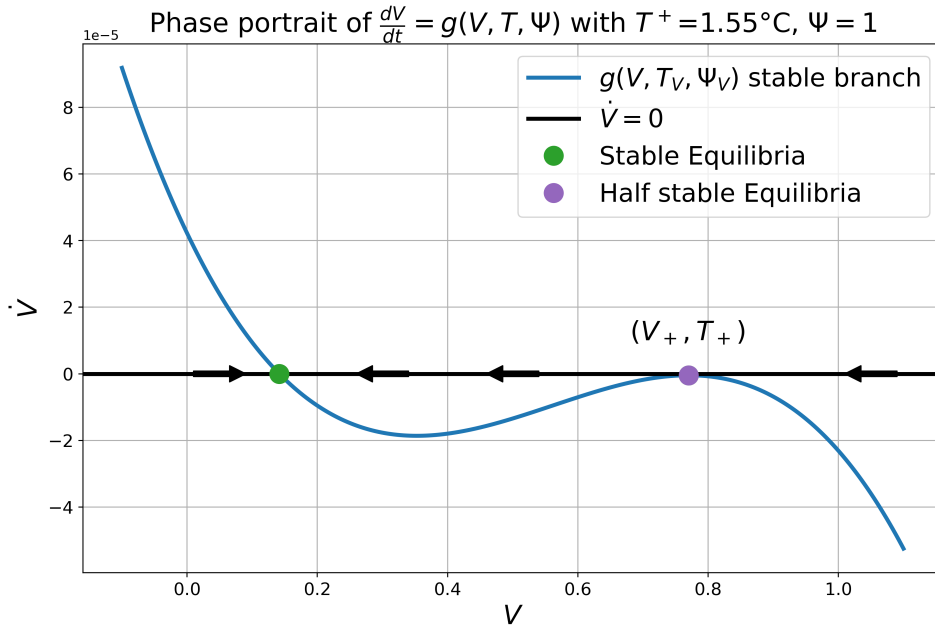


FIGURE 37 – Phase portrait of the equation for the GIS (3.3) at the bifurcation point  $T = T_+$ .

How can we now calculate analytically the values of  $V_{\pm}$ ? Since we are here aiming to derive the values of the coefficients in the equation of Martinez Monteiro et al. (2022)[52] given by equations, we will apply the calculations to the function  $f^{Mont}(V)$ . From Figure (37), it is apparent that the points  $V_{\pm}$  are the values of  $V$  such that,

$$\frac{df^{Mont}(V)}{dV} = 0. \quad (3.37)$$

However, we calculate using equation (3.31),

$$\frac{df^{Mont}(V)}{dV} = (-3V^2 + 2aV + b)\mu(V) + f(V) \frac{d\mu(V)}{dV} \quad (3.38)$$

In our case of the AGTCCM model, the term  $\mu(V)$  in equation (3.31) is merely a constant that does not depend on  $V$ . Thus, to find the values of  $V_{\pm}$ , we reduce the problem to finding the roots of the following second-order polynomial :

$$-3V^2 + 2aV + b = 0. \quad (3.39)$$

We calculate the discriminant,

$$\Delta = 4a^2 + 12b. \quad (3.40)$$

To obtain real roots, we need  $4a^2 + 12b \geq 0$ , in which case we find the following two real roots,

$$V_+ = \frac{a}{3} + \frac{1}{6}\sqrt{4a^2 + 12b} = V_+(a, b), \quad (3.41)$$

$$V_- = \frac{a}{3} - \frac{1}{6}\sqrt{4a^2 + 12b} = V_-(a, b). \quad (3.42)$$

We have here two functions of  $a$  and  $b$  that give the values of  $V_{\pm}$ . To solve this system of linear equations, we can start by adding equations (3.41) and (3.42), which allows us to isolate and obtain,

$$a = \frac{3(V_- + V_+)}{2}. \quad (3.43)$$

With a bit more algebra, if we subtract equation (3.41) from equation (3.42) and isolate  $b$  with a substitution of the value found for  $a$  from equation (3.162), we finally obtain,

$$b = -3V_-V_+. \quad (3.44)$$

How can we now find the expressions for  $c$  and  $d$  as given by equations (3.34-3.35)? To do this, we use the fact that the bifurcation points  $(V_+, T_+)$  and  $(V_-, T_-)$  are also equilibrium points. In other words, we have that  $f^{Mont}(V_+, T_+) = 0 = f^{Mont}(V_-, T_-)$ . By evaluating the function  $f^{Mont}$  at these points, we obtain the following two equations,

$$-V_+^3 + aV_+^2 + bV_+ + cT_+ + d = 0 \quad (3.45)$$

$$-V_-^3 + aV_-^2 + bV_- + cT_- + d = 0 \quad (3.46)$$

By substituting the values of the coefficients  $a$  and  $b$  found earlier (3.32-3.33) into equations (3.45-3.46), we obtain a system of two linear equations with two unknowns to express  $c$  and  $d$  in terms of  $(V_+, T_+, V_-, T_-)$ . After several lines of elementary algebra that we will not detail further here as they are not particularly instructive, we obtain the following value for  $c$ ,

$$c = -\frac{(V_+ - V_-)^3}{2(T_+ - T_-)}. \quad (3.47)$$

Finally, by substituting this last equality into equation (3.45), we obtain after simplification,

$$d = \frac{T_+V_-^2(V_- - 3V_+) - T_-V_+^2(V_+ - 3V_-)}{2(T_- - T_+)}. \quad (3.48)$$

Thus, based on mathematical intuition, we have been able to rederive the calibration methodology of Martinez Monteiro et al.

### Generalizing the Martinez Monteiro Method to multiple forcings

Now that we have understood how to derive an efficient calibration method for the coefficients of the Martinez Monteiro et al. double-fold model based on the critical coordinates of bifurcation points, we can generalize this method. We need to generalize it because in the case of the AGTCCM, we no longer have just one forcing variable (which is a bifurcation parameter in the nonlinear dynamics jargon) but two in the case of the GIS and the AMOC in **Param A**, and even three forcing variables for the AMOC in **Param B**.

Our generalized calibration methodology is based on two assumptions. The first epistemological assumption is that our equations (3.2,3.3) accurately represent reality, or at least the models we aim to emulate. This assumption is reasonable because, as developed in Chapter I, we can understand the hysteresis dynamics of many tipping elements such as the AMOC and the GIS to first order through a double-fold structure. Furthermore, previous works such as the glacier ice model in SURFER v2.0 illustrated in Figure (35) have demonstrated the validity of this approach. The second methodological assumption is that the models we will use to calibrate the hysteresis of the AMOC and the GIS allow for independent forcing of the AMOC and the GIS. In other words, if we take our AGTCCM model for the AMOC (3.2), we should be able to access hysteresis models that can force the AMOC solely through temperature while keeping the two freshwater forcings constant, and vice versa. Fortunately, due to the construction of the vast majority of climate models, this is technically entirely feasible, as will be illustrated in the case of cGenie later in this chapter.

Although we aim to calibrate a system of coupled ODEs, we can independently calibrate the AMOC and the GIS in the sense that Equation (3.2) and Equation (3.3) can be calibrated separately. Of course, each of these equations includes a coupling term with the other, but this calibration of their coupling is performed within the same model using different experiments. Specifically, to calibrate the AMOC, we need a model that can produce hysteresis loops of AMOC intensity  $\Psi$  as a function of anomalies in global mean temperature and freshwater fluxes. To calibrate the GIS equation, we need a model that can produce hysteresis loops of sensitivity experiments of GIS volume as a function of anomalies in global mean temperature and AMOC intensity.

If we consider our AGTCCM model with **Param B** (3.2-3.3), we need in our case to find a way to calibrate the coefficients  $a_1, b_1, c_1, d_1, e_{12}, f$  for the AMOC and the coefficients  $a_2, b_2, c_2, d_2, e_{21}$  for the GIS. We aim to express all these coefficients, where the coefficients  $e_{12}, e_{21}$  hold the special ontological value of being the coupling coefficients linking the dynamics of the AMOC to that of the GIS and vice versa, in terms of the following critical coordinates for the AMOC,

$$\{\Psi^+, T_\Psi^+, F_{GIS}^+, F_O^+, \Psi^-, T_\Psi^-, F_{GIS}^-, F_O^-\}, \quad (3.49)$$

and the following critical coordinates for the GIS,

$$\{V^+, T_V^+, \Psi_V^+, V^-, T_V^-, \Psi_V^-\}. \quad (3.50)$$

It is important to emphasize that  $T_\Psi^\pm \neq T_V^\pm$  just as  $\Psi^\pm \neq \Psi_V^\pm$ . Indeed, in the case of temperature forcing, the AMOC and the GIS are two different dynamic systems, each with its own critical thresholds for temperature anomalies that trigger system transitions. As for the values of  $\Psi$ , one should not confuse the critical values at which the AMOC transitions, denoted  $\Psi^\pm$ , due to temperature or freshwater forcing, with the critical values of the AMOC that may trigger the GIS collapse, denoted  $\Psi_V^\pm$ . Similarly, despite the chosen parameterization for the freshwater flux of the GIS (3.8), it is important to understand that,

$$F_{GIS}^\pm = \alpha_{GIS} \dot{V}_\Psi^\pm \quad (3.51)$$

with  $\dot{V}_\Psi^\pm \neq \dot{V}^\pm$  as the critical freshwater fluxes from the GIS that trigger the AMOC transition are not associated with the critical volume values of the GIS at which the GIS undergoes a transition. These are two distinct dynamics, albeit not independent.

We will now use our methodological assumption that we can access independent sensitivity experiments in our complex models of the AMOC and the GIS. In the following, we will detail our calibration algorithm in the case of the AMOC, but the method is identical for our GIS model. In practice, this assumption implies that, for the AMOC, we can conduct sensitivity experiments where we keep the freshwater fluxes constant and only vary the temperature. Similarly, it implies that we can conduct sensitivity experiments on freshwater fluxes in isolation while keeping the other forcings of our simplified dynamics constant. The recipe for our calibration, which is generalizable to  $N$  forcings, is as follows. To calibrate the coupling coefficients associated with the  $N$  forcing variables, we perform  $N$  independent sensitivity experiments to independently calibrate the associated bifurcation diagrams by systematically reducing the calibration to a Martinez Monteiro et al.-type model with only one forcing variable, as the other  $N - 1$  variables become constants.

### Calibration of the AMOC for Param B

Here we aim to calibrate the coefficients  $a_1, b_1, c_1, d_1, e_{12}, f$  of the following ODE,

$$\frac{d\Psi}{dt} = (-\Psi^3 + a_1\Psi^2 + b_1\Psi + c_1 + d_1T + e_{12}F_{GIS} + fF_O)\mu_\Psi(\Psi), \quad (3.52)$$

based on the knowledge of the following critical bifurcation points,

$$\{\Psi^+, T_\Psi^+, F_{GIS}^+, F_O^+, \Psi^-, T_\Psi^-, F_{GIS}^-, F_O^-\}, \quad (3.53)$$

which are provided by hysteresis experiments from more complex models.

Let us denote EXPA as the first sensitivity experiment using an AMOC model that measures the variation of AMOC intensity ( $\Psi$ ) as a function of a forcing by the global mean temperature  $T$ . EXPA provides us with the critical values

$$(\Psi^+, T_\Psi^+), (\Psi^-, T_\Psi^-). \quad (3.54)$$

In this sensitivity experiment, the values of the other forcings, namely  $F_{GIS}$  and  $F_O$ , are kept constant at arbitrary values denoted as  $F_{GIS}^A$  and  $F_O^A$ . In this case, Equation (3.52) can be written as :

$$\frac{d\Psi}{dt} = (-\Psi^3 + a_1\Psi^2 + b_1\Psi + c_1 + e_{12}F_{GIS}^A + fF_O^A + d_1T)\mu_\Psi(\Psi). \quad (3.55)$$

Since the terms  $e_{12}F_{GIS}^A + fF_O^A$  are now constants, we are effectively dealing with a single forcing parameter, similar to Martinez Monteiro et al. We can thus find the values of the coefficients in a similar manner :

$$a_1 = \frac{3(\Psi^- + \Psi^+)}{2} = a_1(\Psi^+, \Psi^-), \quad (3.56)$$

$$b_1 = -3\Psi^-\Psi^+ = b_1(\Psi^+, \Psi^-), \quad (3.57)$$

$$c_1 + e_{12}F_{GIS}^A + fF_O^A = \frac{T_\Psi^+\Psi^{-2}(\Psi^- - 3\Psi^+) - T_\Psi^-\Psi^{+2}(\Psi^+ - 3\Psi^-)}{2(T_\Psi^- - T_\Psi^+)}, \quad (3.58)$$

$$d_1 = -\frac{(\Psi^+ - \Psi^-)^3}{2(T_\Psi^+ - T_\Psi^-)} = d_1(\Psi^+, T_\Psi^+, \Psi^-, T_\Psi^-). \quad (3.59)$$

Let's now denote EXPB as the second sensitivity experiment for the AMOC, where we measure the dependence of the AMOC intensity on the freshwater flux  $F_{GIS}$  while keeping the other two forcing variables, denoted by  $T^B$  and  $F_O^B$ , constant at arbitrary values. The chosen model we wish to emulate now provides us with the values of the following bifurcation points :

$$\{(\Psi^+, F_{GIS}^+), (\Psi^-, F_{GIS}^-)\}. \quad (3.60)$$

In this case, Equation (3.52) is rewritten as :

$$\frac{d\Psi}{dt} = (-\Psi^3 + a_1\Psi^2 + b_1\Psi + c_1 + d_1T^B + fF_O^B + e_{12}F_{GIS})\mu_\Psi(\Psi). \quad (3.61)$$

Again, by term-by-term identification, Martinez Monteiro et al.'s methodology yields :

$$a_1 = \frac{3(\Psi^- + \Psi^+)}{2} = a_1(\Psi^+, \Psi^-), \quad (3.62)$$

$$b_1 = -3\Psi^-\Psi^+ = b_1(\Psi^+, \Psi^-), \quad (3.63)$$

$$c_1 + d_1T^B + fF_O^B = \frac{F_{GIS}^+\Psi^{-2}(\Psi^- - 3\Psi^+) - F_{GIS}^-\Psi^{+2}(\Psi^+ - 3\Psi^-)}{2(F_{GIS}^- - F_{GIS}^+)}, \quad (3.64)$$

$$e_{12} = -\frac{(\Psi^+ - \Psi^-)^3}{2(F_{GIS}^+ - F_{GIS}^-)} = e_{12}(\Psi^+, F_{GIS}^+, \Psi^-, F_{GIS}^-). \quad (3.65)$$

Finally, let's call EXPC the sensitivity experiment of the AMOC to the freshwater flux  $F_O$ , in which we keep the other two forcings, denoted  $T^C$  and  $F_{GIS}^C$ , at

constant and arbitrary values. EXPC provides us with the coordinates of the following bifurcation points :

$$\{(\Psi^+, F_O^+), (\Psi^-, F_O^-)\} \quad (3.66)$$

and allows us to rewrite Equation (3.52) as follows :

$$\frac{d\Psi}{dt} = (-\Psi^3 + a_1\Psi^2 + b_1\Psi + c_1 + d_1T^C + e_{12}F_{GIS}^C + fF_O)\mu_\Psi(\Psi) \quad (3.67)$$

Once again, by term-to-term identification, the methodology of Martinez Monteiro et al. provides us with<sup>9</sup> :

$$a_1 = \frac{3(\Psi^- + \Psi^+)}{2} = a_1(\Psi^+, \Psi^-), \quad (3.68)$$

$$b_1 = -3\Psi^-\Psi^+ = b_1(\Psi^+, \Psi^-), \quad (3.69)$$

$$c_1 + d_1T^C + e_{12}F_{GIS}^C = \frac{F_O^+\Psi^{-2}(\Psi^- - 3\Psi^+) - F_O^-\Psi^{+2}(\Psi^+ - 3\Psi^-)}{2(F_O^- - F_O^+)}, \quad (3.70)$$

$$f = -\frac{(\Psi^+ - \Psi^-)^3}{2(F_O^+ - F_O^-)} = f(\Psi^+, F_O^+, \Psi^-, F_O^-). \quad (3.71)$$

Before solving this system of equations, it is necessary to realize that we have implicitly made the following assumption :

$$\Psi_A^+ = \Psi_B^+ = \Psi_C^+ \equiv \Psi^+, \Psi_A^- = \Psi_B^- = \Psi_C^- \equiv \Psi^- \quad (3.72)$$

Physically, this assumption implies that in our simplified model, the critical value at which the AMOC collapses ( $\Psi^+$ ) or recovers ( $\Psi^-$ ) is the same whether the AMOC is triggered solely by temperature, freshwater flux from the GIS, or freshwater fluxes from other components of the cryosphere and the precipitation-evaporation balance ( $P-E$ ). While we understand that ultimately what matters for an AMOC collapse is a critical level of stratification, and in this sense, reaching this critical stratification through temperature increase or freshwater addition, or a combination of both, may not matter much, it is not certain whether this assumption is entirely valid based on the literature. Moreover, as we will directly observe in the data from cGenie experiments, our model falsifies this assumption. However, if we remain within the framework of our mathematical model in Equation (3.52) and revisit the intuition developed in Figure (37), namely that mathematically, a temperature or freshwater input merely shifts our curve in phase space until critical values are reached where there is a stability change, it is reasonable to adopt this assumption. Indeed, this critical threshold at which a bifurcation of  $\Psi$  occurs is the same whether

---

9. It might have been thought necessary to differentiate the coupling coefficients to the forcings according to the sensitivity experiment. For example, to write  $d_1 \neq d_1^A \neq d_1^B \neq d_1^C$ . However, between the sensitivity experiments, we do not physically change the impact of a forcing, in this case, temperature, on the system.

the forcing involves  $T, F_{GIS}$ , or  $F_O$ . However, since these forcings each have a distinct impact on the AMOC, which is encoded by their coefficients  $d_1, e_{12}$  and  $f$  hence the values that  $T, F_{GIS}$  and  $F_O$  must assume to reach this critical threshold will differ but not the threshold for the bifurcation set by  $\Psi^+$  and  $\Psi^-$ . Moreover, as seen in our simplified model (3.52), the temporal dynamics of  $\Psi$  dependent on its state are calibrated using the coefficients  $a_1$  and  $b_1$ , whose values determined by calibrations depend solely on  $\Psi^+$  and  $\Psi^-$ . Finally, from a more pragmatic standpoint, even if we accept that this assumption is simplifying and introduces error (which will be analyzed in a subsequent section), we realize that abandoning this assumption would render the Martinez Monteiro et al. calibration algorithm less effective. The number of variables would then be too large to find solutions in such a manner.

Taking this hypothesis into account moving forward, we now have data from our three sensitivity experiments, each of which has provided us with 4 equations. On paper, we have a total of 12 equations, but the equations for  $a_1$  and  $b_1$  are redundant in each of the experiments. Therefore, we are left with 8 equations. However, we still have 6 unknowns, which are :

$$a_1, b_1, c_1, d_1, e_{12}, f \quad (3.73)$$

The different calibrations by reducing them to the method of Martinez Monteiro et al. give us the values of :

$$a_1, b_1, c_1 + e_{12}F_{GIS}^A + fF_O^A, e_{12}, f, d_1, c_1 + d_1T^B + fF_O^B, c_1 + d_1T^C + e_{12}F_{GIS}^C. \quad (3.74)$$

Of the 6 unknowns, the only one that remains and is not directly explicit in the previous equations is the coefficient  $c_1$ , which is the term independent of any forcing. However, this quantity is over-determined by the following equations :

$$c_1 = \frac{T_\Psi^+ \Psi^{-2} (\Psi^- - 3\Psi^+) - T_\Psi^- \Psi^{+2} (\Psi^+ - 3\Psi^-)}{2(T_\Psi^- - T_\Psi^+)} - e_{12}F_{GIS}^A - fF_O^A, \quad (3.75)$$

$$c_1 = \frac{F_{GIS}^+ \Psi^{-2} (\Psi^- - 3\Psi^+) - F_{GIS}^- \Psi^{+2} (\Psi^+ - 3\Psi^-)}{2(F_{GIS}^- - F_{GIS}^+)} - d_1T^B - fF_O^B, \quad (3.76)$$

$$c_1 = \frac{F_O^+ \Psi^{-2} (\Psi^- - 3\Psi^+) - F_O^- \Psi^{+2} (\Psi^+ - 3\Psi^-)}{2(F_O^- - F_O^+)} - d_1T^C - e_{12}F_{GIS}^C. \quad (3.77)$$

Therefore, we have calibrated all coefficients using this generalized method, which aims to systematically reduce, thanks to the assumption of independent sensitivity experiments, to the well-known single forcing parameter case.

### Calibration of the AMOC for Parameterization A

We now aim to calibrate the AMOC model in the case of **Param A** to enable the use and comparison of this model with that of **Param A**. Therefore, we seek to calibrate the coefficients  $a_1, b_1, c_1, d_1, e_{12}$  of the following equation :

$$\frac{d\Psi}{dt} = (-\Psi^3 + a_1\Psi^2 + b_1\Psi + c_1 + d_1T + e_{12}F_{GIS})\mu_\Psi(\Psi), \quad (3.78)$$

whose bifurcation points' coordinates are given by :

$$\{(\Psi^+, T_\Psi^+, F_{GIS}^+), (\Psi^-, T_\Psi^-, F_{GIS}^-)\}. \quad (3.79)$$

The procedure to follow is exactly the same as that for **Param B** but even simpler because in this case we have only two forcing variables  $(T, F_{GIS})$  instead of three  $(T, F_{GIS}, F_O)$ . We denote **EXPA** as the first sensitivity experiment of the AMOC with respect to the global mean temperature performed with a constant but arbitrary freshwater flux forcing  $F_{GIS} = F_{GIS}^A$ . We denote **EXPB** as the second sensitivity experiment which provides the AMOC intensity response to an increase in freshwater flux from the GIS but under a constant global mean temperature at an arbitrary value  $T = T^B$ . **EXPA** provides the coordinates of the following critical points :

$$\{(\Psi^+, T_\Psi^+), (\Psi^-, T_\Psi^-)\}, \quad (3.80)$$

and the following equations for the calibration coefficients :

$$a_1 = \frac{3(\Psi^- + \Psi^+)}{2} = a_1(\Psi^+, \Psi^-), \quad (3.81)$$

$$b_1 = -3\Psi^-\Psi^+ = b_1(\Psi^+, \Psi^-), \quad (3.82)$$

$$c_1 + e_{12}F_{GIS}^A = \frac{T_\Psi^+\Psi^{-2}(\Psi^- - 3\Psi^+) - T_\Psi^-\Psi^{+2}(\Psi^+ - 3\Psi^-)}{2(T_\Psi^- - T_\Psi^+)}, \quad (3.83)$$

$$d_1 = -\frac{(\Psi^+ - \Psi^-)^3}{2(T_\Psi^+ - T_\Psi^-)} = d_1^A(\Psi^+, T_\Psi^+, \Psi^-, T_\Psi^-). \quad (3.84)$$

The second experiment **EXPB** gives us the knowledge of the following bifurcation points :

$$\{(\Psi^+, F_{GIS}^+), (\Psi^-, F_{GIS}^-)\}, \quad (3.85)$$

which in turn allow us to determine the values of the following coefficients :

$$a_1 = \frac{3(\Psi^- + \Psi^+)}{2} = a_1(\Psi^+, \Psi^-), \quad (3.86)$$

$$b_1 = -3\Psi^-\Psi^+ = b_1(\Psi^+, \Psi^-), \quad (3.87)$$

$$c_1 + d_1T^B = \frac{F_{GIS}^+\Psi^{-2}(\Psi^- - 3\Psi^+) - F_{GIS}^-\Psi^{+2}(\Psi^+ - 3\Psi^-)}{2(F_{GIS}^- - F_{GIS}^+)}, \quad (3.88)$$

$$e_{12} = -\frac{(\Psi^+ - \Psi^-)^3}{2(F_{GIS}^+ - F_{GIS}^-)} = e_{12}^B(\Psi^+, F_{GIS}^+, \Psi^-, F_{GIS}^-) \quad (3.89)$$

In this case with two forcing parameters, we have a system of 6 equations (again, the ones for  $a_1$  and  $b_1$  are redundant) with 5 unknowns.

$$a_1, b_1, c_1, e_{12}, d_1. \quad (3.90)$$

As previously, only one unknown is not uniquely defined by the Martinez Monteiro et al. method, which is the coefficient  $c_1$ , which is overdetermined by the equations :

$$c_1 = \frac{T_\Psi^+ \Psi^{-2} (\Psi^- - 3\Psi^+) - T_\Psi^- \Psi^{+2} (\Psi^+ - 3\Psi^-)}{2(T_\Psi^- - T_\Psi^+)} - e_{12} F_{GIS}^A \quad (3.91)$$

$$c_1 = \frac{F_{GIS}^+ \Psi^{-2} (\Psi^- - 3\Psi^+) - F_{GIS}^- \Psi^{+2} (\Psi^+ - 3\Psi^-)}{2(F_{GIS}^- - F_{GIS}^+)} - d_1 T_\Psi^B. \quad (3.92)$$

### Calibration of the GIS

For the GIS, we must calibrate the coefficients  $a_2, b_2, c_2, d_2, e_{21}$  of the following model.

$$\frac{dV}{dt} = (-V^3 + a_2 V^2 + b_2 V + c_2 + d_2 T + e_{21}(1 - \Psi)) \mu_V(V) = g(V, T, \Psi). \quad (3.93)$$

Given that this is once again a model with two forcing parameters, the calibration methodology is analogous to that presented for the AMOC in the case of **Param A**. In this case, the coordinates of the bifurcation points are given by,

$$\{V^+, T_V^+, \Psi_V^+, V^-, T_V^-, \Psi_V^-\}. \quad (3.94)$$

We denote EXPC in the case of the GIS as the first sensitivity experiment of the GIS volume in relation to temperature, in which the forcing from the AMOC intensity is held constant at an arbitrary value  $\Psi_V = \Psi_V^C$ . In this case, equation (??) is written as,

$$\frac{dV}{dt} = (-V^3 + a_2 V^2 + b_2 V + c_2 + e_{21}(1 - \Psi^C) + d_2 T) \mu_V(V) \quad (3.95)$$

This first sensitivity experiment provides us with the data for the following bifurcation points,

$$\{(V^+, T_V^+), (V^-, T_V^-)\}. \quad (3.96)$$

In this case with a single forcing variable, the method of Martinez Monteiro et al. gives us,

$$a_2 = \frac{3(V^- + V^+)}{2} = a_2(V^+, V^-), \quad (3.97)$$

$$b_2 = -3V^-V^+ = b_2(V^+, V^-), \quad (3.98)$$

$$c_2 + e_{21}(1 - \Psi^C) = \frac{T_V^+V^{-2}(V^- - 3V^+) - T_V^-V^{+2}(V^+ - 3V^-)}{2(T_V^- - T_V^+)}, \quad (3.99)$$

$$d_2 = -\frac{(V^+ - V^-)^3}{2(T_V^+ - T_V^-)} = d_2(V^+, T_V^+, V^-, T_V^-). \quad (3.100)$$

Finally, we refer to EXPD as the second sensitivity experiment in which we fix the global mean temperature  $T_V = T_V^D$  at an arbitrary value but vary the intensity of the AMOC  $\Psi_V$ . This sensitivity experiment provides us with the coordinates of the following bifurcation points,

$$\{(V^+, \Psi_V^+), (V^-, \Psi_V^-)\} \quad (3.101)$$

while equation (3.3) takes the following form :

$$\frac{dV}{dt} = (-V^3 + a_2V^2 + b_2V + c_2 + d_2T^D + e_{21}(1 - \Psi))\mu_V(V, T, \Psi). \quad (3.102)$$

Please note that in this case, we cannot exactly apply the same calculation procedures<sup>10</sup> for the coefficients due to the formulation of the AMOC forcing, which has a different form than those encountered before. We need to slightly adjust the calculation for the coefficients  $c_2 + d_2T^D, e_{21}$ , although the methodology to find them remains the same as described above. Therefore, we obtain :

$$a_2 = \frac{3(V^- + V^+)}{2} = a_2(V^+, V^-), \quad (3.103)$$

$$b_2 = -3V^-V^+ = b_2(V^+, V^-), \quad (3.104)$$

$$c_2 + d_2T^D = V^{+3} - a_2V^{+2} - b_2V^+ - e_{21}(1 - \Psi_V^+), \quad (3.105)$$

$$e_{21} = -\frac{(V^+ - V^-)^3}{2(\Psi_V^- - \Psi_V^+)} = e_{21}(V^+, \Psi_V^+, V^-, \Psi_V^-). \quad (3.106)$$

So, we finally end up with the following 5 unknowns :

$$a_2, b_2, c_2, e_{21}, d_2, \quad (3.107)$$

and 6 equations, with the only coefficient not explicitly determined being  $c_2$ . However, a closer look reveals that it is doubly determined by,

$$c_2 = \frac{T_V^+V^{-2}(V^- - 3V^+) - T_V^-V^{+2}(V^+ - 3V^-)}{2(T_V^- - T_V^+)} - e_{21}(1 - \Psi^C) \quad (3.108)$$

$$c_2 = (V^{+3} - a_2V^{+2} - b_2V^+ - e_{21}(1 - \Psi_V^+)) - d_2T_V^D. \quad (3.109)$$

Therefore, we have once again determined all the coefficients through this method.

---

10. Details are available in the appendix.

### Conclusion of this calibration method

Theoretically, we have the necessary and sufficient mathematical framework to calibrate our simplified nonlinear dynamical models on the hysteresis loops of more complex models. Whether for the AMOC or the GIS, and regardless of the number of forcings, we have been able to generalize the methodology of Martinez Monteiro et al. through the assumption of the technical feasibility of conducting independent sensitivity experiments. This strong assumption, although realistic for many existing models with more advanced physics, systematically allows us to reduce to the case of a model with a single forcing parameter.

With hindsight, it is interesting to see what the generalization of Martinez Monteiro et al.'s methodology for dynamics with multiple forcing variables implies. In the case of Martinez Monteiro et al., we had a single forcing parameter. In our modeling of the GIS (3.3) and that of the AMOC in **Param A**, we had two, while in the AMOC modeling with **Param B**, we had three. In Table (4), we have summarized the algebraic constraints in each case.

Model	# Forcing	# Equations	# Unknowns	# Overdetermined equations
Martinez Monteiro et al.	1	4	4	0
GIS and AMOC ParamA	2	6	5	1
AMOC ParamB	3	8	6	2
Other Model	$N$	$4N - 2(N - 1)$	$4 + (N - 1)$	$(N - 1)$

TABLE 4 – Number of equations, unknowns, and overdetermined equations as a function of the number of forcings for the different calibrations.

It is interesting to observe and understand the sequence of implications of adding an additional forcing variable. We realize that when adding a forcing variable, if we follow this calibration methodology through independent sensitivity experiments, we add 4 additional equations per additional forcing variable. However, there are systematically those regarding the coefficients  $a_i$  and  $b_i$ , which are redundant, so in reality we have  $4N - 2(N - 1)$  equations for  $N$  forcing variables. Moreover, the introduction of a new forcing variable introduces an additional unknown, which is the coupling coefficient of this new forcing variable. In the case of **Param B** of the AMOC, for example, this is the coefficient  $f$  for  $F_O$ , which did not exist in **Param A**. In other words, by complexifying our model with an additional forcing variable, we introduce a new unknown but two new equations. Thus, in the case where we have  $N = 2$  forcings, we find ourselves in a situation with one overdetermination on the coefficient  $c_i$ . This coefficient  $c_i$ , being the shared constant across all calibrations of different sensitivity experiments, is the component of our model that must adjust to each sensitivity experiment while being common to all. Unlike the coefficients  $a_i$  and  $b_i$ , which

encode the internal dynamics of the model, these, although common to all sensitivity experiment calibrations, do not depend on the forcing parameters. One may wonder if the overdeterminations of the coefficients  $c_1$  are consistent, in other words, if they all yield the same value. We will see in the next section, using the example of calibration on cGenie data, that this is not always the case. Indeed, if we take, for example, equations (3.75-3.77), we understand that these depend on the *a priori* arbitrary values of the forcings kept constant in each sensitivity experiment. Using the results of the calibration on cGenie data as a basis for discussion, we will develop in the section on the limitations of the calibration model the operational consequences of these constraints.

### 3.3.3 Validation Test : Calibration with the model itself

The AGTCCM model was numerically translated into *Python* code in two *Jupyter Notebooks*, namely `Tipping Module Calibration ParamA.ipynb` and `Tipping Module Calibration ParamB.ipynb`, representing `Param A` and `Param B` of the AMOC, respectively. These two notebooks, along with all numerical data and scripts used for this thesis, are available on the GitHub repository created for this purpose.<sup>11</sup>

To verify the coherence and proper functioning of our calibration methodology, we will perform a validation test. We will calibrate our model on itself. In other words, we will generate hysteresis loops from the model described by the AGTCCM Eq. (3.2,3.3) by arbitrarily fixing values of the coefficients  $a_i^*, b_i^*, c_i^*, d_i^*, e_{ij}^*, f^*$ . Subsequently, we will calculate the coordinates of the critical bifurcation points associated with these hysteresis loops and use these coordinates in the calibration algorithm to retrieve the values of the coefficients  $a_i, b_i, c_i, d_i, e_{ij}, f$  and compare these values to the initially arbitrarily fixed ones. Ideally, these values should correspond if our calibration algorithm is well constructed mathematically and numerically.

These validation tests were conducted for both `Param B` and `Param A`. However, due to the increased complexity of `Param B`, only the results of the latter will be comprehensively presented here. The validation test methodology is identical in both parameterization cases and also in both systems to be calibrated, whether it is the AMOC or the GIS. Therefore, it has been decided to provide comprehensive results only for the AMOC in the case of `Param B`.

---

11. <https://github.com/AmauryLaridon/LPHYS2299-Master-s-Thesis>

### AMOC Validation Test for Param B

To test Param B, we arbitrarily fix the following values for the coefficients :

$$a_1^* = 1.5, \quad (3.110)$$

$$b_1^* = -0.5, \quad (3.111)$$

$$c_1^* = 0.3, \quad (3.112)$$

$$d_1^* = -0.2, \quad (3.113)$$

$$e_{12}^* = -0.1, \quad (3.114)$$

$$f_1^* = -0.15. \quad (3.115)$$

Next, I conduct hysteresis experiments by simulating the EXP A, EXP B, EXP C experiments, respectively. For each of them, simulations of a duration of 400 000 years are performed to produce a forcing slow enough to remain almost constantly at equilibrium and to trigger the AMOC switch. The choice of the parametrization of the forcings  $T, F_{GIS}, F_O$  is purely arbitrary in this numerical experiment. Consistently, a forcing in the form of a "tent" function will be parameterized. In these experiments, the arbitrary values of the constant forcings were defined as uniformly zero. The plots of the bifurcation diagrams include the hysteresis simulated by the model in dashed black lines and the "exact" hysteresis calculated analytically based on our knowledge of the fixed coefficients. Displaying both hystereses allows for comparison of the quality of our simulation in its ability to reproduce the actual hysteresis.

$$F_{GIS}^A = 0 \text{ Sv}, F_O^A = 0 \text{ Sv}, T^B = 0^\circ\text{C}, F_O^B = 0 \text{ Sv}, T^C = 0^\circ\text{C}, F_{GIS}^C = 0 \text{ Sv}. \quad (3.116)$$

For the sensitivity experiment to the global mean temperature anomaly forcing, EXP A, the hysteresis produced with the model (3.2,3.3) is shown in Figure (38). The simulations of EXP B, EXP C are conducted in the same manner, and the hysteresis loops are shown in Figures (39,40).

Based on this numerical hysteresis, the critical values of the bifurcation point coordinates are identified. These coordinates are determined through visual inspection ; while a more sophisticated numerical method could have been developed, it was deemed unnecessary for the purposes of this validation test. Here are the selected values of the bifurcation points <sup>12</sup> based on the Figures (38,39,40),

12. In this case, we have exactly  $\Psi^+ \equiv \Psi_A^+ = \Psi_B^+ = \Psi_C^+$  et  $\Psi^- \equiv \Psi_A^- = \Psi_B^- = \Psi_C^-$ . This is consistent with what was discussed in Section (3.3.2) regarding this assumption. Since we are generating the hysteresis loops with our simplified model, this working hypothesis is precisely valid. However, we will see that this is not the case for hysteresis loops originating from more process-based models, which will result in an error term that we will optimize in Section (3.4).

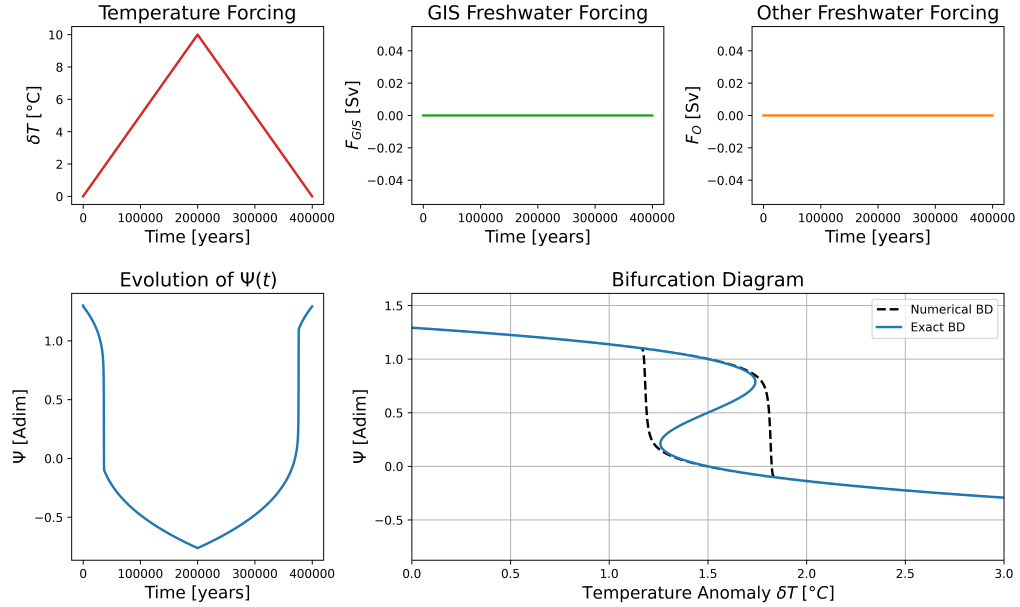


FIGURE 38 – EXP A Hysteresis product for validation testing.

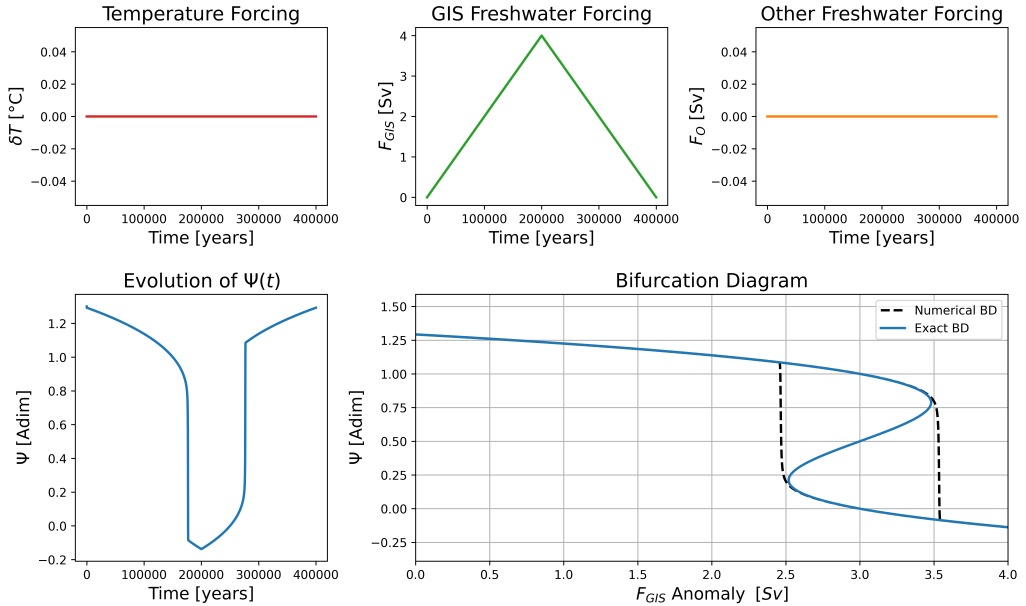


FIGURE 39 – EXP B Hysteresis product for validation testing.

$$\Psi^+ = 0.79, \quad (3.117)$$

$$\Psi^- = 0.18, \quad (3.118)$$

$$T^+ = 1.76 \text{ } ^\circ\text{C}, \quad (3.119)$$

$$T^- = 1.23 \text{ } ^\circ\text{C}, \quad (3.120)$$

$$F_{GIS}^+ = 3.55 \text{ Sv}, \quad (3.121)$$

$$F_{GIS}^- = 2.5 \text{ Sv}, \quad (3.122)$$

$$F_O^+ = 2.33 \text{ Sv}, \quad (3.123)$$

$$F_O^- = 1.63 \text{ Sv}. \quad (3.124)$$

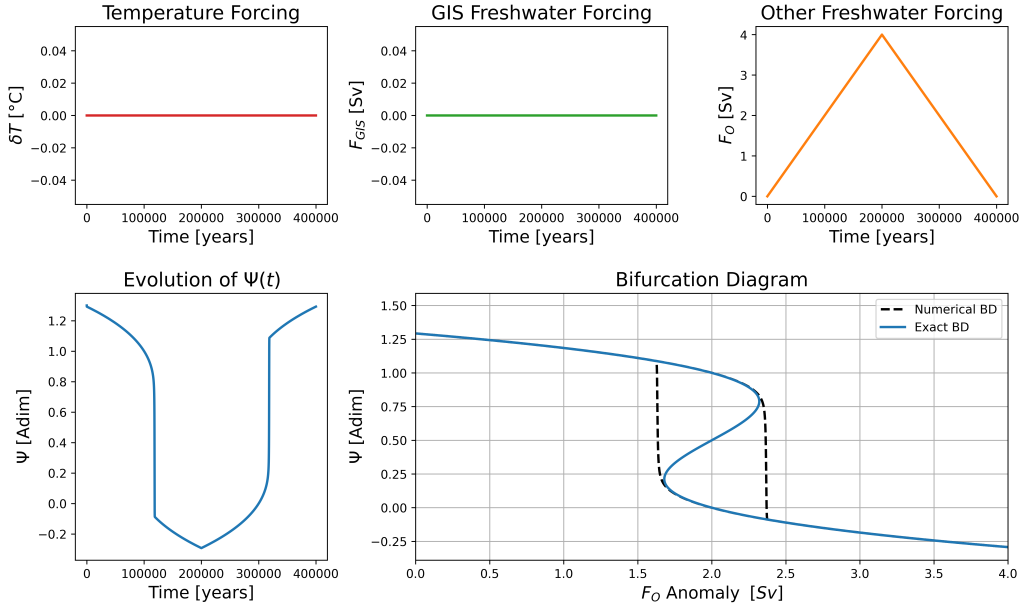


FIGURE 40 – EXPC Hysteresis product for validation testing.

Next, to calculate the coefficients  $a_1, b_1, c_1, d_1, e_{12}, f$ , I input these values into the created function,

$$\begin{aligned} \text{calib\_module\_AMOC\_ParamB}(\Psi^+, \Psi^-, T^+, T^-, F_{GIS}^+, F_{GIS}^-, \\ F_O^+, F_O^-, F_{GIS}^A, F_O^A, T^B, F_O^B, T^C, F_{GIS}^C) \\ = a_1, b_1, c_1, d_1, e_{12}, f. \quad (3.125) \end{aligned}$$

This function `calib_module_AMOC_ParamB` is the numerical implementation of Equations (3.56-3.77) described above. It should be noted, however, that the value of  $c_1$  used is taken from Equation (3.75). The comparison between the values of the coefficients arbitrarily defined initially and those calculated by the AGTCCM is shown in Table (5).

An important initial observation is that the values of  $c_1$  differ depending on whether they are calculated by EXP A, EXP B, or EXP C. This arises from the fact that the term  $c_1$  is the independent term present in all simulations of independent forcing. In other words, it is the coefficient to be calibrated across three different hysteresis experiments. Consequently, it is overdetermined, and an exact value cannot be assigned to it for each of the three sensitivity experiments. Similarly, this holds true for the coefficients  $c_1$  in the case of Param A or for the coefficient  $c_2$  for the GIS. In reality, each equation overdetermining  $c_1$  defines a  $c_1$  coefficient that significantly differs depending on the sensitivity experiment. The same holds true for  $c_2$ . Referring back to Equations (3.75, 3.76, 3.77), it should be noted taking this now into account that,

	Arbitrary Fixed Coefficients	AGTCCM Coefficients	Absolute Error <sup>13</sup> ( $ x_i - x_i^* /x_i$ ) × 100
$a_1$	1.5	1.455	3.09%
$b_1$	-0.5	-0.427	17.21%
$c_1$	0.3	0.306	1.86%
$d_1$	-0.2	-0.214	6.6%
$e_{12}$	-0.1	-0.108	7.48%
$f$	-0.15	-0.162	7.48%
$c_1$ from Eq.(3.76)	0.3	0.306	1.86%
$c_1$ from Eq.(3.77)	0.3	0.3	0%

TABLE 5 – Comparison between coefficients  $a_1^*, b_1^*, c_1^*, d_1^*, e_{12}^*, f^*$  and the ones computed by AGTCCM :  $a_1, b_1, c_1, d_1, e_{12}, f$ .

$$c_1^A \equiv \frac{T_\Psi^+ \Psi^{-2} (\Psi^- - 3\Psi^+) - T_\Psi^- \Psi^{+2} (\Psi^+ - 3\Psi^-)}{2(T_\Psi^- - T_\Psi^+)} - e_{12} F_{GIS}^A - f F_O^A, \quad (3.126)$$

$$c_1^B \equiv \frac{F_{GIS}^+ \Psi^{-2} (\Psi^- - 3\Psi^+) - F_{GIS}^- \Psi^{+2} (\Psi^+ - 3\Psi^-)}{2(F_{GIS}^- - F_{GIS}^+)} - d_1 T^B - f F_O^B, \quad (3.127)$$

$$c_1^C \equiv \frac{F_O^+ \Psi^{-2} (\Psi^- - 3\Psi^+) - F_O^- \Psi^{+2} (\Psi^+ - 3\Psi^-)}{2(F_O^- - F_O^+)} - d_1 T^C - e_{12} F_{GIS}^C. \quad (3.128)$$

In the `calib_module_AMOC_ParamB` model, and this will also be the case in the `calib_module_AMOC_ParamA` model, we define that,

$$c_1 \equiv c_1^A. \quad (3.129)$$

In the analogous model for the GIS, numerically named `calib_module_GIS`, we define that,

$$c_2 \equiv c_2^C, \quad (3.130)$$

where  $c_2^C$  represents the value of  $c_2$  as defined in Equation (3.108). This decision is motivated by the fact that, given the presence of an error, we aim to minimize it primarily in relation to the temperature forcing, which serves as the dominant primary forcing for both the GIS and the AMOC. Thus, to capture the dynamics of the AMOC and the GIS as faithfully as possible to nature, it is essential to model the temperature forcing accurately. In other words, our priority is to optimize the hysteresis loops of the AMOC and the GIS based on the temperature forcing, even if it means accepting a less precise calibration of the AGTCCM for other forcings. Alternative approaches to this decision will be explored in Section (3.5) on the Limitations of AGTCCM.

Once this initial reflection and observation are made, we realize that the AGTCCM is very successful in recovering the arbitrary coefficient values that we initially defined. The largest absolute error we obtain is 17.21% for the term  $b_1$ , but we

are able to achieve absolute errors as low as 1.86% for  $c_1$ , for example. In Figures (41,42,43), the hysteresis simulated by the AGTCCM model with the arbitrary coefficient values for the validation experiment is displayed in solid black dashed lines. The exact bifurcation diagram calculated analytically based on these known coefficients is plotted in dashed blue lines. The simulated bifurcation diagram using the output model of the AGTCCM with the coefficients calibrated by the method is shown in olive green lines. Lastly, the critical bifurcation points are depicted in red. Thus, a very good calibration of the hysteresis from the AGTCCM, which seeks to emulate that provided by the initial model<sup>14</sup>, is observed.

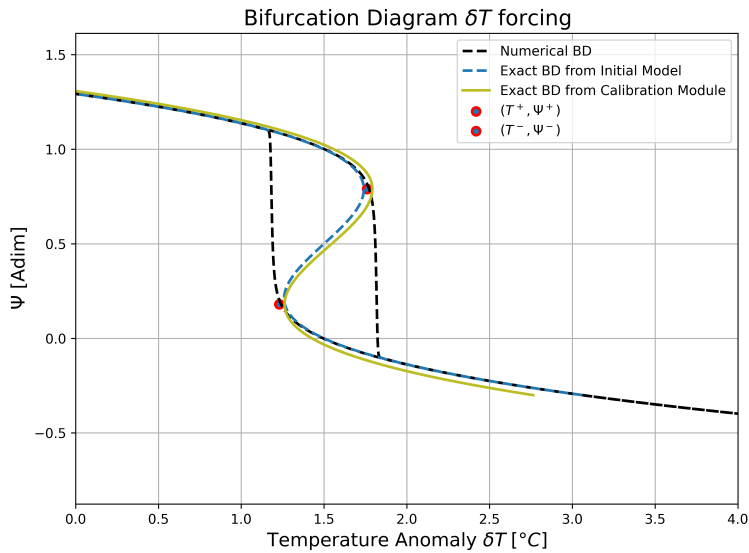


FIGURE 41 – *EXPA* Bifurcation Diagram product for validation testing.

However, this significant difference cannot be ignored without comment, especially since we had stated theoretically that it was possible to retrieve their exact values. The reason for the difference has already been mentioned ; here, we are merely conducting a "visual" calibration of the critical bifurcation point coordinates. Several experiments have shown that the closer we refine the estimations of these coordinates towards their true values, the more we tend to reduce the error term towards zero. Various avenues of numerical algorithm to find the exact bifurcation points could be designed and implemented without too much difficulty. However, regardless of the physical model used to produce hysteresis loops, the exact bifurcation point is never an exact science but is based on multiple experiments and cross-research that allow us to identify a reasonable range where we can place the bifurcation points. We will indeed see a manifestation of this difficulty in the following section where we will calibrate the AGTCCM on cGenie hysteresis loops. As explained in Chapter I, obtaining precise values for the bifurcation points of the AMOC, the GIS, and any other

14. which in this specific case is the same model but with "forgotten" coefficients

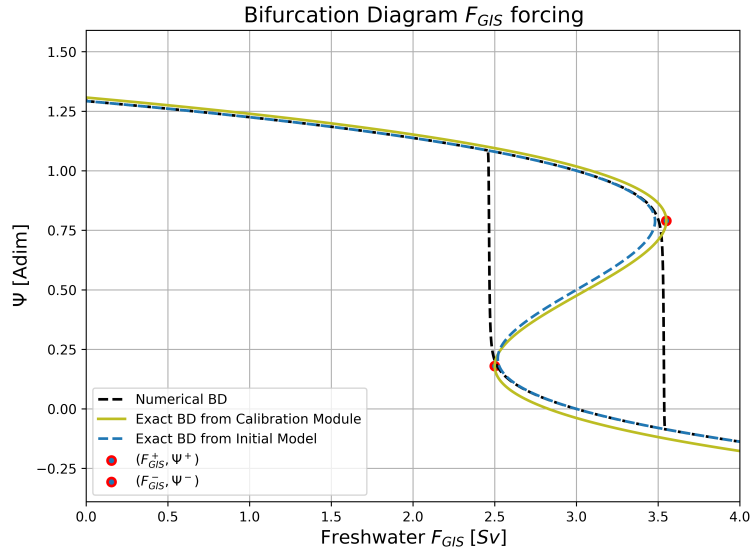


FIGURE 42 – EXPB Bifurcation Diagram product for validation testing.

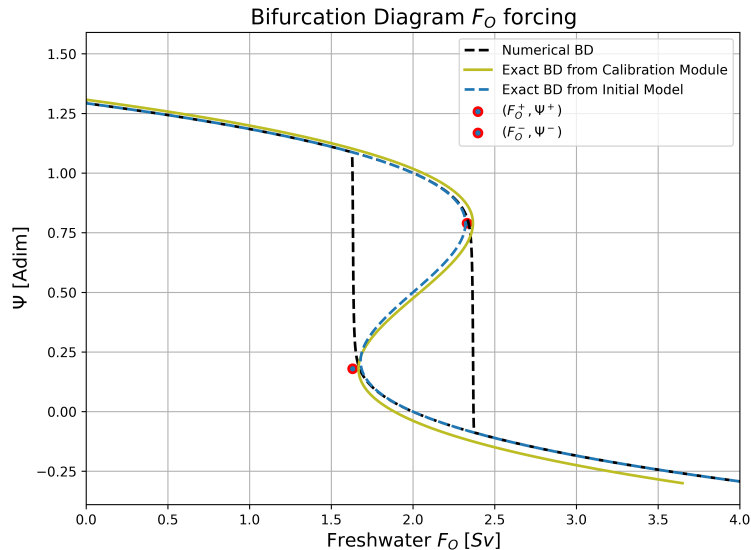


FIGURE 43 – EXP C Bifurcation Diagram product for validation testing.

tipping element is very challenging. Depending on the model used, discrepancies can sometimes be significant. Therefore, there is inevitably an element of expert judgment that must be provided by the researcher to assign a reasonable value to these bifurcation points based on the hysteresis loops. For these two reasons, it did not seem necessary or useful to provide a numerical implementation for calculating the bifurcation points. This operationally and pragmatically allows for more flexibility in defining the "expert" chosen on the coordinates of the bifurcation points from the hysteresis loops that we wish to emulate.

Finally, from Figures (41,42,43), we can observe that the bifurcation diagram provided by the AGTCCM does not exactly match the critical bifurcation point

coordinates. Although this is an unsatisfactory result, it is still a consequence of the fact that we do not have identical  $c_1$  coefficients in each of the sensitivity experiments. This is a weakness of the AGTCCM, inherent to its simplification methodology, which will be even more pronounced in the next section but will also be criticized and discussed in the final section on the limitations of this method at the end of the chapter. Fortunately, however and as will be shown, this does not prevent the AGTCCM from being able to produce simplified hysteresees calibrated in a usable and reasonable manner.

As stated in the introduction to this sub-subsection, we will not extensively present the results of this validation test for the GIS model as well as for the **Param A** configuration of the AMOC. The results, observations, and conclusions are identical, which is why it was not deemed necessary to present them in order to make the exposition more concise and avoid unnecessarily burdening this thesis. Based on these encouraging results, we will therefore proceed to practically implement the AGTCCM by testing it in an operational framework, for which it was designed : to emulate hysteresis of more complex systems.

### 3.4 Calibration with cGenie

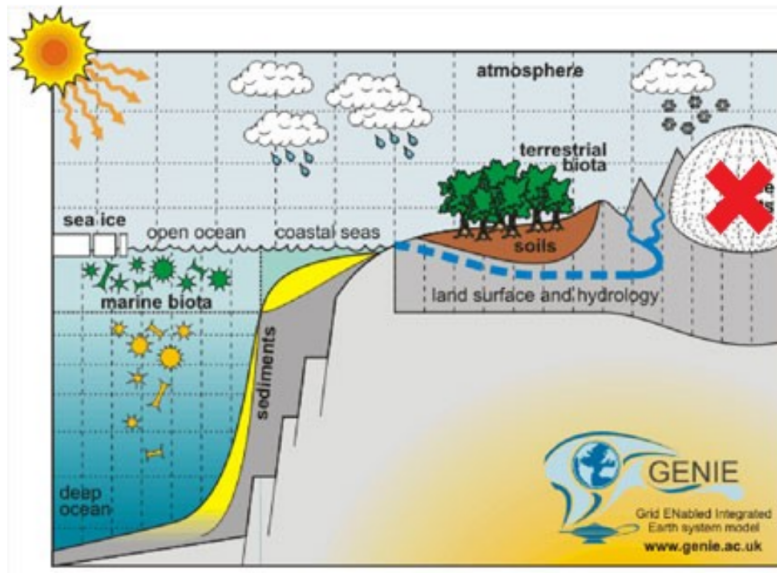


FIGURE 44 – Scheme of the cGenie model. Figure from cGenie documentation.[60]

#### What is cGenie and why using this model ?

cGenie is an EMIC (Earth System Model of Intermediate Complexity), which is a type of climate model used to simulate Earth's climate and its interactions with different components of the Earth system, such as the atmosphere, hydrosphere, cryosphere, and biosphere, as shown in Figure (44). EMIC models

lie between complex General Circulation Models (GCMs) and simplified low-resolution models (such as SURFER). They are designed to incorporate enough detail to capture key climate processes while remaining faster and more easily interpretable than GCMs. These models are often used to study large-scale climate interactions, long-term climate changes, and the responses of the climate system to various forcing scenarios. Therefore, cGenie should be regarded more as a tool that is not overly cumbersome to use, with physics sufficiently coherent to serve as a "discovery and exploration" tool for understanding how the Earth system might operate, rather than necessarily as a detailed "simulation" tool. [60]

We have chosen to use cGenie as the initial model with higher physical complexity to calibrate the Atlantic Meridional Overturning Circulation (AMOC) in the AGTCCM because it is recognized for its consistency in modeling the AMOC. Additionally, it enables hysteresis experiments with relatively limited computational time. This is indeed an important criterion because, in practice, generating AMOC collapse hystereses requires fairly long simulation times to perturb the AMOC while maintaining proximity to equilibrium as much as possible. The final reason is the expertise within Prof. Crucifix's research team regarding cGenie, particularly from PhD student Justin Gérard, who works extensively with this model.

### The hysteresis produced with cGenie

Our objective is therefore to conduct independent sensitivity experiments on the AMOC that reflect the three sources of forcing specified in `Param B` of the AGTCCM, namely global average temperature, a freshwater flux from GIS, and a freshwater flux associated with an anomaly in the precipitation-evaporation ( $P - E$ ) balance over the Atlantic. Based on these experiments, the goal will be to identify the coordinates of the critical bifurcation points, which will then be supplied to the AGTCCM to calibrate our simplified dynamics accordingly.

In the calibration methodology, a fundamental assumption we rely on is the independence of forcings and the capability to individually manipulate these forcings in model simulations we aim to emulate. Considering the cGenie model, it includes a representation of the water cycle with a parametrization of the  $P - E$  (precipitation-evaporation) balance, which is temperature-dependent. In the initial sensitivity experiment `EXPA`, it was not feasible to isolate this particular contribution. In other words, in our `EXPA`, there is also an implicit consideration of salinity variations induced by  $P - E$ . However, this effect is minimal enough that we can consider the primary forcing to be almost exclusively on the thermal branch of the thermohaline circulation. Thus, it is a reasonable approximation to state that in cGenie, a forcing by atmospheric temperature on the AMOC effectively creates a thermal forcing on the thermohaline circulation.

### EXPA Temperature Forcing Sensibility Experiment

As part of EXPA, a sensitivity experiment for the AMOC under global average temperature forcing, we utilized a simulation spanning 40 000 years during which a *tent function* forcing was artificially applied to atmospheric  $CO_2$  concentrations, increasing from pre-industrial levels of 280 ppm to 2800 ppm. This forcing is depicted in Figure (45a), while the response in terms of global average temperature anomaly at 2 meters above ground level is shown in Figure (45b). It is important to note that the transition from an atmospheric  $CO_2$  concentration anomaly to a global average temperature anomaly is quantified by the climate sensitivity inherent to the cGenie model we are using. Compared to the existing literature and models, cGenie possesses a moderate climate sensitivity, within the range of accepted values. Based on this moderate climate sensitivity, it is observed that a tenfold increase in atmospheric  $CO_2$  concentration leads to a global average temperature anomaly of approximately  $10^{\circ}C$ . Additionally, the response of the average surface ocean temperature, shown in Figure (46a), is noteworthy. Due to the greater thermal inertia of the ocean compared to the atmosphere, a more subdued response is observed, although a maximum temperature anomaly of approximately  $4.5^{\circ}C$  is still noted. The global average ocean salinity is also displayed, where it is seen to vary insignificantly.

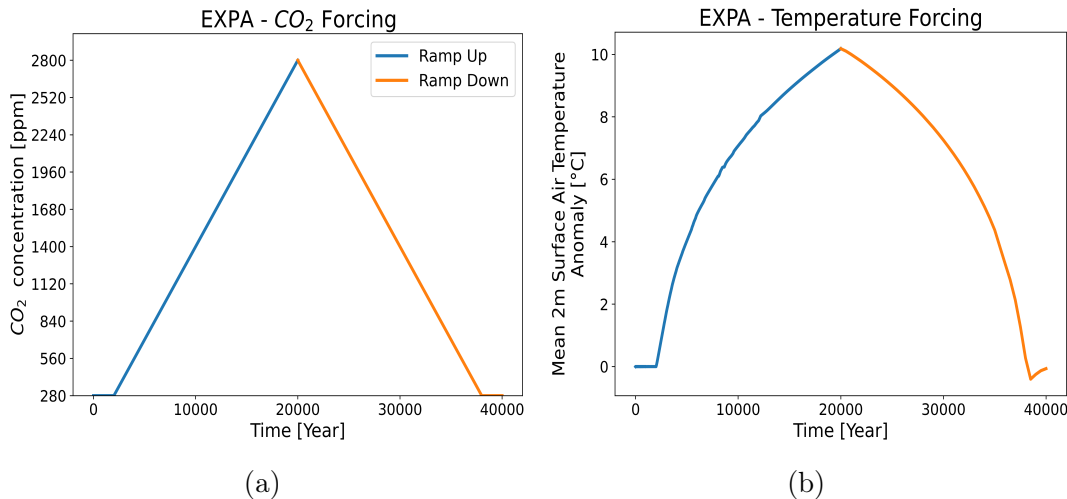


FIGURE 45 – (a)  $CO_2$  and (b) Global Mean Temperature forcing in the EXPA sensibility experiment with cGenie.

Now let us delve into EXPA to explore what really interests us : the response of the AMOC to this temperature forcing. To characterize the intensity of the AMOC, we will use  $\Psi$ , which is the streamfunction of the Atlantic overturning ocean circulation as defined in Chapter I. This is directly calculated by cGenie as an output variable of the model. Figure (46b) depicts the bifurcation diagram along with the hysteresis behavior resulting from the sensitivity experiment to global mean temperature.

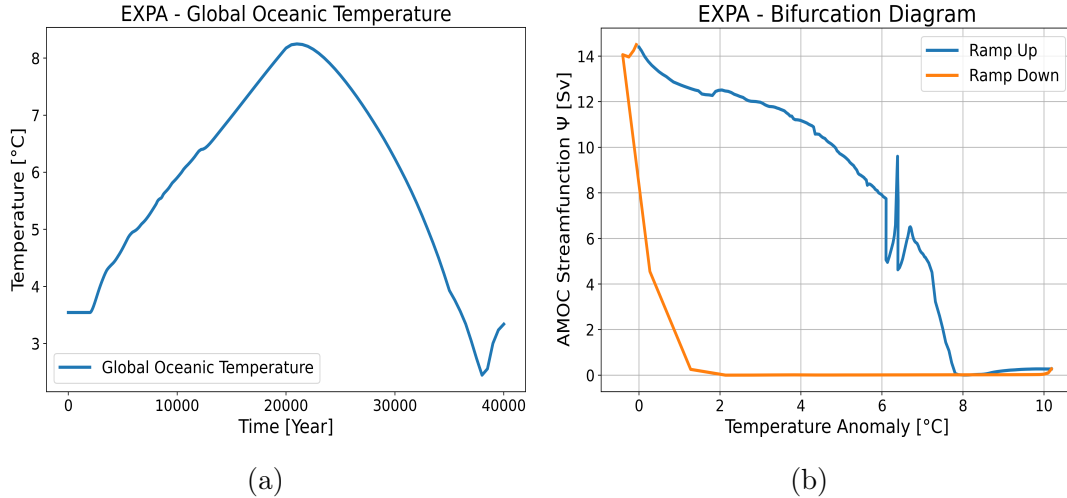


FIGURE 46 – (a) Mean Global Surface Oceanic Temperature and Salinity from EXPA. (b) Bifurcation Diagram and Hysteresis from EXPA. The maximum of the AMOC’s streamfunction  $\Psi$  is plotted against the anomaly of the mean global air temperature at 2 meters above the surface.

We indeed observe a collapse of the AMOC during this experiment solely due to a temperature forcing. However, it is worth noting that we are forcing with an extreme temperature anomaly reaching up to  $+10^{\circ}\text{C}$  in global mean temperature. Nevertheless, the rate at which we warm up is very low, as we warm by  $10^{\circ}\text{C}$  over 20 000 years, resulting in a warming of  $0.0005^{\circ}\text{C}$  per year. For comparison, this represents a factor nearly ten times smaller than the  $\approx 1.1^{\circ}\text{C}$  increase since the industrial revolution, which corresponds to an average annual warming of  $\approx 0.003^{\circ}\text{C}$ .

We also observe the expected behavior, namely that after the ramp-up phase, we can reach a cooling and a reduction of the anomaly significant enough to recreate the AMOC and restore it to its initial state.

Furthermore, we encounter an initial difficulty, namely that hysteresis loops from more complex models such as cGenie never allow for an explicit and direct reading of the bifurcation points. Indeed, even if the AMOC collapses, determining the exact bifurcation point in Figure (46b) is not straightforward. In reality, there is no canonical method to determine the exact bifurcation point based on a complex hysteresis. The best technique remains a visual estimation aided by expert judgment. Furthermore, another simulation challenge is the difficulty in estimating whether we are indeed at a stable equilibrium point or not, as due to the limitations of available simulation times on more complex models, we might not be precisely at equilibrium for the AMOC. In other words, it could be that if we had access to a much longer integration time, we would realize that we are still at a point of the hysteresis on a stable equilibrium.

To address these difficulties, I sought the expertise of J.Gérard who has been working on cGenie for a long time and had conducted stability tests of the AMOC in cGenie for his thesis. A first comment is that the oscillation appears

ring around  $\approx 6^{\circ}C$  does not have a real physical meaning but is due to the internal dynamics of the model ; thus, it is not the marker of the beginning of the bifurcation as one might have thought. Based on the stability tests conducted by J. Gérard, the most faithful bifurcation point to what happens in the simulations is the peak around  $T = 6.7^{\circ}C$ . Indeed, from his personal work, he observed that if the AMOC was allowed to evolve for a sufficiently long time for a temperature forcing lower than this value, it did not collapse. However, as will be seen in the rest of this sub-subsection, the calibration with the AGTCCM will require significant modification of this critical point artificially to optimize the calibration.

With this identification of the critical bifurcation point made, we can also conclude from the analysis of this first hysteresis that we distinctly observe the hysteresis behavior announced in Chapter I. Indeed, the point at which the AMOC returns to its initial state is reached for a temperature forcing value significantly lower (approx.  $1.5^{\circ}C$ ) than that for its collapse. In other words, we find that the evolution of the AMOC, as a dynamical system, depends on its past history.

### EXPB $F_{GIS}$ Sensibility Experiment

In both EXPB and EXPC, we apply the same parametrization of the freshwater flux, namely a *tent function* that ranges from  $-0.2 \text{ Sv}$  to  $0.3 \text{ Sv}$  over 10 000 years, and then decreases at the same rate back to the initial state. This freshwater forcing<sup>15</sup> is depicted in Figure (47). This quantity of freshwater flux falls within the range of typical fluxes used for hosing experiments aiming to approximate the typical idealized GIS freshwater forcing used in GIS hosing studies.[41, 83] It is the same parametrization as that performed in the seminal paper by Rahmstorf et al.[58] It constitutes a sufficiently slow forcing so that the circulation can adjust to this change while remaining close to equilibrium. Again, this is necessary because it is through the study of equilibrium states in the model that we obtain the basis for understanding the response to transient simulations.[58]

The only, and significant, difference between EXPB and EXPC lies in the geographic location where this forcing in the Atlantic is applied. In EXPB, we aim to simulate a freshwater flux forcing originating from the melting of the Greenland Ice Sheet (GIS). Therefore, the freshwater flux we add in this sensitivity experiment will be applied within a rectangle between  $50^{\circ}N$  and  $70^{\circ}N$  and between  $45^{\circ}W$  and  $5^{\circ}E$ . This forcing thus alters the large-scale freshwater balance of the North Atlantic, without directly affecting the high-latitude convection regions.[58] The area where the forcing is applied is depicted in Figure (48). This serves as a good approximation to the areas where a freshwater input from

15. Note that in reality, the simulations maintain a constant sea level, meaning that in the model, we only add or remove salinity to the water and do not actually add freshwater. This is a technical detail but does not pose any problem and does not lead to aberrant results. This methodology is the standard one used in the vast majority of hosing experiments.

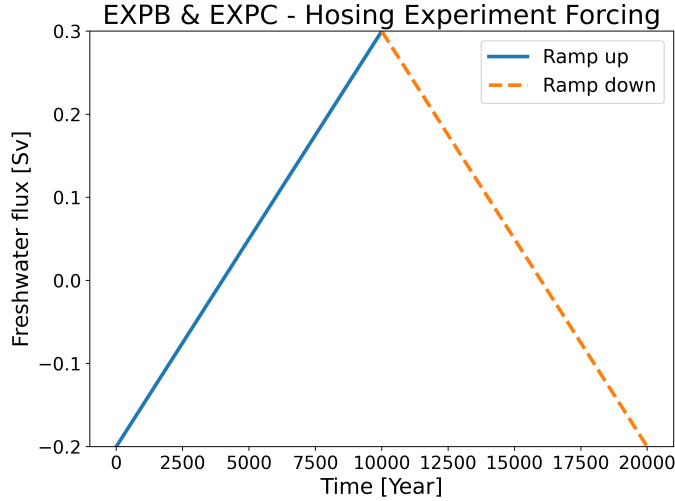


FIGURE 47 – Parameterization of freshwater flux forcing in the hosing experiments EXPB and EXPC.

the GIS will have a primary impact, especially since we are directly forcing in the critical zones for the AMOC, namely the deep convection formation areas in the North Atlantic. It is important to note that this freshwater input into the Atlantic is exactly compensated by increased evaporation, which is parametrized in the Pacific, to maintain a constant salinity in the global ocean and avoid inducing effects due to physically unrealistic imbalances within the model. This was done for the sake of detail, although studies have shown that compensating for this freshwater input in the Pacific makes little difference.[59]

Furthermore, it is useful to note that in dark gray on Figure (48), the land mask as seen by cGenie is depicted. We can observe the implications of EMICs models having an intermediate level of spatial resolution, allowing for the representation of continents but with very coarse estimation, leading, for example, to the fact that places like Madagascar have a resolution lower than that of the grid and therefore cannot be represented. In green are the grid elements considered as oceanic.

The bifurcation diagram of the AMOC for this sensitivity experiment to a freshwater flux representing the consequence of GIS melting is shown in Figure (49).

We observe a more abrupt collapse of the AMOC than in the case of temperature forcing. The oscillation appearing in EXPB is not present in this case, and the response of the AMOC is much smoother to freshwater forcing. Again, although the exact location of the stable-to-unstable state bifurcation remains difficult to determine, a reasonable range based on the literature that reproduces these data is between [0.02 Sv, 0.1 Sv]. By taking a value for the critical bifurcation point within this interval, we distinctly observe again the hysteresis behavior and the abrupt recovery of the AMOC for slightly negative freshwater flux anomaly values of approximately  $-0.02 \text{ Sv}$ .

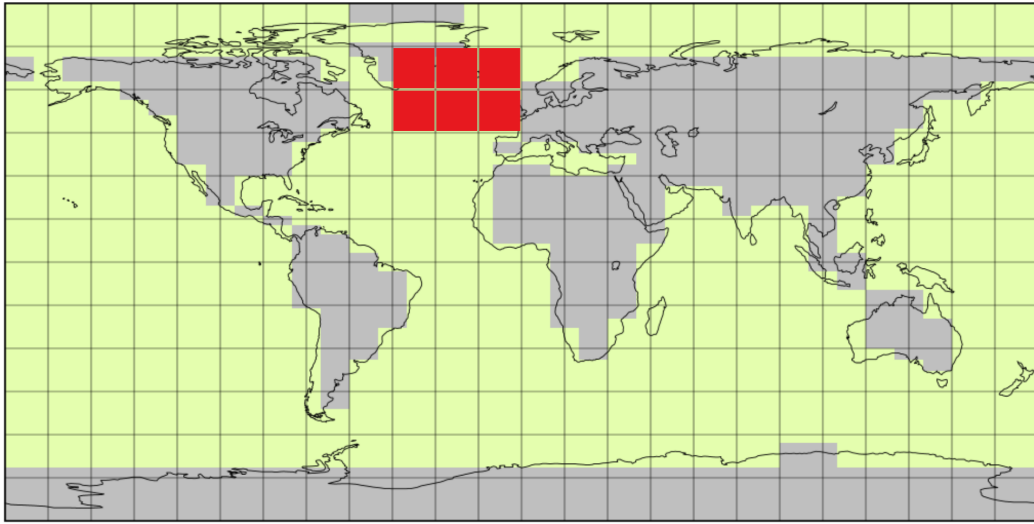


FIGURE 48 – *Geographical region where hosing forcing is applied in EXPB.*

### **EXPC $F_O$ Sensibility Experiment**

For the last sensitivity experiment, a freshwater flux forcing similar to that described in Figure (47) is used, but applied this time to the geographical region between 20° N and 50° N and across the entire width of the Atlantic basin. The geographical hosing area is shown in Figure (50). The reason for this specific hosing application area is to emulate the effect of a modification in the freshwater flux by altering the precipitation-evaporation balance around the latitude of the Tropic of Cancer.

In Figure (51), the bifurcation diagram for this last sensitivity experiment is depicted. Qualitatively, we observe the more abrupt and smoother response of the AMOC in its collapse to the freshwater flux forcing, as described in EXPB. Apart from a slightly more abrupt collapse in the intensity of the AMOC in the case of EXPC, the bifurcation diagram is very similar to that of EXPB. The hysteresis behavior is again pronounced. This likely stems from the fact that the distinction between the hosing application areas is actually quite subtle. Although freshwater is added a bit further south than in the most critical deep water formation zones, applying freshwater across the entire width of the Atlantic basin likely compensates for this difference and even slightly dominates this effect.

### **Calibration and emulation of cGenie by the AGTCCM**

Now that we have produced and detailed the three sensitivity experiments at our disposal, we can extract the critical coordinates of the bifurcation points to calibrate the AGTCCM accordingly. We will calibrate the AMOC by emulating its behavior as described by cGenie. Taking into account the previous

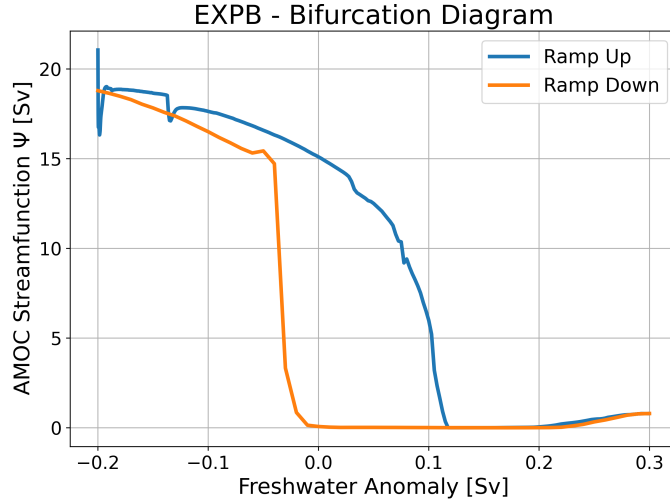


FIGURE 49 – *Bifurcation diagram and hysteresis from EXPB. The maximum of the AMOC’s streamfunction  $\Psi$  is plotted against the anomaly of freshwater flux applied in the region depicted on Fig.(48)*

considerations, the initial version of the critical bifurcation point coordinates considered are displayed in Figures (52a, 52b, 53)<sup>16</sup> and summarized in Table (6).

There are two challenges in selecting the best critical coordinates for bifurcation points. The first, as previously described in more detail, is inherent in the identification of bifurcation points based on hysteresis in climate components. This involves the difficulty of simulating hystereses and accurately pinpointing the exact location of the bifurcation point due to an inability to determine if the system is truly at equilibrium at the considered location. The second challenge is specific to our simplified calibration methodology. As we will see, the choice of these coordinates fundamentally impacts the quality of calibrations that can be performed with our simplified dynamics in relation to the more complex hysteresis.

A primary challenge in the AGTCCM is that, as stated, we hypothesized that  $\Psi^+ \equiv \Psi_A^+ = \Psi_B^+ = \Psi_C^+$  and  $\Psi^- \equiv \Psi_A^- = \Psi_B^- = \Psi_C^-$ . However, as observed in Figures (52a, 52b, 53), although it is possible to identify critical forcing coordinates for  $F_{GIS}$  and  $F_O$  that correspond to points on the hysteresis curve which we might consider as bifurcation points under this working hypothesis, there is no guarantee of its accuracy. Indeed, as illustrated in Table (6), the critical values of AMOC at which it bifurcates are notably different across the three

16. It should be noted that from now on, to facilitate comparisons with the literature and to simplify the interpretation of results, we will systematically normalize the states of the AMOC as well as those of the GIS. We thus redefine  $x \rightarrow x/x_{max}$ , where  $x$  is any state variable of the tipping element under consideration and  $x_{max} = x(t = t_{PI})$ . This is solely a scaling normalization aimed at eliminating the precise numerical values of the tipping element’s state.

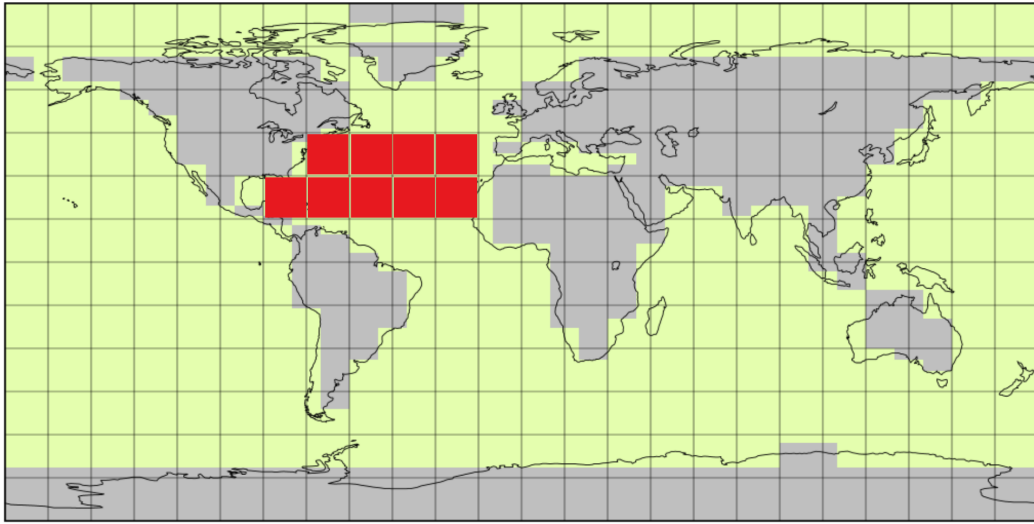


FIGURE 50 – Geographical region where hosing forcing is applied in EXPc.

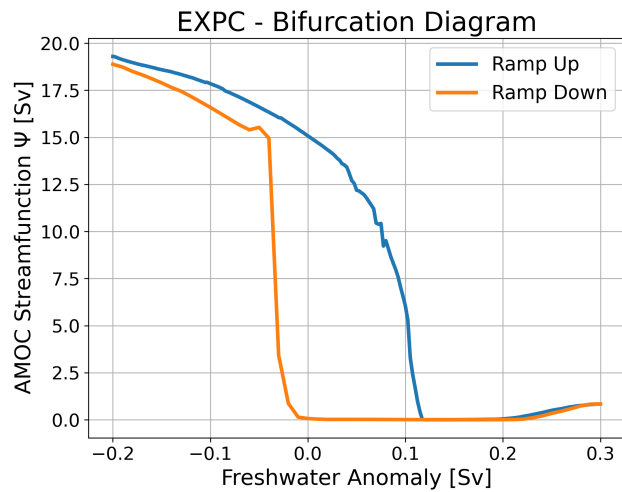


FIGURE 51 – Bifurcation diagram and hysteresis from EXPc. The maximum of the AMOC's streamfunction  $\Psi$  is plotted against the anomaly of freshwater flux applied in the region depicted on Fig.(48)

experiments. This simplification results in an inherent error in our AGTCCM methodology. Unfortunately, this is the price paid to maintain a mathematical framework that is as coherent, effective, and understandable as possible. Without this working hypothesis, it would indeed be impossible to calibrate the inter-hysteresis relationships with such a reduced set of equations. Once this hypothesis is accepted, we must then consider which effective values to take for  $\Psi^+$  and  $\Psi^-$ . In other words, should we use the values from EXPa, EXPb, or EXPc? This anticipates a broader and more synthetic discussion that we will

Coordinates	Values from cGenie hysteresis
$\Psi^+ \equiv \Psi_A^+$	0.6
$\Psi^- \equiv \Psi_A^-$	0.022
$T^+$	5.5
$T^-$	1.27
$F_{GIS}^+$	0.045
$F_{GIS}^-$	-0.015
$F_O^+$	0.065
$F_O^-$	-0.015
$\Psi_B^+$	0.45
$\Psi_B^-$	0.16
$\Psi_C^+$	0.495
$\Psi_C^-$	0.18

TABLE 6 – *Different critical coordinates retained from the cGenie hystereses for the calibration of the AGTCCM*

have in the following subsection on the limitations of AGTCCM, namely, how should we distribute the inherent modeling errors. In other terms, which forcing variable, which hysteresis should we prioritize for refinement, and therefore, on which are we willing to accept a greater calibration error? Motivated by literature suggesting that temperature forcing is dominant in the dynamics of GIS and AMOC collapse, we will always strive to minimize errors in the initial sensitivity experiments in this work. Furthermore, the uncertainty surrounding freshwater flux forcing terms is also greater in the literature because they are more challenging to simulate. Therefore, it seems more reasonable to accept a larger margin of error in the sensitivity experiments EXPB and EXPC. Based on these motivations, we decide that,

$$\Psi^+ \equiv \Psi_A^+, \quad (3.131)$$

$$\Psi^- \equiv \Psi_A^-. \quad (3.132)$$

A second important remark is that contrary to what we stated in the analysis of the EXPB hysteresis, we have chosen bifurcation coordinates for  $T^+$  much lower than the value of  $T^+ \approx 6,5^\circ C$  which had been motivated by J.Gérard's research. Why this contradiction? Figures (54a, 54b) show the initial results of calibrating the AGTCCM emulation on the cGenie hysteresis for EXPB. As seen in Figures (54a, 54b), if we were to take the "true value" of  $T^+ \approx 6,5^\circ C$ , we would achieve a very poor calibration of the simplified model on the hysteresis. Even if we were to use what would be a more accurate bifurcation point, the remaining dynamics leading to the bifurcation points would be of very poor quality. Furthermore, and this is not a minor issue, we would have a very poor calibration of the AMOC on the pre-industrial state, or at least on any state without forcing with  $T = 0^\circ C$ .

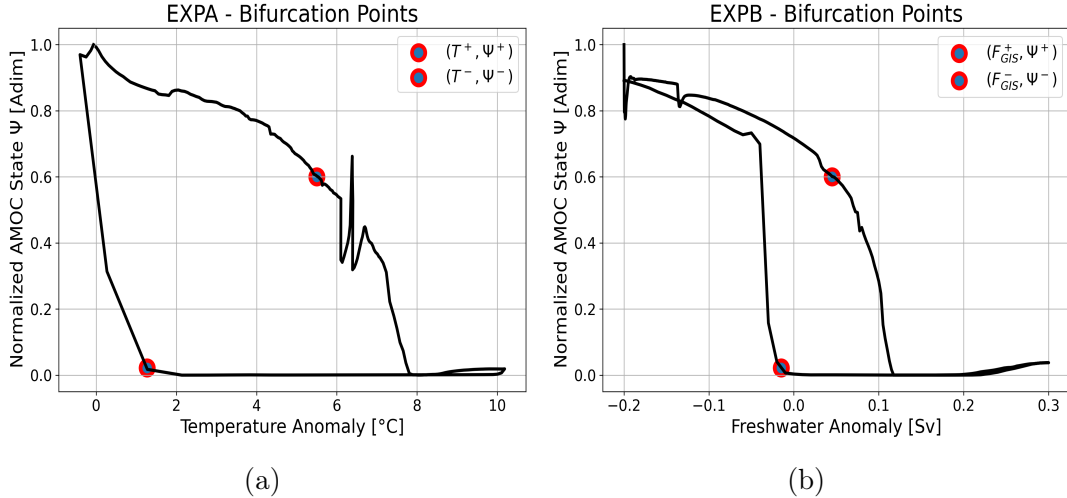


FIGURE 52 – (a) Localization of the selected bifurcation points on the hysteresis of EXPA. (b) Localization of the selected bifurcation points on the hysteresis of EXPB.

What is the source of this latter problem? In the simplified double-fold model with a single forcing parameter by Martinez Monteiro et al.[52], an additional algebraic constraint is developed to ensure that when the forcing is zero, the state of the GIS is at its pre-industrial value. If we go back to Eq.(3.31), this constraint is found by imposing that  $V(T = 0) = 1$ , and since  $V(t = t_{PI})$  is also an equilibrium point, we have as a second condition that  $\frac{dV}{dt}(t = t_{PI}) = 0$ . By combining these two constraints based on equation (3.31), we obtain that,

$$-1 + a + b + c = 0. \quad (3.133)$$

Next, the idea is to inject the values of  $a, b, c, d$  as functions of  $(V_+, V_-, T_+, T_-)$  and isolate  $V_-$  in order to express this last calibration constraint on the pre-industrial value through the coefficient  $V_-$ . Out of the four critical coordinates of the two bifurcation points, the value of  $x_-$  is consistently the least interesting of the four, so we reasonably decide to significantly modify its value to achieve calibration in the case of zero forcing, which is more important. After a lot of tedious algebra, one can fall back on the constraints by Martinez Monteiro et al., following this logic.

$$V_- = \frac{-2 + V_+(1 + G^{1/3} + G^{-1/3})}{-1 + G^{1/3} + G^{-1/3}}, \quad (3.134)$$

with,

$$G = \left( \frac{T_+ + T_- + 2\sqrt{T_- T_+}}{T_+ - T_-} \right). \quad (3.135)$$

We can then ask whether we can generalize this calibration method on the pre-industrial value to our choices of parameterization with 2 and 3 forcing variables. Analogously, we pose as a constraint for the Param B of the AMOC that,

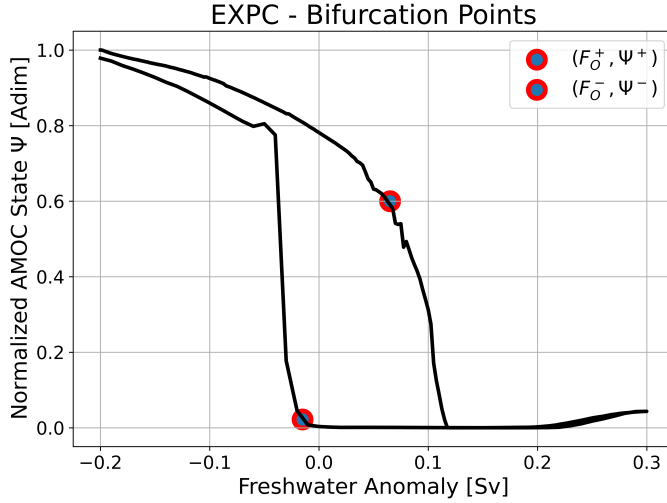


FIGURE 53 – Localization of the selected bifurcation points on the hysteresis of EXPC

$$\Psi(T = 0, F_{GIS} = 0, F_O = 0) = 1, \quad (3.136)$$

and that

$$\frac{d\Psi}{dt}(t = t_{PI}) = 0. \quad (3.137)$$

In equation (3.2), these two constraints yield,

$$-1 + a_1 + b_1 + c_1 = 0. \quad (3.138)$$

However, attempting to substitute the values of  $a_1, b_1, c_1$  in terms of the coordinates  $(\Psi^+, \Psi^-, T_\Psi^+, T_\Psi^-, F_{GIS}^A, F_O^A)$  and then isolate and express this final equation in terms of  $\Psi^-$  has not been feasible in practice. Theoretically, we are searching, without loss of generality, for a function  $l : \mathbb{R}^7 \rightarrow \mathbb{R}$  such that,

$$\Psi^- = g(\Psi^+, \Psi^-, T^+, T^-, F_{GIS}^A, F_O^A), \quad (3.139)$$

and that respects Eq.(3.138). Unfortunately, it has not been possible to find such a function. Furthermore, it should be noted that if this function is found, it will introduce a new dependence between the constant forcings in the sensitivity experiments. In other words, not all possible sensitivity experiments will be feasible anymore; only a narrower range will allow for calibrating the AMOC while maintaining consistency with the pre-industrial value calibration.

Given that the generalization of pre-industrial calibration in our case to multiple forcing variables could not be achieved, we also need to ensure that the pre-industrial equilibrium value is not aberrant. Based on Figures (54a,54b), it is clear that artificially increasing the value of the critical bifurcation point  $\Psi^+$ , besides fitting the intermediate dynamics before the first bifurcation point much better, has the merit of providing a fairly good calibration for the pre-industrial

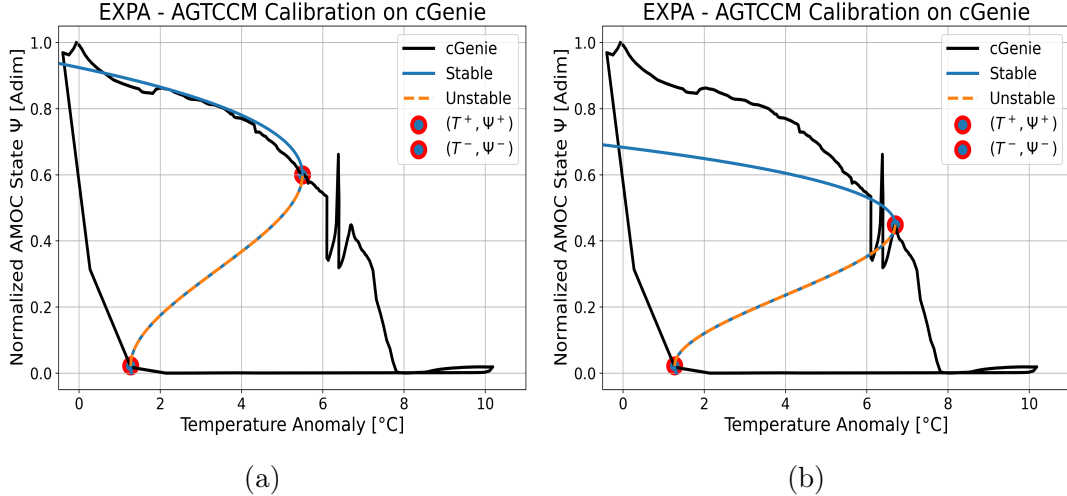


FIGURE 54 – (a) Calibration of the AGTCCM on the EXPA from cGenie in the case where  $\Psi^+ = 0, 6$ . (b) in the case where  $\Psi^+ = 0, 449$ .

value. This statement holds even more true when comparing with Figure (54b), which would have given us a value of  $\Psi(t = t_{PI}) = 0, 7$ , while the one chosen in Figure (54a) yields a value of  $\Psi(t = t_{PI}) = 0, 93$ .

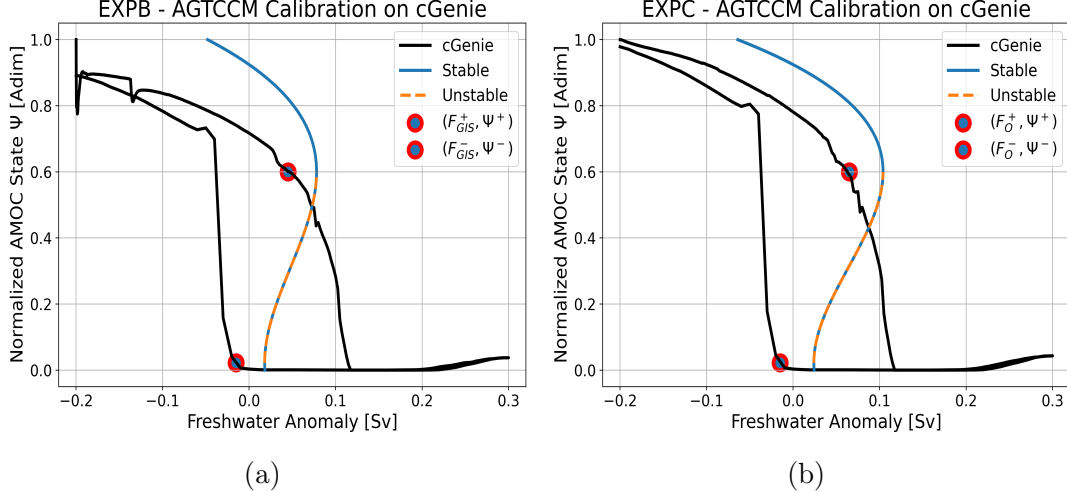


FIGURE 55 – (a) Calibration of the AGTCCM on the EXPB from cGenie. (b) same for EXPC.

Finally, Figures (55a,55b) depict the calibrations of the AGTCCM on cGenie's hysteresis loops for the EXPB and EXPC experiments. The first notable observation is that our simplified hysteresis loops do not precisely pass through the identified critical bifurcation points. This phenomenon is the same as observed in the previous subsection on the validation test. Since we decide to take the value of  $c_1$  determined by the EXPA experiment to maximize the calibration accuracy on temperature, we do not have an exact value of  $c_1$  that allows ca-

libration on the bifurcation points for EXPB and EXPC. This is regrettable, but it is once again an inherent limitation of our extreme simplification logic of a complex dynamics. However, to mitigate the impact of this error, given the considerable variability in critical threshold ranges provided by the literature, we actually have a difference of about  $\approx 0,02$  Sv between the chosen bifurcation point and where our simplified hysteresis loop actually passes. Considering the literature itself is fraught with significant uncertainty, the result presented here seems acceptable.

However, we observe that the calibration of the simplified dynamics remains qualitatively correct ; the simplified hysteresis manages to capture the shape of the complex hysteresis relatively well. This is especially true for the sensitivity experiment EXPC. Regarding the challenge of calibration on the pre-industrial value, we have acceptable results here since we find that  $\Psi(t = t_{PI}) \approx 0,95$  for these last two sensitivity experiments.

A graphical representation of the two-dimensional forcing space of  $\Psi$  as a function of  $T$  and  $F_{GIS}$  is shown in Figure (56). The same figure depicting the forcing space as a function of  $T$  and  $F_O$  is presented in Figure (57). Such figures provide insight into a portion of the forcing space, which is actually three-dimensional in the case of Param B, and importantly, they elucidate the utility of the AGTCCM. While generating hysteresis loops using process-based models like cGenie is time-consuming due to experiment preparation and computational expenses, these two figures illustrate that once the AGTCCM is calibrated, we have at our disposal the most faithful emulation possible. This allows for exploration of other regions of the forcing space. Indeed, the three sensitivity experiments conducted with cGenie only examined the evolution of AMOC intensity for specific combinations of forcing parameters  $T$ ,  $F_{GIS}$ , and  $F_O$ . As demonstrated in the next chapter, by integrating the AGTCCM into SURFER, we gain access to an AMOC emulation capable of responding to a much broader spectrum of forcings, which are also dynamic as simulated within the model.

### Calibration for the GIS

Given the primary importance of the AMOC in the potential cascading collapse dynamics of the AMOC-GIS system, as well as the time constraints, I focused my efforts on using hysteresis experiments only for the AMOC. Indeed, it was more feasible to do so due to access to simulations using cGenie provided by J. Gerard. However, the calibration for the GIS relies on critical bifurcation point values already present in SURFER v2.0, which are derived from hysteresis studies in the literature.

## 3.5 Limitations of the AGTCCM and Paths for Improvement

Before presenting the numerical integration of the AGTCCM into SURFER v3.1, which will form SURFER v3.2, it was deemed useful to revisit, in this

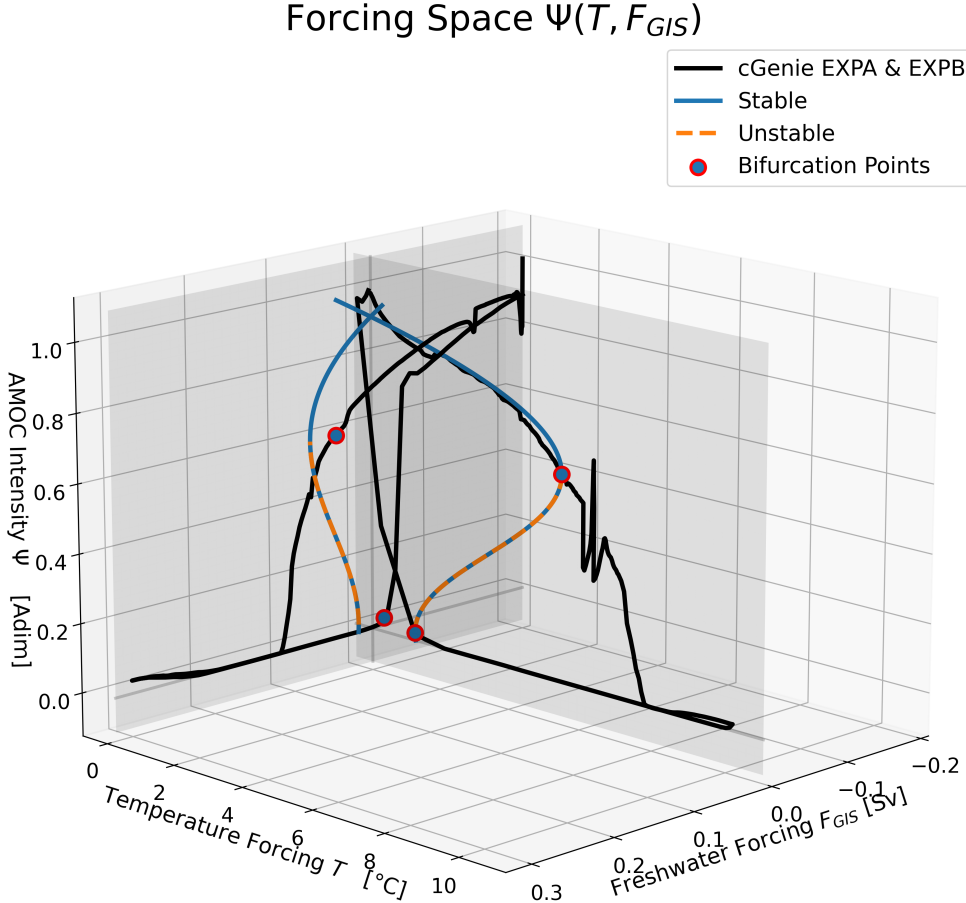


FIGURE 56 – Forcing space of  $\Psi$  in terms of forcing by temperature  $T$  and freshwater flux from the GIS  $F_{GIS}$ . Figure produced using AGTCCM calibration on cGenie

penultimate section of this technical chapter, the inherent limitations of the AGTCCM, the difficulties encountered, and further justify the choices made regarding each of these challenges. Despite the identified limitations, this section also serves as a defense of the relevance of the created model and the original methodological paradigm it establishes. Paths for improvement will also be proposed regarding several current challenges to provide clear perspectives based on the innovative methodology presented here. We will divide the discussion into two parts : first, on the limitations of the simplified model chosen for the AMOC-GIS, and then on the calibration method. Before that, some general remarks on the research paradigm are necessary.

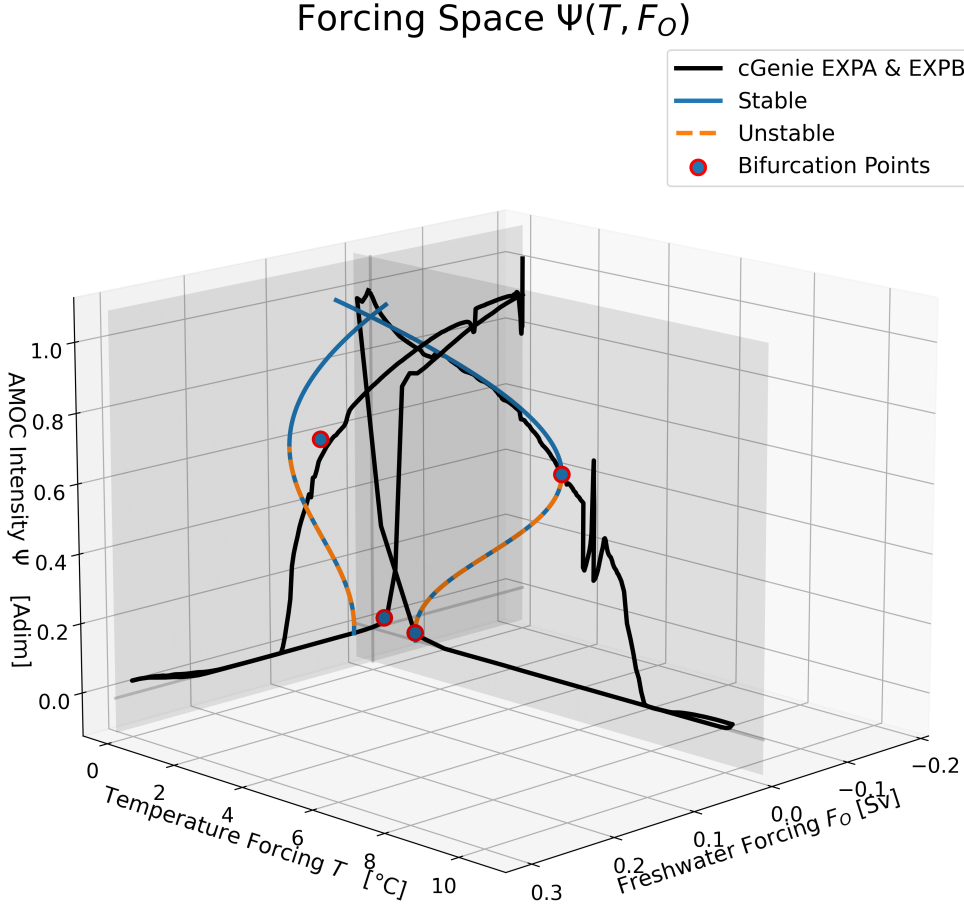


FIGURE 57 – Forcing space of  $\Psi$  in terms of forcing by temperature  $T$  and freshwater flux from the Other components  $F_O$ . Figure produced using AGTCCM calibration on cGenie

### 3.5.1 Limitations of the Conceptual Approach

The first remark is that, as we have seen and will elaborate on, there are inherent limitations to the conceptual approach we have taken. We recall that the primary objective here was to produce a methodology for emulating the complex collapse dynamics of the AMOC and the GIS, derived from process-based models, to calibrate a simplified dynamics. In concrete terms, we aim to model as faithfully as possible physically complex dynamics involving numerous physical processes on various spatiotemporal scales with a third-order polynomial. We seek to reduce the range of forcing dynamics that can occur on the AMOC and the GIS to a limited number of forcing variables. Once the program is outlined in this way, it is evident that this methodology, while having enormous advantages such as allowing the production of reliable experiments at very low

costs, will have significant limitations in precision.

These limitations and the fact that we would not be able to achieve perfect calibration were, with a little common sense, already known results before even putting this methodology on paper and into numerical code. The real challenge that follows is to optimize the inherent errors of the methodology to produce a calibration model that remains usable and relevant while staying within the basic research paradigm of the most extreme reductionism possible and integration into the SURFER model for rapid simulations. As we will see, we can certainly improve the AGTCCM at many levels by adding physical parameterizations, but that is not the scientific objective of this project. Thus, this entire chapter and the work that has been done to write it are the result of a continuous reflection to find the best trade-off between efficacy and scientific validity.

Finally, it is worth recalling that the literature itself, even with the aid of higher-resolution models such as GCMs, retains a fairly wide domain of uncertainty regarding the coordinates of critical bifurcation points, the dynamics of the GIS and the AMOC to and between these bifurcation points, or even the associated timescales. The AGTCCM is a model that allows for the emulation of the behavior of more process-based models of the AMOC and the GIS, but as the literature shows us, these more process-based models themselves are not truths in themselves. Therefore, this reduces the epistemological necessity of having the most precise calibration possible of our simplified AMOC dynamics on cGenie in our case because cGenie remains just one model among others with a truncated AMOC dynamics that produces values with their own uncertainty. Put another way, it is not useful to have precision to the millimeter on an object that can only be located in space to the meter. The AGTCCM should therefore not be seen as a model to be used for precise quantitative projections ; it is highly likely that the model values are wrong, but it is also very likely that the values given by the model are plausible. Indeed, as presented in the preceding sections, the results obtained by the AGTCCM fall within the plausible value ranges given by the literature and thus guarantee the relevance of this model.

### 3.5.2 The Hypothesis of Forcing Independence

One of the strongest assumptions underlying the logic of AGTCCM is that of the independence of forcings and the capability within the models we wish to emulate to independently manipulate the AMOC and GIS forcings. Like any model based on assumptions, these obviously set limitations that are worth discussing.

Firstly, from the perspective of the physical dynamics of the AMOC, we know that any alteration in the deep ocean circulation of the Atlantic will significantly impact both temperature and salinity patterns throughout the Atlantic Ocean, and even beyond. In other words, even if we induce the collapse of the thermohaline circulation solely by manipulating its thermal branch, during the

dynamics of collapse, we will also affect the salinity distribution in the ocean. It is therefore overly simplistic to state that we are triggering the AMOC collapse purely through temperature or solely through freshwater flux. What matters for the collapse of the AMOC is reaching a critical level of stratification, which indeed depends on both the temperature and the salinity of the water.

We aim to study the dynamics of the AMOC collapse by identifying its responses to forcings through the two levers of action that can lead to critical stratification. However, it is crucial to acknowledge that in reality and in more complex models, a temperature forcing will ultimately induce a variation in salinity distribution, and a salinity forcing will induce a variation in the temperature distribution of ocean water. Even if the forcing is solely thermal or solely haline, the fact that the circulation changes will impact these two variable fields to such an extent that after some time, the original signal of the forcing will be lost.

Furthermore, concerning the models' capacity to simulate forcings independently, our experiences with cGenie have revealed that due to the incorporation of a water cycle model that establishes a dependency of the  $P - E$  (precipitation-evaporation) balance on temperature, asserting strict forcing of the AMOC solely through temperature in the case of EXPa is untenable. Implicitly, a haline forcing will also manifest. However, in cGenie, as an initial approximation, it can be posited that the atmospheric temperature forcing predominantly induces a thermal forcing on the AMOC, with minimal impact on freshwater flux caused by variations in  $P - E$  in this context.

Expanding upon the point made in the preceding paragraph regarding the mixing of forcings, in the case of EXPa, a change in atmospheric temperature will affect oceanic circulation, subsequently influencing ocean temperature. Subsequently, this same ocean temperature will also influence atmospheric temperature and thereby  $P - E$ . In other words, in EXPa,  $P - E$  will follow the thermal forcing. However, according to J. Gérard's expertise on cGenie,  $P - E$  will never serve as a driver in these simulations due to the poor representation of the atmosphere in cGenie.

Thus, in general, it is essential to be aware that the sensitivity experiments we aim to conduct using our process-based models that we seek to emulate will always remain highly idealized. Whether it concerns the AMOC, the GIS, or other tipping elements that we wish to model with simplified dynamics, there is potential overlap of forcings between them, and considering their strict independence is rarely correct. Within the dynamics of tipping elements, all forcings interact. Nevertheless, through our methodology, we seek to capture the signature of the response of each lever of action to the collapse of the tipping elements of interest using idealized, albeit unrealistic, experiments, in order to subsequently study the dynamics when these forcings combine in more realistic situations.

### 3.5.3 Limitations of the AMOC-GIS Model and Paths for Improvement

The primary limitations of the chosen AMOC-GIS model that warrant further development pertain to the parameterizations of freshwater fluxes within the AMOC model, specifically that of  $F_O$ .

#### Parametrizations of freshwater flux

An important limitation is the assignment of the same coupling coefficient  $f$  to both the  $F_W$  forcings and the  $F_{P-E}$  forcing. If the goal is to maintain a distinction between the contributions from freshwater flux resulting from the melting of all cryospheric components excluding the GIS and the contribution from an anomaly in the  $P-E$  balance, then it would be advisable to differentiate between these two forcings. Beyond this, further refinement could enhance the physical consistency of the model by differentiating the coupling coefficients among the cryosphere components as follows :

$$\frac{d\Psi}{dt} = (-\Psi^3 + a_1\Psi^2 + b_1\Psi + c_1 + d_1T + e_{12}F_{GIS}(V) + e_{13}F_W^{WAIS} + e_{14}F_W^{EASB} + e_{15}F_W^{EAIS} + fF_{P-E})\mu_\Psi(\Psi) \quad (3.140)$$

Indeed, the melting of the West Antarctic Ice Sheet (WAIS) does not generate a freshwater flux that impacts the AMOC in the same way as a melt from the East Antarctic Ice Sheet (EAIS) would, for example. A motivation for such detailed discretization of forcings among cryosphere components is their dynamic simulation within SURFER, which would allow for dynamic forcing. However, operationally implementing this is mathematically feasible but would require, in this extreme case of equation (3.140), access to no fewer than six sensitivity experiments providing hystereses of AMOC responses to these distinct forcings. The design and production of these experiments would undoubtedly be the most challenging aspect, as already seen in the case of GIS, where hosing experiments with realistic freshwater flux parameterization are not very common and require preliminary work in simulation setup. This is even truer for the differentiation of Antarctic ice sheet components, whose dynamics are less well understood and subject to greater uncertainty than those of Greenland. Nevertheless, a distinction between the coupling to the AMOC of  $F_W$  and  $F_{P-E}$  forcing remains relevant and would be easier to implement, as one could consider two distinct hosing experiments : one in a subtropical latitude region and another with freshwater addition around Antarctica. In this case, we could set  $e_{13} = e_{14} = e_{15} \equiv e$ , leading to a model with explicit forcings of  $T, F_{GIS}, F_W, F_{P-E}$  and coupling coefficients on the AMOC of  $d, e_{12}, e, f$ . This would highlight interesting coupling phenomena given the different characteristic timescales between the  $P-E$  anomaly and the melt from Antarctic components.

Another source of error, which is not an inherent limitation of the AGTCCM but rather of the calibration performed using cGenie, stems from the choice of hosing experiment used for  $F_{GIS}$ . As described in Section (3.4), we conduct a hosing experiment between  $50^{\circ}N$  and  $70^{\circ}N$ , and between  $45^{\circ}W$  and  $5^{\circ}E$  to simulate a freshwater flux originating from the GIS. Although this is a coherent approach, it remains a relatively imprecise region for reproducing a freshwater flux from the GIS. More refined parameterizations using more complex models, as demonstrated in studies by Lenaerts et al.[41] and Jackson et al.[32], are of interest in this context. These more precise simulations of hosing, however, could not be carried out due to time constraints.

Another limitation of the AGTCCM is our parameterization of freshwater fluxes from cryospheric components other than the GIS. While in the case of the GIS sensitivity experiment, we can avoid introducing a geographical correction factor due to the hosing region, this is necessary for all sub-components of  $F_W$ . However, it is overly simplistic to reduce the dynamics of freshwater transport from Antarctica to the region described in Figure (50) by a mere constant reduction factor. To correct this error, a relatively straightforward solution is to conduct a sensitivity experiment on AMOC hosing in a region surrounding Antarctica. Thus, as we more reasonably did for the GIS, we could eliminate this geographical correction factor to access the AMOC's response in the emulated model to a freshwater flux from the South Atlantic proximate to Antarctica.

### The specific case of $F_{P-E}$

The parameterization choices for freshwater fluxes, namely  $F_{GIS}$ ,  $F_W$ , and  $F_{P-E}$ , have all been decided based on simplicity, adopting a linear model. While literature suggests that this approach may be acceptable for  $F_{GIS}$  and  $F_W$ , reducing the dynamics of the evaporation-precipitation balance in the Atlantic basin to a linear relationship is more questionable. Therefore, the greatest limitation within the AGTCCM lies in the parameterization of  $F_{P-E}$ . Although there is genuine scientific interest in studying and emulating the impact of a precipitation-evaporation balance anomaly on AMOC intensity with the simplest possible dynamics, this is a highly complex endeavor. As described in the section outlining the parameterization of  $F_{P-E}$ , the literature itself is sparse on understanding the projections of the  $P - E$  balance over the Atlantic as it relates to warming. We have not found access to precise data that would allow us to easily reduce the dynamics of the  $P - E$  balance to our linear temperature-dependent relationship. The data we have found allowed us to provide a likely range in the calibration of this parameterization, but it must be acknowledged that it remains inadequate. To more finely calibrate this relationship, further research and experimentation on the specific projections of the  $P - E$  anomaly are necessary. A solution that would undoubtedly allow for calibration based on more data would be to develop a small hydrological module of the water cycle in SURFER and calibrate it based on experiments conducted by more process-based models. Indeed, studies already exist in this methodological fra-

mework. Nevertheless, in order to address the scientific questions and within the allocated time for work, this path of developing a small hydrological model in SURFER was not chosen.

Beyond calibrating the parameterization of  $F_{P-E}$ , we must question the quality of our calibration of the coupling between this forcing and the intensity of the AMOC. To account for the global effect of the  $P - E$  balance across the entire Atlantic basin, it would be beneficial to conduct a hosing experiment throughout the Atlantic basin and thereby calibrate the coupling coefficient  $f$  based solely on this experiment. Indeed, by calibrating in our case on a hosing experiment between  $20^\circ N$  and  $50^\circ N$  across the entire width of the Atlantic, we do not capture the full effect of hosing on the entire Atlantic basin from a  $P - E$  anomaly. Moreover, it is necessary to emphasize that our hosing experiment, EXPC, does not directly capture the contribution of  $P - E$  (precipitation-evaporation). It involves an idealized hosing forcing, which technically represents a freshwater flux but is in fact not realistic. We merely apply a freshwater flux to a different region of the Atlantic in an attempt to collapse the circulation, thereby trying to replicate the idealized consequences that a variation in the  $P - E$  balance would entail.

Despite these inherent limitations in the parameterization of  $F_{P-E}$ , it seemed appropriate to nonetheless document and implement a preliminary version of this parameterization, albeit unsatisfactory in many respects. Indeed, it has the merit of allowing us to test our generalized methodology with three forcing variables and to understand the complex dynamics that can occur in the response of the AMOC to an increase in temperature. As shown in the following chapters presenting the results in SURFER v3.2 of this parameterization, the numerical values of this forcing term should be taken with caution. Instead of providing plausible quantitative values, this parameterization illustrates distinct and relevant qualitative regimes for analysis. Finally, to avoid compromising all simulations by this less well-determined forcing term, it is possible to simply deactivate this freshwater flux in SURFER v3.2 and revert to the **Param A** of the AMOC, which we will indeed do in Chapter III.

### 3.5.4 Limitations of the Calibration Module and the best trade-off

Three sources of errors have been identified that limit the calibration capacity of our simplified double-fold dynamics on the hysteresees of process-based models. Each will be presented, and the choices made to address them as effectively as possible will be discussed.

#### The overdetermination of the coefficient $c_1$

The first source of error stems from the values of the independent terms  $c_1$ , which must be shared across each sensitivity experiment. As observed, there is an over-determination of coefficients per sensitivity experiment available. The

direct effect of these over-determinations is that if we choose a specific value of  $c_1$  precisely from one sensitivity experiment, we can then calibrate precisely to the bifurcation points associated with that sensitivity experiment but not to others.

Faced with the challenge of having as many different values of  $c_1$  as there are available hysteresis experiments, several approaches have been considered. Given that we have more constraints than unknowns, it is not possible to analytically solve this system for  $c_1$ . Thus, it is necessary to resort to optimization mechanisms for the value of  $c_1$ . The first approach considered was to optimize the value of  $c_1$  using the least squares method. Specifically, we could define a *distance* or *cost* function, denoted by  $J$ , which we seek to minimize. Mathematically, we are looking for  $J$  such that  $J = \underline{A}\underline{x} - \underline{b}$ , for which we aim to solve by least squares to find the optimal solution  $\underline{x}^*$  such that<sup>17</sup>,

$$\|\underline{A}\underline{x}^* - \underline{b}\|^2 = \min_{MSE}(\|\underline{A}\underline{x}^* - \underline{b}\|^2) \quad (3.141)$$

The technical challenge afterward is to find the form of the matrix  $A$  that encodes the function with respect to which we seek to minimize the quantity  $J$ . An intuitive choice can be made by starting from equations (3.75,3.76,3.77), which can be rewritten as follows :

$$c_1^A = c_1^{A*} - e_{12}F_{GIS}^A - fF_O^A, \quad (3.142)$$

$$c_1^B = c_1^{B*} - d_1T^B - fF_O^B, \quad (3.143)$$

$$c_1^C = c_1^{C*} - d_1T^C - e_{12}F_{GIS}^C, \quad (3.144)$$

by using the definitions of the terms  $c_1^A$ ,  $c_1^B$ , and  $c_1^C$  from equations (3.126,3.127,3.128) and a new notation convention,

$$c_1^{A*} = \frac{T_\Psi^+ \Psi^{-2} (\Psi^- - 3\Psi^+) - T_\Psi^- \Psi^{+2} (\Psi^+ - 3\Psi^-)}{2(T_\Psi^- - T_\Psi^+)}, \quad (3.145)$$

$$c_1^{B*} = \frac{F_{GIS}^+ \Psi^{-2} (\Psi^- - 3\Psi^+) - F_{GIS}^- \Psi^{+2} (\Psi^+ - 3\Psi^-)}{2(F_{GIS}^- - F_{GIS}^+)}, \quad (3.146)$$

$$c_1^{C*} = \frac{F_O^+ \Psi^{-2} (\Psi^- - 3\Psi^+) - F_O^- \Psi^{+2} (\Psi^+ - 3\Psi^-)}{2(F_O^- - F_O^+)}. \quad (3.147)$$

The goal then becomes to seek to express a function  $J$  such that the different expressions of  $c_1^A$ ,  $c_1^B$ ,  $c_1^C$  are as close as possible. Here, the coefficients, which become variables with respect to which we will perform optimization, are  $e_{12}$ ,  $f$ ,  $d_1$ ,  $F_{GIS}^A$ ,  $F_O^A$ ,  $T^B$ ,  $F_O^B$ ,  $T^C$ , and  $F_{GIS}^C$ . We then understand a problem, and not the least, that this method would raise. By wanting to optimize the value of  $c_1$ , we would have to modify the values of  $e_{12}$ ,  $f$ , and  $d_1$ , which would negate the interest of their previous calibration performed using the hystereses. In reality,

---

17. In the following, I abandon explicit vector and matrix notations.

we would only be shifting the problem by finding intermediate values for these coefficients, which would also produce simplified hysteresis loops that are not exactly calibrated. To remedy this, we could decide not to adjust the coefficients  $e_{12}$ ,  $f$ , and  $d_1$  as adjustment variables in the optimization of  $c_1$ , but rather the constant forcings of the sensitivity experiments. In this case, the price to pay for this optimization would be that we have a reduced range of experiments that we can produce to calibrate our hystereses. However, in the vast majority of cases, and except for exceptional cases in independent sensitivity experiments, we will seek to observe the effect of a single forcing by generally considering the others as being null. An intuitive way to define the function  $J$  would then be as follows<sup>18</sup> :

$$J = \sqrt{((c_1^{A*} - e_{12}F_{GIS}^A - fF_O^A) - (c_1^B - d_1T^B - fF_O^B))^2} + \sqrt{((c_1^B - d_1T^B - fF_O^B) - (c_1^C - d_1T^C - e_{12}F_{GIS}^C))^2} \quad (3.148)$$

where we seek to minimize the distances between the values of  $c_1^A$ ,  $c_1^B$ , and  $c_1^C$ . To solve this minimization problem of the function  $J$ , numerical libraries such as SciPy or algorithms like the *Trust-Region Constrained Algorithm* or the *Sequential Least Squares Programming Algorithm* (SLSQP) can be used. However, due to the time constraints of this thesis and the fact that the priority was first to produce a coherent integration of the AGTCCM into SURFER that already provides relevant results, we did not further develop this approach. However, further work could be pursued from this point onwards.

Another method that could be considered to optimize the value of  $c_1$  would be to always use the least squares method, but this time directly between the points of the simplified hysteresis and those of the process-based model. We would then define a *cost* function,

$$J = \sum_{i=1}^N (y_i - f(x_i, \underline{\theta}))^2 \quad (3.149)$$

where  $y_i$  represents the set of discretized points of the process-based hysteresis over an interval of size  $N$ , and  $f(x_i, \underline{\theta})$  represents the corresponding  $N$  points on the hysteresis of the simplified model given by the function  $f$  of the considered model, where  $\underline{\theta}$  represents the configuration of the values of the calibration and coupling coefficients. This approach, although practicable, was not pursued because it is in complete contradiction with our research paradigm, namely, through an identification of the critical coordinates of the bifurcation points based on the method of Martinez Monteiro et al., to provide a reductionist methodology that captures dynamics at the first order while maintaining a

---

18. Please note that the expression of  $J$  proposed contains all terms under the same square root. The fact that the display here is on two different roots stems from LaTeX's inability to break the line while preserving the root.

physical understanding of calibration mechanisms. Furthermore, as stated earlier, seeking to minimize the distance between the simplified and process-based hysteresis, although necessary to make our model valid, is not the ultimate goal in itself given the uncertainties present in models and literature on the exact locations of bifurcations.

Finally, one could consider much simpler methods to find intermediate values of the coefficients  $c_1$ . For example, we conducted tests by simply taking the average value of  $c_1$  from the three sensitivity experiments, in other words :

$$c_1 = \frac{c_1^A + c_1^B + c_1^C}{3}. \quad (3.150)$$

However, the results are not satisfactory because then we only achieve three "moderately correct" calibrations instead of having one "very good" and two "average" ones. As described earlier, it is preferable to obtain the best possible calibration for the temperature forcing, which remains the dominant term for both the GIS and the AMOC.

This challenge of overdetermination of the coefficient  $c_1$  is the major obstacle to this calibration methodology. As shown in the preceding subsection, making the AMOC-GIS model more complex to achieve a physically faithful representation of reality is not inherently difficult. However, the price to pay will directly manifest in this overdetermination of the coefficient  $c_1$ . Indeed, it is important to remember that making additional forcings explicit, beyond the necessity of additional sensitivity experiments, will also increase the overdetermination of the coefficients  $c_1$ . In fact, as described in Table (4), each time we add a forcing variable, we add two equations and one unknown, thus introducing an additional overdetermination of the coefficient and independent term  $c_1$ . The consequences of these determinations have been demonstrated in the results of the validation test and also in the calibration on cGenie, where we find the calibration becoming progressively less accurate for forcings taken separately. Furthermore, this creates an inability of the double-fold approach to effectively pass through the critical coordinates of the bifurcation points selected for all sensitivity experiments other than those of temperature, if we adhere to the paradigm that  $c_1 \equiv c_1^A$ . Any addition of forcing terms in this methodology presented in this chapter must therefore be judged between the importance of obtaining an additional explicit forcing and that of reducing the precision of the calibration on the forcings.

### **Calibration on the pre-industrial value**

The second major source of error lies in the calibration to the pre-industrial value or, more generally, in the case of zero forcing. As described in the subsection on calibration using cGenie's EXPB, it was not possible to generalize the Martinez Monteiro method directly and effectively. Furthermore, if such a method were to be found, it would entail restricting the range of sensitivity experiments that could be conducted by adding constraints, once again, on the

constant forcings in sensitivity experiments. Faced with the failure of this initial attempt to generalize the Martinez Monteiro method, another approach would be to add an additional term in the equations (3.2,3.3) of the model to calibrate using this value in the case of zero forcing. However, this approach would come at the cost of significantly complicating the calibration methodology of other coefficients and would therefore only further complicate the problem. A third approach that was considered would have been to perform a global scaling of the simplified double fold. However, this is not feasible in practice as it would distort other parts of the simplified hysteresis, resulting in a final outcome worse than before any operation.

For pragmatic and operational purposes, it was therefore decided to artificially adjust the double fold to obtain a reasonable value of  $\Psi$  for zero forcing ( $\Psi = 0.93$ ) by exploiting the uncertainty surrounding the coordinates of critical bifurcation points. To compensate for this difference between the initial state of the AMOC in the ideal case ( $\Psi = 1$ ) and the one actually considered in the model ( $\Psi = 0.93$ ), we numerically initialize the AMOC in our simulations with SURFER v3.2 at  $\Psi(t = 0) = 0.93$  to avoid creating a discontinuity. The numerical implementation will therefore take into account this particularity in the impacts of the AMOC on SURFER's carbon cycle, which will be discussed in the following section to maintain coherence.

### The $\Psi \equiv \Psi^A$ hypothesis

Finally, the third limitation and a source of error in the AGTCCM is the following assumption :

$$\Psi^+ \equiv \Psi_A^+ = \Psi_B^+ = \Psi_C^+ \quad \text{and} \quad \Psi^- \equiv \Psi_A^- = \Psi_B^- = \Psi_C^-. \quad (3.151)$$

As explained in the previous section, in practice, we are forced to operate under this assumption because differentiating the various values of  $\Psi^\pm$  per sensitivity experiment would render our calibration methodology impossible by introducing too many variables. Faced with the necessity of accepting it to stay within our research paradigm, we must again consider the best way to distribute the error it produces.

A first option would be to take an average value for  $\Psi^\pm$  or apply a different relative weighting between the three sensitivity experiments. Simulations were conducted, but the results are inconclusive. Once again, we find ourselves in the discussion of where our priority lies in calibration. As motivated several times already, the most important first-order dynamics in the collapse of the AMOC and the GIS is that of the temperature forcing. Thus, regarding this third error, we prefer to also minimize the discrepancies in EXPA. Hence, our choice is to set,

$$\Psi^+ \equiv \Psi_A^+ \quad \text{and} \quad \Psi^- \equiv \Psi_A^-. \quad (3.152)$$

A third option to address this issue was to fix only  $\Psi^+ \equiv \Psi_A^+$  and allow more flexibility in defining  $\Psi^-$ . For example, one could take an average value from

the three sensitivity experiments for this variable. This could be motivated by the fact that the most important bifurcation point is the one denoted by a +, the one that transitions from the nominal state to the collapsed state. Thus, one might be more willing to accept that calibration at the lower bifurcation point, even for the temperature forcing, is less precise. However, tests conducted did not show significant improvement when considering this intermediate solution. This is because the values of  $\Psi^-$  in the three experiments are, unlike the values of  $\Psi^+$ , very close to each other, so the impact is barely visible.

### Other Development Avenues

To conclude this section, we would like to comment on other calibration algorithm philosophies that could be developed, as well as suggestions for analysis and presentation of results.

Looking at the bi-dimensional forcing space, which corresponds to the plane  $\Psi = 0$  in Figures (5657), it could be interesting to represent in this plane the experiments that, for a given constant forcing pair  $(T^*, F_{GIS}^*, F_O^*)$ , result in an AMOC that has collapsed or not at equilibrium. This would involve projecting onto the  $\Psi = 0$  plane the system's state  $\Psi$  for specific values of the forcings. Based on the simplified hysteresis curves that have been calibrated, we understand that these projections would form a cloud of points in the  $\Psi = 0$  plane, which could be divided into two domains : one for combinations of forcing variables that result in a collapsed AMOC at equilibrium, and another for combinations that result in a sustained AMOC. Without loss of generality, we denote by  $W_c : (T, F_{GIS}, F_O) \rightarrow \mathbb{R}^3$  the critical variety in the  $\Psi = 0$  plane that separates these two regions. Indeed, we can understand the simplified dynamical system used in the AGTCCM by writing it as follows,

$$\frac{dx}{dt} = -x^3 + ax^2 + bx + c + W \quad (3.153)$$

where  $x = V, \Psi$  depending on the model used,  $a, b$ , and  $c$  are the calibration coefficients encoding the internal dynamics of the system, and  $W$  is the set of forcings related to the chosen parameterization and model. For example, in the case of the AMOC and **Param A**, we have that,

$$W = d_1 T + e_{12} F_{GIS}. \quad (3.154)$$

From a strictly mathematical point of view, the dynamical system we simulate is sensitive to its potential bifurcation only at the critical value of the linear combination of the forcing terms. Mathematically, the forcings will be only a constant term in equation (3.153) that can imply a sufficiently critical shift in phase space to change the nature and number of equilibria. This has already been described in section (3.3.2).

A schematic illustration of this variety is presented in Figure (58) for the forcing pair  $(T, F_{GIS})$  in the plane  $\Psi = 0$ . In essence, what we have accomplished with

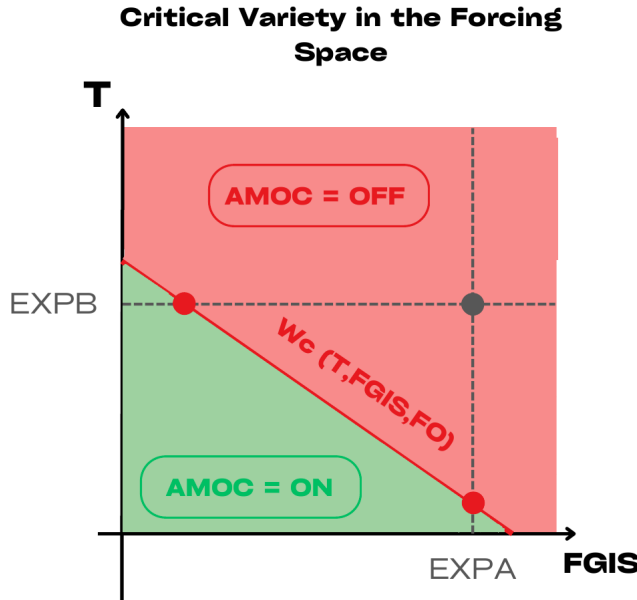


FIGURE 58 – *The Critical Variety  $W_c$  in the forcing space  $(T, F_{GIS})$  delineates the region where the AMOC collapses at equilibrium from the region where it maintains deep convection. The specific cases of EXPB and EXPA are also depicted.*

EXPA and EXPB is to obtain two points (represented by the red dots in Fig. (58)) and, as a representation of the critical variety  $W_c$ , draw a line between these points due to the form of the AGTCCM model. However, each calibration performed with different models will delineate a unique critical variety  $W_c$  by yielding new calibration points, which can be regarded as the "identity card" indicating the location of the unstable variety for the specific AMOC model. Comparing these critical varieties  $W_c$  also offers a method for comparing the inherent sensitivities of each model to AMOC collapses.

Furthermore, once the AGTCCM model has been calibrated against a process-based AMOC model (and ideally a process-based GIS model), we could then leverage the low computational cost of simulations in SURFER v3.2, as outlined in the following chapter, to generate a cloud of points in the  $(T, F_{GIS})$  plane depicted in Figure (58). This demonstrates the usefulness of the AGTCCM as an exploratory tool for parameter configurations, highlighting regions where tipping may occur following the emulator. Consequently, it could function as a pre-diagnostic tool prior to embarking on more resource-intensive simulations using process-based models, especially when approaching the boundary delineated by the variety  $W_c$ . If successful, significant time savings in terms of computation and experimental design could be realized.

A final interesting avenue for using this representation in forcing space would be to plot the trajectories of  $\Psi(t)$ . This would notably highlight phenomena such as *overshoot without tipping*, where we might observe temporal evolutions of the AMOC that briefly enter the tipping region but do not remain there

long enough to fully tip the system to equilibrium by the end of the simulation. Extending this reasoning to the  $(\Psi, T, F_{GIS})$  space, as depicted in Figure (59), reveals that the critical variety  $W_c$ , which appeared as a line in Figure (58), is actually nothing more than the projection of the plane passing through the tipping point position for each pair of forcing parameters. Once again, it could be insightful, for the purpose of illustrating the phenomenon of *overshoot without tipping*, to represent trajectories in this space, denoted as  $(\Psi(t), T(t), F_{GIS}(t))$ . This would allow for observing overshoot phenomena not only in the bifurcation diagrams but also in the  $(F_{GIS}, T)$  plane, indicating a time spent by the system in the tipping region at equilibrium.

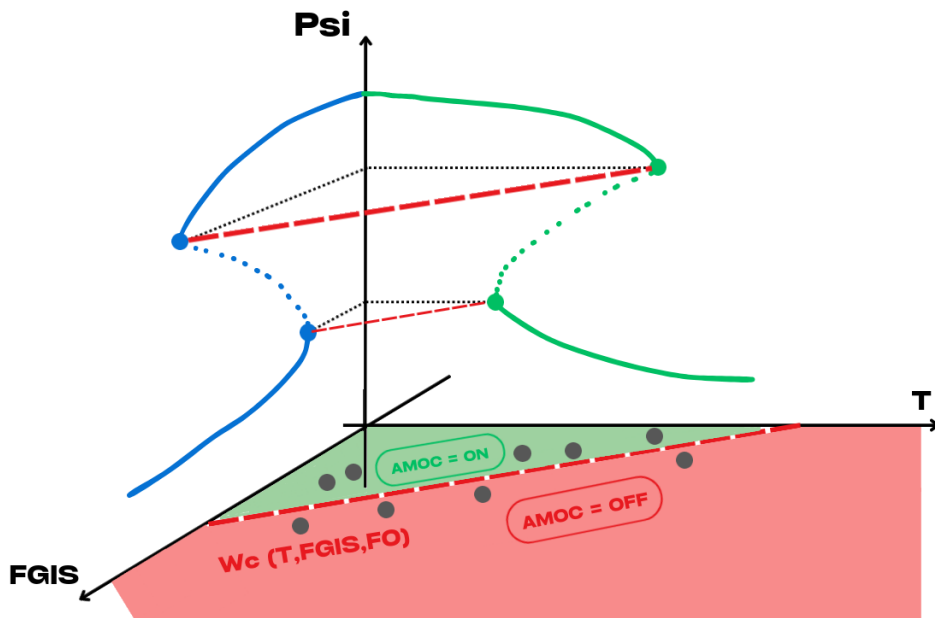


FIGURE 59 – The Critical Variety  $W_c$  in the forcing space  $(\Psi, T, F_{GIS})$  with the two calibrated hystereses depicted in the  $(F_{GIS}, \Psi)$  and  $(T, \Psi)$  planes. Experiments with other combinations of forcings are shown by the gray points.

Finally, these graphical representations also enable us to explore other avenues of algorithmic calibration methods that could be developed and subsequently compared to those described in this chapter. For instance, one could devise an algorithm known as an "incremental method" which would operate as follows :

- Random values are sampled for the forcings, which are then held constant, and an experiment is conducted with SURFER v3.2 under this configuration.
- It is determined whether the AMOC has tipped into equilibrium or not.
- If the AMOC has tipped, one of the two forcings is decreased by an amount  $\delta$  while the other is held constant.
- If the AMOC does not tip into equilibrium, the value of the free forcing term is increased by an amount  $\delta$  while the other forcing is kept constant.
- A specified number  $N$  of random draws and simulations of this nature are executed.
- A method to find the optimal

bisector separating these two regions is conducted on the scatter plot depicted in Figure (58), which would allow for determining the analytical equation of variety  $W_c$ . To refine the determination of this variety, once it is observed that we are in the vicinity of  $W_c$ , experiments are no longer randomly sampled for the initial values of the forcings. Instead, starting intentionally close to what appears to be this variety, the increment step is systematically reduced by a constant factor to enhance the resolution of the critical variety.

## Conclusion

In conclusion, we have presented the AGTCCM, an innovative and original method for emulating dynamic systems such as the AMOC and GIS through a first-order dynamics described by a double fold based on process-based models. Although inherent limitations of the reductionist research paradigm used in this work are present, calibration on cGenie hystereses demonstrates the utility and validity of such an approach. The enormous advantage of producing an efficient emulator of the AMOC with simplified dynamics becomes apparent because, through low-cost simulations made possible after calibration, a valuable pre-diagnostic tool is created for further in-depth research with the process-based model that has been emulated. Moreover, clear avenues for development are identified, allowing continued research on this useful path in studying tipping element collapse dynamics. Here, we focused on the study of the AMOC and GIS due to their relevance in the near-future climate regarding tipping points and potential cascading collapses. However, this mathematical and numerical framework can certainly be adapted to other tipping elements. We will now conclude this chapter by describing how the coupling of the AGTCCM was achieved with the latest version of SURFER to produce a new operational version of SURFER useful for more precisely studying the risks of cascading collapse between the AMOC and GIS.

## 3.6 SURFER v3.2, coupling AGTCCM with SURFER v3.1

In this concluding section of the technical chapter delineating the development of the AGTCCM, we will proceed with the ultimate phase of constructing a model capable of simulating the cascading collapses of the AMOC-GIS system for climate projection purposes. We aim to incorporate our simplified model of collapse dynamics between the AMOC and the GIS into a climate model, thereby addressing our fifth scientific subsection. Specifically, we will integrate the AGTCCM into SURFER v3.1. This new version, named SURFER v3.2 according to the convention described in Table (1), is located in the *Jupyter Notebook* `SURFER_v4.0.ipynb` within a specific folder in the GitHub repository of the thesis already presented.

How to consistently integrate the AGTCCM into SURFER v3.1? Given the scientific aim of ultimately comparing the results of our new version of SURFER, which incorporates the AGTCCM, with the previous version that does not, we

have integrated the AGTCCM into the numerical model SURFER\_v4.0.ipynb in a modular manner. Specifically, we have retained the entire structure of SURFER v3.1 while clearly organizing the code and providing comments, allowing us to decide, in specific sections called 'Setting-Up', by means of boolean variables, whether to activate the AGTCCM in the simulations or not.

In the case where we activate the AGTCCM in SURFER v3.2, we maintain the double fold dynamics already present in SURFER v3.1, except for the AMOC and GIS. Indeed, for these two tipping elements, we will obviously retrieve the dynamics defined by equations (3.2,3.3). Furthermore, we calibrate the coefficients of the AMOC and GIS using the calibration module described in **Tipping Module Calibration ParamB.ipynb**, which has been added to the SURFER code in **SURFER\_v4.0.ipynb**. An additional boolean option, controlled by a variable called `cGenie_calib`, allows us to decide whether to use critical data from bifurcation points obtained from cGenie hysteresis, as presented, or to use other values, for instance, from future additional data from other models that we might want to emulate.

An important technical detail for understanding the code of SURFER v3.2 is that, for ease of implementation and analysis, we have redefined the state vector by changing the position of the GIS and AMOC, placing the GIS as the first tipping element and the AMOC as the second. Furthermore, to facilitate analysis, we have added the time integration of freshwater fluxes, denoted respectively with lowercase letters  $f_{GIS}$ ,  $f_W$ ,  $f_{P-E}$  and  $f_O$ , to the state vector. Thus, the state vector, which contains the quantities to be integrated with their respective dynamics in SURFER v3.2, is as follows :

$$\begin{aligned} y = [ & M_A, M_L, M_U, M_I, M_D, Q_U, Q_I, Q_D, M_S, T_U, T_I, T_D, M_{CH_4}, M_L, V_{gl}, \\ & GIS, AMOC, WAIS, EASB, EAIS, AWSI, AMAZ, PERM, \\ & f_{GIS}, f_W, f_{P-E}, f_O ] \quad (3.155) \end{aligned}$$

For further information on the meaning of the various variables, other than those related to tipping elements and freshwater quantities, the reader may refer to the paper by Couplet et al. [17].

Lastly, as seen in section (3.2.2), coupling effects between tipping elements are already accounted for in version 3 of SURFER. However, the values taken for these couplings between AMOC and GIS, in both directions, were partly set arbitrarily. In SURFER v3.2, we adopt the idea of having a matrix that encodes coupling effects between tipping elements, except now we explicitly incorporate into the dynamic equations of AMOC and GIS their respective coupling through the terms  $e_{12}F_{GIS}$  et  $e_{21}(1 - \Psi)$ . With the AGTCCM, the coupling coefficients  $e_{12}$  and  $e_{21}$  will be calibrated via cGenie hysteresis. To avoid double counting, we set the entries AMOC→GIS and GIS→AMOC to zero in the matrix  $S_{moy}$  that was showed in Table (3).

### 3.6.1 Modification of the carbon cycle model of SURFER

The greatest task and challenge in integrating the AGTCCM into SURFER v3.2 is to enable a consistent modeling of the AMOC and its impact on SURFER's carbon cycle. As emphasized in the literature review in Chapter I, an AMOC collapse will have significant effects on ocean ventilation and hence on the Atlantic Ocean's capacity to absorb  $CO_2$  from the atmosphere. Moreover, by nearly halting vertical advection at the NADW site and in upwelling areas in the South Atlantic, the entire carbon transport engine from the upper ocean to the lower ocean in the North Atlantic and from the lower ocean to the upper ocean in the South Atlantic is halted. Phenomenologically, one expects an AMOC collapse, and hence increased stratification of the Atlantic Ocean, to create a carbon bottleneck in the ocean surface layer since carbon transport between the surface and bottom layers will be greatly reduced.

The challenge is thus to implement a dynamic modeling of these carbon transports within the ocean layers of SURFER v3.1 that takes into account the state of the AMOC at each simulation time step. Clearly, SURFER v3.1 is merely a three-layer ocean model with no representation of ocean currents, let alone an explicit representation of the AMOC. The only way material transport between vertical layers is considered is through carbon and sediment exchanges. Our goal will therefore be to significantly change the parameterizations of these carbon transports to make them dependent on the state of the AMOC. What we aim to achieve is an equilibrium scenario, wherein an AMOC collapse leads to a rise in atmospheric  $CO_2$  concentration, denoted as  $M_A$ , by 20 ppm. As demonstrated by Stocker et al.[70] and Zickfeld et al.[89], this is a typically expected value in response to an AMOC shutdown.

### The Experiment of an AMOC Shutdown in SURFER

Before conceptualizing a dynamic parameterization of carbon transport coefficients between layers in SURFER, we conducted an initial series of experiments aimed at identifying the responses of carbon reservoirs to a modification of these coefficients  $k$ , which were introduced in Section (3.2.1). The objective is to arbitrarily change the values of the coefficients  $k$  to roughly emulate an AMOC shutdown initially and then identify whether we can quantitatively reproduce the desired effect on the respective increases and decreases of different carbon reservoirs. We carried out this initial sensitivity experiment of SURFER to carbon transport coefficients with version v2.0 because v3.0 was not already accessible at that time. In this case, there are only two ocean layers, and thus, we can only adjust the parameters of carbon flux intensities between the upper and lower ocean layers, denoted as  $k_{UD}$  and  $k_{DU}$  respectively. We also conduct sensitivity tests on the coefficient  $k_{AU}$ , which represents the intensity of carbon exchanges between the atmosphere and the surface ocean.

The experimental protocol was as follows. A control simulation, denoted  $CTL$ , based on an SSP scenario is run from year 1750 to 4000 AD. At an arbitrary

time, in our case,  $t_c = 2050 \text{ AD}$ , the state of the control simulation is retrieved to initiate a new sensitivity simulation, denoted *EXP*, in which the values of the coefficients  $k_{ij}$  with  $i, j = U, D, A$  are significantly modified.

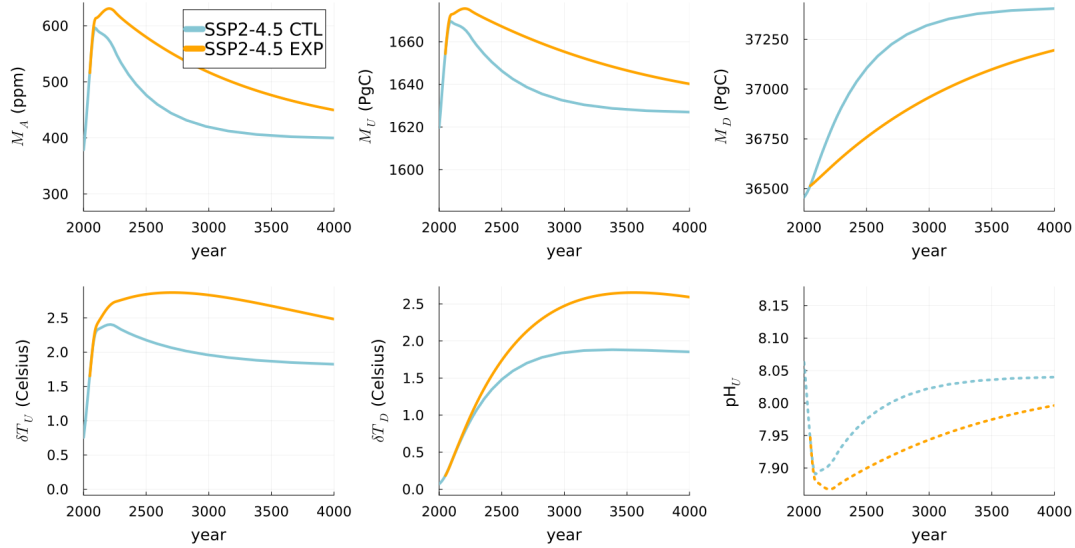


FIGURE 60 – *Sensitivity experiment of  $k_{UD}$  in SURFER v2.0. From top left to bottom right are respectively represented : (i) Atmospheric  $CO_2$  concentration  $M_A$ , (ii) Amount of carbon in the surface ocean  $M_U$ , (iii) Amount of carbon in the deep ocean  $M_D$ , (iv) Surface ocean temperature anomaly  $\delta T_U$  (also representing the atmosphere in SURFER), (v) Deep ocean temperature anomaly  $\delta T_D$ , (vi) Surface ocean pH. The chosen baseline scenario is SSP2-4.5, to which in the sensitivity experiment, denoted as *EXP*, we reduced the value of  $k_{UD}$  by 30% compared to its value in the control run denoted as *CTL* i.e.  $k_{UD}^{EXP} = 0.7k_{UD}^{CTL}$*

We expect that in the case of a collapsed AMOC, we would have a value of the transport coefficients  $k_{UD}^{EXP} < k_{UD}^{CTL}$ ,  $k_{DU}^{EXP} < k_{DU}^{CTL}$ . Indeed, due to the increased stratification, both upward and downward transport within the ocean are expected to decrease. However, the effect is different for the carbon transport coefficient between the atmosphere and the surface ocean  $k_{AU}$ . In fact, since the dynamics of carbon transfer between the atmosphere and the surface ocean occur proportionally to the differences in partial pressure (cfr Martinez Monteiro et al.[52]), the timescales associated with these equilibrations between the atmosphere and the ocean are very short compared to those between the ocean layers. Indeed, around 6 months, equilibrium is achieved.[27] Simulations, not shown here, confirm this assertion, namely that a modification of the coefficient  $k_{AU}$  is not significantly visible in the variations of carbon contents in the different reservoirs due to the very rapid equilibration between the atmosphere and the surface ocean. Moreover, even though during an AMOC shutdown, the physics of carbon exchanges between the atmosphere and the ocean itself do not change, what induces an increase in atmospheric  $CO_2$  concentration is the carbon bottleneck that forms in the ocean and the loss of ventilation of the carbon contained in the surface ocean. Therefore, there is actually no reason to

modify the coefficient  $k_{AU}$  in our emulation of an AMOC shutdown.

Figure (60) presents the results of this sensitivity experiment to carbon flux coefficients. Arbitrarily, the value of  $k_{UD}$  in the sensitivity experiment, denoted  $k_{UD}^*$ , was reduced by 30% of its nominal value in the control run. We observe the expected effects, namely an increase in atmospheric  $CO_2$  concentration  $M_A$ , an increase in the amount of carbon stored in the upper ocean layer  $M_U$ , and a decrease in that of the deep ocean  $M_D$  due to less transport between the two ocean layers. This increase in  $CO_2$  in the atmosphere naturally leads to a temperature increase, which then distributes evenly within the ocean layers. These results confirm that emulation of the impacts of an AMOC shutdown on the carbon cycle can be achieved through parameterization of carbon transport coefficients between oceanic layers.

### Parameterization of an AMOC Shutdown on the Carbon Cycle in SURFER v3.2

Now we will construct and test a dynamic parameterization, thus dependent on the state of the AMOC, of the variations in carbon transport coefficients between ocean layers in SURFER v3.2. We aim to reproduce the suggested increase of 20 *ppm* in atmospheric  $CO_2$  concentration as suggested by the literature.[70, 89]

To do this, it is important to understand how the carbon cycle is modeled in previous versions of SURFER. In version v2.0 by Martinez Monteiro et al., the transport coefficients between different carbon reservoirs are fixed and constant. They are calibrated based on the values of carbon reservoirs at the pre-industrial time. The exchange of carbon between the two layers of the ocean (in version v2.0) depends on the total amount of inorganic carbon dissolved in each layer.

$$F_{UD}(t) = k_{UD}M_U(t) - k_{DU}M_D(t). \quad (3.156)$$

As described in Martinez Monteiro et al.[52], it is considered that the different carbon reservoirs were in equilibrium during the pre-industrial period, and thus,

$$F_{UD}(t = t_{PI}) = 0 = k_{UD}M_U(t_{PI}) - k_{DU}M_D(t_{PI}). \quad (3.157)$$

From this last equation, we have a simple relationship between the two coefficients,

$$k_{DU} = k_{UD} \frac{M_U(t_{PI})}{M_D(t_{PI})}. \quad (3.158)$$

We can substitute this last equality into equation (3.156), yielding,

$$F_{UD}(t) = k_{UD} \left( M_U(t) - \frac{M_U(t_{PI})}{M_D(t_{PI})} M_D(t) \right). \quad (3.159)$$

In SURFER v3.1, the modeling of carbon flux, this time between the upper layer  $U$  and the intermediate layer  $I$ , denoted as  $F_{U \rightarrow I}(t)$ , is expressed as follows,

$$F_{U \rightarrow I}(t) = \underbrace{k_{UI}^* \left[ M_U(t) - \frac{M_U^*}{M_I^*} M_I(t) \right]}_{\equiv F_{UI}} + sed(F_{CaCO_3}^* + F_{CaSiO_3}^*) \frac{M_I(t)}{M_I^*} \quad (3.160)$$

with  $k_{UI} = k_{UI}(t = t_{PI}) \equiv k_{UI}^*$  and  $k_{IU} = k_{IU}(t = t_{PI}) \equiv k_{IU}^*$ . To simplify notation, we also denote  $M_U^* \equiv M_U(t = t_{PI})$  and  $M_D^* \equiv M_D(t = t_{PI})$ . What we denote as  $F_{UI}$  is exactly the analogue in the 3-layer model of SURFER v3.0 to the term  $F_{UD}$  in SURFER v2.0, which we have re-derived to understand its origin in equation (3.159). The second term in equation (3.160) is a novelty in SURFER v3.0 that takes into account sediment burial (cfr Couplet et al.[17]). For the purpose of simplifying the model, we aim here to represent the impact on the carbon cycle of an AMOC shutdown, so we will not modify this term in our dynamic parameterization.

To develop our dynamic parameterization, we aim to stay within the paradigm of the carbon cycle model already present in previous versions of SURFER. Thus, we maintain and do not challenge the assumption that,

$$F_{UI}(t) = k_{UI}(t) M_U(t) - k_{IU}(t) M_I(t). \quad (3.161)$$

We have now added a time dependence for the carbon flux coefficients  $k_{UI}(t)$  and  $k_{IU}(t)$ , which we will characterize to encode the impact of the AMOC state on carbon fluxes. For the parameterization of the coefficients  $k_{UI}(t)$  and  $k_{IU}(t)$ , I choose a linear parameterization as a function of the AMOC state  $\Psi(t)$  in the following form,

$$k_{UI}(t) = k_{UI}^* + c_{UI} k_{UI}^* (1 - \Psi(t)), \quad (3.162)$$

$$k_{IU}(t) = k_{IU}^* + c_{IU} k_{IU}^* (1 - \Psi(t)). \quad (3.163)$$

Therefore, we consider that our transport coefficient will decrease from its initial equilibrium state of the pre-industrial period linearly with a weakening of the AMOC. Thus, we understand physically with this parameterization that when the AMOC is in its ON state at the pre-industrial equilibrium, i.e  $\Psi(t = t_{PI}) = 1$ , then the second term of equations (3.162) and (3.163) vanishes to retrieve the initial constant value. In the other extreme case where the AMOC has completely collapsed, i.e  $\Psi = 0$ , we then add to  $k_{UI}(t)$  a quantity  $c_{UI} k_{UI}^*$  to its initial state  $k_{UI}^*$ .

We know from Stocker et al.[70] that we can consider an AMOC shutdown to diminish the uptake flux of  $CO_2$  from the atmosphere to the surface ocean by approximately 30%. Therefore, we will decompose the parameterization coefficient  $c_{UI}$  as follows,

$$c_{UI} = c_{Sto} \chi. \quad (3.164)$$

The coefficient  $c_{Sto} = -0.3$  encodes the 30% decrease in ventilation as given by Stocker et al.[70], while the coefficient  $\chi$  will be our calibration parameter to achieve the expected increase in atmospheric  $CO_2$  concentration when the AMOC collapses.

Note that it is not physically necessary to introduce a time dependence in the coupling coefficients between the state of the AMOC and the carbon transport coefficients, in other words, we should not introduce  $c_{UI}(t)$  and  $c_{IU}(t)$ . Physically and phenomenologically, we consider that there is a linear dependence between the state of the AMOC and the carbon transport coefficient between layers, but that the coupling between the state of the AMOC and its impact on the transport coefficient itself is fixed. In terms of the level of physics we aim to capture while remaining within the paradigm of the simplest possible model, this is a coherent choice. Introducing this additional dependence would technically require more development and would further delay the question of where to stop the parameterization.

If we directly insert the parameterizations described in (3.162) and (3.163), we find that the equation for the flux  $F_{UI}$  (3.161) becomes,

$$F_{UI}(t) = (k_{UI}^* + c_{UI}k_{UI}^*(1 - \Psi(t))) M_U(t) - (k_{IU}^* + c_{IU}k_{IU}^*(1 - \Psi(t))) M_I \quad (3.165)$$

We now seek to express equation (3.165) by highlighting terms to bring it to the form (3.160) for a better understanding of the model. We revisit the analysis and development from SURFER v2.0 described in equations (3.156-3.159), except that here, since  $k_{UI}$  and  $k_{IU}$  are now dynamic variables, we will have only,

$$F_{UI}^* = 0 = k_{UI}^* M_U^* - k_{IU}^* M_I^* \quad (3.166)$$

At pre-industrial equilibrium, equation (3.166) gives us that,

$$k_{IU}^* = k_{UI}^* \frac{M_U^*}{M_I^*}. \quad (3.167)$$

If we substitute the result (3.167) into the parameterization (3.163) and insert the parameterizations (3.163) and (3.162) into equation (3.161), after some algebra we obtain that the carbon flux from the upper ocean layer  $U$  to the intermediate layer  $I$  is given by,

$$F_{UI}(t) = k_{UI}^* \left[ M_U(t) - \frac{M_U^*}{M_I^*} M_I(t) \right] + k_{UI}^*(1 - \Psi(t)) [c_{UI} M_U(t) - c_{IU} M_I(t)]. \quad (3.168)$$

So far, we have assumed that  $c_{UI} \neq c_{IU}$ . However, it seems reasonable from a physical standpoint to consider that the slowdown induced on the carbon fluxes from the upper layer to the lower layer is identical to that from the lower layer to the upper layer. Considering the AMOC as a predominantly advective

circulation, it is correct to assume that over an initial range of slowdown, material exchanges will be slowed down uniformly in both vertical directions. When the AMOC is close to complete collapse, diffusive orders will become dominant, and in this case, the previous justification becomes incorrect. However, given the purpose of the parameterization here to provide a conceptual model allowing for a signature of non-linearities in the carbon cycle due to AMOC collapse rather than exact flux values, it does not seem unreasonable to make this assumption. Thus, with the assumption that  $c_{UI} = c_{IU}$ , equation (3.165) becomes,

$$F_{UI}(t) = k_{UI}^* \left[ M_U(t) - \frac{M_U^*}{M_I^*} M_I(t) \right] + k_{UI}^* c_{UI} (1 - \Psi(t)) [M_U(t) - M_I(t)] \quad (3.169)$$

Finally, we must consider whether this dynamic parameterization is mathematically and physically consistent. First, we have the coherence that if the coupling between the AMOC and the transport coefficients were non-existent, i.e., if  $c_{UI} = 0$ , we would indeed revert to equation (3.161). With the temporal dependence in the coefficients contained in the second term of the parameterization, nullifying it is equivalent to the base case with static coefficients. At pre-industrial equilibrium, we also have that for  $t = t_{PI}$ , the second term of equation (3.169) cancels out, and again, we revert to equation (3.160). Finally, this parameterization highlights the importance of the carbon content gradient between the layers because the second term, multiplied by the coupling coefficients with the AMOC, has the following physical significance. What matters in the flux is indeed the gradient, the difference in carbon content between the ocean reservoirs. The greater this difference, the greater the flux. The more significant the impact of the AMOC on the flux, the more this gradient will be modulated.

Following the same logic, we must also parameterize the carbon fluxes between the intermediate layer  $I$  and the deep layer  $D$  of the ocean. In SURFER v3.0, the equation for  $F_{I \rightarrow D}(t)$  is as follows,

$$F_{I \rightarrow D}(t) = \underbrace{k_{ID}^* \left[ M_I(t) - \frac{M_I^*}{M_D^*} M_D(t) \right]}_{\equiv F_{ID}} + sed(F_{CaCO_3}^* + F_{CaSiO_3}^*) \frac{M_D(t)}{M_D^*}. \quad (3.170)$$

It seems physically coherent to consider that if deep convection and upwelling are reduced due to a weaker AMOC, this will affect transfers between all ocean layers, not just between the upper and intermediate layers. Thus, it is also necessary to implement a parameterization that allows for the carbon flux between the intermediate (I) and deep (D) layers, denoted as  $F_{ID}(t)$ , to account for a potential slowdown of the AMOC. To do this, we will simply use the same parameterization methodology as for  $F_{UI}(t)$  to model this homogeneous slowdown effect. Therefore, analogous to the previous reasoning for  $F_{UI}(t)$ , we adopt the dynamic postulate from SURFER v3.0 for  $F_{ID}(t)$ .

$$F_{ID}(t) = k_{ID}(t)M_I(t) - k_{DI}(t)M_D(t) \quad (3.171)$$

For the parameterizations of  $k_{ID}(t)$  and  $k_{DI}(t)$ , we adopt a similar linear modeling approach.

$$k_{ID}(t) = k_{ID}^* + c_{ID}k_{ID}^*(1 - \Psi(t)), \quad (3.172)$$

$$k_{DI}(t) = k_{DI}^* + c_{DI}k_{DI}^*(1 - \Psi(t)). \quad (3.173)$$

Once again, we choose that,

$$c_{ID} = c_{Sto}\chi. \quad (3.174)$$

Indeed, the physical rationale behind this choice is that if surface ventilation is reduced by 30%, we assume that the slowdown in vertical convection is the same throughout the water column. If this assumption later proves to be too simplistic, a modification of the coefficient  $c_{Sto}$  in the case of layers  $I$  and  $D$  would allow for its consideration.

If we directly insert the parameterizations described in (3.172) and (3.173), we obtain that the flux equation (3.171) becomes :

$$F_{ID}(t) = [k_{ID}^* + c_{ID}k_{ID}^*(1 - \Psi(t))] M_I(t) - [k_{DI}^* + c_{DI}k_{DI}^*(1 - \Psi(t))] M_D(t). \quad (3.175)$$

Again, we seek to make some rearrangements for better analysis. To do so, we utilize the fact that at pre-industrial equilibrium, equation (3.171) yields :

$$F_{ID}^* = 0 = k_{ID}^*M_I^* - k_{DI}^*M_D^*, \quad (3.176)$$

$$k_{DI}^* = k_{ID}^* \frac{M_I^*}{M_D^*}. \quad (3.177)$$

If we substitute the result (3.177) into the parameterization (3.173) and insert the parameterizations (3.173) and (3.172) into equation (3.171), we obtain, after a little algebra, that the carbon flux from the intermediate ocean layer  $I$  to the deep layer  $D$  is given by :

$$F_{ID}(t) = k_{ID}^* \left[ M_I(t) - \frac{M_I^*}{M_D^*} M_D(t) \right] + k_{ID}^*(1 - \Psi(t)) [c_{ID}M_I(t) - c_{DI}M_D(t)] \quad (3.178)$$

Once again, the physical intuition as well as the mathematical coherence are exactly the same as for  $F_{UI}(t)$  described earlier. In the next chapter presenting the results of SURFER v3.2, we will demonstrate that it is possible to find a precise value of  $\chi$  that enables us to achieve the intended outcomes of the AMOC collapse's impact on the carbon cycle.

Finally, to provide a comprehensive justification for our parameterization, we must consider whether it would have been necessary to distinguish between the different carbon fluxes within the ocean layers to achieve a more physically realistic representation of the impact of an AMOC slowdown. As we know, there are various physical mechanisms that vertically transport matter within the ocean. Among the downward fluxes are those associated with the *soft-tissue pump*, the *carbonate pump*, or the *solubility pump*, while an upward flux can be associated with diffusive *ocean mixing*. Therefore, the question arises as to whether we should distinguish the carbon flux from the surface to the ocean floor as follows :

$$F_{UD} = F_{\text{soft tissue}} + F_{\text{carbonate}} + F_{\text{residual}} \quad (3.179)$$

avec,

$$F_{\text{residual}} = F_{\text{ocean mixing}} + F_{\text{solubility}}. \quad (3.180)$$

Even though this approach might be more physically realistic, personal work by V. Couplet has shown that it was not necessary to push this parameterization to such an extent. In fact, the first-order dynamics of a linear decrease in vertical material transports as described by our parameterization (3.162, 3.163, 3.172, 3.173) already captures the expected effect.

### Parameterization Calibration : Results and Analysis

After presenting and justifying the parameterization choices made on the carbon cycle of SURFER to account for the impact of an AMOC collapse, we seek to calibrate this parameterization. Specifically, we aim to find the value of the coefficient  $\chi$  that reproduces, in the case of AMOC shutdown at equilibrium, an increase in atmospheric  $CO_2$  concentration of  $\approx 20 \text{ ppm}$ , as suggested in the literature from Zickfeld et al.[89, 70].

To do this, we employ the following experimental protocol. We utilize SURFER v3.2 with the carbon flux parameterizations dependent on the AMOC as presented above, and we conduct two simulations, each with a constant  $CO_2$  emission scenario.<sup>19</sup> In the first experiment, denoted as `carb_calib_amoc_on`, we artificially maintain the AMOC in its pre-industrial state, thus keeping it active. In the second sensitivity experiment, denoted as `carb_calib_amoc_off`, we artificially maintain the AMOC in a collapsed state by initializing it with  $\Psi(t = t_0) = 0$ . By doing so, we produce two distinct regimes for the values of the coefficients  $k_{ij}$ , where  $i, j = U, I, D$  as depicted in Figure (61).

Next, we compare the differences in atmospheric  $CO_2$  concentrations at equilibrium and repeat the experiment by adjusting the value of  $\chi$  until we obtain a value that allows us to reproduce the expected  $\approx 20 \text{ ppm}$  increase in

---

19. We arbitrarily chose to use historical emissions from 1750 to 2010 AD, followed by an emission scenario that results in a total of 2000;  $PgC$  emissions.

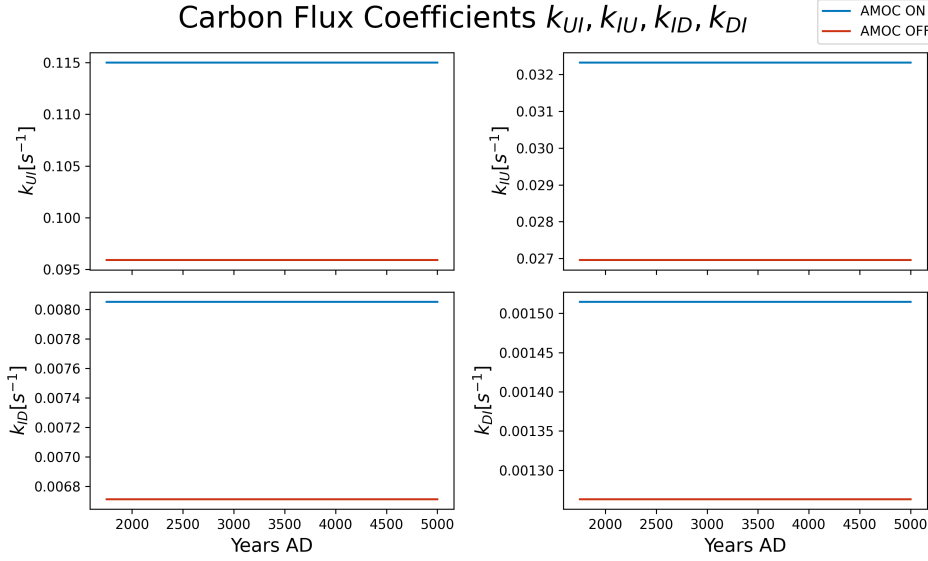


FIGURE 61 – Values of the coefficients  $k_{UI}$ ,  $k_{IU}$ ,  $k_{ID}$ ,  $k_{DI}$  controlling the carbon flux in the two sensitivity experiments for a value of  $\chi = 0,5535$ .

$CO_2$ . The points on Figure (63) correspond to the reference points against which we compare concentrations for calibration. This reference point is marked at the peak of concentrations before the ocean's uptake of atmospheric carbon becomes significant enough to decrease atmospheric  $CO_2$  concentration. Using this experimental protocol, we find that for a value of  $\chi = 0,5535$ , we obtain a  $CO_2$  concentration difference of  $\Delta CO_2 = 20,5 \text{ ppm}$ , precisely within the range suggested by the literature. Thus, considering the  $c_{Sto}$  factor as well, we realize that in our calibrated parameterization, an interruption of the thermohaline circulation implies a 17% homogeneous decrease in vertical carbon transports between the ocean layers of SURFER. Furthermore, the manner in which atmospheric concentration increases is consistent with the study by Zickfeld et al. [89] (cfr. Figure (62)), where they utilized a General Circulation Model (GCM) to investigate the impact of an AMOC shutdown on the carbon cycle.

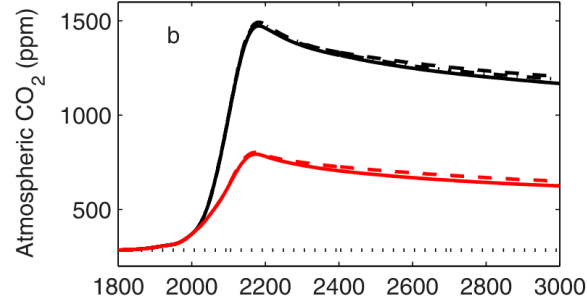


FIGURE 62 – Evolution of atmospheric  $CO_2$  concentrations for two different emission scenarios (red and black). The dashed lines represent simulations where the AMOC was halted. Figure from Zickfeld et al.[89]

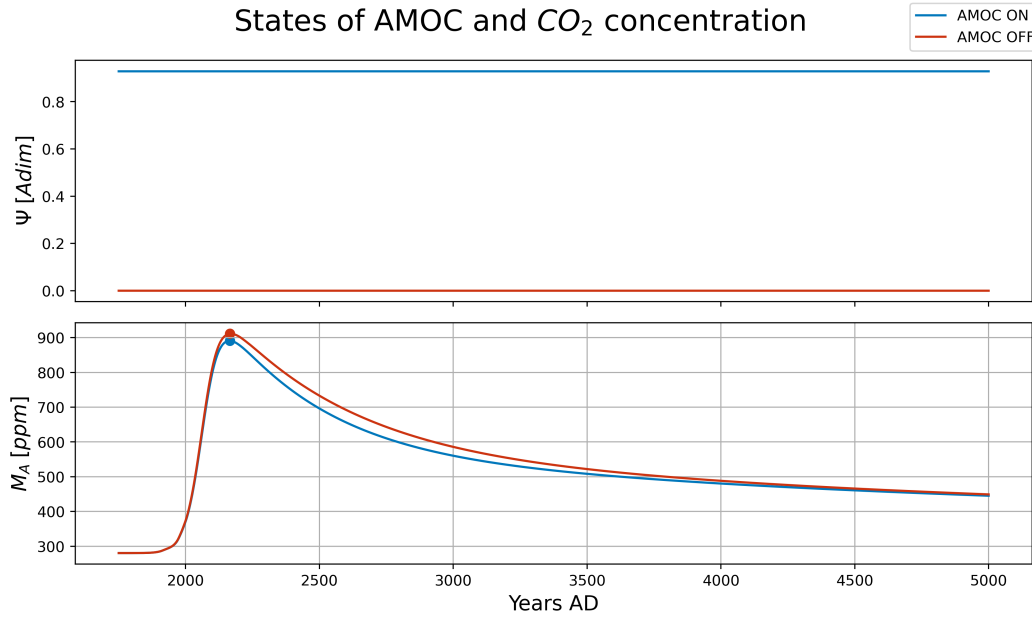
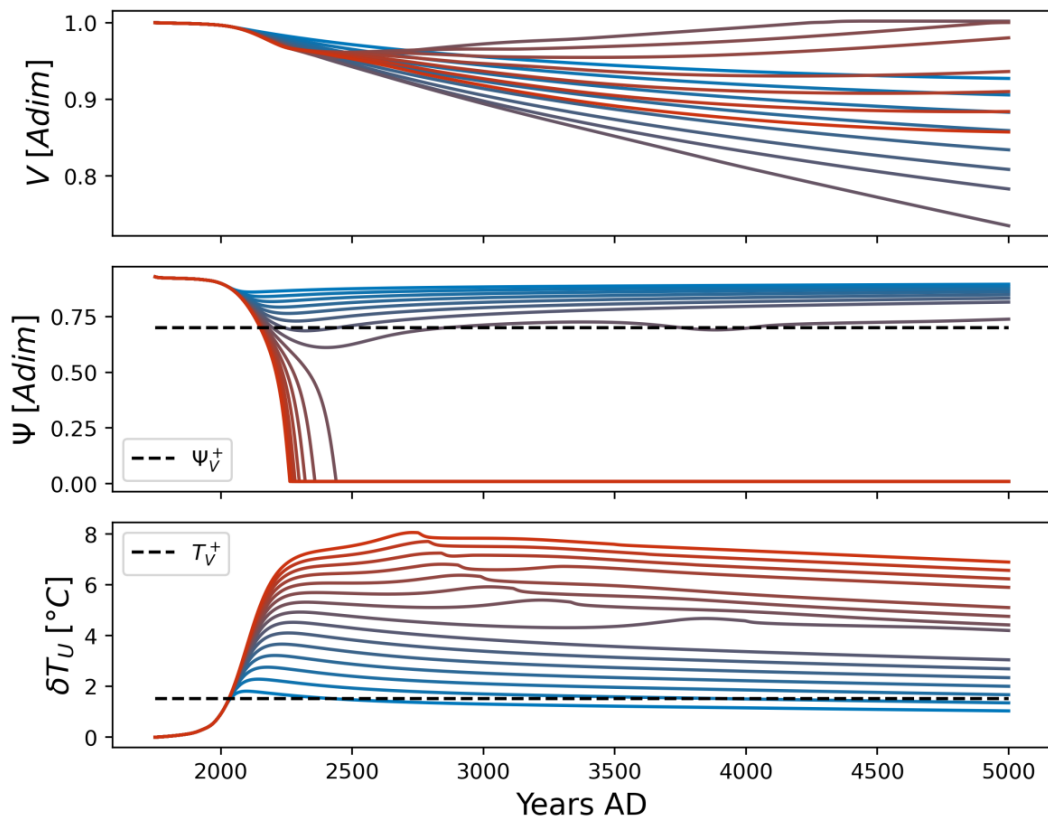


FIGURE 63 – *State of the AMOC and concentration of CO<sub>2</sub> in the atmospheric reservoir M<sub>A</sub> for the two sensitivity simulations. The points on the bottom figure correspond to the chosen equilibrium points against which concentrations are compared to conduct the calibration of  $\chi$ .*

## Conclusion

In this chapter, we have presented the AGTCCM, a model of nonlinear dynamics capable of capturing the primary-order dynamics necessary to simulate potential collapses and the coupling effects between the AMOC and the GIS that may lead to cascades. The AGTCCM also provides a calibration methodology for the simplified hysteresis it produces, which can be based on critical coordinates of bifurcation points derived from hystereses of more complex models, as demonstrated with cGenie. The limitations of this innovative methodology, as well as avenues for further development, have been outlined, along with the methodology chosen to integrate the AGTCCM into the carbon-cycle and climate model SURFER. New parameterizations have been introduced into SURFER’s carbon cycle to enable a coherent integration of the impacts on the biogeochemical cycle resulting from an AMOC shutdown.

# Chapter III - Results and Discussion



## 4 Chapter III - Results and Discussion

In this final chapter, we will be able to utilize SURFER v3.2, our new tool that has been developed and introduced in the preceding chapter, to address our fundamental scientific question. With the assistance of the AGTCCM, a simplified nonlinear dynamics model capturing the primary-order dynamics of the AMOC and the GIS and offering an innovative calibration method based on process-based models, we will investigate the effect of a realistic coupling between the AMOC and the GIS on their collapse dynamics.

Three distinct categories of results will be discussed and analyzed. The first will focus on the impact on the carbon cycle of potential AMOC collapses. Secondly, we will present key findings regarding the cascade-collapse dynamics of the AMOC and the GIS, comparing the results obtained using the AGTCCM with those achievable with SURFER v3.1. Thirdly, we will demonstrate and analyze results illustrating the phenomenon of *overshoot without tipping* that can be generated using SURFER v3.2. For each of these three categories, results will first be presented descriptively, followed by a comprehensive analysis incorporating concepts and critical comparisons with the literature introduced in Chapter I.

### 4.1 Methodology

#### Emission Scenarios

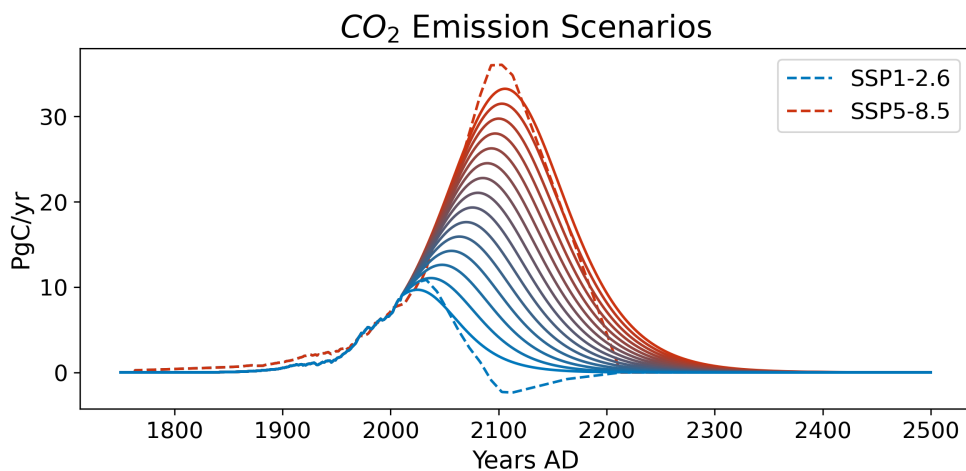


FIGURE 64 – Spectrum of CO<sub>2</sub> emission scenarios used in the various result chapters. From 1750 until 2010, historical emissions are utilized, followed by 15 scenarios, which are interpolations of total emission quantities between SSP1-2.6 and SSP5-8.5. The slight discrepancy between the historical emissions for the SSP scenarios and those utilized is attributed to minor differences in the datasets employed. A color gradient ranging from light blue for low-emission scenarios to red for those with the highest emissions is employed for identification purposes.

Before presenting these results, we must introduce the spectrum of forcing scenarios that will be systematically used. Given that we aim to conduct simulations using SURFER for the purpose of realistically projecting possible futures, we will consistently initiate our simulations from the pre-industrial period in 1750 and consider historical greenhouse gas emissions until 2010. From 2010 onwards, we will consider a spectrum of 15 emission scenarios of  $CO_2$ , which are interpolations derived from the SSP scenarios. These are illustrated in Figure (64). These 15 scenarios are constructed to produce carbon emissions ranging from 1000  $PgC$  to 5000  $PgC$ , roughly corresponding to the limits defined by the SSP1-2.6 and SSP5-8.5 scenarios. However, it is observed that even in the most aggressive emission scenario, we assume that by 2500, there are no further  $CO_2$  emissions. Note that we will not utilize methane emission scenarios in all configurations chosen for the experiments in this chapter. Methane emissions may occur, however, only in the event of an Amazon forest collapse and particularly the permafrost collapse as parameterized in SURFER v3.1. It was deemed unnecessary to add methane emission scenarios to those of carbon dioxide as it would only unnecessarily complicate the analysis, which aims to focus on cascade collapses between the AMOC and the GIS.

The significance of utilizing 15 forcing scenarios will be clearly demonstrated in the presentation of the various AMOC-GIS cascade collapse dynamics, but it can already be stated that they enable us to explore a sufficiently broad spectrum of forcing to effectively map the responses of the climate system of interest. Indeed, between a scenario of lower emissions, akin to SSP1-2.6, and the most aggressive scenario, akin to SSP5-8.5, having numerous cases of intermediate emissions allows for illustrating the complexities of interaction between AMOC and GIS behaviors.

### Coupling Scenarios

Lastly we must introduce two different configuration scenarios for SURFER v3.2. As previously mentioned, SURFER v3.1 has the advantage of already modeling 8 different tipping elements through equations (3.1) and also introduces a parameterization of their couplings (cf. Table (6)).

In the first configuration, referred to as **CONF1**, we will retain the parameterizations of interactions between tipping elements as chosen in SURFER v3.1 and defined in Table (6). In the second configuration, named **CONF2**, we will disable all interactions between tipping elements, thus technically defining a matrix  $S_{moy}$  from Table (6) as identically null, and retain only the interactions between the AMOC and the GIS denoted as  $e_{12}, e_{21}$  derived from the AGTCCM and the calibration with cGenie. However, indirect interactions such as the impacts of tipping elements on the Earth's radiative balance with a modification of albedo, or the emissions of greenhouse gases that may occur with the Amazon forest and the permafrost, will remain active. These latter implicit interactions between tipping elements via temperature forcing will only serve as a backdrop to the interactions.

Thus, CONF2 will allow us to study collapse dynamics with greater precision and simplicity, without direct impacts from other tipping elements besides the GIS and the AMOC. Even though no results with CONF1 will be presented here as they do not pertain to the data relevant to address our main research question, simulations with CONF1 are also available on the GitHub repository. These simulations are particularly useful for complementary research purposes on the differences created in hothouse narratives - where the interactions between all tipping elements is relevant - through improved calibration and consideration of the couplings between the AMOC and the GIS provided by the AGTCCM.

## 4.2 Discontinuities in the carbon cycle

Since capturing consistently the impact of an AMOC collapse on the carbon cycle can have critical consequences for the evolution of other key climatic variables and thus other tipping elements, we begin the presentation of the results of this thesis with those pertaining to the impact on the carbon cycle of a shutdown of the thermohaline circulation. This will serve as a response to the second main scientific question of this thesis.

### 4.2.1 Results

#### Dynamic Variation of the Carbon Flux in Response to the AMOC

To investigate the impact of the AMOC on carbon fluxes using SURFER v3.2, we conducted simulations across 15 predefined forcing scenarios spanning from the pre-industrial period to 5000 AD. For the production and analysis of these results, we utilize CONF1 to capture the most realistic response of the AMOC, considering all potential interactions with other tipping elements available to us. The state of the AMOC during these simulations is illustrated in Figure (65). We rely on the AMOC modeling integrated into SURFER v3.2 by the AGTCCM, calibrated against cGenie's hysteresis. As depicted, a complete collapse of the AMOC occurs in eight out of the 15 simulations. Remarkably, these collapses correspond to the eight highest emission scenarios. In the scenario with the highest emissions, this collapse transpires around 2240 AD, while for the last scenario associated with an AMOC collapse, it occurs around 4000 AD. Conversely, in the remaining seven simulations, which represent the lowest seven emission scenarios, the thermohaline circulation does not collapse, at least not by 5000 AD. Although there is an initial weakening over the first few centuries, the five lowest emission scenarios ultimately seem to converge to a complete recovery of the AMOC. For the sixth and seventh lowest emission scenarios, they appear to converge towards a full recovery of the AMOC; however, these trajectories still exhibit a slight tendency toward a collapsed state of the AMOC by 5000 AD. Nonetheless, experiments spanning 500,000 years demonstrate that these trajectories do converge towards the nominal state of the AMOC. In terms

of nonlinear dynamics, these trajectories approach the boundary of changing attractors and the basin of attraction of the stable equilibrium associated with collapse but do not enter it. Instead, these trajectories remain within the attractor of the stable equilibrium of the nominal state, implying that for an infinite time, these trajectories will converge towards this equilibrium.

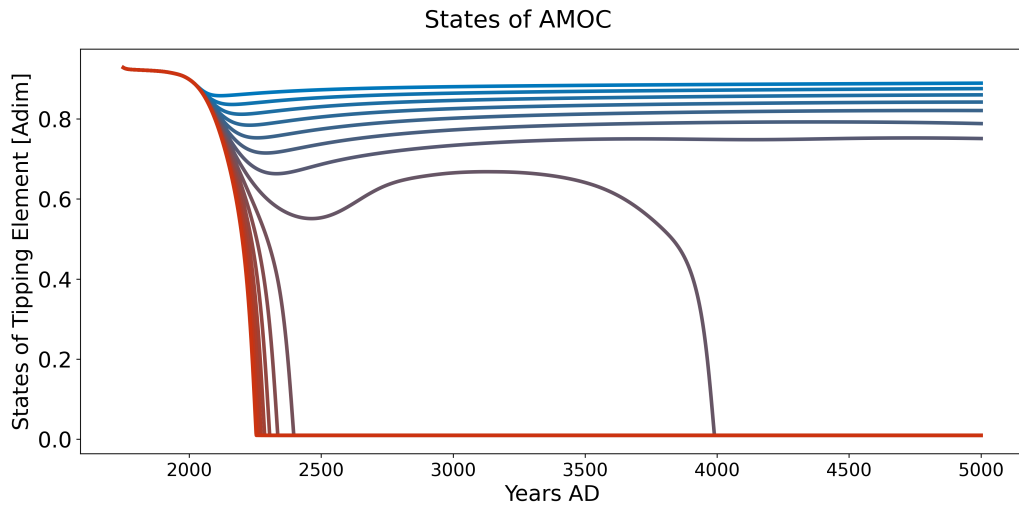


FIGURE 65 – *Temporal evolution up to 5000 AD of the AMOC state  $\Psi$  for the 15 selected emission scenarios in SURFER v3.2 CONF1*

The causes and couplings of these AMOC dynamics with the GIS will be studied in the following section, but we are currently considering how these AMOC trajectories impact carbon fluxes within the ocean in SURFER v3.2. In Figure (66), the temporal evolution of the carbon transport coefficients between the ocean layers of SURFER v3.2 is shown. As observed, these coefficients  $k_{UI}, k_{IU}, k_{ID}, k_{DI}$  follow the same dynamics derived from the parameterization described in Section (3.6), namely that of the AMOC. Each coefficient varies within a domain such that, in the case where each of these coefficients takes its minimum value, an increase of 20, 5 ppm of  $CO_2$  in the atmosphere is created at equilibrium.

### **The signature of the AMOC shutdown on the carbon cycle**

We now seek to understand how these changes in carbon fluxes within the SURFER ocean have affected the different carbon reservoirs and thus the entire carbon cycle. Figure (67) displays the temporal evolutions of the four carbon reservoirs of interest, namely the atmosphere reservoir  $M_A$ , as well as the three reservoirs of the three oceanic layers  $M_U, M_I$  and  $M_D$ .

A first common observation across all four reservoirs is the clear signature of nonlinearity just before 4000 AD, with a significant distinction in the content

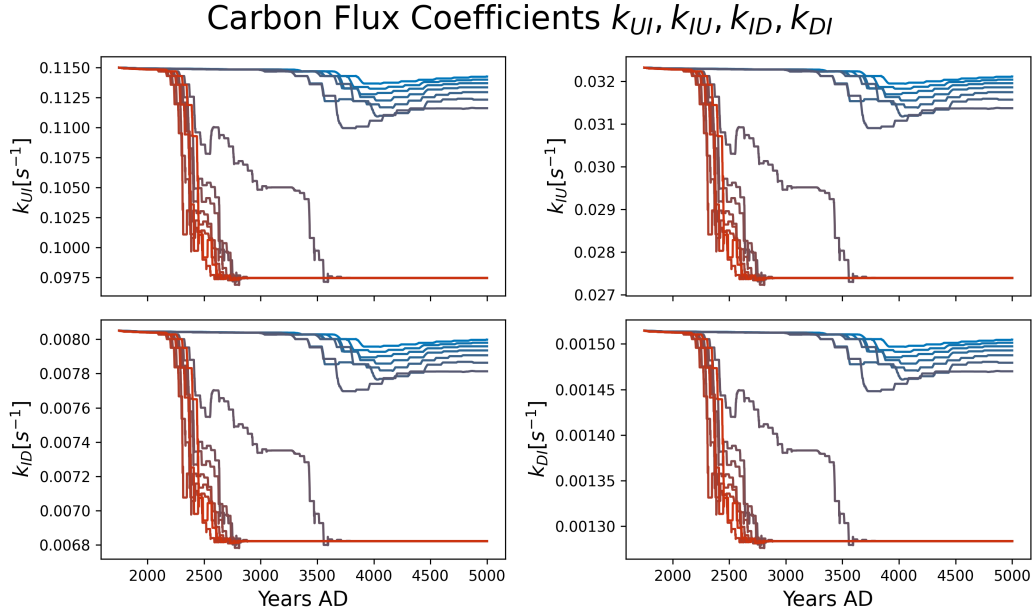


FIGURE 66 – *Temporal evolution of  $k_{UI}, k_{IU}, k_{ID}, k_{DI}$ , the carbon flux coefficients.*

of all reservoirs between the seventh and eighth emission scenarios.<sup>20</sup> Indeed, at equilibrium in 5000 AD, this difference is significant, as there is a 23,58 PgC disparity in storage within the surface ocean reservoir  $M_U$  between these two scenarios, whereas between the ninth and eighth emission scenarios, this difference is only 10,38 PgC. However, between these emission scenarios, a constant step of 285 PgC of total emissions separates them. In other words, we observe a nonlinear response in the quantity of carbon stored in the  $M_U$  reservoir. The same applies to the quantities of carbon stored in the intermediate ocean layer  $M_I$  or the deep layer  $M_D$ . For the atmosphere, the results are shown here in terms of atmospheric CO<sub>2</sub> concentration, but the same nonlinear response is observed, with a difference of 195 ppm between the seventh and eighth scenarios, while there is only a 76 ppm difference between the eighth and ninth scenarios. This response exemplifies the type of non-linearity we aim to analyze, as described in Section (2.2). Confronted with a range of forcing scenarios, we observe a discontinuity in the model output; in this instance, it manifests in the carbon content of various reservoirs.

In addition, we observe the usual signatures of carbon storage in these various carbon reservoirs. Following an increase in emissions into the atmosphere, this concentration gradually decreases due to carbon absorption by the ocean. Primarily, the surface ocean captures this carbon, which is then transferred to the intermediate ocean and, finally, with even greater inertia due to the time required for this transfer, to the deep ocean. It is also interesting to note that

20. Hereafter, when referring to the "nth" emission scenario, it will always be counted starting from the one with the smallest amount of emitted carbon.

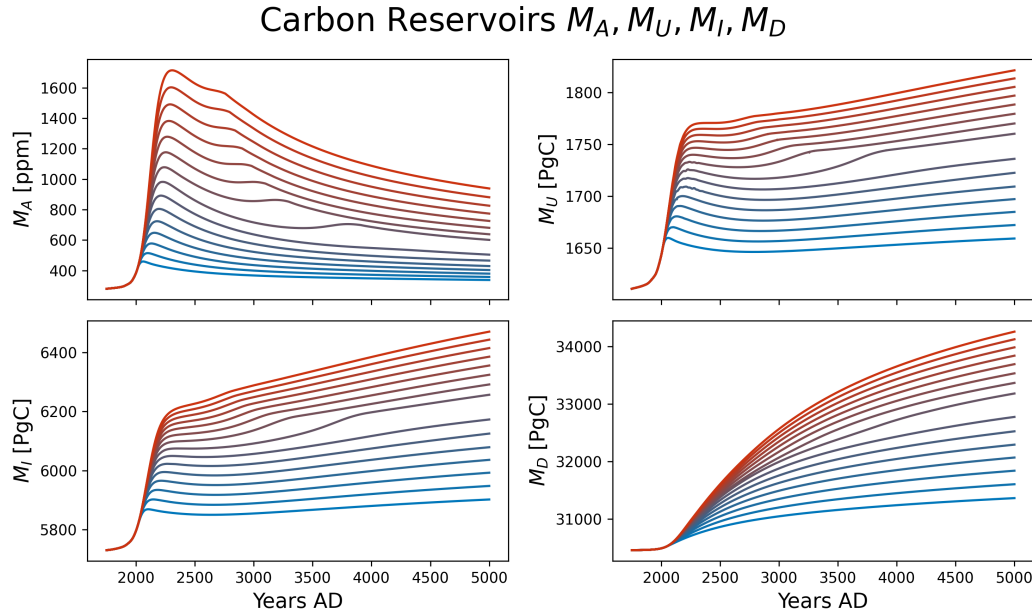


FIGURE 67 – *Temporal evolution of the 4 carbon reservoirs of interest, namely the atmosphere  $M_A$ , and the three associated with the ocean layers  $M_U, M_I, M_D$ .*

the three layers of the SURFER ocean encode significant differences in the orders of magnitude of carbon storage capacities. Indeed, the intermediate ocean, which constitutes the oceanic layer between 150 m and 500 m, stores nearly three times more carbon than the surface ocean. The difference is even more pronounced with the deep ocean, which in SURFER lies between 500 m and 2500 m and stores nearly 18 times more carbon than the surface ocean. At the peak of its concentration around 2300 AD, the atmosphere contains 3500 PgC, ten times less carbon than the deep ocean for comparison.

#### 4.2.2 Discussion

Regarding the differing responses between the oceanic and atmospheric reservoirs described earlier, these are simply the result of the SURFER model's encoding of behaviors expected from more complex model literature. Moreover, at this level, as described in Couplet et al. [17], SURFER possesses a carbon cycle that reproduces the results of more process-based models with high accuracy.

Let us now analyze and attempt to understand the origins of the non-linearities observed in the carbon reservoirs. The emergence of non-linearity in the carbon reservoirs begins to occur between the 7th lowest emission scenario and the 8th. Furthermore, as seen in Figure (65), these trajectories also approach the threshold for a collapse of the AMOC in the 8th lowest emission scenario. Between the 7th and 9th lowest emission scenarios, a collapse of the AMOC occurs by the end of the simulation. Due to the parameterization of carbon flux coefficients between the layers, these results are also transmitted to the carbon

cycle as shown in Figure (66).

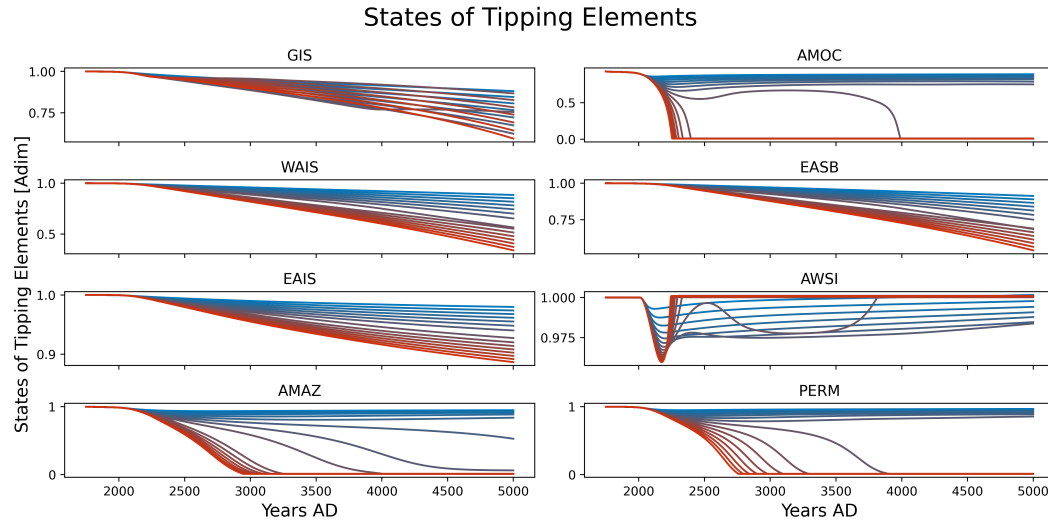


FIGURE 68 – *Temporal evolution up to 5000 AD of the 8 Tipping Elements in SURFER for the 15 selected emission scenarios.*

Can we conclude that the collapse of the AMOC is responsible for these nonlinearities in the carbon cycle ? No, at least not in such a significant way. Indeed, Figure (68) displays the trajectories of all tipping elements. As can be observed, under the same critical trajectories identified for the thermohaline circulation, two other tipping elements collapse : the Amazonian rainforest and the Permafrost. As explained in Subsection (3.3.2), SURFER features a simplified parameterization of feedbacks on the radiative balance and also on greenhouse gas emissions that can result from the collapse of certain tipping elements. Taking this into account, we analyze that the nonlinearities visible in the carbon cycle, previously identified, are actually due to collapses of the Amazon rainforest and permafrost. Indeed, if we conduct the same simulations (cf. Figure (69)), with the same emission scenarios but disabling the feedback effects of these two tipping elements, we do not reproduce the observed nonlinearities.

However, as shown in the last section of the previous chapter and in Figure (66), the dynamic parameterization of the impact of an AMOC collapse on the carbon cycle is effectively implemented. What actually occurs is that even in the case of an AMOC collapse, given that it results in a steady-state increase of 20,5 ppm of  $CO_2$  in the atmosphere, this difference is too minor to be detected in the resolution of the emission scenarios conducted here. Further experiments conducting two simulations for quantities of greenhouse gas emissions closer to the critical threshold for tipping the AMOC have been carried out, but we qualitatively observe the same behavior as described in Figure (63). The variation in carbon transport coefficients is relatively mild compared to the absolute effects of a 20,5 ppm increase it can produce, thus there is no clear signal of nonlinearity in the carbon cycle in SURFER v3.2 resulting from an AMOC

collapse. However, this accurately replicates the expected results from the literature, as demonstrated in Section (3.6.1) (cf. Figure (62)). Indeed, beyond the absolute amount of additional carbon in the atmosphere that this entails, the response in SURFER v3.2 replicates the dynamics of the expected response, similar to those observed in General Circulation Models (GCMs) such as the one used in the study by Zickfeld et al. [89]. However, it is worth mentioning that it is entirely possible that this increase of approximately 20 *ppm* of  $CO_2$  in the atmosphere could lead to surpassing a tipping point in terms of the temperature forcing associated with another tipping element. This absolute increase, although occurring gradually and being small compared to emissions in the scenarios, remains non-negligible in absolute terms.

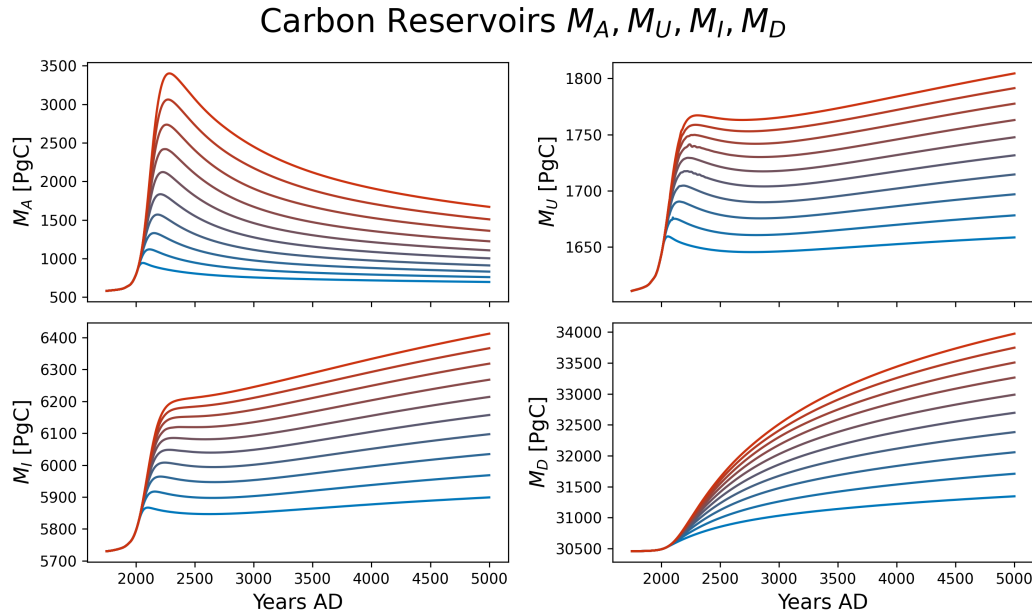


FIGURE 69 – *Temporal evolution of the four carbon reservoirs of interest—the atmospheric reservoir  $M_A$  and the three associated with oceanic layers  $M_U, M_I, M_D$ —in cases where feedbacks on greenhouse gas emissions from permafrost and the Amazon rainforest are disabled.*

### 4.3 Cascade collapse of the AMOC-GIS in SURFER v3.2

In this second part of the presentation and discussion of the results of this thesis, we will address the main scientific question of this study, namely, understanding the cascade collapse dynamics between the AMOC and the GIS that can be created with this simplified model paradigm of nonlinear dynamics. In order to focus on the analysis of interactions between the AMOC and the GIS, all simulations in this subsection will be conducted in CONF2, retaining only the coupling terms between the AMOC and the GIS. Once again, we present all relevant results pertaining to our research question before discussing and analyzing them further.

### 4.3.1 Results

#### Experimental protocol and Bifurcation Diagrams

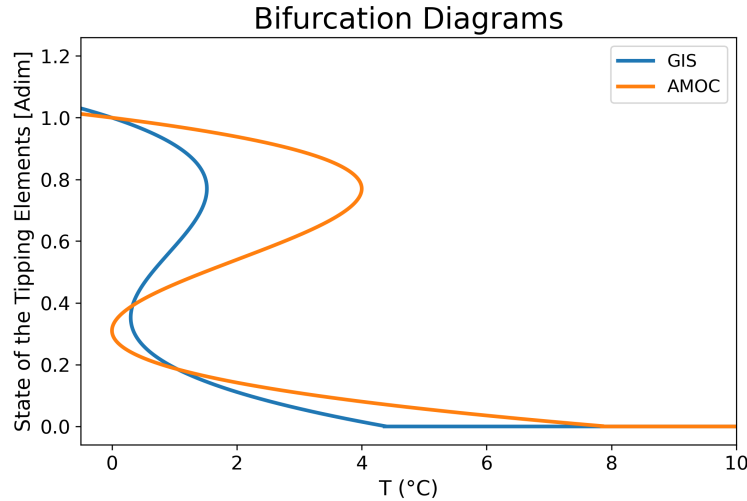


FIGURE 70 – *Bifurcation Diagrams for the tipping elements in SURFER v3.1*

To understand the effects of a realistic coupling between the AMOC and the GIS on their collapse dynamics, we will throughout this chapter compare the results produced by SURFER v3.1 with those by the AGTCCM embedded in SURFER v3.2.

Figure (70) depicts the bifurcation diagram of the AMOC and the GIS associated with the existing model in SURFER v3.1. As explained in subsection (3.2.3), the limitation of this model for tipping elements is that they have calibration coefficients that are partly arbitrary, not rigorous, and based retrospectively on the effects they produce. They are not directly calibrated on a specific process-based model experiment. Furthermore, while a parameterization exists (albeit with the flaws mentioned) for the stabilizing effect of an AMOC collapse on the GIS, no parameterization is available to represent the coupling of a GIS collapse on the AMOC. However, as discussed in Chapter I, this destabilizing effect of the GIS on the AMOC, which can provide a forcing through freshwater flux, may be crucial in weakening the AMOC.

Figure (71) shows the bifurcation diagram of the AMOC and the GIS derived from SURFER v3.2. The AMOC diagram is directly derived from the AGTCCM and the calibration on cGenie introduced in Chapter II. Since we did not have access to hysteresis from process-based models for the GIS, we retrieved critical bifurcation point data from SURFER v3.1. Therefore, it is normal that in the bifurcation diagram with respect to temperature forcing, we obtain the same result between SURFER v3.1 and SURFER v3.2. It is important to note that in the case of the AMOC, the one modeled in SURFER v3.1 (cfr. Fig.(70)) has a

critical bifurcation threshold with respect to temperature that is smaller,  $T_{\Psi}^+ = 4^\circ\text{C}$  compared to  $T_{\Psi}^+ = 5.5^\circ\text{C}$  in SURFER v3.2. Regarding the downward shift of the AMOC bifurcation diagram in SURFER v3.2, it is due to the calibration limit on the pre-industrial value developed in Chapter II.

The six additional bifurcation diagrams of the other tipping elements in SURFER v3.2, inherited from SURFER v3.1, are also presented. These simplified dynamics of the other tipping elements remain the same in both SURFER v3.1 and SURFER v3.2. They are illustrated to demonstrate significant differences in collapse dynamics among the various tipping points, as these will be relevant in the subsequent analyses. However, Figure (71) illustrates significant differences in terms of critical collapse thresholds and collapse dynamics among tipping elements. For instance, extreme cases such as the East Antarctic Ice Sheet (EAIS) exhibit a tipping point at  $T_{EAIS}^+ = 7.5^\circ\text{C}$  and a critical volume value for the bifurcation from the nominal state to the collapse state at  $V_{EAIS} = 0.44$ . On the other hand, contrasting behaviors can be observed, for example, in the West Antarctic Ice Sheet (WAIS), which is also a component of the cryosphere. WAIS shares a tipping point temperature of  $T_{WAIS} = 1.5^\circ\text{C}$  with the GIS, but possesses a value of  $V_{WAIS}^+ = 0.75$ , thus leading to a much quicker transition to the collapse state under the same temperature forcing compared to EAIS.

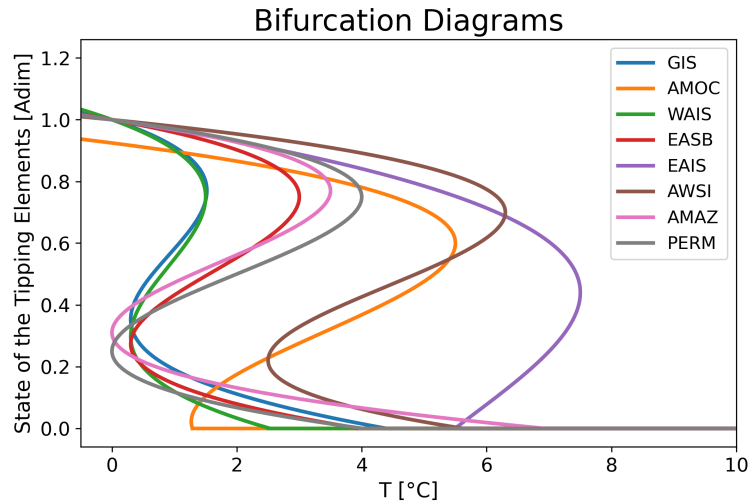


FIGURE 71 – *Bifurcation Diagrams for the tipping elements in SURFER v3.2 with the ones for AMOC and GIS obtained with AGTCCM*

### The collapses of the AMOC

We will present and compare the collapse dynamics produced between SURFER v3.1 and SURFER v3.2. In Figure (72), trajectories for the 15 emission scenarios presented previously in the forcing space of the AMOC in **ParamA** of the AGTCCM, namely  $T$  and  $F_{GIS}$ , are depicted. These simulations extend

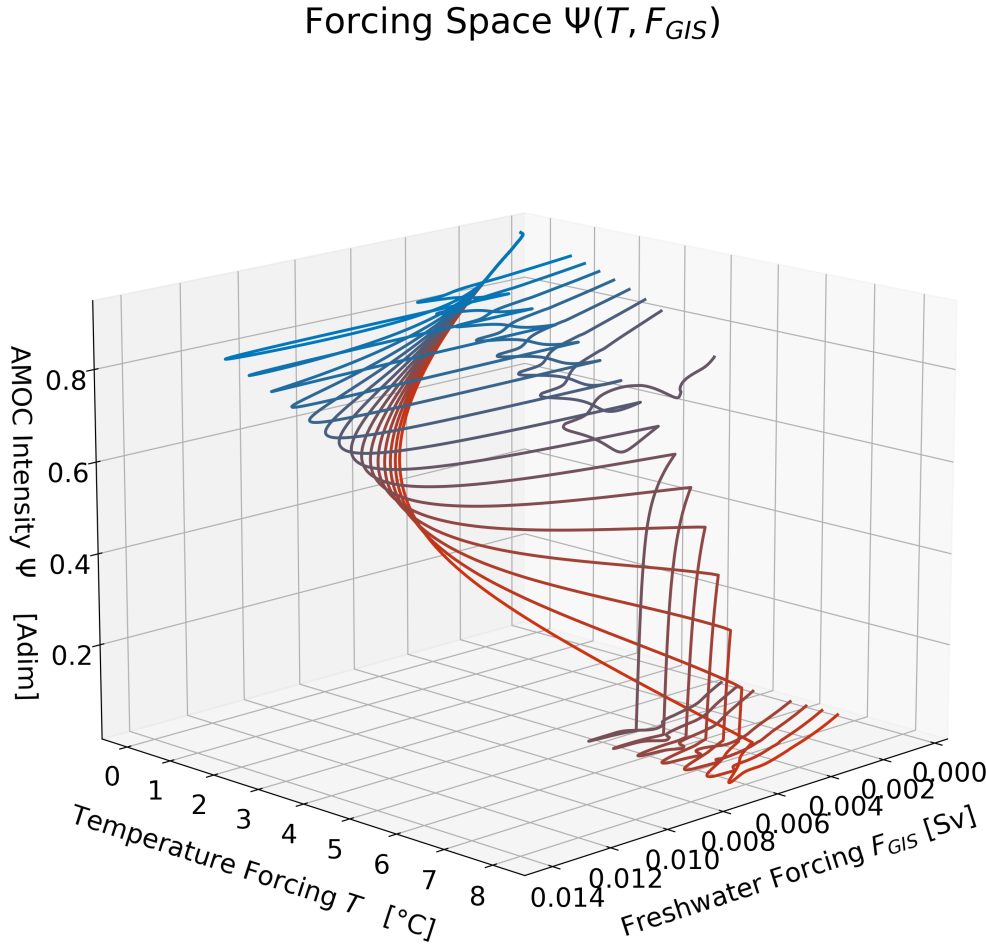


FIGURE 72 – Trajectories of the AMOC in the forcing space  $(F_{GIS}, T)$  in the *ParamB* of the AGTCCM in SURFER v3.2

until 5000 AD. Despite the somewhat complex perspective of the third dimension on a 2D plane, it is already noticeable that for the eight lowest emission scenarios, the AMOC does not collapse by the end of the simulations. It is also observed that freshwater fluxes from the GIS reach higher values in the case of the lowest emission scenarios, with a maximum value around 0,014 Sv. The atmospheric temperature forcing, on the other hand, reaches maximum values of almost 8°C anomaly on a global average in the case of the highest emission scenario of 5000 PgC. Finally, it is observed that in scenarios where there is a collapse of the AMOC, it appears to be quite abrupt.

In Figure (73), the state of the AMOC until 5000 AD is depicted alongside its forcing variables, namely the atmospheric global mean temperature anomaly (denoted in SURFER as  $\delta T_U$ , which is also the global mean temperature anomaly of the upper ocean by construction of SURFER), as well as the two

freshwater fluxes  $F_{GIS}$  and  $F_O$ . Due to the inherent limitations of the parameterization of  $F_O$  described in subsection (3.3.1), it will be deactivated initially, thus reverting the model used in the AGTCCM from the **ParamB** choice to the **ParamA** choice with two forcing variables on the AMOC. The results shown in the forcing space in Figure (72) are more distinctly observed. In 7 simulations, the AMOC undergoes a collapse, corresponding to the 7 forcings with the highest  $CO_2$  emissions. Subsequently, it is observed that the critical threshold for temperature forcing is reached at least temporarily for the six highest-emission scenarios. For the highest emission scenario, the critical temperature threshold is surpassed from 2175 AD onwards, which, coupled with a freshwater flux forcing  $F_{GIS}$  peaking at  $F_{GIS}^{max} = 0,014 \text{ Sv}$  also in 2175 AD, triggers the first complete collapse of the AMOC in 2260 AD.<sup>21</sup> In 2260 AD, the global mean temperature anomaly reaches  $T = 6,8^\circ\text{C}$ , well beyond the threshold of  $T_\Psi^+ = 5,5^\circ\text{C}$ . However, in none of the emission scenarios does a forcing term associated with  $F_{GIS}$  exceed the critical threshold found in the cGenie experiments.

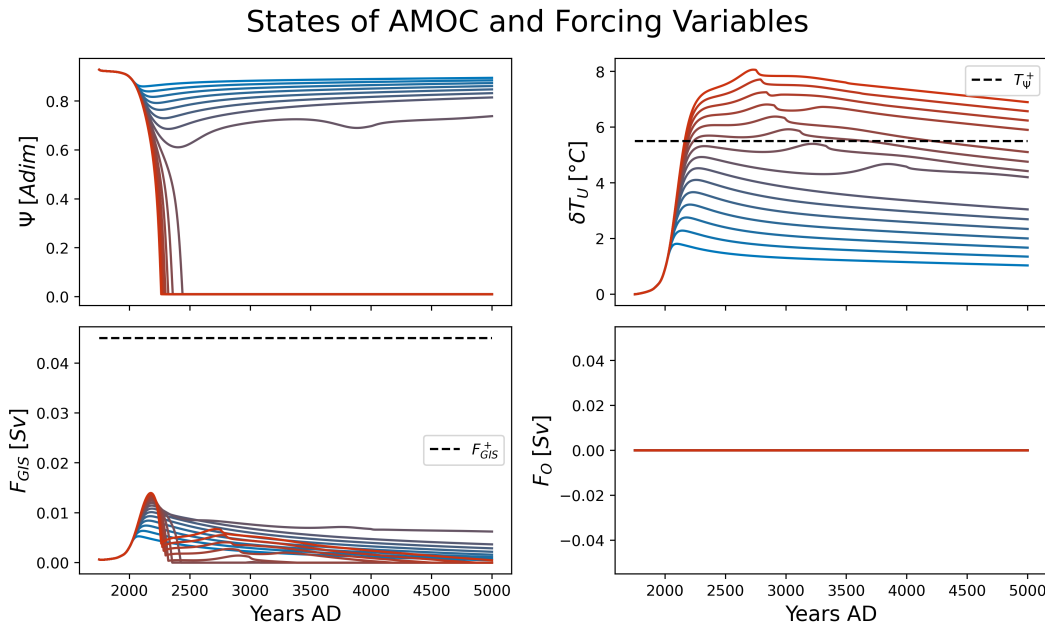


FIGURE 73 – States of the AMOC  $\Psi$  as well as forcing variables ( $T, F_{GIS}, F_O$ ) across 15 simulations until 5000 AD in SURFER v3.2. The critical values of the forcings for  $F_{GIS}$  and  $T$  are displayed as black dashed lines.

In Figure (74), the same simulations with the same forcing scenarios are depicted, but this time using SURFER v3.1. In this case, only the six lowest emission scenarios do not trigger an AMOC collapse. However, as mentioned earlier, the critical threshold for the sole temperature forcing is  $4^\circ\text{C}$  in this case. As a result, in the case of SURFER v3.1, the 10 most significant forcing scenarios with

21. On the GitHub repository of this thesis, numerous additional figures associated with simulations over other time spans, such as up to 2300 AD, facilitate a more localized analysis of the trajectories of various variables.

respect to temperature exceed the critical temperature threshold at least at some point. The first collapse of the AMOC under the highest emission scenario occurs in SURFER v3.1 in 2340 *AD*, whereas the temperature-associated tipping point  $T_{\Psi}^+ = 4^{\circ}\text{C}$  (which is the sole forcing of the AMOC in this version of SURFER) is already exceeded from 2100 *AD* onwards. At the time of the initial collapse of the AMOC in 2340 *AD*, the global mean temperature anomaly reaches  $7^{\circ}\text{C}$ .

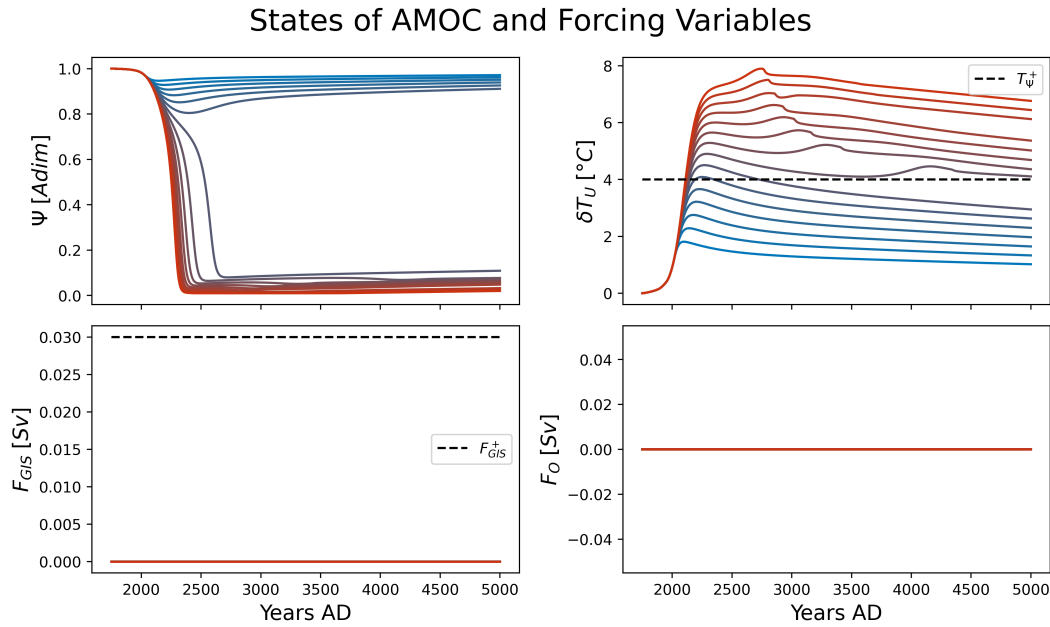


FIGURE 74 – *States of the AMOC  $\Psi$  as well as forcing variables ( $T, F_{\text{GIS}}, F_O$ ) across 15 simulations until 5000 *AD* in SURFER v3.1. The critical values of the forcing for  $T$  is displayed with a black dash line.*

### The collapses of the GIS

In the same simulations, using the identical 15 forcing scenarios, the trajectories of the GIS until 5000 *AD* are illustrated in Figure (75) in SURFER v3.2. Even though no total collapse of the GIS occurs by 5000 *AD*, it is noteworthy to observe that scenarios associated with the most significant global mean temperature forcings are not necessarily those leading to the greatest melting of the GIS. The scenario inducing the most extensive GIS melting is the eighth most impactful greenhouse gas emission scenario. Additionally, it is observed that only the six lowest emission scenarios do not lead to a decrease in the AMOC intensity to the point of reaching its associated upper tipping point critical value related to the GIS. However, in terms of temperature forcing, all emission scenarios, including the lowest, surpass the critical value of  $T_V^+ = 1,52^{\circ}\text{C}$  for a significant period (two centuries).

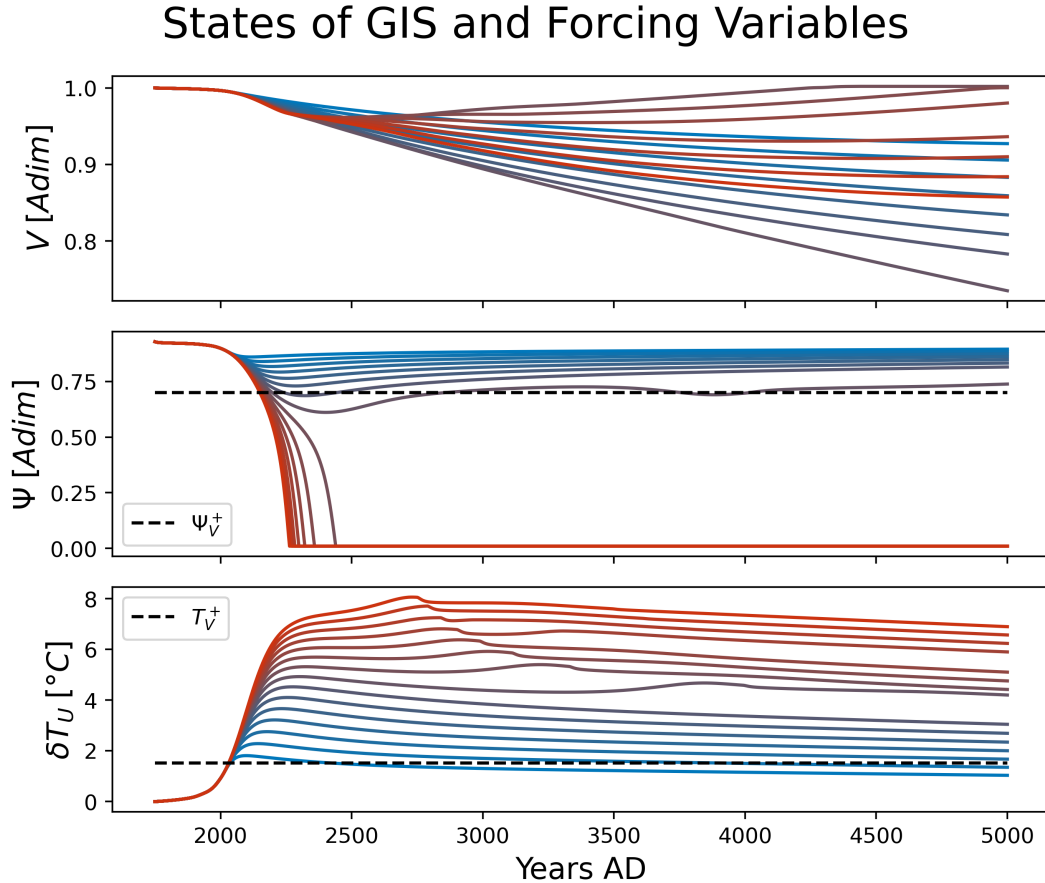


FIGURE 75 – States of the GIS  $V$  as well as forcing variables ( $T, \Psi$ ) across 15 simulations until 5000 AD in SURFER v3.2. The critical values of the forcing for  $T$  and  $\Psi$  are displayed with a black dash line.

Figure (76) depicts the evolution of the GIS under the same 15 emission scenarios in SURFER v3.1. A similar intriguing phenomenon is observed as in SURFER v3.2, namely, that the most significant emission scenarios do not necessarily lead to the greatest decrease in the GIS. However, it is noted that the decrease in GIS volume by 5000 AD is more substantial in SURFER v3.2 ( $V = 0, 73$ ) compared to SURFER v3.1 ( $V = 0, 94$ ). Furthermore, whereas the most significant emission scenarios led to a decrease followed by growth in ice volume in SURFER v3.2, Figure (76) demonstrates that the ice melt in SURFER v3.1 is both smaller in volume and faster in time. The subsequent growth phase of ice is also shorter. Moreover, the nine most significant emission scenarios in SURFER v3.1 result in a return to pre-industrial levels of GIS volume within a few centuries, and even slightly higher volumes in some scenarios. Obviously, in SURFER v3.1, there is no calibrated coupling. As explained in subsection (3.2.3), an arbitrarily chosen value was used to encode the stabilizing effect of an AMOC collapse on the GIS, but this is not from process-based model experiments. The evolutions of AMOC forcing are the same as those described

in Figure (74). Concerning the temperature forcing tipping points for the GIS, similar results are naturally obtained as in SURFER v3.2, with all emission scenarios crossing this tipping point at least at some point. This is because the forcing scenarios are identical, and especially because the critical threshold  $T_V^+$  is the same in both the GIS model of SURFER v3.1 and the AGTCCM of SURFER v3.2.

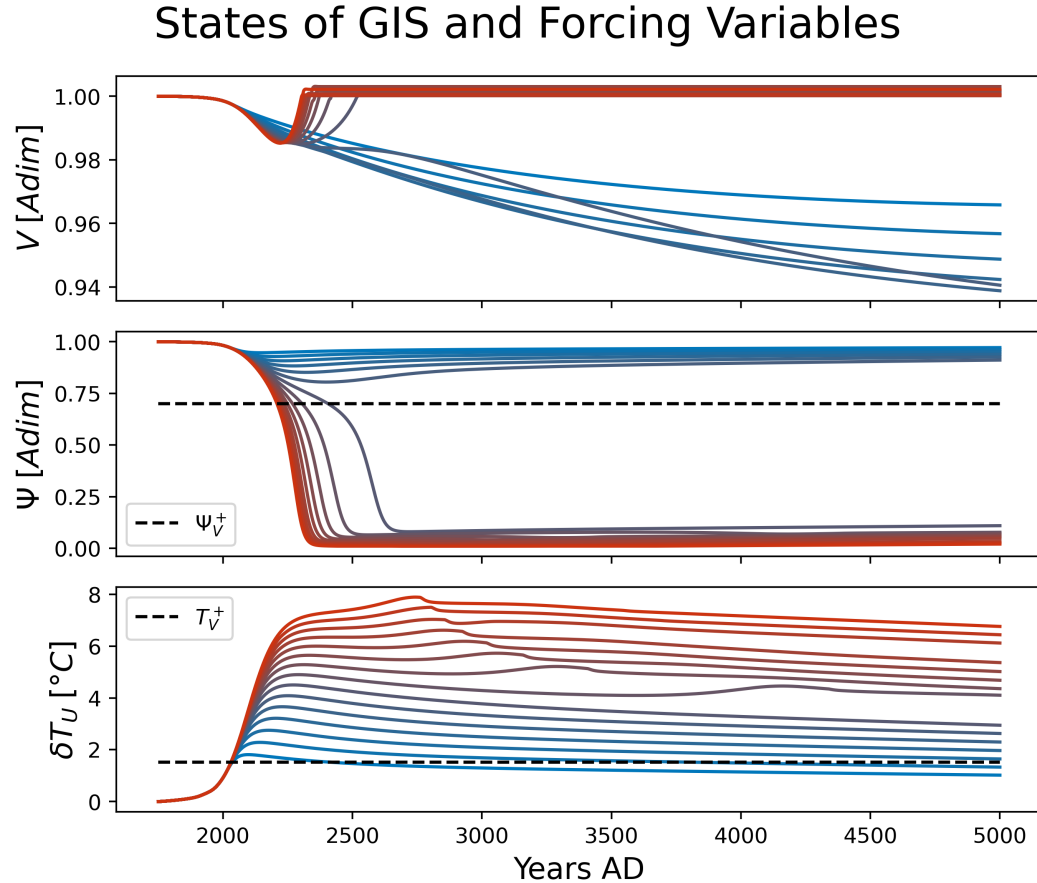


FIGURE 76 – *States of the GIS  $V$  as well as forcing variable ( $T, \Psi$ ) across 15 simulations until 5000 AD in SURFER v3.1. The critical values of the forcing for  $T$  and  $\Psi$  is display with a black dash line.*

### The impacts of $F_O$

The final results we wish to present in this section are simulations where the forcings by  $F_{P-E}$  and thus the term  $F_O$  are activated (Figure (77)). For the reasons discussed in subsection (3.5.3), no simulations with the flux  $F_W$  are presented due to the lack of objective knowledge that would allow us to calibrate  $e_{12}$  in a plausible manner, taking into account freshwater fluxes in the Southern Atlantic associated with Antarctic cryosphere components. In Figure (77), it is observed that the dynamic behavior of the AMOC is generally the same as in

Figure (73), where freshwater fluxes  $F_{P-E}$  were disabled. Indeed, no further AMOC collapse is produced in this case with the additional forcing of  $F_{P-E}$  and we still observe very rapid AMOC collapses for the seven highest emission scenarios. However, a notable difference is found for the seventh lowest emission scenario, which already exhibited a more significant oscillation and a lower drop in the AMOC state before rebounding in Figure (73). In these simulations with freshwater forcing resulting from variations in the precipitation-evaporation balance, a more pronounced overall weakening of around fifteen percent of the AMOC is obtained. For the other lower emission scenarios, a weaker but still notable weakening is observed when this additional freshwater flux forcing is included. However, as observed in Figure (77), the freshwater flux forcing  $F_{P-E}$ , which by its parameterization exactly follows the dynamics of the temperature anomaly  $T$ , takes very low values even in the highest emission scenario. Indeed, at maximum, a flux of  $F_{P-E} = 0,005 \text{ Sv}$  is applied, which remains well below the critical threshold identified in the cGenie hosing experiment, which was  $F_{GIS}^+ = 0,065 \text{ Sv}$ .

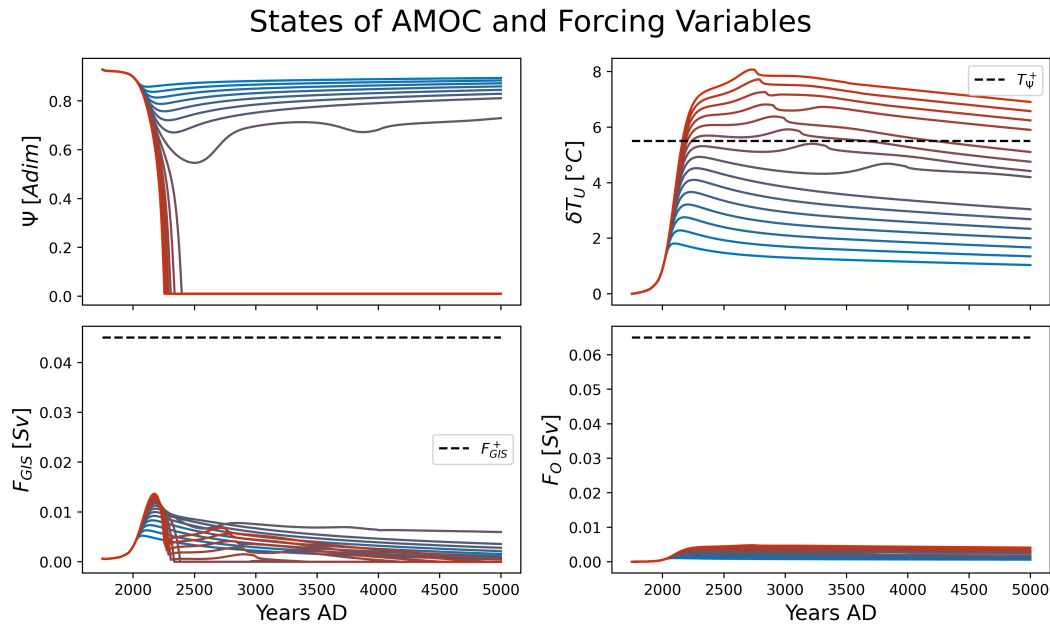


FIGURE 77 – States of the AMOC  $\Psi$  as well as forcing variables ( $T, F_{GIS}, F_O$ ) across 15 simulations until 5000 AD in SURFER v3.2. The critical values of the forcings for  $F_{GIS}$ ,  $F_O$  and  $T$  are displayed as black dashed lines.

#### 4.3.2 Discussion

##### Collapses of the AMOC

In order to address the primary research question regarding the impact on cascade collapse dynamics that can be simulated by realistically considering the

couplings between the AMOC and the GIS, we will analyze the results between version v3.1 of SURFER and version v3.2, which incorporates the AGTCCM. To streamline the analysis, we will first focus on the collapse dynamics of the AMOC and then on those of the GIS.

Before analyzing the effect of the coupling coefficients, it is important to note that the calibrations of the simplified AMOC dynamics between SURFER v3.1 and SURFER v3.2 are not the same. As seen in Figures (70) and (71), the AMOC in the AGTCCM has a tipping point with respect to temperature forcing that is significantly higher than in SURFER v3.1. This *a priori* has the effect of making the collapse of the AMOC seemingly easier in SURFER v3.1. However, in SURFER v3.2, an additional forcing term with the freshwater flux from the GIS is included, whereas in SURFER v3.1, even in the form of an arbitrary coefficient, this parameterization does not exist.

Despite an additional forcing term with  $F_{GIS}$ , the AMOC in the AGTCCM thus produces 7 collapse scenarios (see Figure (73,74)) compared to 9 in SURFER v3.1. The difference is therefore due to the lower tipping point in the case of SURFER v3.1, and these results also underline a first conclusion, namely that the forcing by the freshwater flux from the GIS, while having an impact, is not strong enough to counteract the increase in the critical forcing threshold of the AMOC in the AGTCCM.

Additionally, we also reproduce the scenarios expected by the literature[34, 74], namely that it is not possible to tip the AMOC solely through forcing associated with GIS melting. Indeed, at the peak of the decline in ice volume that occurs with the highest emission scenario, only a freshwater flux of  $F_{GIS}^{max} = 0,014 \text{ Sv}$  is produced, which remains well below the tipping point associated with this forcing, which is  $F_{GIS}^+ = 0,045 \text{ Sv}$ .

As demonstrated in Figure (73), the collapses of the AMOC are primarily due to the exceeding of the tipping point associated with temperature forcing. In SURFER v3.2, under the highest emission scenario, it takes the AMOC 85 years to collapse once the global mean temperature anomaly alone exceeds the tipping point. Conversely, in SURFER v3.1, under the same emission scenario, the collapse of the AMOC takes 240 years from its crossing of the tipping point. When examining the specific year in which the AMOC collapses, there is a gap of  $\Delta t_{\Psi}^{\text{Collapse}} = 155$  years between the first collapse in SURFER v3.1 and the first in SURFER v3.2, despite operating under identical emission scenarios. Yet, in both versions of the model, the characteristic time of the AMOC collapse dynamics is set to  $\tau = 10$  years in both cases. The fact that the AMOC in SURFER v3.1 takes longer to collapse once its tipping point is surpassed is a consequence of the shape of the stable manifold of the collapse state, as seen in Figure (70) compared to that of Figure (71). Indeed, we observe that in SURFER v3.2, calibration on the hysteresis of cGenie implies that once the tipping point is reached, the bifurcation occurs abruptly onto the collapse state with an AMOC value  $\Psi = 0$ . In the case of the AMOC model in SURFER v3.1, once the tipping point is reached for  $T^+ = 4^\circ\text{C}$ , the AMOC first transitions to a collapse state

with an intensity of  $\Psi = 0,17$ , which then decreases further to reach only a value of  $\Psi = 0$  for  $T = 7,8^{\circ}\text{C}$ . This demonstrates the consequences, also in terms of complete collapse time, of a simplified AMOC dynamics calibrated in a significantly different manner.

The significant differences in terms of duration and timing of the collapse of the AMOC between SURFER v3.1 and SURFER v3.2, and thus, the differences in terms of climatic and societal futures that these discrepancies create, underscore the need for further research to more accurately identify the tipping points associated with the various forcings of tipping elements and to better calibrate models based on them. Indeed, as seen in the literature review in Chapter I, critical thresholds still have considerable uncertainty with wide confidence intervals. This is the case for the AMOC, where the lower bound of its tipping point with temperature is set at  $1,4^{\circ}\text{C}$  while its upper bound is set at  $8^{\circ}\text{C}$  [2]. It is clear from the presented results and their significant differences for a variation of  $T_{\Psi}^{+}$  of "only"  $1,5^{\circ}\text{C}$  between SURFER v3.1 and SURFER v3.2 that currently, it is only possible to provide AMOC collapse scenarios with differences sometimes spanning several centuries regarding the exact timing of the collapse.

Furthermore, these results also allow us to support the nuances discussed regarding the limitations of the calibration methodology of the AGTCCM highlighted in Section (3.5). Indeed, due to the significant differences in potential future collapses that can be obtained based on current uncertainties even in process-based models regarding the exact positions of tipping points, having a calibration method with simplified dynamics that produce differences of the order of ten percent, while unfortunate, does not negate the epistemological utility of this approach. It is also important to recall that the purpose of the AGTCCM and SURFER v3.2 is to produce a coherent model for exploring possible collapse scenarios. This model does not currently have the scope to serve as operational and strategic decision support, which would invalidate the model due to these significant uncertainties.

### **Significance of Calibrating the Coupling Coefficient from the GIS to the AMOC $e_{12}$**

Even though it has a second-order effect compared to temperature forcing, the forcing by  $F_{GIS}$  can be decisive in certain collapses. In fact, for the 9th lowest emission scenario in SURFER v3.2, it is very interesting to observe that even if the temperature tipping point is not reached, the AMOC still transitions under this scenario. The reason for this is the freshwater flux from the GIS, which acts as an additional forcing and allows the sum of these two forcings to exceed the tipping point associated with both forcings simultaneously.

$$W_c = (d_1 T_{\Psi}^c + e_{12} F_{GIS}^c) = d_1 T_{\Psi}^{+}. \quad (4.1)$$

Indeed, as presented in sub-subsection (3.3.2), in our mathematical model of nonlinear dynamics, it is only when the independent term of the third-order

polynomial reaches a certain critical value, causing a phase space shift until the merging of two equilibrium points, that a fold bifurcation occurs. In the parlance of nonlinear dynamics, our variables  $T$  and  $F_{GIS}$  act as our bifurcation parameters, allowing the system to reach one of its bifurcation points when  $T$  and  $F_{GIS}$  take values such that their sum, modulated by the intensity of their couplings with the AMOC dynamics ( $d_1T + e_{12}F_{GIS}$ ), reaches the critical value of the tipping point denoted in terms of temperature as  $d_1T_\Psi^+$ .

In this experiment depicted in Figure (73), this threshold is therefore exceeded significantly and for a sufficient duration to completely tip the AMOC due to the forcing of  $F_{GIS}$  in addition to that of temperature. We must therefore conclude that the consideration of the second dominant forcing for the AMOC, namely the freshwater flux from the GIS, can be decisive in the possible collapse trajectories of the AMOC. If this additional forcing term can be decisive, it demonstrates the importance and utility of having, through the AGTCCM, the most precise calibration possible of our simplified dynamics based on process-based models of the coupling coefficient from the GIS to the AMOC, denoted as  $e_{12}$ .

### **Collapses of the GIS**

How to explain the fact that it is not the highest emission scenarios that cause the most melting of the GIS by 5000 AD, whether in SURFER v3.1 or SURFER v3.2? The answer to this lies in the stabilizing feedback of an AMOC collapse on the GIS. As explained in Chapter I, a slowdown of the AMOC will lead to a significant decrease in average temperature in the North Atlantic and thus notably over the GIS. This decrease can reach an average of  $-12^\circ C$  in cities like Reykjavik at the same latitude as Greenland. Thus, an AMOC collapse will counterintuitively allow for regional cooling in the Northern Hemisphere, which can be more intense than the temperature increase associated with climate warming. In other words, under climate warming scenarios that leads to a collapse of the AMOC, it is possible that in certain regions of the Northern Hemisphere, we observe not warming but rather cooling of average temperatures.

This physical reality is translated into our simplified GIS dynamics model with the term  $e_{21}(1 - \Psi_V)$  (see Eq. (3.3)), both in SURFER v3.1 and SURFER v3.2. This is why we observe that the most significant emission scenarios lead to GIS collapse until the point where the stabilizing effect of the AMOC is strong enough to reproduce ice volume growth for some scenarios. In SURFER v3.1 (see Fig. (76)), we observe that the stabilizing feedback is much stronger than in SURFER v3.2 (see Fig. (77)). Indeed, in SURFER v3.1, even the highest emission scenarios are capable of reforming the pre-industrial level of ice volume after the AMOC collapse bien avant 5000 AD. For some high emission scenarios, the ice volume even finds a new stable equilibrium with a value higher than the initial condition. We realize that the intensity of the stabilizing interaction is likely excessively strong in SURFER v3.1. Indeed, even in the highest emission

scenario, which creates a nearly  $8^{\circ}\text{C}$  global average temperature anomaly and persists well beyond the GIS tipping point set at  $1.5^{\circ}\text{C}$  for thousands of years, the GIS will never melt again.<sup>22</sup>

In SURFER v3.2, the stabilizing effect of the AMOC on the GIS is present but to a more realistic extent. Indeed, even though the most significant emission scenarios significantly reduce the rate of GIS melting after an AMOC collapse, they are unable to completely halt the melting due to the very substantial temperature anomaly that is created. Longer simulations up to 10 000 *AD*, available on GitHub, show that a cessation of GIS melting, even for the highest emission scenario, is achieved by 5800 *AD* due to a decrease in the temperature anomaly. This decrease in the temperature anomaly is attributed to the gradual absorption of atmospheric CO<sub>2</sub> by the ocean over long timescales, which sufficiently reduces the anomaly so that shortly after 10 000 *AD*, the GIS returns to its initial state in SURFER v3.2 under the highest emission scenario.

If it is an intermediate emission scenario that causes the most long-term melting of the GIS, it is because it represents a critical scenario combining a temperature anomaly ( $T = 5^{\circ}\text{C}$  at its maximum in 3800 *AD*) without an AMOC collapse, which would stabilize the GIS melting. This dynamic result is crucial because it demonstrates that due to the interactions between tipping elements, the AMOC indirectly increases the forcing value of the GIS tipping point.

If we revisit the GIS model (cf. Eq.(3.3)), we have that the critical bifurcation parameter can be expressed as follows,

$$W_c(T, \Psi) = d_2 T_V^c + e_{21}(1 - \Psi_c). \quad (4.2)$$

We know that a bifurcation occurs when this parameter  $W$ , which combines the two forcings, takes the value  $W_c$ , which can be easily calculated in the case where there is only one forcing on temperature,

$$W_c = d_2 T_V^+. \quad (4.3)$$

In doing so, we can calculate  $T_V^{equiv;\Psi}$ , the equivalent in terms of temperature forcing of a complete AMOC collapse on the GIS. This is simply given by the ratio  $e_{21}/d_2$ , which based on the values of these coefficients calculated in the AGTCCM, allows us to find that,

$$T_V^{equiv;\Psi} = -6.06^{\circ}\text{C}. \quad (4.4)$$

In other words, an AMOC collapse in the AGTCCM increases the GIS tipping point by  $6.06^{\circ}\text{C}$ , shifting it from  $T_V^+ = 1.5^{\circ}\text{C}$  to  $T_V^+ = 7.56^{\circ}\text{C}$ . This is observed in the highest emission scenario of SURFER v3.2, where shortly after 2500 *AD*, the temperature anomaly exceeds  $7.56^{\circ}\text{C}$ . However, since the AMOC has collapsed, even with a maximum temperature anomaly of  $8.1^{\circ}\text{C}$  in 2700 *AD*, the GIS only exceeds its tipping point by  $\delta T = 0.54^{\circ}\text{C}$ . Although significant, this

---

22. Simulations up to 500 000 *AD* with SURFER v3.1 confirm this.

temperature reduction effect<sup>23</sup> for the GIS of  $T_V^{equiv;\Psi} = -6.06^\circ C$  falls within the expected value range for this location, as demonstrated in the study using an ESM by van Westen et al.[78].

Moreover, due to the subsequent decrease in temperature anomaly, the GIS actually surpasses its tipping point, but with sufficiently low intensity and especially over a period of time short enough compared to the characteristic timescales of the internal dynamics of the GIS, such that the GIS does not bifurcate towards its collapse state. We are facing an *overshoot without tipping* phenomenon induced by the interaction of the AMOC on the GIS. This will be studied in more detail in the following section.

### **Significance of Calibrating the Coupling Coefficient from the AMOC to the GIS $e_{21}$**

As observed between SURFER v3.1 and SURFER v3.2, having a precise value of the coupling coefficient of the AMOC on the GIS,  $e_{21}$ , which encodes the intensity of the stabilizing effect of an AMOC collapse on the GIS, is crucial. Indeed, this determines which future greenhouse gas emission regimes, although they trigger the collapse of the AMOC and have significant effects on other components of the climate and thus society, can prevent the GIS from collapsing itself. Considering the potential 7 meters of sea-level rise attributed to the GIS if it were to collapse entirely, the importance of accurately calibrating this stabilizing effect of the AMOC is well justified.

However, it is important to note that in SURFER v3.2, due to the absence of hysteresis from process-based models of the GIS within the time constraints of this thesis, the calibration of  $e_{21}$  had to be partially arbitrary. Therefore, even though we kept the coordinates of the critical bifurcation points associated with temperature present in SURFER v3.1, we had to set the values of  $\Psi_V^+$  and  $\Psi_V^-$  based on qualitative judgment informed by the literature. In doing so, we partially arbitrarily modify the value of  $e_{21}$  as shown in Equation (3.106). Different personal experiments for other values of  $\Psi_V^+$  and  $\Psi_V^-$  (whose figures are available on the GitHub of this thesis) have demonstrated the high sensitivity of these values in the intensity of the stabilizing interaction of the AMOC on the GIS. However, given the good results of the AGTCCM for the AMOC with the calibration of the cGenie experiments, this motivates us to further push future work once hysteresis from process-based models of the GIS becomes available.

### **The Importance of Different Time Scales in Cascade Collapses**

As analyzed in the study by Dekker et al. [19] on cascading collapses, we observe that the coupling of the two systems (cf. Fig. (18,19)), in our case the AMOC

---

23. The impact of an AMOC collapse on the GIS can be understood in two ways : either by the fact that it raises the tipping point associated with the average global temperature of the GIS by  $6.06^\circ C$ , or by the fact that it reduces the actual temperature experienced by the GIS by  $6.06^\circ C$ . Both interpretations are correct.

and the GIS, introduces a direction to the cascade. In their study, only a unidirectional and destabilizing interaction is examined between tipping elements, whereas in our case, we have a bidirectional interaction between the AMOC and the GIS, with the peculiarity that one is stabilizing and the other destabilizing. Furthermore, the study by Dekker et al. [19] is limited solely to a forcing of the following system by its interaction with the leading system. In our study, we have a more complex situation where both systems share a temperature forcing, the impacts of which on each of the tipping elements are differentiated by a distinct calibration taking into account their internal dynamics.

However, we can adopt the semantics of the *leading system* and *following system* introduced in the study by Dekker et al.[19] and generalize it by applying it to our findings. If we consider the destabilizing interaction of the GIS on the AMOC, we can view the GIS as the *leading system* and the AMOC as the *following system*. Indeed, in the case of the 9th lowest emission scenario in the simulations of SURFER v3.2 (cf. Fig. (73)), we previously observed that the tipping point by temperature forcing is not reached. Instead, it is a critical freshwater flux from the GIS that, together with the sum of these two forcings, causes the AMOC to bifurcate towards complete collapse. It is the change in the *following system* induced by the *leading system* that brings the *following system* closer to its bifurcation point and ultimately leads to its collapse. In the case of the stabilizing interaction of the AMOC on the GIS, the roles are reversed. The AMOC becomes the *leading system*, and its collapse induces a change in the bifurcation parameter of the GIS. In this particular case, it prevents the GIS from bifurcating by moving it away from its bifurcation point. In the context of this stabilizing interaction from the *leading system* (AMOC) to the *following system* (GIS), we observe that the *leading system* (AMOC) is capable of significantly repositioning the equilibrium point of the *following system* (GIS), as seen earlier in equation (4.4), resulting in a shift of the tipping point by  $6.06^{\circ}\text{C}$ .

If we consider both interactions together, strictly speaking, we are dealing with two systems that are both *following* and *leading systems* simultaneously. The role they effectively play is determined by the form of the temperature forcing that impacts both tipping elements. This dependency arises from the characteristic differences in time scales between these tipping elements. In our collapse results presented for the AMOC and the GIS, the differences between  $\tau_1 = 700$  years and  $\tau_2 = 10$  years play a fundamental role in the evolution of the trajectories of the two coupled systems. These coefficients, which encode the physical differences in time scales for significant variations in the intensity of the AMOC and the volume of the GIS, create a strong dependence in the form of the non-stationary background forcing[15], which is that of temperature. Different combinations of collapses, potentially cascading, can be created due to the specific form of the chosen temperature forcing. This is particularly evident for the GIS, which, due to its very large inertia of several centuries, can withstand significant overshoots on its temperature tipping point, thanks to the stabilizing

effect of the AMOC. In the opposite direction, it is the large melting inertia of the GIS that allows, despite its considerable volume, for freshwater fluxes to be produced that are sufficiently low to not exceed the tipping point of the AMOC solely via the haline branch of the circulation. These differences in time scales were also something missing in the study by Dekker et al.[19], and our study thus shows that the separation of time scales between the coupled tipping elements also leads to some of the rich behavior of collapse of the systems.

### Conclusions on the AGTCCM’s Ability to Produce Tipping Cascades

Through these results and discussions, we have demonstrated the relevance, validity, and utility of the AGTCCM and the v3.2 version of SURFER developed in this thesis for simulating the cascade collapses of the AMOC-GIS. Taking into account, in a realistic manner yet within a framework of nonlinear dynamics capturing the dominant mechanisms of AMOC and GIS evolution, allows for a more accurate constraint on the possible collapse scenarios of these two fundamental tipping elements in the climate system. Indeed, although we have studied cascade collapses, given the nature of the AMOC and GIS and one of the two interactions being stabilizing, no collapse scenario of the GIS followed by the AMOC, or vice versa, has been produced. The most common scenario encountered is that of an *incomplete cascade*, where the onset of GIS collapse contributes to that of the AMOC but once the AMOC collapses, it in turn spares the GIS due to a sufficiently rapid decrease in forcing.[14] Table (7) summarizes the different collapse configurations that could potentially be simulated *a priori* and what is produced in the AGTCCM. To streamline the synthesis, exceptions related to the overshoot without tipping phenomenon will be discussed in the following section.

In conclusion, we can support the findings of the study by Sinet et al. [68], namely that the stability of the climate system, particularly of the AMOC and the GIS, is drastically altered when considering interactions between the tipping elements, in agreement with the more abstract results of Wunderling et al. [85]. Addressing our research question regarding the consequences of a realistic coupling between the AMOC and the GIS on their collapse dynamics, we have thus better constrained and illustrated the various possible trajectories under 15 plausible emission scenarios covering the spectrum of typical SSP scenarios. Compared to SURFER v3.1, we have seen the utility of more realistic calibration of the internal dynamics of the AMOC and the GIS, but especially of their interactions. The main difference has been to illustrate a case of AMOC collapse triggered by considering the freshwater flux  $F_{GIS}$  in addition to the temperature forcing. Furthermore, although SURFER v3.2 did not highlight a new collapse configuration that could not already be illustrated in SURFER v3.1, the first added value of SURFER v3.2 was to more realistically constrain the possible collapse scenarios. This is particularly useful when also considering possible interactions with other tipping elements. Indeed, as the AMOC and GIS are key tipping elements in the climate system capable of triggering cascading

First Tipping	Second Tipping	Results in AGTCCM
AMOC	GIS	Not possible to tip GIS thanks to AMOC because stabilizing interaction.
AMOC	No GIS Tipping	Most common configuration, call the <i>incomplete cascade</i> . Appears for the highest emission scenarios such that $d_2T + e_{21}(1 - \Psi) \leq d_2T_V^+$ but $T \geq T_V^+$ . Shown in Fig.(75)
GIS	AMOC	$F_{GIS}$ not sufficient for tipping AMOC alone. Possible key role of $F_{GIS}$ for tipping AMOC if temperature forcing $T$ near $T_\Psi^+$ . Shown in Fig.(73).
GIS	No AMOC Tipping	Possible for a range of emission scenarios such that $T \in [T_V^+, T_\Psi^+]$ . Shown in Fig.((75))
No GIS Tipping	No AMOC Tipping	Possible for emission scenarios such that $T \leq T_V^+ \ll T_\Psi^+$ .

TABLE 7 – *Synthesis of the various combinations of potential dynamics and commentary on their production in the AGTCCM.*

collapses involving other tipping elements, better constraining their dynamics of potential collapses helps to better constrain the regimes of emission scenarios that could lead to *hothouse narratives*.

In addition, we were able to fully exploit the richness of the nonlinear systems dynamics framework, namely the ability to conduct more in-depth analysis and understanding of the results based on physical and mathematical intuitions. Moreover, being a model composed solely of coupled ODEs, we benefit from very significant computational savings with the AGTCCM. Indeed, with SURFER v3.2, we have a tool for simulating AMOC and GIS collapses that can extend over very long time scales up to 500 000 years, capable of running 15 simulations over this time scale in approximately 11 seconds on a laptop<sup>24</sup>. This efficiency, combined with the quality of the model, allows it to serve as an exploratory emulator for possible collapse scenarios under various forcing conditions.

Finally, our study has highlighted the crucial role of the coupling coefficients  $e_{12}$  and  $e_{21}$  in the possible worlds that can be created. We believe that further work using this paradigm of emulation through simplified nonlinear dynamics of process-based model hysteresis is important for better constraining these possible worlds.

24. CPU : 11th Gen Intel® Core™ i7-1165G7 @ 2.80GHz × 8, RAM : 16GB

## 4.4 Overshooting phenomena in the bifurcation diagram

### 4.4.1 Results

We now wish to focus on a final interesting and important phenomenon in terms of mitigation policies, which is that of *overshoot without tipping*. Although some of the simulations already presented, extending up to 5000 AD, hinted at this phenomenon, we aim to investigate it more thoroughly in this section. To do so, 15 simulations, still under the same  $CO_2$  emission forcing scenarios, were conducted, but this time leveraging the capabilities of SURFER v3.2 to extend the simulations up to 500 000 AD.

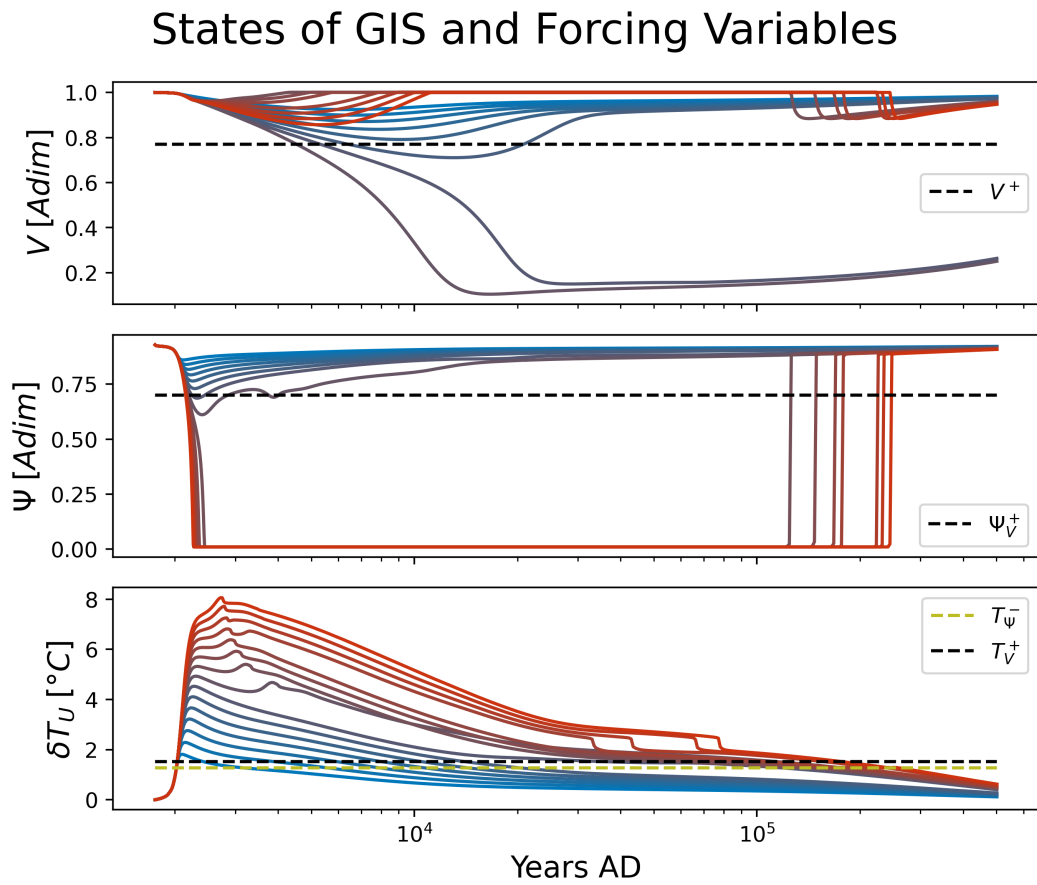


FIGURE 78 – Trajectories of the AMOC and GIS and the global mean temperature forcing for 15 simulations up to 500 000 AD in SURFER v3.2.

The Figure (79) depicts the trajectories of the GIS and AMOC in their bifurcation diagrams relative to the forcing of global mean temperature. These trajectories in the bifurcation diagrams provide an alternative perspective for understanding the results of the different collapse dynamics of the AMOC and GIS discussed in the preceding section. To provide a comprehensive view, the trajectories of the AMOC and GIS, along with the atmospheric temperature

anomaly, are also shown in Figure (78).

### **Evolution of the GIS and AMOC over 500 000 years**

Noting that on this latter figure, the  $x$ -axis is on a logarithmic scale, we observe the sequence of evolutions of the trajectories of the different variables from Figure (75). For the GIS, it is observed that the trajectories of scenarios with the highest  $CO_2$  emissions stabilize completely beyond 5000 AD, reaching a new stable equilibrium of the nominal state, which even has a value slightly higher than that of the pre-industrial equilibrium. An interesting phenomenon occurs with destabilizations that take place after 100 000 AD on these same trajectories, resulting from a reformation of the AMOC transitioning from collapse to its nominal state. Indeed, observing the temperature anomaly, it is noted that around 100 000 AD, this anomaly drops below  $T_\Psi^- = 1.27^\circ C$ , and since  $\Psi^- = 0.022$ , the tipping point associated with this stable equilibrium is surpassed, allowing the AMOC to bifurcate and reform. While the AMOC has a stabilizing effect on the GIS when it collapses due to its regional temperature anomaly reduction effect, the reformation of the AMOC, by transporting heat back to the Northern Hemisphere, has a destabilizing effect on the GIS. This physical reality is also mathematically reflected by the term  $e_{21}(1 - \Psi)$  in Eq. (3.3).

Additionally, Figure (78) and Figure (79), which depict the trajectories of the AMOC bifurcating towards its nominal state at the end of the simulation, illustrate the hysteresis effect introduced in Chapter I. The critical threshold necessary for the reformation of the AMOC is significantly lower ( $T = 1.27^\circ C$ ) than that associated with its collapse ( $T = 5.5^\circ C$ ), indicating that the AMOC exhibits a loss of reversibility once the system has collapsed.

Moreover, Figure (78) confirms over longer time scales that only intermediate scenarios of greenhouse gas emissions, which do not trigger AMOC collapse but still produce a significant atmospheric temperature anomaly ( $\approx 5^\circ C$ ), will almost completely melt the GIS in the long term.

A final observation concerns the time scales required for the carbon cycle to absorb the disturbance from anthropogenic emissions, as even after 500 000 AD, the temperature anomaly is not completely absorbed for the most significant emission scenarios.

### ***Overshoot without tipping* in the Bifurcation Diagrams**

In Figure (79), by depicting the trajectories of the AMOC and GIS directly within their bifurcation diagrams relative to the atmospheric temperature anomaly, a clearer identification of bifurcations is facilitated. This is particularly evident for the AMOC, where it is observed that once the tipping point is surpassed concerning temperature forcing, the AMOC bifurcates towards its collapse state. The subtle differences between the actual trajectories, which surpass the tipping point before bifurcating, are due to the forcing occurring

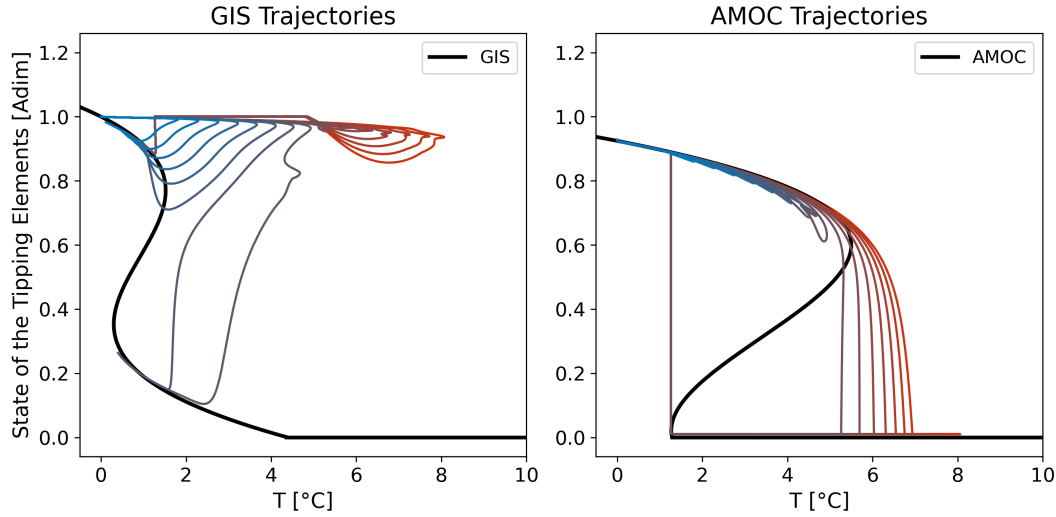


FIGURE 79 – *Trajectories of the AMOC and GIS in their bifurcation diagrams with respect to the forcing of global mean temperature for 15 simulations up to 500 000 AD in SURFER v3.2.*

"too rapidly" for the system to remain in equilibrium. Conversely, trajectories that bifurcate just before the temperature tipping point allow identification of the effect of the GIS forcing, which occurs concurrently but is not represented in this two-dimensional bifurcation diagram. It is important to note that Figure (79) represents only the projection onto the plane  $F_{GIS} = 0 \text{ Sv}$  of the trajectories depicted in Figure (72). Furthermore, in Figure (79), the bifurcation from the collapse state to the nominal state for the highest emission scenarios is distinctly observed once the temperature anomaly surpasses the lower tipping point. It is noteworthy that in the reformation of the AMOC, it is purely through temperature forcing that it occurs ; however, a destabilizing forcing by  $F_{GIS}$  is subsequently created due to significant GIS melting with the reformation of the AMOC. Nevertheless, this latter interaction is of second order and cannot counterbalance the AMOC bifurcation. Lastly, for the lowest emission scenarios, trajectories experiencing only a decrease in AMOC intensity due to a decrease in the equilibrium value of the nominal state are observed, but not sufficiently to reach the upper bifurcation point.

The interesting findings in this section concern the trajectories of the GIS in the bifurcation diagram relative to the temperature anomaly. Indeed, this enables us to distinctly observe that all trajectories surpass the GIS bifurcation point concerning temperature for a sufficiently long period. The temperature forcing has the effect of displacing the GIS from its stable equilibrium for a very extended period. Specifically, calculations based on simulation data reveal that the GIS spends nearly 50 000 years in a state outside of the stable equilibrium of the nominal state and its normal evolution with temperature forcing. In other words, the GIS remains out of equilibrium for 50 000 years, yet the

intensity and duration of the forcing pushing it outside of its stable equilibrium are insufficient to move the GIS away from this attractor. Lastly, it is evident how the collapse of the AMOC, due to its stabilizing effect on the GIS, enables surpassing the GIS tipping point by over  $6^{\circ}\text{C}$  without triggering a shift.

#### 4.4.2 Discussion

The results just mentioned for the GIS are indicative of *overshoot without tipping* phenomena as described by Ritchie et al.[61, 62]. If we focus on emission scenarios that do not trigger AMOC tipping initially, the sixth scenario from the least intense produces a maximum temperature anomaly of  $4^{\circ}\text{C}$ , well beyond the tipping point of  $T_V^+ = 1,5^{\circ}\text{C}$ . However, despite the intensity of the disturbance, the characteristic time scale for the change in forcing - denoted as  $d$  following the notations of Section (2.2) - remains sufficiently small compared to the characteristic time scale of the system's internal dynamics,  $\tau$ . Thus, the GIS can still venture far from the bifurcation point without tipping. We have thus identified global warming trajectories that permit a safe overshoot of the prescribed thresholds. Therefore, we understand that while the critical temperature of each tipping element is important as it determines the magnitude of the possible overshoot of the tipping point, it is the characteristic time scale of the internal dynamics  $\tau_i$  that determines the critical time beyond which an overshoot transforms into a bifurcation.[15, 62]

These results are not surprising for Greenland due to the fact that it takes a considerable amount of time and energy to melt large quantities of ice, which gives it a characteristic time scale of  $\tau \approx 700$  years in SURFER v3.2. However, climate change is occurring very rapidly, as evidenced by the interpolation of SSP scenarios conducted here, with a duration of  $d \approx 450$  between 1750 *AD*, the onset of the disturbance, and 2200 *AD*, the peak of the temperature anomaly under this scenario.

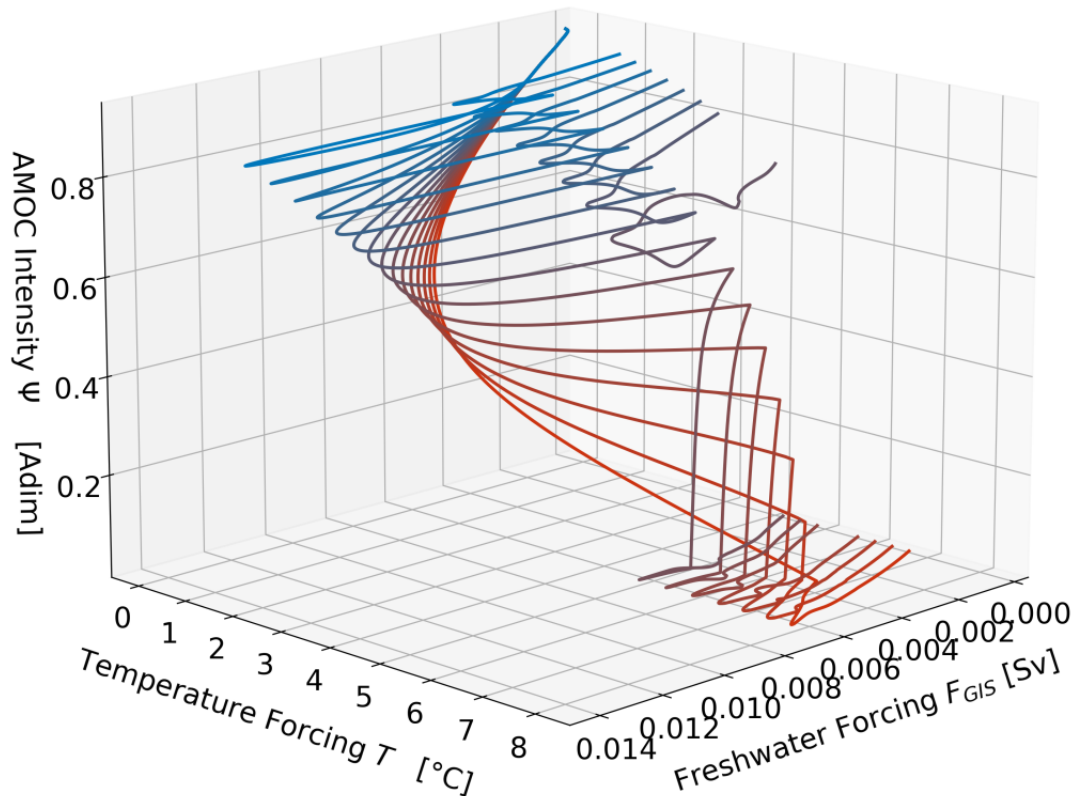
Thus, cryospheric components such as the GIS or the WAIS may be resilient to collapse even with relatively low tipping points in terms of temperature anomaly because they have long tipping time scales. They are what Ritchie et al.[62] call *slow-onset tipping points* while other tipping elements such as the AMOC, permafrost, or the Amazon rainforest could be at risk due to their shorter time scales.[15] These differences between tipping elements with the earliest thresholds, which also possess the longest timescales, and faster tipping elements, which tend to have higher thresholds (such as permafrost and the Amazon rainforest), imply that the safe levels of peak warming are determined by faster-onset tipping points, whereas the safe stabilization warming levels are set by slower-onset tipping points.[62] These findings underscore the importance of constructing the most precise mapping possible of safe overshoot domains for each tipping element, taking into account their interactions with others. By doing so, based on the intersections of safe overshoot regions, we can determine which warming trajectories are more desirable than others.

Moreover, given that SURFER is not a model for assessing the impacts of climate warming, it is crucial not to underestimate the catastrophic impacts on both human society and biodiversity from trajectories that, even if they do not tip the Greenland Ice Sheet (GIS), do tip the Atlantic Meridional Overturning Circulation (AMOC). For instance, a scenario with an  $8^{\circ}\text{C}$  global average atmospheric temperature anomaly, even if an AMOC collapse leads to a local decrease to approximately  $2^{\circ}\text{C}$  in the Northern Hemisphere, would already likely result in a significant increase in the frequency and intensity of extreme weather events. Furthermore, while the temperature anomaly may be "only"  $\approx 2^{\circ}\text{C}$  in the North Atlantic region, it would be  $\approx 8^{\circ}\text{C}$  elsewhere in the world, thus carrying devastating consequences.

Finally, this study of overshoot without tipping phenomena involving multiple tipping elements and considering their interactions advances the characterization of safe overshoot, a topic still insufficiently explored in that framework. Indeed, research into the safe and unsafe boundaries of tipping elements has thus far been conducted only for individual elements.[62] However, as we have demonstrated, interactions can significantly lower but also raise (as in the case of the GIS) individual tipping point thresholds, potentially drastically altering the regions of safe and unsafe overshoot.

In conclusion, we observe that the AGTCCM effectively reproduces relevant phenomena of *overshoot without tipping* while considering interactions between tipping elements. Given the significance of these phenomena for human society and life on Earth, this underscores the importance of continuing efforts to improve methodologies such as the AGTCCM. This involves reducing calibration errors and conducting more emulations using data from process-based models. Constraining tipping point dynamics more realistically will enable a more accurate identification of emission scenario regimes that not only overshoot tipping points but also do so safely by avoiding the triggering of irreversible shifts in underlying systems.

# Conclusion and Outlook



## 5 Conclusion and outlook

### 5.1 *Tipping Points, Tipping Elements and Tipping Cascade*

Our primary research question in this thesis was to understand the effect of realistically accounting for the couplings between the AMOC and the GIS on their collapse dynamics. To address this, we began in Chapter I by motivating this study through the definition of the concepts of *tipping points*, *tipping elements*, and *tipping cascades*. It was explained that a tipping point is a critical threshold beyond which a system reorganizes, often abruptly and/or irreversibly. Tipping elements, on the other hand, are large-scale components of the Earth system that may reach a tipping point. Each tipping element has its own internal dynamics centered around feedback processes of specific physical phenomena. Tipping can occur when amplifying/reinforcing (positive) feedback mechanisms overwhelm damping/balancing (negative) ones and become strong enough to support self-perpetuating change. Due to their interactions, these tipping elements can have stabilizing or destabilizing impacts on each other's dynamics, potentially creating tipping cascades, also known as domino effects.

### 5.2 The Importance of the AMOC and the GIS as Tipping Elements

#### 5.2.1 AMOC

The AMOC and the GIS are tipping elements. In the case of the AMOC, the source is the ocean advective or salinity advection feedback. The intensity of the AMOC is determined by the advection of warm, salty water from the South Atlantic to the North Atlantic, which, once cooled in the North Atlantic, becomes dense enough to sink and form the North Atlantic Deep Water (NADW). The ocean advective feedback is positive because if the intensity of the circulation decreases due to any haline or thermal perturbation mentioned in Chapter I (such as an increase in temperature or the addition of freshwater), the salinity transport towards high latitudes is reduced. This induces a decrease in density there, thus decreasing the intensity of the flow, which reinforces the initial perturbation. Consequently, there exists a threshold in the intensity of the initial perturbation beyond which the circulation system collapses into equilibrium.

The AMOC is identified as a tipping element because simulation data have shown that, beyond a certain critical stratification threshold in the North Atlantic waters, the circulation can collapse and reorganize within a few decades, reaching a second stable equilibrium known as a collapse state, in which the circulation ceases. These collapse experiments are conducted using various types of models, ranging from conceptual models and EMICs to ESMs. In these models, once a critical threshold of water warming or freshwater input (in hosing experiments) is surpassed, the circulation collapses. When these forcings are reversed,

### 5.3 The Physical Coupling Mechanisms for the AMOC-GIS Tipping Cascade

---

the recovery of the AMOC occurs at significantly lower levels of freshwater forcing compared to the levels that initially triggered its collapse, indicating pronounced hysteresis behavior, a characteristic phenomenon of tipping points. In addition to its role as a tipping element, the AMOC is a key climate system because it is a major mechanism for distributing heat from the Southern Hemisphere to the Northern Hemisphere in the Atlantic, thereby having significant consequences for the climate in this region. A complete collapse of the AMOC would result in a reduction of the global mean temperature by  $-0.5^{\circ}C$ , and locally, it could decrease temperatures by nearly  $7^{\circ}C$  in cities like London. Furthermore, the absence of surface water transport to the depths of the Atlantic due to an AMOC collapse would reduce Atlantic ventilation by nearly 30%. A recent study quantified that the equilibrium impact on atmospheric  $CO_2$  concentration following an AMOC shutdown would range between 13  $ppm$  and 34  $ppm$  by 2500. Other impacts, such as a southward shift of the ITCZ, changes in monsoon patterns, and effects on marine ecosystems, are also expected following an AMOC collapse.

Observations of AMOC intensity show a slowdown, and the critical threshold associated with global mean temperature starts at  $1.4^{\circ}C$  in some models, a temperature anomaly that will be reached in a few years. Additionally, AMOC collapses have occurred in the past. Consequently, Wang et al. consider the probability of its collapse during the 22nd century to be significant under middle-of-the-road emission scenarios, underscoring the importance of studying the AMOC for all the reasons mentioned.

#### 5.2.2 GIS

The GIS is the second largest ice cap after Antarctica and is currently melting at an increasing rate due to global warming. It is also a tipping element because models have demonstrated the existence of a critical warming threshold beyond which the melt-elevation feedback becomes strong enough to support self-sustaining melt. As the ice melts, its highest layers lose altitude, exposing them to warmer air, which further accelerates melting and the loss of altitude. Although complete melting would take centuries, the total melt of the GIS has the potential to raise sea levels by 7.42;  $m$ , submerging cities like New York, Jakarta, and parts of Bangladesh. As with other tipping elements, there is considerable uncertainty in identifying the critical threshold, but the best estimate, which has the most consensus in the literature, is  $1.5^{\circ}C$ .

### 5.3 The Physical Coupling Mechanisms for the AMOC-GIS Tipping Cascade

Beyond their respective collapse dynamics, the central focus of this thesis is the study of their interactions that could lead to tipping cascade phenomena. Indeed, the melting of the GIS produces freshwater that flows into the North

Atlantic and the NADW formation regions, exerting a destabilizing effect on the AMOC by promoting surface water stratification and bringing the AMOC closer to its tipping point. Conversely, the interaction of the AMOC with the GIS is stabilizing because a slowdown of the AMOC reduces heat transport to the Northern Hemisphere, significantly lowering the average temperature around the GIS. This, in turn, stabilizes the melting process. Thus, these two physical mechanisms can produce a cascade collapse dynamic; specifically, a collapse of the GIS could contribute to or trigger a collapse of the AMOC. Given the crucial role of realistically accounting for the couplings between the AMOC and the GIS in their future evolution, we sought to develop a model that better evaluates these interactions.

## 5.4 A Simplified AMOC-GIS Model Capable of Emulating Complex Models

Complex models such as EMICs and ESMs have limitations in simulating the cascade collapses of the AMOC and GIS due to their overly stabilizing systematic biases and operational constraints related to their computational time requirements. Furthermore, even with process-based model identification, the critical values of the tipping points associated with different tipping elements remain highly uncertain. Consequently, a growing portion of recent literature has begun to study tipping elements not by attempting to describe the physical processes in their dynamics in the greatest possible detail, but by using dynamical systems theory to capture the essential first-order dynamics necessary to produce the expected collapse phenomena. This reductionist approach has the advantage of clearly identifying the different forcing terms and the various collapse dynamics that can occur, especially with the concepts related to non-linear dynamics introduced in Chapter I. To this end, the dynamics of tipping elements are modeled using the canonical form of double-fold bifurcation. Several studies have validated this assumption by demonstrating the existence of at least two stable equilibria for the AMOC and GIS, separated by an unstable equilibrium, along with the bifurcation dynamics associated with a double-fold. Moreover, since these models consist of only fairly elementary coupled ODE systems, they are very computationally efficient, allowing for easy exploration of the different time scales associated with the tipping elements of interest.

In line with the work of Wunderling et al. [85, 86, 88], Sinet et al. [68], and V. Couplet [16, 13, 15], we decided in this thesis to adopt the model proposed by V. Couplet described in Section (3.2.2). However, the limitations of this model included the absence of the stabilizing interaction of the AMOC on the GIS and, most importantly, the lack of a realistic methodology for calibrating the coupling coefficients between the AMOC and the GIS.

The methodological challenge at the heart of this thesis was the development of the AMOC-GIS Tipping Cascade Calibration Model (AGTCCM). This mo-

del, utilizing a simplified double-fold dynamics for the AMOC and the GIS, allows for the consideration of their respective couplings while calibrating their dynamics based on hysteresis curves derived from any more complex model.

To this end, in the parameterization of the intensity  $\Psi$  of the AMOC and the volume  $V$  of the GIS, an additional forcing term was added to V. Couplet's AMOC model to account for the forcing by the freshwater flux  $F_{GIS}$ , such that it is proportional to the temporal variation of the GIS volume denoted by  $V$ . A third forcing term (temperature  $T$  already being present) was also added to model the second freshwater flux  $F_{P-E}$ , which can be crucial in the collapse of the AMOC and is physically associated with variations in  $P - E$ . For the GIS model, a term proportional to the intensity of the AMOC ( $\Psi$ ) was added to account for the stabilizing effect of the AMOC on the GIS dynamics.

The calibration part of the AGTCCM was developed based on a generalization of the method by Martinez Monteiro et al. [52] used in SURFER v2.0 to calibrate ice caps. The challenge was that in SURFER v2.0, only a temperature forcing term was present in the double-fold dynamics, whereas in our parameterization of the AGTCCM, we have two forcing terms for the GIS ( $T, \Psi$ ) and three for the AMOC ( $T, F_{GIS}, F_{P-E}$ ). To address this issue, we assumed that we could produce independent sensitivity experiments using process-based models of the AMOC or the GIS. From an operational standpoint, many models allow for this experimental design, thus making this assumption not overly restrictive. Building on this working hypothesis, an original methodology for calibrating the double-fold dynamics was developed.

After a preliminary validation test, this calibration methodology was successfully applied to the AMOC based on three hysteresis experiments from cGenie, an EMIC. The first experiment involved a sensitivity test of the AMOC intensity with respect to atmospheric CO<sub>2</sub> concentration, thus representing a temperature forcing, while the other two simulations were hosing experiments aimed at reproducing the effects of the  $F_{GIS}$  and  $F_{P-E}$  forcings.

Limitations of the AGTCCM and its original calibration methodology have been identified. Firstly, it was *a priori* expected that it would not be possible to perfectly encode the richness of the complexity of hysteresis from process-based models with a simplified dynamics that is mathematically only a third-order polynomial. Errors between the real hysteresis of the emulated model and that of the emulation will inevitably appear, but the approach has always been to calibrate the temperature forcing hystereses as accurately as possible, given that for both the AMOC and the GIS, these are the dominant forcing terms. Regarding the AMOC and GIS models themselves, it concerns the parameterizations of freshwater fluxes, especially  $P - E$ . In practice, the proposed linear parameterization is too simplistic and does not scientifically reproduce reality acceptably. Furthermore, the literature lacks precise data on the evolution of  $P - E$  anomaly over the Atlantic basin with climate warming, further limiting its calibration. Therefore, in the numerical code of the AGTCCM, this  $F_{P-E}$  flux forcing can be easily deactivated. As for the calibration model of the AGTCCM,

three limitations have been identified : the overdetermination of independent terms  $c_i$ , calibration to pre-industrial values, and the equality of critical values of tipping elements between sensitivity experiments.

## 5.5 SURFER v3.2, the integration of the AGTCCM into SURFER, and its impact on the carbon cycle

Next, for analysis purposes under future emission scenarios, we aimed to integrate the AGTCCM into a climate model. We chose SURFER, an efficient conceptual and partly process-based climate model with a carbon cycle that accurately reproduces results from more complex models even over long time scales. Tipping element modelings, including the AMOC and the GIS, are already present in SURFER version v3.1. However, the GIS and AMOC suffer from the same limitations as the preceding Couplet model. The destabilizing feedback of the GIS on the AMOC is absent, and most importantly, coupling coefficients are not calibrated based on complex model experiments.

The major task in integrating the AGTCCM into SURFER (to form SURFER v3.2) was to parameterize SURFER's carbon cycle so that an AMOC shutdown could reproduce an increase in atmospheric  $CO_2$  concentration as expected in the literature. To achieve this, a linear parameterization of the carbon transport coefficients between SURFER's three ocean layers was added, creating a dependency on the intensity of the AMOC. In this way, an AMOC shutdown, by emulating increased stratification of the ocean layers, reduces the carbon transport between these layers, reproducing the expected carbon buildup in the upper ocean layer and ultimately resulting in a 20.5;  $ppm$  increase in atmospheric  $CO_2$ .

In Chapter III, we presented results obtained with this new version of SURFER v3.2 developed. Systematically, we force the model with 15 scenarios, ranging from historical emissions from 1750 to 2010, followed by Gaussian interpolations between the SSP1-2.6 and SSP5-8.5 scenarios. Based on this spectrum of simulations, various trajectories of AMOC collapses were simulated. However, no nonlinear response in the different carbon reservoirs of SURFER was observed. While an equilibrium increase of 20.5  $ppm$  in atmospheric  $CO_2$  is indeed produced, the linear parameterization of the dependency on the intensity of the collapsing AMOC is not sufficiently abrupt to induce a nonlinear response in the carbon cycle reservoirs. The increase in atmospheric concentration and the bottleneck phenomenon in the upper ocean are quantifiable but not distinguishable from background emissions associated with anthropogenic forcings. However, it is worth noting that scenarios in which these 20.5  $ppm$  of  $CO_2$  lead to crossing the tipping point associated with GIS temperature could indeed be simulated.

## 5.6 Cascade Collapses of the AMOC-GIS

Finally, to address the question of the effect of a realistic coupling between the AMOC and the GIS on their collapse dynamics, we conducted simulations up to 5000 AD of the AMOC and the GIS under the 15 emission scenarios described above using SURFER v3.2, which we compared with the trajectories of these systems under the same forcing scenarios in SURFER v3.1. Due to the absence of hysteresis experiments found for the GIS within the time frame of this thesis, the dynamics of the GIS in SURFER v3.1 and SURFER v3.2 with respect to temperature forcing will be the same. In contrast, the dynamics of the AMOC in SURFER v3.2 are calibrated to emulate as closely as possible the response produced in the cGenie experiments. Thus, the AMOC in SURFER v3.2 has a tipping point associated with temperature that is higher,  $T_{\Psi}^+ = 5.5^{\circ}\text{C}$ , than that in SURFER v3.1,  $T_{\Psi}^+ = 4^{\circ}\text{C}$ . However, the AMOC in SURFER v3.2 has an additional forcing term with the freshwater flux, which is coupled to the state of the GIS.

### 5.6.1 AMOC collapses

It has been shown that this new destabilizing coupling of the GIS on the AMOC can be decisive in scenarios where temperature forcing alone does not reach the tipping point of the AMOC. Indeed, the additional forcing by  $F_{GIS}$  is crucial in a simulation, even if this  $F_{GIS}$  forcing alone does not exceed the tipping point associated with freshwater flux ; it is the combination of these two forcings that shifts the AMOC by crossing the critical threshold associated with the sum of the two forcings. This result underscores the importance of considering the destabilizing interaction of the GIS on the AMOC. Furthermore, our results confirm those of the literature, namely that it is not possible to trigger the AMOC solely by the freshwater flux from the GIS. To achieve this, values of flux that are physically unattainable would be required, even in cases of maximum melting rates of the GIS. However, it is indeed the temperature forcing that dominates under future emission scenarios for the AMOC.

The comparison between the trajectories of the AMOC in SURFER v3.1 and SURFER v3.2 reveals significant differences. Despite the addition of an additional forcing term  $F_{GIS}$  in SURFER v3.2, the latter version, which incorporates the AGTCCM, simulates 7 collapse scenarios of the AMOC, while 9 collapse scenarios are simulated in SURFER v3.1. This is primarily due to the difference in the position of the critical tipping point threshold between the two versions, highlighting the importance of accurately identifying this value. Furthermore, nearly 155 years separate the first collapse of the AMOC in SURFER v3.2 compared to SURFER v3.1. This is a consequence of the shape of the stable manifold associated with the stable equilibrium of the nominal state, which differs between the two versions of SURFER. This supports the previous conclusion regarding the importance of fine calibration of the hysteresis, as even slight differences can produce vastly different collapse outcomes.

### 5.6.2 GIS collapses

SURFER v3.2 effectively accounts for the stabilizing effect of an AMOC collapse on the GIS. Indeed, it is not the most significant emission scenarios that cause the GIS to melt the most, as for these scenarios, an AMOC collapse helps maintain the trajectories of the GIS within the attractor of its nominal state, even if the tipping point associated with the temperature  $T_V^+ = 1.5^\circ C$  is widely exceeded. In fact, it is calculated that an AMOC collapse in the AGTCCM with the specific critical point coordinates taken here has the effect of increasing the GIS temperature tipping point by nearly  $T_V^{equiv;\Psi} = 6.06^\circ C$ . Based on studies[78] of the cooling impact of an AMOC collapse around the GIS, this result appears acceptable.

While the calibration of the stabilizing effect of the AMOC on the GIS is better addressed in SURFER v3.2 with the AGTCCM, as this coupling was overly stabilizing in SURFER v3.1, it must be acknowledged that due to the absence of process-based model hysteresis for the GIS, this calibration, even in SURFER v3.2, was partly arbitrary because it still required defining values for  $\Psi_V^+$  and  $\Psi_V^-$ . However, the emulation framework enabled by the AGTCCM has proven effective for the AMOC, and once process-based model hystereses for the GIS become available, the simplified dynamics of the GIS can be efficiently and more realistically calibrated accordingly.

### 5.6.3 Overshoot Without Tipping

SURFER v3.2 also allows illustrating the phenomena of *overshoot without tipping*. These phenomena emphasize the importance of considering interactions between tipping elements and accurately parameterizing them as they prove decisive in defining emission-safe pathways. Since trajectories with the same total emission quantity but emitted over time in different ways produce significantly different future climates, better parameterization of tipping element dynamics is fundamental.

### 5.6.4 The innovative methodology of the AGTCCM and its perspectives

In conclusion, it can be seen that the AGTCCM, along with SURFER and the additional temperature forcing, allows for the generation of all possible combinations of collapses between the AMOC and the GIS. Most importantly, the AGTCCM, through its emulation of process-based models, enables a more realistic constraint on collapse scenarios and thus on potential future climates. This is crucial for adaptation and mitigation policies in response to climate change, given the significant impacts that the collapse of these two tipping elements would have on human society and biodiversity. Furthermore, these more realistic parameterizations allow for the simulation of a new dynamic that could not be present in the previous version of SURFER, namely, a collapse of the

AMOC resulting from the combination of temperature forcing and freshwater flux from the GIS. In terms of cascade collapse, we observe the case of an *incomplete cascade* for the highest emission scenarios due to the stabilizing effect of the AMOC on the GIS. Indeed, the AMOC collapses but then prevents the collapse of the GIS. All these results demonstrate the importance of considering, in the most realistic manner possible, the interactions between tipping elements because they can significantly alter their collapse trajectories.

In this thesis, we have developed and demonstrated an original and innovative methodology for emulating simplified dynamics of tipping elements on process-based models to study cascade collapse dynamics of the AMOC-GIS. This methodology allows us to obtain the benefits of simplified dynamics in terms of computational time, but more importantly, in terms of understanding the physical processes and interactions by addressing the question of what the minimal conditions are for distinct collapse phenomena to occur. The inspiring results obtained with this methodology motivate its application to other tipping elements as well, based on complex hysteresis from other models. More broadly, SURFER v3.2 with its emulations of process-based models can serve as a pre-diagnostic tool in the future before launching simulations with more complex models, leveraging the ease of sampling the forcing space provided by SURFER v3.2 with its very limited computational time. Moreover, conceptual models such as the AGTCCM have always been the basis for future developments. The reductionist approach is one of the successes of science, and simulations of the AGTCCM can provide insights into improving the parameterizations of collapse dynamics of tipping elements in more complex models. Finally, coupling SURFER v3.2 with a spatial emulator such as MESMER[5] in the future would enable the production of a coherent and efficient climate model, which not only includes realistic tipping element emulation but also serves as a basis for impact analysis on extreme events associated with the collapse of these tipping elements. In addition to the consequences on the anomaly of global mean temperature, key variables in terms of impact analysis such as sea level rise are already simulated in SURFER and can subsequently serve as a basis for spatial impact assessments using emulators. Thus, given the importance of tipping elements in possible future climates, further research, particularly using tools like the emulator developed here, is crucial to shed as much light as possible on the long-term consequences of the societal choices we make today.

## Code and Data Availability

The numerical codes of the various models used, including different versions of SURFER and the AGTCCM in its various configurations, can be found on the GitHub repository of this thesis : <https://github.com/AmauryLaridon/LPHYS2299-Master-s-Thesis>

Due to their substantial size, the data from the three cGenie simulations are available by contacting the author of this thesis. The Python script used to analyze these simulations is available on the GitHub repository.

All figures produced using the simulation data from SURFER, cGenie, or the AGTCCM are also available on the repository.

## Références

- [1] IPCC AR6 WGI Annex VII - Glossary.
- [2] ARMSTRONG MCKAY, D. I., STAAL, A., ABRAMS, J. F., WINKELMANN, R., SAKSCHEWSKI, B., LORIANI, S., FETZER, I., CORNELL, S. E., ROCKSTRÖM, J., AND LENTON, T. M. Exceeding 1.5°C global warming could trigger multiple climate tipping points. *Science* 377, 6611 (Sept. 2022), eabn7950.
- [3] ASHWIN, P., WIECZOREK, S., VITOLO, R., AND COX, P. Tipping points in open systems : bifurcation, noise-induced and rate-dependent examples in the climate system. *Philosophical Transactions of the Royal Society A : Mathematical, Physical and Engineering Sciences* 370, 1962 (Mar. 2012), 1166–1184. Publisher : Royal Society.
- [4] BETTS, R., SANDERSON, M., AND WOODWARD, S. Effects of large-scale Amazon forest degradation on climate and air quality through fluxes of carbon dioxide, water, energy, mineral dust and isoprene. *Philosophical Transactions of the Royal Society B : Biological Sciences* 363, 1498 (Feb. 2008), 1873–1880. Publisher : Royal Society.
- [5] BEUSCH, L., GUDMUNDSSON, L., AND SENEVIRATNE, S. I. Emulating Earth system model temperatures with MESMER : from global mean temperature trajectories to grid-point-level realizations on land. *Earth System Dynamics* 11, 1 (2020), 139–159. Accepted : 2020-02-28T09 :56 :14Z Publisher : Copernicus.
- [6] BROVKIN, V., BROOK, E., WILLIAMS, J. W., BATHIANY, S., LENTON, T. M., BARTON, M., DECONT, R. M., DONGES, J. F., GANOPOLSKI, A., McMANUS, J., PRAETORIUS, S., DE VERNAL, A., ABE-OUCHI, A., CHENG, H., CLAUSSEN, M., CRUCIFIX, M., GALLOPÍN, G., IGLESIAS, V., KAUFMAN, D. S., KLEINEN, T., LAMBERT, F., VAN DER LEEUW, S., LIDDY, H., LOUTRE, M.-F., MCGEE, D., REHFELD, K., RHODES, R., SEDDON, A. W. R., TRAUTH, M. H., VANDERVEKEN, L., AND YU, Z. Past abrupt changes, tipping points and cascading impacts in the Earth system. *Nature Geoscience* 14, 8 (Aug. 2021), 550–558. Publisher : Nature Publishing Group.
- [7] BUCKLEY, M. W., AND MARSHALL, J. The Importance of the Transition Zone to Decadal AMOC Variability. PO43A–08. Conference Name : American Geophysical Union, Ocean Sciences Meeting ADS Bibcode : 2016AGUOSPO43A..08B.

- [8] BUCKLEY, M. W., AND MARSHALL, J. Observations, inferences, and mechanisms of the Atlantic Meridional Overturning Circulation : A review. *Reviews of Geophysics* 54, 1 (2016), 5–63. \_eprint : <https://onlinelibrary.wiley.com/doi/10.1002/2015RG000493>.
- [9] BULGIN, C. E., MECKING, J. V., HARVEY, B. J., JEVREJEVA, S., MCCARROLL, N. F., MERCHANT, C. J., AND SINHA, B. Dynamic sea-level changes and potential implications for storm surges in the UK : a storylines perspective. *Environmental Research Letters* 18, 4 (Apr. 2023), 044033. Publisher : IOP Publishing.
- [10] CAESAR, L., RAHMSTORF, S., ROBINSON, A., FEULNER, G., AND SABA, V. Observed fingerprint of a weakening Atlantic Ocean overturning circulation. *Nature* 556, 7700 (Apr. 2018), 191–196. Number : 7700 Publisher : Nature Publishing Group.
- [11] CESSI, P. A Simple Box Model of Stochastically Forced Thermohaline Flow. *Journal of Physical Oceanography* 24, 9 (Sept. 1994), 1911–1920. Publisher : American Meteorological Society Section : Journal of Physical Oceanography.
- [12] CIMATORIBUS, A. A., DRIJFHOUT, S. S., AND DIJKSTRA, H. A. Meridional overturning circulation : stability and ocean feedbacks in a box model. *Climate Dynamics* 42, 1 (Jan. 2014), 311–328.
- [13] COUPLET, V. Investigating tipping cascades and the ‘hothouse narrative’ in the model of reduced complexity SURFER. *Personal Communication with the Author*.
- [14] COUPLET, V. Notes Personnelles de Thèse -Avril 2021. *Personal Communication with the Author* (Apr. 2021).
- [15] COUPLET, V. PhD Thesis : What I’ve done so far ... *Personal Communication with the Author* (Mar. 2021).
- [16] COUPLET, V., MARTÍNEZ MONTERO, M., AND CRUCIFIX, M. An extension of SURFER to study tipping cascades on multiple time scales. other, oral, May 2023.
- [17] COUPLET, V., MONTERO, M. M., AND CRUCIFIX, M. SURFER v3.0 : an upgrade of the carbon cycle for longer time scales. *Pre-print, Personal Communication with the Author*.
- [18] DEFRENCE, D., RAMSTEIN, G., CHARBIT, S., VRAC, M., FAMIEN, A. M., SULTAN, B., SWINGEDOUW, D., DUMAS, C., GEMENNE, F., ALVAREZ-SOLAS, J., AND VANDERLINDEN, J.-P. Consequences of rapid ice sheet melting on the Sahelian population vulnerability. *Proceedings of the National Academy of Sciences* 114, 25 (June 2017), 6533–6538. Publisher : Proceedings of the National Academy of Sciences.
- [19] DEKKER, M. M., VON DER HEYDT, A. S., AND DIJKSTRA, H. A. Cascading transitions in the climate system. *Earth System Dynamics* 9, 4 (Nov. 2018), 1243–1260. Publisher : Copernicus GmbH.
- [20] DIJKSTRA, H. A. *Nonlinear physical oceanography : a dynamical systems approach to the large scale ocean circulation and El Niño*, 2nd rev. and enlarged ed ed. No. v. 28 in Atmospheric and oceanographic sciences library. Springer, Dordrecht ; New York, 2005.

- [21] DITLEVSEN, P., AND DITLEVSEN, S. Warning of a forthcoming collapse of the Atlantic meridional overturning circulation. *Nature Communications* 14, 1 (July 2023), 4254. Number : 1 Publisher : Nature Publishing Group.
- [22] ELSWORTH, G., GALBRAITH, E., HALVERSON, G., AND YANG, S. Enhanced weathering and CO<sub>2</sub> drawdown caused by latest Eocene strengthening of the Atlantic meridional overturning circulation. *Nature Geoscience* 10, 3 (Mar. 2017), 213–216. Publisher : Nature Publishing Group.
- [23] FLORES, B. M., MONTOYA, E., SAKSCHEWSKI, B., NASCIMENTO, N., STAAL, A., BETTS, R. A., LEVIS, C., LAPOLA, D. M., ESQUÍVEL-MUELBERT, A., JAKOVAC, C., NOBRE, C. A., OLIVEIRA, R. S., BORMA, L. S., NIAN, D., BOERS, N., HECHT, S. B., TER STEEGE, H., ARIEIRA, J., LUCAS, I. L., BERENGUER, E., MARENKO, J. A., GATTI, L. V., MATTOS, C. R. C., AND HIROTA, M. Critical transitions in the Amazon forest system. *Nature* 626, 7999 (Feb. 2024), 555–564. Number : 7999 Publisher : Nature Publishing Group.
- [24] GARBE, J., ALBRECHT, T., LEVERMANN, A., DONGES, J. F., AND WINKELMANN, R. The hysteresis of the Antarctic Ice Sheet. *Nature* 585, 7826 (Sept. 2020), 538–544. Publisher : Nature Publishing Group.
- [25] GENT, P. R. A commentary on the Atlantic meridional overturning circulation stability in climate models. *Ocean Modelling* 122 (Feb. 2018), 57–66.
- [26] GIEC. Assessment Report 6 - Working Group 1, The Scientific physical base.
- [27] GOOSSE, H. *Climate System Dynamics and Modelling* :, 1 ed. Cambridge University Press, Aug. 2015.
- [28] GÉRARD, J., AND CRUCIFIX, M. Diagnosing the AMOC slowdown in a coupled model : a cautionary tale. *Preprint* (2024).
- [29] HAWKINS, E., SMITH, R. S., ALLISON, L. C., GREGORY, J. M., WOOLLINGS, T. J., POHLMANN, H., AND DE CUEVAS, B. Bistability of the Atlantic overturning circulation in a global climate model and links to ocean freshwater transport. *Geophysical Research Letters* 38, 10 (2011). \_eprint : <https://onlinelibrary.wiley.com/doi/pdf/10.1029/2011GL047208>.
- [30] HU, A., MEEHL, G. A., HAN, W., TIMMERMANN, A., OTTO-BLIESNER, B., LIU, Z., WASHINGTON, W. M., LARGE, W., ABE-OUCHI, A., KIMOTO, M., LAMBECK, K., AND WU, B. Role of the Bering Strait on the hysteresis of the ocean conveyor belt circulation and glacial climate stability. *Proceedings of the National Academy of Sciences* 109, 17 (Apr. 2012), 6417–6422. Publisher : Proceedings of the National Academy of Sciences.
- [31] IPCC. *Climate Change 2021 – The Physical Science Basis : Working Group I Contribution to the Sixth Assessment Report of the Intergovernmental Panel on Climate Change*, 1 ed. Cambridge University Press, 2021.
- [32] JACKSON, L. C., ALASTRUÉ DE ASENJO, E., BELLOMO, K., DANABASOGLU, G., HAAK, H., HU, A., JUNGCLAUS, J., LEE, W., MECCIA, V. L., SAENKO, O., SHAO, A., AND SWINGEDOUW, D. Understanding AMOC stability : the North Atlantic Hosing Model Intercomparison Project. *Geoscientific Model Development* 16, 7 (Apr. 2023), 1975–1995. Publisher : Copernicus GmbH.
- [33] JACKSON, L. C., BIASTOCH, A., BUCKLEY, M. W., DESBRUYÈRES, D. G., FRAJKA-WILLIAMS, E., MOAT, B., AND ROBSON, J. The evolution of the

- North Atlantic Meridional Overturning Circulation since 1980. *Nature Reviews Earth & Environment* 3, 4 (Apr. 2022), 241–254. Publisher : Nature Publishing Group.
- [34] JACKSON, L. C., KAHANA, R., GRAHAM, T., RINGER, M. A., WOOLLINGS, T., MECKING, J. V., AND WOOD, R. A. Global and European climate impacts of a slowdown of the AMOC in a high resolution GCM. *Climate Dynamics* 45, 11 (Dec. 2015), 3299–3316.
  - [35] JACKSON, L. C., AND WOOD, R. A. Hysteresis and Resilience of the AMOC in an Eddy-Permitting GCM. *Geophysical Research Letters* 45, 16 (2018), 8547–8556. \_eprint : <https://onlinelibrary.wiley.com/doi/pdf/10.1029/2018GL078104>.
  - [36] JACKSON, L. C., AND WOOD, R. A. Timescales of AMOC decline in response to fresh water forcing. *Climate Dynamics* 51, 4 (Aug. 2018), 1333–1350.
  - [37] KLOSE, A. K., DONGES, J. F., FEUDEL, U., AND WINKELMANN, R. Rate-induced tipping cascades arising from interactions between the Greenland Ice Sheet and the Atlantic Meridional Overturning Circulation. *Earth System Dynamics Discussions* (Sept. 2023), 1–25. Publisher : Copernicus GmbH.
  - [38] KRIEGLER, E., HALL, J. W., HELD, H., DAWSON, R., AND SCHELLNHUBER, H. J. Imprecise probability assessment of tipping points in the climate system. *Proceedings of the National Academy of Sciences* 106, 13 (Mar. 2009), 5041–5046. Publisher : Proceedings of the National Academy of Sciences.
  - [39] KUEHN, C. A mathematical framework for critical transitions : Bifurcations, fast–slow systems and stochastic dynamics. *Physica D : Nonlinear Phenomena* 240, 12 (June 2011), 1020–1035.
  - [40] KWIAKOWSKI, L., TORRES, O., BOPP, L., AUMONT, O., CHAMBERLAIN, M., CHRISTIAN, J. R., DUNNE, J. P., GEHLEN, M., ILYINA, T., JOHN, J. G., LENTON, A., LI, H., LOVENDUSKI, N. S., ORR, J. C., PALMIERI, J., SANTANA-FALCÓN, Y., SCHWINGER, J., SÉFÉRIAN, R., STOCK, C. A., TAGLIABUE, A., TAKANO, Y., TJIPUTRA, J., TOYAMA, K., TSUJINO, H., WATANABE, M., YAMAMOTO, A., YOOL, A., AND ZIEHN, T. Twenty-first century ocean warming, acidification, deoxygenation, and upper-ocean nutrient and primary production decline from CMIP6 model projections. *Biogeosciences* 17, 13 (July 2020), 3439–3470. Publisher : Copernicus GmbH.
  - [41] LENAERTS, J. T. M., LE BARS, D., VAN KAMPENHOUT, L., VIZCAINO, M., ENDERLIN, E. M., AND VAN DEN BROEKE, M. R. Representing Greenland ice sheet freshwater fluxes in climate models. *Geophysical Research Letters* 42, 15 (2015), 6373–6381. \_eprint : <https://onlinelibrary.wiley.com/doi/pdf/10.1002/2015GL064738>.
  - [42] LENTON, T. M., AND CISCAR, J.-C. Integrating tipping points into climate impact assessments. *Climatic Change* 117, 3 (Apr. 2013), 585–597.
  - [43] LENTON, T. M., HELD, H., KRIEGLER, E., HALL, J. W., LUCHT, W., RAHMSTORF, S., AND SCHELLNHUBER, H. J. Tipping elements in the Earth’s climate system. *Proceedings of the National Academy of Sciences* 105, 6 (Feb. 2008), 1786–1793. Publisher : Proceedings of the National Academy of Sciences.

- [44] LENTON, T. M., ROCKSTRÖM, J., GAFFNEY, O., RAHMSTORF, S., RICHARDSON, K., STEFFEN, W., AND SCHELLNHUBER, H. J. Climate tipping points — too risky to bet against. *Nature* 575, 7784 (Nov. 2019), 592–595. Bandiera\_ab-test : a Cg\_type : Comment Number : 7784 Publisher : Nature Publishing Group Subject\_term : Climate change, Climate sciences, Environmental sciences, Policy.
- [45] LENTON, T. M., AND WILLIAMS, H. T. P. On the origin of planetary-scale tipping points. *Trends in Ecology & Evolution* 28, 7 (July 2013), 380–382. Publisher : Elsevier.
- [46] LIU, W., XIE, S.-P., LIU, Z., AND ZHU, J. Overlooked possibility of a collapsed Atlantic Meridional Overturning Circulation in warming climate. *Science Advances* 3, 1 (Jan. 2017), e1601666.
- [47] LOHMANN, J., CASTELLANA, D., DITLEVSEN, P. D., AND DIJKSTRA, H. A. Abrupt climate change as a rate-dependent cascading tipping point. *Earth System Dynamics* 12, 3 (July 2021), 819–835. Publisher : Copernicus GmbH.
- [48] LOHMANN, J., DIJKSTRA, H. A., JOCHUM, M., LUCARINI, V., AND DITLEVSEN, P. D. Multistability and Intermediate Tipping of the Atlantic Ocean Circulation, Apr. 2023. arXiv :2304.05664 [nlin, physics :physics].
- [49] LOHMANN, J., AND DITLEVSEN, P. D. Risk of tipping the overturning circulation due to increasing rates of ice melt. *Proceedings of the National Academy of Sciences* 118, 9 (Mar. 2021), e2017989118. Publisher : Proceedings of the National Academy of Sciences.
- [50] LYNCH-STIEGLITZ, J. The Atlantic Meridional Overturning Circulation and Abrupt Climate Change. *Annual Review of Marine Science* 9, Volume 9, 2017 (Jan. 2017), 83–104. Publisher : Annual Reviews.
- [51] LYRA, A. D. A., CHOU, S. C., AND SAMPAIO, G. D. O. Sensitivity of the Amazon biome to high resolution climate change projections. *Acta Amazonica* 46 (June 2016), 175–188. Publisher : Instituto Nacional de Pesquisas da Amazônia.
- [52] MARTÍNEZ MONTERO, M., CRUCIFIX, M., COUPLET, V., BREDE, N., AND BOTTA, N. SURFER v2.0 : a flexible and simple model linking anthropogenic CO<sub>2</sub> emissions and solar radiation modification to ocean acidification and sea level rise. *Geoscientific Model Development* 15, 21 (Nov. 2022), 8059–8084. Publisher : Copernicus GmbH.
- [53] MECKING, J. V., DRIJFHOUT, S. S., JACKSON, L. C., AND GRAHAM, T. Stable AMOC off state in an eddy-permitting coupled climate model. *Climate Dynamics* 47, 7 (Oct. 2016), 2455–2470.
- [54] MILKOREIT, M. Social tipping points everywhere?—Patterns and risks of overuse. *WIREs Climate Change* 14, 2 (2023), e813. \_eprint : <https://onlinelibrary.wiley.com/doi/pdf/10.1002/wcc.813>.
- [55] MORLIGHEM, M., WILLIAMS, C. N., RIGNOT, E., AN, L., ARNDT, J. E., BAMBER, J. L., CATANIA, G., CHAUCHÉ, N., DOWDESWELL, J. A., DORSCHEL, B., FENTY, I., HOGAN, K., HOWAT, I., HUBBARD, A., JAKOBSSON, M., JORDAN, T. M., KJELDSEN, K. K., MILLAN, R., MAYER, L., MOUGINOT, J., NOËL, B. P. Y., O'COFAIGH, C., PALMER, S., RYSGAARD, S., SE-ROUSSI, H., SIEGERT, M. J., SLABON, P., STRANEO, F., VAN DEN BROEKE,

- M. R., WEINREBE, W., WOOD, M., AND ZINGLERSEN, K. B. BedMachine v3 : Complete Bed Topography and Ocean Bathymetry Mapping of Greenland From Multibeam Echo Sounding Combined With Mass Conservation. *Geophysical Research Letters* 44, 21 (2017), 11,051–11,061. \_eprint : <https://onlinelibrary.wiley.com/doi/pdf/10.1002/2017GL074954>.
- [56] NOBRE, P., VEIGA, S. F., GIAROLLA, E., MARQUEZ, A. L., DA SILVA, M. B., CAPISTRANO, V. B., MALAGUTTI, M., FERNANDEZ, J. P. R., SOARES, H. C., BOTTINO, M. J., KUBOTA, P. Y., FIGUEROA, S. N., BONATTI, J. P., SAMPAIO, G., CASAGRANDE, F., COSTA, M. C., AND NOBRE, C. A. AMOC decline and recovery in a warmer climate. *Scientific Reports* 13, 1 (Sept. 2023), 15928. Number : 1 Publisher : Nature Publishing Group.
- [57] RAHMSTORF, S. On the freshwater forcing and transport of the Atlantic thermohaline circulation. *Climate Dynamics* 12, 12 (Nov. 1996), 799–811.
- [58] RAHMSTORF, S., CRUCIFIX, M., GANOPOLSKI, A., GOOSSE, H., KAMENKOVICH, I., KNUTTI, R., LOHMAN, G., MARSH, R., MYSAK, L. A., WANG, Z., AND WEAVER, A. J. Thermohaline circulation hysteresis : A model intercomparison. *Geophysical Research Letters* 32, 23 (2005). \_eprint : <https://onlinelibrary.wiley.com/doi/pdf/10.1029/2005GL023655>.
- [59] RAHMSTORF, S., AND GANOPOLSKI, A. Long-Term Global Warming Scenarios Computed with an Efficient Coupled Climate Model. *Climatic Change* 43, 2 (Oct. 1999), 353–367.
- [60] RIDGWELL, A. cGENIE.muffin EMIC Documentation.
- [61] RITCHIE, P., KARABACAK, , AND SIEBER, J. Inverse-square law between time and amplitude for crossing tipping thresholds. *Proceedings of the Royal Society A : Mathematical, Physical and Engineering Sciences* 475, 2222 (Feb. 2019), 20180504. Publisher : Royal Society.
- [62] RITCHIE, P. D. L., CLARKE, J. J., COX, P. M., AND HUNTINGFORD, C. Overshooting tipping point thresholds in a changing climate. *Nature* 592, 7855 (Apr. 2021), 517–523. Publisher : Nature Publishing Group.
- [63] ROBERTSON, F. R., ROBERTS, J. B., BOSLOVICH, M. G., BENTAMY, A., CLAYSON, C. A., FENNIG, K., SCHRÖDER, M., TOMITA, H., COMPO, G. P., GUTENSTEIN, M., HERSBACH, H., KOBAYASHI, C., RICCIARDULLI, L., SARDESHMUKH, P., AND SLIVINSKI, L. C. Uncertainties in Ocean Latent Heat Flux Variations over Recent Decades in Satellite-Based Estimates and Reduced Observation Reanalyses. *Journal of Climate* 33, 19 (Oct. 2020), 8415–8437. Publisher : American Meteorological Society Section : Journal of Climate.
- [64] ROBINSON, A., CALOV, R., AND GANOPOLSKI, A. Multistability and critical thresholds of the Greenland ice sheet. *Nature Climate Change* 2, 6 (June 2012), 429–432. Number : 6 Publisher : Nature Publishing Group.
- [65] ROMANOU, A., RIND, D., JONAS, J., MILLER, R., KELLEY, M., RUSSELL, G., ORBE, C., NAZARENKO, L., LATTO, R., AND SCHMIDT, G. A. Stochastic Bifurcation of the North Atlantic Circulation under a Midrange Future Climate Scenario with the NASA-GISS ModelE. *Journal of Climate* 36, 18 (Aug. 2023), 6141–6161. Publisher : American Meteorological Society Section : Journal of Climate.

- [66] SCHELLNHUBER, H. J., RAHMSTORF, S., AND WINKELMANN, R. Why the right climate target was agreed in Paris. *Nature Climate Change* 6, 7 (July 2016), 649–653. Publisher : Nature Publishing Group.
- [67] SCHWINGER, J., ASAADI, A., GORIS, N., AND LEE, H. Possibility for strong northern hemisphere high-latitude cooling under negative emissions. *Nature Communications* 13, 1 (Mar. 2022), 1095. Publisher : Nature Publishing Group.
- [68] SINET, S., VON DER HEYDT, A. S., AND DIJKSTRA, H. A. AMOC Stabilization Under the Interaction With Tipping Polar Ice Sheets. *Geophysical Research Letters* 50, 2 (2023), e2022GL100305. \_eprint : <https://onlinelibrary.wiley.com/doi/pdf/10.1029/2022GL100305>.
- [69] STEFFEN, W., ROCKSTRÖM, J., RICHARDSON, K., LENTON, T. M., FOLKE, C., LIVERMAN, D., SUMMERHAYES, C. P., BARNOSKY, A. D., CORNELL, S. E., CRUCIFIX, M., DONGES, J. F., FETZER, I., LADE, S. J., SCHEFFER, M., WINKELMANN, R., AND SCHELLNHUBER, H. J. Trajectories of the Earth System in the Anthropocene. *Proceedings of the National Academy of Sciences* 115, 33 (Aug. 2018), 8252–8259. Publisher : Proceedings of the National Academy of Sciences.
- [70] STOCKER, T. F., AND SCHMITTNER, A. Influence of CO<sub>2</sub> emission rates on the stability of the thermohaline circulation. *Nature* 388, 6645 (Aug. 1997), 862–865. Number : 6645 Publisher : Nature Publishing Group.
- [71] STOMMEL, H. Thermohaline convection with two stable regimes of flow. *Taylor & Francis*.
- [72] STOUFFER, R. J., YIN, J., GREGORY, J. M., DIXON, K. W., SPELMAN, M. J., HURLIN, W., WEAVER, A. J., EBY, M., FLATO, G. M., HASUMI, H., HU, A., JUNGCLAUS, J. H., KAMENKOVICH, I. V., LEVERMANN, A., MONTOYA, M., MURAKAMI, S., NAWRATH, S., OKA, A., PELTIER, W. R., ROBITAILLE, D. Y., SOKOLOV, A., VETTORETTI, G., AND WEBER, S. L. Investigating the Causes of the Response of the Thermohaline Circulation to Past and Future Climate Changes. *Journal of Climate* 19, 8 (Apr. 2006), 1365–1387. Publisher : American Meteorological Society Section : Journal of Climate.
- [73] STROGATZ, S. H. *Nonlinear Dynamics and Chaos : With Applications to Physics, Biology, Chemistry, and Engineering*, 2 ed. CRC Press, Boca Raton, May 2019.
- [74] SWINGEDOUW, D., HOUSAIS, M.-N., HERBAUT, C., BLAIZOT, A.-C., DEVILIERS, M., AND DESHAYES, J. AMOC Recent and Future Trends : A Crucial Role for Oceanic Resolution and Greenland Melting? *Frontiers in Climate* 4 (2022).
- [75] T. M. LENTON, L. LABOURN, D. A. M. S. L. J. A. S. L. J. D. M. M. S. S. E. B. T. P. L. F. C. Z. C. B. J. B. J. D. A. G. Global Tipping Point Report 2023 : 'Full Report'.
- [76] VAN BREEDAM, J., GOELZER, H., AND HUYBRECHTS, P. Semi-equilibrated global sea-level change projections for the next 10&thinsp;000 years. *Earth System Dynamics* 11, 4 (Nov. 2020), 953–976. Publisher : Copernicus GmbH.
- [77] VAN WESTEN, R. M., KLIPHUIS, M., AND DIJKSTRA, H. A. New Physics-Based Early Warning Signal shows AMOC is on Tipping Course, Aug. 2023. arXiv :2308.01688 [physics].

- [78] VAN WESTEN, R. M., KLIPHUIS, M., AND DIJKSTRA, H. A. Physics-based early warning signal shows that AMOC is on tipping course. *Science Advances* 10, 6 (Feb. 2024), eadk1189.
- [79] VON DER HEYDT, A. S., ASHWIN, P., CAMP, C. D., CRUCIFIX, M., DIJKSTRA, H. A., DITLEVSEN, P., AND LENTON, T. M. Quantification and interpretation of the climate variability record. *Global and Planetary Change* 197 (Feb. 2021), 103399.
- [80] WANG, S., FOSTER, A., LENZ, E. A., KESSLER, J. D., STROEVE, J. C., ANDERSON, L. O., TURETSKY, M., BETTS, R., ZOU, S., LIU, W., BOOS, W. R., AND HAUSFATHER, Z. Mechanisms and Impacts of Earth System Tipping Elements. *Reviews of Geophysics* 61, 1 (2023), e2021RG000757. \_eprint : <https://onlinelibrary.wiley.com/doi/pdf/10.1029/2021RG000757>.
- [81] WEIJER, W., CHENG, W., DRIJFHOUT, S. S., FEDOROV, A. V., HU, A., JACKSON, L. C., LIU, W., McDONAGH, E. L., MECKING, J. V., AND ZHANG, J. Stability of the Atlantic Meridional Overturning Circulation : A Review and Synthesis. *Journal of Geophysical Research : Oceans* 124, 8 (2019), 5336–5375. \_eprint : <https://onlinelibrary.wiley.com/doi/pdf/10.1029/2019JC015083>.
- [82] WEIJER, W., CHENG, W., GARUBA, O. A., HU, A., AND NADIGA, B. T. CMIP6 Models Predict Significant 21st Century Decline of the Atlantic Meridional Overturning Circulation. *Geophysical Research Letters* 47, 12 (2020), e2019GL086075. \_eprint : <https://onlinelibrary.wiley.com/doi/pdf/10.1029/2019GL086075>.
- [83] WEIJER, W., MALTRUD, M. E., HECHT, M. W., DIJKSTRA, H. A., AND KLIPHUIS, M. A. Response of the Atlantic Ocean circulation to Greenland Ice Sheet melting in a strongly-eddying ocean model. *Geophysical Research Letters* 39, 9 (2012). \_eprint : <https://onlinelibrary.wiley.com/doi/pdf/10.1029/2012GL051611>.
- [84] WIECZOREK, S., ASHWIN, P., LUKE, C. M., AND COX, P. M. Excitability in ramped systems : the compost-bomb instability. *Proceedings of the Royal Society A : Mathematical, Physical and Engineering Sciences* 467, 2129 (Nov. 2010), 1243–1269. Publisher : Royal Society.
- [85] WUNDERLING, N., DONGES, J. F., KURTHS, J., AND WINKELMANN, R. Interacting tipping elements increase risk of climate domino effects under global warming. *Earth System Dynamics* 12, 2 (June 2021), 601–619. Publisher : Copernicus GmbH.
- [86] WUNDERLING, N., GELBRECHT, M., WINKELMANN, R., KURTHS, J., AND DONGES, J. F. Basin stability and limit cycles in a conceptual model for climate tipping cascades. *New Journal of Physics* 22, 12 (Dec. 2020), 123031. Publisher : IOP Publishing.
- [87] WUNDERLING, N., STUMPF, B., KRÖNKE, J., STAAL, A., TUINENBURG, O. A., WINKELMANN, R., AND DONGES, J. F. How motifs condition critical thresholds for tipping cascades in complex networks : Linking micro- to macro-scales. *Chaos : An Interdisciplinary Journal of Nonlinear Science* 30, 4 (Apr. 2020), 043129.
- [88] WUNDERLING, N., VON DER HEYDT, A. S., AKSENOV, Y., BARKER, S., BASTIAANSEN, R., BROVKIN, V., BRUNETTI, M., COUPLET, V., KLEINEN, T.,

- LEAR, C. H., LOHMANN, J., ROMAN-CUESTA, R. M., SINET, S., SWINGEDOUW, D., WINKELMANN, R., ANAND, P., BARICHIVICH, J., BATHIANY, S., BAUDENA, M., BRUUN, J. T., CHIESI, C. M., COXALL, H. K., DOCQUIER, D., DONGES, J. F., FALKENA, S. K. J., KLOSE, A. K., OBURA, D., ROCHA, J., RYNDERS, S., STEINERT, N. J., AND WILLEIT, M. Climate tipping point interactions and cascades : a review. *Earth System Dynamics* 15, 1 (Jan. 2024), 41–74. Publisher : Copernicus GmbH.
- [89] ZICKFELD, K., EBY, M., AND WEAVER, A. J. Carbon-cycle feedbacks of changes in the Atlantic meridional overturning circulation under future atmospheric CO<sub>2</sub>. *Global Biogeochemical Cycles* 22, 3 (2008). \_eprint : <https://onlinelibrary.wiley.com/doi/pdf/10.1029/2007GB003118>.